



Minnesota State University, Mankato
**Cornerstone: A Collection of Scholarly
and Creative Works for Minnesota
State University, Mankato**

All Graduate Theses, Dissertations, and Other
Capstone Projects

Graduate Theses, Dissertations, and Other
Capstone Projects

2015

Air Flow and Rain Water Penetration Analysis on Generator Enclosures Using CFD Simulations

Sasanka Andawatta Kankanamge
Minnesota State University - Mankato

Follow this and additional works at: <https://cornerstone.lib.mnsu.edu/etds>



Part of the [Automotive Engineering Commons](#), and the [Mechanical Engineering Commons](#)

Recommended Citation

Andawatta Kankanamge, S. (2015). Air Flow and Rain Water Penetration Analysis on Generator Enclosures Using CFD Simulations [Master's thesis, Minnesota State University, Mankato]. Cornerstone: A Collection of Scholarly and Creative Works for Minnesota State University, Mankato. <https://cornerstone.lib.mnsu.edu/etds/434/>

This Thesis is brought to you for free and open access by the Graduate Theses, Dissertations, and Other Capstone Projects at Cornerstone: A Collection of Scholarly and Creative Works for Minnesota State University, Mankato. It has been accepted for inclusion in All Graduate Theses, Dissertations, and Other Capstone Projects by an authorized administrator of Cornerstone: A Collection of Scholarly and Creative Works for Minnesota State University, Mankato.

Air Flow and Rain Water Penetration Analysis on Generator Enclosures Using CFD Simulations

By

Sasanka, Andawatta Kankanamge

A Thesis Submitted in Partial Fulfillment of the requirements for the

Master of Science Degree

In

Automotive Engineering Technology

Minnesota State University, Mankato

Mankato, Minnesota

May 2015

Air Flow and Rain Water Penetration Analysis on Generator Enclosures Using
CFD Simulations

Sasanka, Andawatta Kankanamge

This thesis has been examined and approved by the following members of the
student's committee.

Dr. Bruce Jones - Advisor

Dr. Gary Mead - Committee Member

Dr. Kuldeep Agarwal - Committee Member

Abstract

Rain water penetration testing on power generator units requires a number of complicated procedures, requiring many resources. As such, a Computational Fluid Dynamics (CFD) tool, “FloEFD for Creo,” is used to study the water penetration behavior on a OM924 diesel power generator enclosure in a computational environment. First, the three governing equations in fluid dynamics are derived and explained using simple methods. Next, behavior of rain water droplets upon impact is briefly discussed. Air velocity, volumetric flow rate and static pressure drop were measured physically in the OM924 generator enclosure. Then, a CFD model for the OM924 enclosure was developed and validated using the measured data. Using the particle studies option in FloEFD, rain water penetration studies were conducted on the CFD model. The terminal velocity of the droplets was assumed as a function of droplet diameter and the coefficient of restitution was measured using basic observational methods. In an enclosure, the water penetration can be explained using three methods; free flowing, dripping and splashing. Each of the methods was tested using water droplet diameters that ranged from 0.1 to 2.5 mm. Results verified that the current baffle plate design was capable of preventing water penetration with the exception of those droplets with the smallest diameters.

Key words: Modeling and simulations, fluid as particle packets, forces and stress on fluids, fluid dynamic governing equations, material derivation, computational fluid dynamics and rain water penetration testing.

Table of Contents

ABSTRACT	II
ACKNOWLEDGEMENTS	V
LIST OF TABLES.....	VI
LIST OF FIGURES	VII
INTRODUCTION.....	1
LITERATURE REVIEW	2
1.1 INTRODUCTION FOR MODELING AND SIMULATIONS	2
1.1.1 <i>History of Modeling and Simulations.....</i>	3
1.1.2 <i>What is modeling.....</i>	6
1.1.3 <i>What are Simulations</i>	7
1.2 FLUID DYNAMICS	9
1.2.1 <i>Fluid vs. Solid</i>	10
1.2.2 <i>The theory of fluid as particle packets.....</i>	11
1.2.3 <i>Fluid Kinematics.....</i>	11
1.2.4 <i>Forces and stresses</i>	15
1.3 MATERIAL DERIVATIVE AND GOVERNING EQUATIONS	24
1.4 COMPUTATIONAL FLUID DYNAMICS (CFD)	51
1.4.1 <i>Problem Identification and Pre-Process.....</i>	53
1.4.2 <i>Numerical Analysis and CFD Solver</i>	61
1.4.3 <i>Results, analysis and visualization.....</i>	63
1.4.4 <i>Finite Volume Method (FVM)</i>	64
1.5 MTU ONSITE ENERGY GENERATORS	65
1.6 RAIN WATER TESTING	67
1.7 BEHAVIOR OF WATER DROPLETS.....	68
1.7.1 <i>Droplet Diameter</i>	72
1.7.2 <i>Droplet Terminal velocity.....</i>	72
1.7.3 <i>Coefficient of Restitution</i>	74
2 OM924 GENERATOR CFD MODEL DESIGN	76
2.1.1 <i>OM924 CFD Model 1.....</i>	77
2.1.2 <i>OM924 CFD Model 2.....</i>	80
2.1.3 <i>OM924 CFD Model 3.....</i>	82
3 VALIDATION OF THE MODEL.....	85
3.1 VELOCITY DATA	85
3.1.1 <i>Measured Air Velocity Values</i>	86
3.1.2 <i>Simulated Air Velocity Values.....</i>	87
3.2 VOLUMETRIC FLOW RATE DATA	90
3.2.1 <i>Measured Volumetric Flow Rate Values.....</i>	90
3.2.2 <i>Simulated Volumetric Flow Rate Values.....</i>	91
3.3 PRESSURE LOST DATA.....	92

3.3.1	Measured Static Pressure Values.....	94
3.3.2	Simulated Pressure Values.....	94
3.4	DISCUSSION OF THE CFD MODEL	98
4	RAIN WATER PENETRATION ANALYSIS.....	101
4.1	FREE FLOWING	103
4.2	DRIPPING	109
4.2.1	<i>Dripping at the inlet grill.....</i>	<i>110</i>
4.2.2	<i>Dripping at the blade.....</i>	<i>113</i>
4.3	SPLASHING	121
5	DISCUSSION AND RECOMMENDATIONS	122
6	BIBLIOGRAPHY.....	123
	APPENDIX A	126
	Appendix A-1.....	126
	Appendix A-2.....	127
	APPENDIX B	129
	APPENDIX C.....	133
	APPENDIX D	150
	APPENDIX E.....	151
	APPENDIX E.1.....	151
	APPENDIX E.2.....	153
	APPENDIX E.3.....	155
	APPENDIX F.....	157
	APPENDIX G	161
	APPENDIX H	163
	APPENDIX H.1.....	163
	APPENDIX H.2.....	165
	APPENDIX H.3.....	167
	APPENDIX I.....	171
	APPENDIX J	193
	APPENDIX K.....	198
	APPENDIX L	206
	APPENDIX M	212

Acknowledgements

The author would like to thank those who helped this research come to fulfillment:

Dr. Bruce Jones

Dr. Garry Mead

Dr. Kuldeep Agarwal

MTU Onsite Energy, Mankato

Mr. JD Carsten

Mr. Paul Steevens

Mrs. Rishani De Costa

Mr. Todd Redmann

Mr. Suranga Uduwage

List of tables

Table 1 Average measured air flow velocity of the enclosure.....	87
Table 2 Simulated velocity magnitude on the right side inlet grill. Yellow – 700 range, green – 800 range, red – 900 range.....	89
Table 3 Simulated velocity magnitude on the left side inlet grill. Yellow – 600 range, green – 700 range, blue – 800 range, red – 900 range, purple – 1000 range.	89
Table 4 Summary of the outlet air velocity	90
Table 5 Volumetric flow rate at outlet.....	91
Table 6 Static pressure values inside and outside the enclosure	98
Table 7 Measured Vs. Simulated velocity values - right side inlet 2.....	99
Table 8 Terminal Velocity as a function of diameter.....	106
Table 10 Goal plot 1 with stopping criteria. The average flow rate value should be used for calculations	161
Table 11 Surface parameter for volumetric flow rate. Outside face of the outlet lid was selected. The value is a negative number indicating the air is flowing outside that face.	161
Table 12 Surface parameter for volumetric flow rate. Outside face of the right-side inlet lid was selected.....	162
Table 13 Surface parameter for volumetric flow rate. Outside face of the left-side inlet lid was selected.....	162
Table 14 Right Side Air Velocity Point Study.....	164
Table 15 Left Side Air Velocity Point Study.....	166
Table 16 Left Inlet static pressure data.....	173
Table 17 Right Inlet static pressure data	176
Table 18 Middle front, static pressure data.....	184
Table 19 Middle side, static pressure data	192

List of Figures

Figure 1 A flow chart of a basic M&S system processors (Maria, 1997, p. 8).....	8
Figure 2 One dimensional example of a Lagrangian Method.....	13
Figure 3 One dimensional example of a Eulerian Method	14
Figure 4 One dimensional example of an ALS method.....	15
Figure 5 Forces acting on a microscopic fluid particle (Hauke, 2008, p. 36)	17
Figure 6 Pressure inserting on all directions (Hauke, 2008, p. 34)	18
Figure 7 Surface of fluid used to demonstrate the traction and stress tensor.....	19
Figure 8 Stress tensor on a 3D fluid particle stacked on one point (Pozrikidis, 2009, p. 167)	21
Figure 9 Normal Stress.....	23
Figure 10 Shear stress.....	23
Figure 11 Location of a fluid particle expressed in a Cartesian coordinates system.....	26
Figure 12 Surface forces acting on the x-direction of a fluid particle (Wendt, Anderson, & Von Karman Institute, 2008)	38
Figure 13 Energy acting on the x direction of a fluid particle (Wendt, Anderson, & Von Karman Institute, 2008).....	46
Figure 14 Flow process of a CFD modeling	52
Figure 15 Relationship of the main elements.....	53
Figure 16 Model 1: flowing between two plates (Tu & Yeoh, Guan Heng, 2007, p. 34)	54
Figure 17 Model 2: Flowing around two cylinders (Tu & Yeoh, Guan Heng, 2007, p. 34).....	55
Figure 18 simple structured meshing for Model 1 (Tu & Yeoh, Guan Heng, 2007, p. 36).....	57
Figure 19 complex unstructured meshing for Model 2 (Tu & Yeoh, Guan Heng, 2007, p. 37)	57
Figure 20 Hybrid mesh (Kleinstreuer, 2010, p. 528).....	58
Figure 21 Flowchart for applying various physics for CFD tools (Tu & Yeoh, Guan Heng, 2007) ..	59
Figure 22 Basic boundary condition of a simple Model.....	60
Figure 23 Boundary conditions of model 2 (Tu & Yeoh, Guan Heng, 2007, p. 42).....	60
Figure 24 monitoring the iterations using a GUI in FloEFD software	63
Figure 25 18V 2000 Generator Set (MTU Onsite Energy)	65
Figure 26 (MTU Onsite Energy).....	66
Figure 27 drop motion A) deposition, B) partial rebound, C) full rebound, D) break up, E) splashing (Van der Wal, 2006)	70
Figure 28 surface tension acting on a droplet (Yuan & Lee, 2013).....	71
Figure 29 Rainwater droplet size vs. shape (Mook, 2003).....	72
Figure 30 Free body diagram of a rain water droplet.....	73
Figure 31 Contact angle on a smooth solid (Yuan & Lee, 2013, p. 4)	75
Figure 32 OM924 Generator Enclosure Original CAD Model	76
Figure 33 OM924 original model – Doors has been removed to illustrate the inside of the enclosure.....	77
Figure 34 CFD Model 1 - crucial components for air flow were imported from the original model and mated as coincident style	78

Figure 35 CFD Model 1 with inlet and outlet covers (in yellow). The fluid domain is sealed using lids (in green). Each lid will act as and boundary as well.	80
Figure 36 CFD model 2 - fan is located outside the enclosure as an external outlet fan	82
Figure 37 volume shrink-wrap of the engine, generator and the master box assembly. The part is hollow inside and only the outer shell is visible.	83
Figure 38 CFD model 3	84
Figure 39 Anemometer is attached to a flat plate, so that the air flow is parallel to the anemometer.	85
Figure 40 Anemometer was placed on each inlet 1 and 2 according to a grid pattern.	86
Figure 41 Air velocity at the right side inlet. High of 1471 ft/min [red] and low of 0 ft/min [Blue]	87
Figure 42 Flow trajectories of the air particles.	88
Figure 43 The red dots marks the locations at which the velocity was simulated	88
Figure 44 front view Cut plot of dynamic pressure inside the enclosure. The cut plot was placed in the middle of the enclosure ($y=0$).....	95
Figure 45 side view Cut plot of dynamic pressure inside the enclosure. Cut plot was placed in the middle of the enclose ($x=0$)	95
Figure 46 Static pressure at the front of the enclosure.....	96
Figure 47 Static pressure at the back of the enclosure	97
Figure 48 The camera was placed parallel to the impact surface.	103
Figure 49 Baffle plate and the blade.....	104
Figure 50 Contour plot in velocity at middle of the enclosure.	105
Figure 51 water droplet injection plane.	107
Figure 52 Water droplet size 0.1 mm. Some of the droplets get carried by the air flow	108
Figure 53 Top view of the 0.1 mm diamter droplets	108
Figure 54 Baffle plate, blade and the inlet grill. Front view.....	109
Figure 55 0.1 mm diameter droplets will penetrate the enclosure.....	111
Figure 56 0.1 mm droplet size penetration location. Top view.....	112
Figure 57 Contour plot across the baffle plate illustrate high velocity near the solid wall and the two sides of the baffle plate	113
Figure 58 Injection point was defined as the bottom surface.....	114
Figure 59 Air flow velocity at the baffle plate. Zoomed into highlight the blade and the lips	115
Figure 60 0.1mm diameter size. Penetration occurs severely.....	116
Figure 61 0.75 mm diameter size. Penetration occurs at the middle and two sides (black circle)	117
Figure 62 Combination of contour plot of velocity and particle study data. This view is presented from the left side in order to bring the particles in front of the plot. The higher simulated velocities near the midpoint and at the two sides are highlighted in the black circles.	118
Figure 63 Droplet size 1.0 mm. Penetration only happens near the middle.....	119
Figure 64 1.5 mm diameter. No penetration.....	120
Figure 65 Rain water test structure	126
Figure 66 Rain water test structure nozzle design.....	127

Figure 67 Water droplet formation at the nozzle.....	128
Figure 68 Fan data - 1	129
Figure 69 Fan data - 02	130
Figure 70 Fan data - 03	131
Figure 71 Fan data was entered to the engineering data base in FloEFD. The curve is developed using the data supplied by multi-wing.....	132
Figure 72 OM924 Engine and Generator, without the enclosure	150
Figure 73 CFD Model 1 front view	151
Figure 74 CFD Model 1 Side View	151
Figure 75 Baffle plates and blades helps to stop water penetration.....	152
Figure 76 CFD model 1 front view	152
Figure 77 in the original CAD model, the fan is located inside the enclosure next to the engine	153
Figure 78 CFD model 2 – the fan is located outside the enclosure	154
Figure 79 CFD model 2, isometric view without side air inlet covers.....	154
Figure 80 Complete CFD model 3 in isometric view	155
Figure 81 CFD model 3. Top view	156
Figure 82 OM924 inlet air flow data and points	158
Figure 83 OM924 outlet air flow data and points	159
Figure 84 OM924 Engine data	160
Figure 85 Outlet air velocity point study locations.....	169
Figure 86 Flow trajectory	170
Figure 87 Droplet size 0.2 mm. No penetration	193
Figure 88 Droplet size 0.3 mm. No penetration	194
Figure 89 Droplet size 0.5 mm. No penetration	195
Figure 90 Droplet size 1 mm. No penetration	196
Figure 91 Droplet size 2mm. No penetration	197
Figure 92 Droplet size 0.1 mm. The penetrating trajectory can be tracked using lines.....	198
Figure 93 Droplet size 0.25 mm. No penetration	199
Figure 94 Droplet size 0.5 mm. No penetration	200
Figure 95 Droplet size 0.75 mm. No penetration	201
Figure 96 Droplet size 1.0 mm. No penetration	202
Figure 97 Droplet size 1.5 mm. No penetration	203
Figure 98 Droplet size 2.0 mm. No penetration	204
Figure 99 Droplet size 2.5 mm. No penetration	205
Figure 100 Droplet size 0.25 mm. Water penetration occurs	206
Figure 101 Droplet size 0.25 mm, top view. Water penetration occurs.....	207
Figure 102 Droplet size 0.75 mm. Water penetration occurs	208
Figure 103 Droplet size 0.75 mm. Water penetration occurs at the middle and two sides.....	209
Figure 104 Droplet size 1.0 mm. Penetration only visible in the middle.....	209
Figure 105 Droplet size 2.0 mm. No penetration	210
Figure 106 Droplet size 2.5 mm. No penetration	211

Figure 107 Mesh - Front view	212
Figure 108 Mesh - Side view	213
Figure 109 A local initial mesh was assign to baffle plates. Baffle lips are 10mm wide, hence this area needed to be precisely calculated.	214

Introduction

Modeling and simulations (M & S) have developed impressively in most of the academic and industrial disciplines over the past decades. Currently, it is recognized as a National Critical Technology by the U.S Government. Fluid dynamic modeling is the most frequently used M&S system, used in nearly every science and engineering discipline. Fluid dynamics is the study of fluid flow, convective heat transfer and species mass transfer. When fluid dynamics concepts are applied within a computational environment (CFD), a set of mathematical methods are used to obtain an approximate solution for a particular application. Fluid Dynamics are governed by three principles; the conservations of mass, Newton's second law and the conservation of energy. This paper illustrates the derivation of the governing equations using more traditional methods. Afterward, the general computational fluid dynamic methods and rain water droplet behavior are explained.

A CFD model of the OM924 diesel powered generator enclosure is designed using the Creo computer-aided drafting tool. Then, using FloEFD, a computational software tool, the model was simulated and the results were validated against measured data. Air flow velocity, volumetric flow rate and the static pressure drop were compared and calculated for errors. Finally, using the particle study option on FloEFD, the model was tested for rain water penetration.

Literature Review

1.1 Introduction for Modeling and Simulations

On July 2007, U.S. House Resolution 487 officially reorganized Modeling and Simulation (M&S) as a National Critical Technology (National Training and Simulation Association, 2011, p. 1). "Simulation is the process of designing a model of a real system and conducting experiments with this model for the purpose of either understanding the behavior of the system and/or evaluating various strategies for the operation of the system" (Pegden, Sadowski, & Shannon, 1991).

The term "simulations" relates to an extensive range of industries, from defense, engineering and science to marketing, economics and finance analysis. M&S tools are used for research and development in many fields. In fact, the National Training and Simulations Association estimates that just in the U.S. defense sector alone, \$4 billion to \$7.5 billion is spent annually on M&S tools, processes and products (National Training and Simulation Association, 2011, p. 1). Nevertheless, human decision making and competency are still required in all stages of M&S system development. Innovation in M&S design and implementation is a continuous process (Maria, 1997, p. 8).

Modeling and Simulations have improved greatly throughout history; in fact, currently, M&S tools are more dominant and popular than most of the engineering computer programs (Kelton, Sadowski, & Sadowski, 1997, p. 3). Also, M&S has become an academic program of choice for students in all disciplines (Sokolowski & Banks, 2010, p. 1). Similarly, science and engineering fields have been uniquely transformed or immensely improved with the integration of Modeling and Simulation methods (Glutzer, 2009, p. 1).

For example, in the field of emergency medicine, M&S tools have been incorporated in to rehearsal environments for first responders and medical personal to improve the speed and quality of care. Thus, using virtual simulation models are a cost effective alternative for replicating real life situations (National Training and Simulation Association, 2011, p. 3).

1.1.1 History of Modeling and Simulations

Even though the origins of modeling and simulations cannot be tracked to any particular date, it is believed that the first known simulation “Caturanga” was a predecessor of modern chess. It was used in India to simulate battle field tactics in 7th century (National Training and Simulation Association, 2011, p. 5).

1.1.1.1 Pre computer era

Before the era of electronics or computers, the Monte Carlo method is considered to be the first simulation that had any significant contribution to the modern M&S techniques. Monte Carlo simulation consisted of “throwing needles randomly onto a plane with equally spaced parallel lines in order to estimate pi” (National Training and Simulation Association, 2011, p. 5). Although original credit goes to Compte De Buffon in 1777, it is believed the extended version of his experiment was corrected by Laplace in 1812. Therefore, the Monte Carlo method is often referred to as the Buffon-Laplace needle problem (Goldsman, Nance, & Wilson, 2010, p. 568).

During World War I, defense programs began adopting M&S systems to train troops for battle conditions. Specifically, ground based flight simulators such as the Ruggles Orientator and the Lender and Heilderberg model were used to train pilots (National Training and Simulation Association, 2011, p. 5).

1.1.1.2 Computer era

The first general purpose computer, the Electronic Numerical Integrator and Calculator (ENIAC) was completed in 1946 at the University of Pennsylvania (Shrader, 2006, p. 111). ENIAC could be described as “A collection of electronic adding machines and other arithmetic units, which were originally controlled by a web of large electrical cables” (Grier, 2004 Jul-Sep, p. 2).

ENIAC was originally designed to simulate and produce ballistics trajectory tables. As a result, the air defense simulations were created by the Army Operations Research Office at Johns Hopkins University. They were part of the first North American Air defense system. However, ENIAC also had various other applications, such as weather prediction, atomic energy calculations, cosmic ray studies, thermal ignition rates, random number studies, wind tunnel designs and other scientific applications (Shrader, 2006, p. 111).

Subsequently in 1946, Polish mathematician Stanislaw Ulam used a computational model to develop the hydrogen bomb (National Training and Simulation Association, 2011, p. 6). Ulam collaborated with John Neumann and others to apply the Monte Carlo method using an electronic computer to solve neutron diffusion problems that led to the design of the hydrogen bomb (Goldsmann, Nance, & Wilson, 2010, p. 568).

The next major breakthrough in the simulation world was performed by operational research professor at the University of Southampton, Keith Douglas Tocher. His innovation, the first general purpose simulator, was used as a method to compute the state of production time in an industrial plant (Tocher & Owen, 2008). His general purpose simulator system contained a model of an industrial plant and a set of machines embedded in it. It reported and computed the condition of each machine in the plant, such as busy, idle, unavailable and failed (Goldsmann,

Nance, & Wilson, 2010, p. 568). By doing so, it could be used to predict the final time needed to complete the manufacturing production task.

1.1.1.3 Present Advancement

The field of M&S has grown rapidly and has become a robust method for research and development in many disciplines (Sokolowski & Banks, 2010). These fields are varied and evolving rapidly with the progression of technology. Furthermore, Deshmukh (2009) stated that, in almost every engineering domain and every phase in the life cycle of an engineered system, computational models and simulations have been extensively used (p. 79).

Furthermore, M&S tools have evolved and grown more complex with time and advancing technology. For instance, M&S tools have developed from standalone tools and languages to advanced network-based languages such fluid dynamics and mechanical analysis tools. Especially with the expansion of the World Wide Web, computing and solving can be done in a different location or server rather than in a dedicated operation system (Fortmann-Roe, 2014, p. 1).

As computers and the internet are becoming more affordable and accessible for students and researchers, the world of simulations has become more comprehensible even as it has grown in complexity. Subsequently, new multicore computer chip architectures now provide exceptional accuracy and resolution (Glotzer, 2009, p. 2). Above all, the internet has made the simulation world closer by providing knowledge to non-experts and students. For example, the website ISI web of knowledge reports that papers published related to modeling and simulations tools has grown immensely, from 299 between 1985 and 1989 to 3,727 between 2005 and 2009 (Fortmann-Roe, 2014).

1.1.2 What is modeling

According to the National Training and Simulations Association, “Modeling is the representation of an object or phenomena, which is used by simulations” (National Training and Simulation Association, 2011, p. 3). In fact, models may be mathematical, physical or logical representations of a system, entity, phenomenon or process, or a combination of two or more of these. Moreover, a model can also be a system with integrated functions constructed in completely an artificial environment. Hence, the only thing that distinguishes a model from reality is that it should be comparable but simpler than a real system.

Creating a model with an approximation of the system is the first step of an M&S system. Then, the model can be modified according to the experimental procedure desired (Sokolowski & Banks, 2010, p. 1). In other words, the main object of a model is to forecast or predict the outcome of an alteration of the system. (Maria, 1997, p. 7). Models can be divided in to two main categories; Physical models and mathematical models.

Physical models are replicas or a scaled version of the actual systems. For an example, in many fast food chains a full scale model is used to experiment with new products and services before launching to the market. Also, flight simulators are commonly used to train pilots in lifelike environments (Kelton, Sadowski, & Sadowski, 1997, p. 6).

Mathematical models, also known as logical models, are argumentative realities with approximations and assumptions about the functionality of the system. A Logical model is frequently inserted into computer software with the required mathematical and scientific functions embedded. Mathematical models are relatively cheaper since models can be built in using computer programs rather than recreating actual systems (Kelton, Sadowski, & Sadowski, 1997, p. 5). However, models need to be validated in order to rationalize the model. A typical

validating technique is to simulate a known system and compare the model's output results with known or observed outputs of the system (Maria, 1997, p. 7). Specifically in computer models, mistakes and errors will not be included, rather in the real systems mistakes and errors are adapted accordingly (Kelton, Sadowski, & Sadowski, 1997, p. 6).

1.1.3 What are Simulations

According to the National Training and Simulations Association, "Simulation is a representation of the functioning of a system or process" (National Training and Simulation Association, 2011, p. 3). Through simulations, a model can be implemented with unlimited variations; as a result, it can produce complex scenarios and results.

Simulations can be the procedure of the modeling system (Maria, 1997, p. 8). Through simulations, models can be used to experiment with or investigate a nearly unlimited variety of situations (see Figure 1). Conversely, experimenting in a real system would be expensive and impractical (Maria, 1997, p. 1). In other words, simulations are a functional approach that can define the performance of a system using either a mathematical model or a representational model, or both (Sokolowski & Banks, 2010, p. 5).

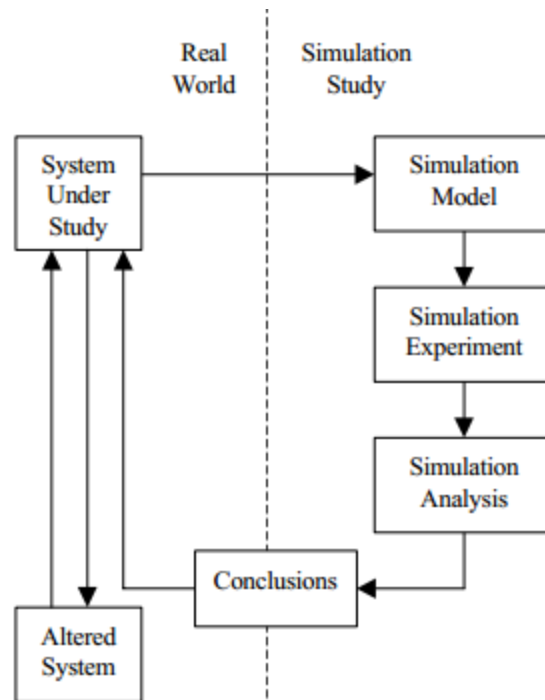


Figure 1 A flow chart of a basic M&S system processors (Maria, 1997, p. 8)

Simulations can be classified under three main categories: Static vs. Dynamic, Continuous vs. Discrete, Deterministic vs. Stochastic (Kelton, Sadowski, & Sadowski, 1997, p. 9). However, whatever category a simulation falls into, each uses an approximate-numerical approach to solving the simulation (Bungartz, Zimmer, Buchholz, & Pfluger, 2014).

Static vs. Dynamic – time will not be used as a function in a static model. Therefore, the system is considered to be in a neutral position relative to time. The “Buffon Needle” problem discussed earlier is an example of a static system. On the other hand, dynamic systems continuously evolve with time. The manufacturing plant model, also presented earlier, would be one example. However, in the interests of simplifying a model, dynamic systems can be treated and analyzed as a static system (Kelton, Sadowski, & Sadowski, 1997, p. 9).

Continuous vs. Discrete – Continuous simulations attempt to compute the deviations in a system continuously over time with regards to feedback controls. In other words, the system clock will continuously advance with time. As an example, flight simulators will continuously adapt to change accordingly as pilots provide feedback or control. While, a system clock in discrete simulations will only move forward from one event to the next. For example, in a plantation model a machine complete its task and changes the statuses from busy to idle (Fayek, 2002, p. 2).

Deterministic vs. Stochastic – Deterministic simulations are frequently defined in differential equations that have unique inputs. In other words, no random inputs are considered. As an example, steady state simulations with no progressive variations. A class schedule with fixed time periods would be an example of deterministic simulations. Conversely, stochastic simulations maneuver with random inputs. Moreover, unique inputs will lead to different outputs as a result of random components of the system. However, single simulations can only give one conceivable result. Therefore, many runs are used to estimate probability distributions and process (Kelton, Sadowski, & Sadowski, 1997, p. 9).

1.2 Fluid Dynamics

The first known documented fluid dynamics application, “the water screw” was invented by Archimedes, the famous Greek mathematician, physicist and inventor. His well-known theorem about fluid equilibrium is considered to be the first theory of fluid dynamics. Leonhard Euler and Daniel Bernoulli, working centuries later, also contributed greatly to the present day fluid dynamics equations (Rieutord, 2015, p. 1).

According to Bungartz, fluid flow modeling is the most common type of M&S system, used in nearly every science and engineering application (Bungartz, Zimmer, Buchholz, &

Pfluger, 2014, p. 355). The nature of the multiplicity motion of fluid can be illustrated and analyzed by examining motion and deformation of materials lines and surfaces of fluids (Pozrikidis, 2009, p. 1). In other words, fluid dynamics could be theorized as the study of fluid flow, convective heat transfer and species mass transfer (Kleinstreuer, 2010, p. 3).

“CFD (computational fluid dynamics) is a set of numerical methods applied to obtain approximate solutions of problems of fluid dynamics and heat transfer” (Zikanov, 2010, p. 1). Fluid dynamics calculations are governed by three rudimentary principles: the conservation of mass, Newton’s second law and the conservation of energy. By using these equations in a form of differential equations, a numerical solution can be obtained. However, the final product of CFD is a collection of numbers; numerical analysis methods should be used to understand the results (Wendt, Anderson, & Von Karman Institute, 2008, p. 6). In depth details about CFD principles and methods are explained in section 1.4.

1.2.1 Fluid vs. Solid

A fluid is anything that flows; it could be either liquid or gas (Pedley, 1997, p. 1). At the same time, a fluid can be distinguished as any material in a condition that cannot stand firm to shear forces (Bungartz, Zimmer, Buchholz, & Pfluger, 2014, p. 356). When presented with shear stress, fluid will deform. Moreover, even when the force is removed, a fluid will continue to deform and will not recover its original shape (Hauke, 2008, p. 7).

To sum up, the differentiations of fluids and solid materials are governed by “rheological Law”, which explains how a matter deforms with respect to the magnitude of the stress (Rieutord, 2015, p. 1). Nevertheless, with sufficient potential and kinetic energy, fluids can be transformed into solids and solids can transform into fluids (Pozrikidis, 2009, p. 2). In simpler terms, a fluid can be defined as continuous media. That means, fluid will adopt the shape of the

vessel it is placed in, while solids have their own identity when it comes to their shape (Pozrikidis, 2009, p. 1).

1.2.2 The theory of fluid as particle packets

The theory of fluid particle is a generalized framework. This is an impeccable view of a piece of fluid; the body of fluid is subdivided into small particles. These particles are small enough so that the fluid properties are uniform inside (Rieutord, 2015, p. 3). Hence, it is assumed that all molecules in that particle are identical, in other words, the fluid is assumed to be a homogeneous mixture (Pozrikidis, 2009, p. 2). Nevertheless, a particle is big enough to enclose a large number of atoms or molecules; so that the fluid will assume the local thermodynamic equilibrium. Yet, such a particle is not considered to be a point mass, but instead, the surface of the particle will allow contacting forces with other particles (Rieutord, 2015, p. 3).

1.2.3 Fluid Kinematics

Establishing a mathematical relationship between the relative motion of fluid particles and structure of a flow is defined as fluid motion. Also, fluid dynamics focuses on the forces acting up on a fluid body by external conditions such as gravitational forces, as well as forces developing inside the fluid such as stress and tension. Hence, the combination of fluid motion and fluid dynamics is called fluid kinematics (Pozrikidis, 2009, p. 2).

1.2.3.1 Continuous Media

The motion and state of a fluid can be identified by its velocity, pressure and density at a given point in space and time (Pedley, 1997, p. 1). Since it is impracticable to describe the motion of every molecule and atoms individually in a fluid, only the mean motion of a fluid can be taken into account. In other words, the atoms or molecules that create the fluid flow will be

replaced by an assumed medium that acts as the mean motion. Therefore, in order to validate that assumption, the scale L , of the interested area must be large compared to mean free path l of atoms and molecules. This equation is defined as Knudsen Number (Rieutord, 2015, p. 2).

$$K_n = \frac{l}{L}$$

Equation 1-1

1.2.3.2 Lagrangian Specification

Lagrangian specification uses the initial position of a fluid particle as a reference to identify changes to a moving particle (Pedley, 1997, p. 7). In other words, the measuring instrument or the computational mesh is not in a fixed position (see Figure 2), instead, the mesh computes and reports the fluid changes while moving through the fluid domain (Kleinstreuer, 2010, p. 22). Thus, every fluid particle has a unique equation following its path. Since, the fluid domains have infinite numbers of particles, the position of any individual particle is identified by stipulating its position x_0 at time $t = 0$. Hence, Equation 1-2 can be used to locate the position of individual particle x at any given time t (Hauke, 2008, p. 11).

$$x = x(t, x_0)$$

Equation 1-2

When Lagrangian specification follows large distortions of the fluid domain it attempts to regenerate the meshing operations recurrently. As a result, this will consume large amounts of computing power when creating the mesh (Donea, Huerta, Ponthot, & Rodriguez-Ferran, 2004, p. 413).

For instance, let's consider an example of measuring the temperature of a flowing stream of a river using a thermometer. Also, the thermometer is fixed in to a very light boat and the boat moves at exactly the same rate as the flowing stream. In this example, because the thermometer moves with the fluid particle, it will be reading the temperature of the same fluid particle with respect to time (Hauke, 2008, p. 12). Hence, the distorted areas of the mesh will frequently regenerate with time.

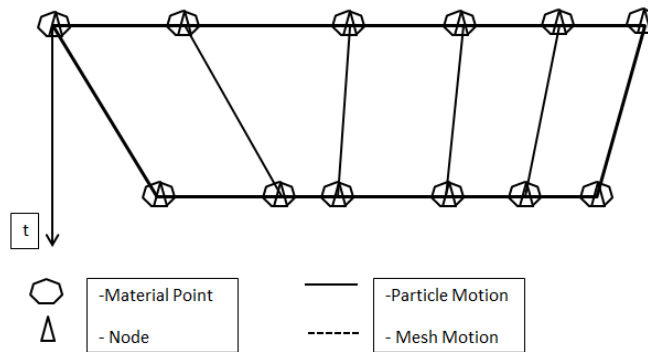


Figure 2 One dimensional example of a Lagrangian Method

1.2.3.3 Eulerian Specification

According to the Encyclopedia of Computational Mechanics, Eulerian specification is broadly used in mathematical modeling of fluid dynamics simulations (Donea, Huerta, Ponthot, & Rodriguez-Ferran, 2004, p. 413). Eulerian method involves measuring the fluid motion with respect to fixed instruments (Pedley, 1997, p. 2). In other words, the measurement instrument or computational mesh is considered to be fixed and the fluid domain is moving relative to the mesh (see Figure 3). Mathematically, the velocity v at every spatial point x in the fluid domain can be calculated at any instant of time t using Equation 1-3 (Hauke, 2008, p. 12).

$$v = v(x, t)$$

A trivial example would be identifying the velocity of stream flow in a river using a flow meter (Rieutord, 2015, p. 3). Depending on the river bank location that the flow meter is fixed, the velocity of the flow could be either fast or slow at any given time. Also, the flow meter is measuring the velocity of the fluid particles as they pass a fixed point. Hence, the fluid domain is not calculated as it changes; instead, the calculations are centered on a fixed three-dimensional domain, and the fluid flows through it (Hauke, 2008, p. 13).

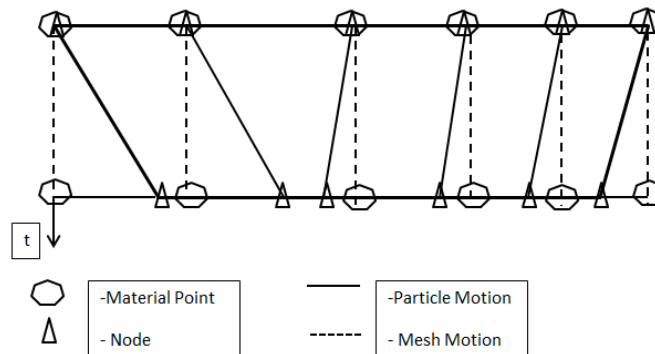


Figure 3 One dimensional example of a Eulerian Method

1.2.3.4 Arbitrary Lagrangian-Eulerian Specification (ALS)

With the effort of improving the accuracy of the mesh, a combination of Lagrangian and Eulerian specification was developed called Arbitrary Lagrangian-Eulerian specification (ALS). Depending on the applications, this method is commonly used in modern computational dynamics tools (Donea, Huerta, Ponthot, & Rodriguez-Ferran, 2004, p. 413). It calculates and records the data at points which move arbitrarily relative to the fluid domain. Moreover, if the fluid properties are computed at the mesh nodes and after that if the mesh moves, ALS can be used to calculate the fluid variables at the mesh nodes (Hauke, 2008, p. 15).

In addition, in ALE specification, the computational mesh could be moved as in the Lagrangian method or be held constant as in the Eulerian method, or, it could be moved in an

arbitrary way as using some combination of both (see Figure 4). Hence, by using the ALS method, the mesh resolution can be increased to a greater extent than it can by only using Eulerian way; or, distortions of the mesh can be adjusted for more precisely than they can by only using the Lagrangian way (Donea, Huerta, Ponthot, & Rodriguez-Ferran, 2004, p. 414).

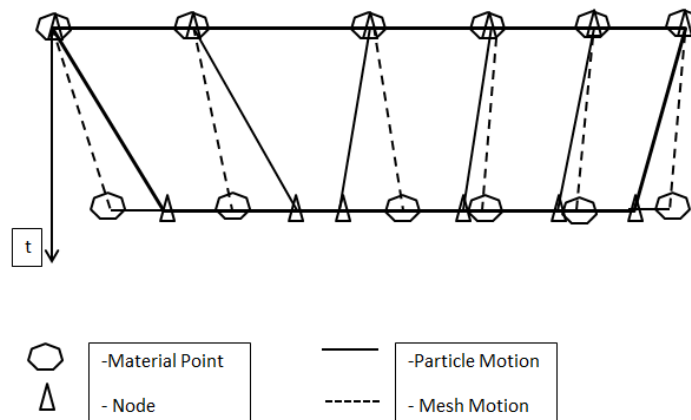


Figure 4 One dimensional example of an ALS method

1.2.4 Forces and stresses

Two main forces act on fluid particles; homogeneous forces acts on the volume surface of the particle, and the surface forces acts on the boundaries of the particle. A moving fluid particle will experience these forces as a total vector for any direction in the Cartesian plane (Rieutord, 2015).

1.2.4.1 Body forces

Body forces act on the whole material volume at a distance; such as gravitational, electrical and magnetic forces. Electrical or electromagnetic forces occur when particles contain molecules of polarized material or the fluid is electrically charged (Pozrikidis, 2009, p. 163). These forces do not have a direct relationship or direct contact with the particle. Instead, the

forces act on a per unit volume or per unit mass of the fluid element (Wendt, Anderson, & Von Karman Institute, 2008, p. 28).

If f_v is the volume force and f_m is the massic force, respectively,

$$f_v = \frac{\text{Force}}{\text{Volume}} \quad f_m = \frac{\text{Force}}{\text{mass}}$$

Hence, body forces acting on the x direction are,

$$\left\{ \begin{array}{l} \text{Body forces on} \\ x \text{ direction} \end{array} \right\} = \rho f_x (dx dy dz)$$

Equation 1-4

For an example, if g is the acceleration of gravity; and dF_g is the gravitational force acting on a fluid particle that has a volume of dV_g , density of ρ and mass $dm_g = \rho dV_g$

$$dF_g = g \rho dV_g$$

Equation 1-5

The right hand side of the Equation 1-5 is acceleration and mass; which means the left hand side will be a force. However, gravitational body forces are independent from molecular motion. In other words, whether the fluid is motionless or flows, a mass of the same fluid weighs the same (Pozrikidis, 2009, p. 164).

Likewise, by integrating the Equation 1-5, total force over a given volume domain(V) as per unit volume is,

$$F_v = \int_v F_v dV$$

Equation 1-6

Or, per unit mass

$$F_v = \int_v \rho F_m dV$$

Equation 1-7

Equation 1-6 and Equation 1-7 can be generalized as,

$$f_v = \rho f_m$$

Equation 1-8

1.2.4.2 Surface forces

On the other hand, surface forces act directly on the fluid element surface; such as, bubbles rising through a liquid or the hood of a moving vehicle (Pozrikidis, 2009, p. 164). There are two main reasons for surface forces. (a) Surrounding fluid elements inflict a pressure on the surface of the fluid element, and (b) due to tugging and pulling actions created by friction of the outside surfaces of fluid elements(see Figure 5), shear and normal stress acts on the fluid particle (Wendt, Anderson, & Von Karman Institute, 2008). In order to understand the physical origin of the surface forces, it is crucial to consider the direction of molecular motion and to differentiate between gases and liquids (Pozrikidis, 2009, p. 164).

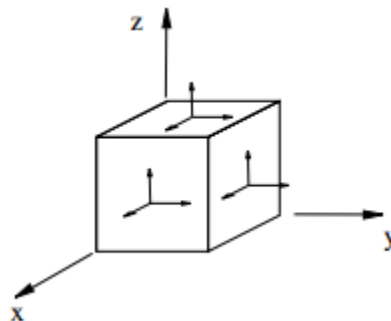


Figure 5 Forces acting on a microscopic fluid particle (Hauke, 2008, p. 36)

The force acting on a surface of dS is,

$$dF_s = f_s dS$$

Equation 1-9

When integrated for the whole surface of the fluid particle,

$$F_s = \int_S f_s dS$$

Equation 1-10

As an example, pressure acting on a fluid particle is illustrated in Figure 6. Therefore, for n number of directions,

$$F_s = -pn$$

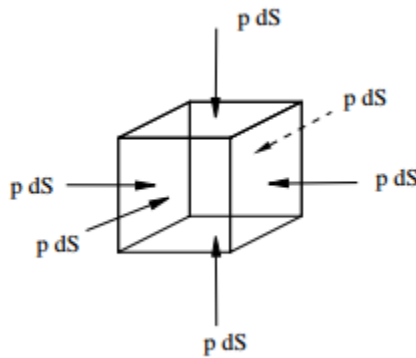


Figure 6 Pressure inserting on all directions (Hauke, 2008, p. 34)

1.2.4.3 Traction and the stress tensor

Surfaces forces and stresses depend on the orientation of the surface. Hence, derivation of the mathematical formulas for surface forces is much more complex than body forces. Specifically, when there are infinite number planes at a point space, this condition needs to be considered for the derivation (Hauke, 2008, p. 35).

To calculate stress on a fluid particle, the planes are broken down to three perpendicular planes. As shown in Figure 7, a surface area dS centered at a point $X = (x, y, z)$ in fluid particle.

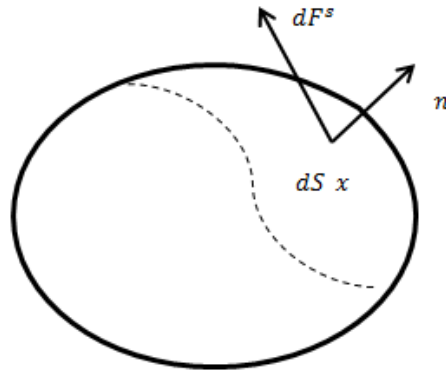


Figure 7 Surface of fluid used to demonstrate the traction and stress tensor

At point x , the direction of the unit vector normal to the surface is defined by $n = (n_x, n_y, n_z)$. As explained in section 1.2.4.2, the surface forces (dF^S) can be in any direction. In other words, it may carry elements tangential to the surface or normal to the surface.

The average stress acting on a surface is a ratio between surface force, dF^S and the area of the surface, dS . Thus, when the surface area becomes microscopic, average stress trends toward a limit called “traction exerted on an infinitesimal surface, f ” (Pozrikidis, 2009).

Hence,

$$f \equiv \frac{dF^S}{dS}$$

Repositioning Equation 1-11,

$$dF^S = f dS$$

Equation 1-12

Equation 1-11 and Equation 1-12 are crucial in understanding that the traction is defined only when the location and the side of the surface are indicated. Likewise, by using the coordinates of point x and the orientation of the unit normal vector, n , can be defined as,

$$f(X, n)$$

Equation 1-13

The three scalar components of traction are denoted by parentheses in the Equation 1-13.

Similarly, using Equation 1-12 and Equation 1-13, traction exerted on a microscopic surface that is represented by perpendicular axis of x, y, z can be defined as,

$$f^x = (f_x^{(x)}, f_y^{(x)}, f_z^{(x)})$$

$$f^y = (f_x^{(y)}, f_y^{(y)}, f_z^{(y)})$$

$$f^z = (f_x^{(z)}, f_y^{(z)}, f_z^{(z)})$$

Equation 1-14

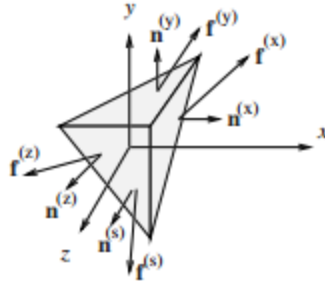


Figure 8 Stress tensor on a 3D fluid particle stacked on one point (Pozrikidis, 2009, p. 167)

By stacking these three vectors on a single point in a specific order, a 3×3 stress tensor can be obtained (see Figure 8).

$$\tau = \begin{Bmatrix} f_x^{(x)}, f_y^{(x)}, f_z^{(x)} \\ f_x^{(y)}, f_y^{(y)}, f_z^{(y)} \\ f_x^{(z)}, f_y^{(z)}, f_z^{(z)} \end{Bmatrix}$$

Equation 1-15

Next, traditional two-index notation can be used to reform the stress tensor.

$$\tau_{ij} \equiv f_j^{(i)}$$

Where $i, j = x, y, z$

Equation 1-16

Hence, Equation 1-15 can be written as,

$$\tau = \begin{Bmatrix} \sigma_{xx}, \sigma_{xy}, \sigma_{xz} \\ \sigma_{yx}, \sigma_{yy}, \sigma_{yz} \\ \sigma_{zx}, \sigma_{zy}, \sigma_{zz} \end{Bmatrix}$$

Equation 1-17

To understand this notation, one must consider a two dimensional flow. Since there is no z axis, all the z axis components would be either zero or constant. Hence, a 2×2 stress tensor would look like,

$$\tau = \begin{Bmatrix} \sigma_{xx}, \sigma_{xy}, \sigma_{xz} \\ \sigma_{yx}, \sigma_{yy}, \sigma_{yz} \\ \sigma_{zx}, \sigma_{zy}, \sigma_{zz} \end{Bmatrix}$$

$$\tau = \begin{Bmatrix} \sigma_{xx}, \sigma_{xy} \\ \sigma_{yx}, \sigma_{yy} \end{Bmatrix}$$

Equation 1-18

The total forces acting on the fluid surface depends on the foreground faces and background faces. Hence, some faces will go through a dragging action and some will go through a tugging action. In Figure 5, foreground faces are those where the normal vectors are line up facing the coordinate axis and background faces are normal vectors in the opposite direction of the coordinate axis (Hauke, 2008).

Moreover, normal stress acts perpendicular to the faces they represent. In Figure 9 normal stress is denoted by τ_{xx} and it acts towards the x direction. Also, τ_{xx} is a function of time rate of change of volume of the fluid particle it represents (Wendt, Anderson, & Von Karman Institute, 2008). To demonstrate, in Equation 1-17, normal stress components are,

$$\tau_{xx}, \tau_{yy}, \tau_{zz}$$

Equation 1-19

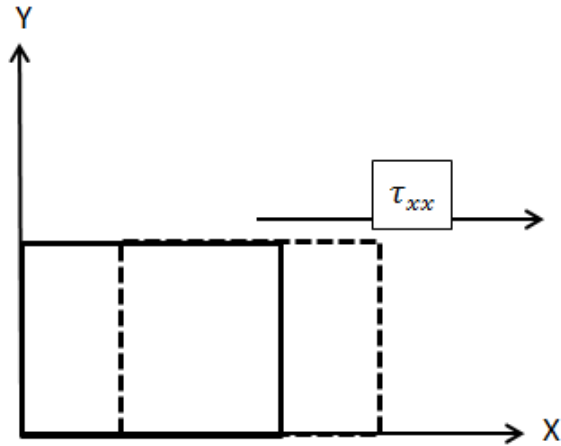


Figure 9 Normal Stress

On the other hand, shear stress acts tangential to the surface they represent. In the Figure 10, shear stress is represented by τ_{xy} acting on the xy plane. Also, τ_{xy} is a function of time rate of change of the shearing deformation of the fluid particle (Wendt, Anderson, & Von Karman Institute, 2008). Using Equation 1-17, shear stress components are,

$$\tau_{xy}, \tau_{xz}, \tau_{yx}, \tau_{yz}, \tau_{zx}, \tau_{zy}$$

Equation 1-20

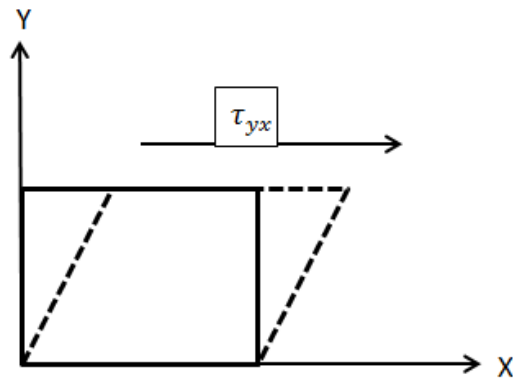


Figure 10 Shear stress

1.3 Material Derivative and Governing Equations

The most common types of specification in CFD applications are Eulerian and ALS specifications. However, in these specifications the fluid particles are not tracked and the fluid motion is given with respect to arbitrary points (Hauke, 2008, p. 15).

As a result, to obtain particle properties, conservation laws needs to be applied to fluid properties as vector or scalar functions of space x and time t ; such as, Velocity $v(x, t)$, Temperature $T(x, t)$ or Density $\rho(x, t)$ or any other fluid properties (Zikanov, 2010, p. 12). Before applying the governing equations of fluid dynamics, it is essential to establish the common aerodynamic notations in vector and scalar units, which is called the substantial derivative (Wendt, Anderson, & Von Karman Institute, 2008, p. 18). It is important to understand the physical aspects of substantial derivative because the basics of deriving the governing equations of fluid dynamics are based on the substantial derivative method.

The governing equations of fluid dynamics are based on three equations; Conservation of mass, conservation of momentum and conservation of energy. The governing equations for unsteady, three dimensional, compressible, viscous flow is,

Conservation of mass,

$$\frac{d}{dt} M(V_c) = \dot{M}_{in} - \dot{M}_{out}$$

Where, \dot{M} is the mass flow rate.

Conservation of momentum,

$$\frac{d}{dt} P(V_c) = L\dot{M}_{in} - L\dot{M}_{out} + \sum F_{ext}$$

Where, $L\dot{M}$ is the linear momentum and $\sum F_{ext}$ is the external forces acting on the particle.

Conservation of energy,

$$\frac{d}{dt} E(V_c) = \dot{E}N_{in} - \dot{E}N_{out} + \dot{W}_{ext} + \dot{Q}_{in}$$

Where, $\dot{E}N$ is energy flux, \dot{W} is work done per unit time and \dot{Q} is the heat added per unit time.

The derivations of the equations are explained in the sections 1.3.1.2, 1.3.1.3 and 1.3.1.4, respectively.

1.3.1.1 Substantial, Local and Convective Derivative

Illustrating the motion of fluids is difficult because fluid moves within a three dimensional environment. When considering fluid motion, an artificial coordinate system is placed relative to the movement being analyzed (Basniev, Dmitriev, & Chilingar, 2012, p. 19). Therefore, a Cartesian coordinate system with three mutually orthogonal axes (x,y,z) will be introduced to describe the fluid motion (see Figure 11). The point $B(x_1, y_1, z_1)$ can be described by vectors \vec{i} , \vec{j} and \vec{k} that start at a common origin of the Cartesian axes and end in any space coordinates (u, v, w) and time (t) (Pozrikidis, 2009, p. 4).

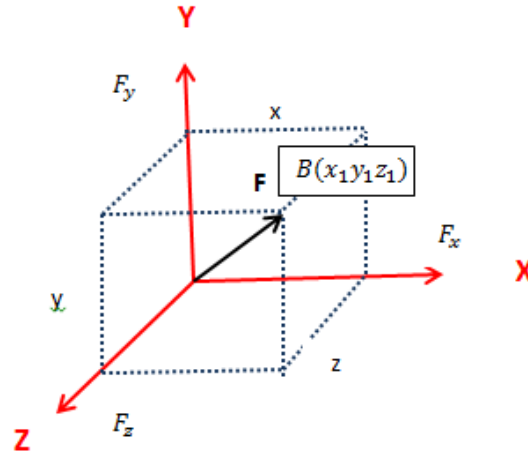


Figure 11 Location of a fluid particle expressed in a Cartesian coordinates system

Before applying fluid conservative rules, it is crucial to understand the substantial derivative physics of fluid mechanics. The following material derivative method was used as presented in the Von Karman Institute for Fluid Dynamics (Wendt, Anderson, & Von Karman Institute, 2008).

The vector velocity in a Cartesian space can be defined by following expression.

$$\vec{V} = u\vec{i} + v\vec{j} + w\vec{k}$$

Equation 1-21

Where velocity components can be defined by,

$$u = u(x, y, z, t)$$

$$v = v(x, y, z, t)$$

$$w = w(x, y, z, t)$$

Equation 1-22

These notations are considered to be general, and will apply to any fluid property such as density or temperature. Also, u, v or w are functions of both space and time in a fluid domain.

Such as,

$$\rho = \rho(x, y, z, t)$$

$$T = T(x, y, z, t)$$

If the density of the fluid particle in Figure 11 at point 0 (common origin of the three axes) and at time $t = 0$ is,

$$\rho = \rho(x, y, z, t)$$

Equation 1-23

After a time of $t = t_1$ the particle has moved to a new point $B(x_1, y_1, z_1)$ (see Figure 11). Hence, at this time and point of space, the density of the particle can be mathematically expressed as,

$$\rho_B = \rho_2 = \rho(x_1, y_1, z_1, t_2)$$

Equation 1-24

Combining the Taylor's series regarding points and Equation 1-23, ρ_2 can be expressed as follows,

$$\rho_2 = \rho_1 + \left(\frac{\partial \rho}{\partial x}\right)_1 (x_2 - x_1) + \left(\frac{\partial \rho}{\partial y}\right)_1 (y_2 - y_1) + \left(\frac{\partial \rho}{\partial z}\right)_1 (z_2 - z_1) + \left(\frac{\partial \rho}{\partial t}\right)_1 (t_2 - t_1)$$

After rearranging and dividing by $(t_2 - t_1)$,

$$\frac{\rho_2 - \rho_1}{t_2 - t_1} = \left(\frac{\partial \rho}{\partial x}\right)_1 \left(\frac{x_2 - x_1}{t_2 - t_1}\right) + \left(\frac{\partial \rho}{\partial y}\right)_1 \left(\frac{y_2 - y_1}{t_2 - t_1}\right) + \left(\frac{\partial \rho}{\partial z}\right)_1 \left(\frac{z_2 - z_1}{t_2 - t_1}\right) + \left(\frac{\partial \rho}{\partial t}\right)_1$$

Equation 1-25

The left side of the equation denotes the average density change with reference to average time change ($\Delta\rho/\Delta t$), when the fluid particle moves from point 1 to 2. By applying limits to the left side of the Equation 1-25,

$$\lim_{t_2 \rightarrow t_1} \left(\frac{\rho_2 - \rho_1}{t_2 - t_1} \right) \equiv \frac{D\rho}{Dt}$$

In the above equation, as the fluid particle moves from point 1, $D\rho/Dt$ the symbol represents the instantaneous time rate of change in density along the fluid particle trajectory. To explain, $D\rho/Dt$ is the change of density in one individual fluid particle as it move in space. In other words, if a density meter is locked onto one individual fluid particle and it measures the change of density as it moves within the space, it will be defined as a time rate of change in density. This is the classification of substantial derivative.

On the contrary, $(\partial\rho/\partial t)$ is the definite time rate of change at the fixed point 1. Such as, the density changes when it moves across the point 1. For instance, the density meter will be fixed to point 1 and it will report the density change of the fluid particle as it moves within it. This is called local derivative. In brief, $D\rho/Dt$ and $(\partial\rho/\partial t)$ are mathematically and physically different (Wendt, Anderson, & Von Karman Institute, 2008, p. 20).

Returning to Equation 1-25 and applying limits,

$$\lim_{t_2 \rightarrow t_1} \left(\frac{x_2 - x_1}{t_2 - t_1} \right) \equiv u$$

$$\lim_{t_2 \rightarrow t_1} \left(\frac{y_2 - y_1}{t_2 - t_1} \right) \equiv v$$

$$\lim_{t_2 \rightarrow t_1} \left(\frac{z_2 - z_1}{t_2 - t_1} \right) \equiv w$$

Hence, Equation 1-25 can be written as,

$$\frac{D\rho}{Dt} = u \left(\frac{\partial \rho}{\partial x} \right) + v \left(\frac{\partial \rho}{\partial y} \right) + w \left(\frac{\partial \rho}{\partial z} \right) + \left(\frac{\partial \rho}{\partial t} \right)$$

Equation 1-26

Likewise, using Cartesian coordinates and vector notations,

$$\nabla \equiv \vec{i} \frac{\partial}{\partial x} + \vec{j} \frac{\partial}{\partial y} + \vec{k} \frac{\partial}{\partial z}$$

Equation 1-27

As a result, Equation 1-26 can be written in vector coordinates as the substantial derivative operator,

$$\frac{D\rho}{Dt} \equiv \frac{\partial}{\partial t} + (\vec{V} \nabla)$$

Equation 1-28

$(\vec{V} \nabla)$ is classified as convective derivative. In other words, it is the time rate of change due to the fluid particle moving from one location to another, where the properties of the fluid are spatially varied. To sum up, $D\rho/Dt$ is the time rate of change following a fluid particle, substantial derivative; $(\partial\rho/\partial t)$ is the time rate of change in a fixed location, local derivative; $(\vec{V} \nabla)$ is the time rate of change due to change of location properties, convective derivative (Wendt, Anderson, & Von Karman Institute, 2008, p. 21). Similarly, the substantial derivative can be applied to any other properties, such as pressure (p), temperature (T) or velocity (u); hence it could be expressed as Dp/Dt , DT/Dt , Dv/Dt .

Time rate of change of temperature can be written as,

$$\underbrace{\frac{DT}{Dt}}_{\text{Substantial Derivative}} \equiv \underbrace{\frac{\partial T}{\partial t}}_{\text{Local Derivative}} + \underbrace{(\vec{V} \cdot \nabla)}_{\text{Convective Derivative}}$$

Where,

$$T = u \left(\frac{\partial T}{\partial x} \right) + v \left(\frac{\partial T}{\partial y} \right) + w \left(\frac{\partial T}{\partial z} \right) + \left(\frac{\partial T}{\partial t} \right)$$

Equation 1-29

As an example, let us consider the scenario of a very large pot of water placed over an open flame. The flame is concentrated on the middle of the pot. A thermometer is used to take the temperature of the water in different locations. The first position is in an area furthest away from the middle; hence, it will read the lowest temperature. The thermometer is gradually moved towards the middle of the pot; the temperature readings will increase as it gets closer to the middle of the pot. This is equivalent to the convective derivative in Equation 1-29. At the same time, let us consider a situation when a cup of boiling water is added near the location of the thermometer. The temperature readings will momentarily increase at the same time when the hot water is added. This is similar to the local derivative in Equation 1-29. The net temperature difference as the thermometer is moving closer to the center is a combination of both the actions of moving the thermometer to the center and adding boiling water at the same instant, hence, this net temperature change is analogous to the substantial derivative in Equation 1-29.

The above process is used to explain the substantial derivative physics. However, for Equation 1-23, total differential calculus could be used to archive Equation 1-26.

That is, $\rho = \rho(x, y, z, t)$

by apply the chain rule using differential calculus,

$$D\rho = \frac{\partial\rho}{\partial x} dx + \frac{\partial\rho}{\partial y} dy + \frac{\partial\rho}{\partial z} dz + \frac{\partial\rho}{\partial t} dt$$

$$\frac{D\rho}{dt} = \frac{\partial\rho}{\partial x} \frac{dx}{dt} + \frac{\partial\rho}{\partial y} \frac{dy}{dt} + \frac{\partial\rho}{\partial z} \frac{dz}{dt} + \frac{\partial\rho}{\partial t}$$

Equation 1-30

Since $dx/dt = u$, $dy/dt = v$ and $dz/dt = w$,

$$\frac{D\rho}{dt} = \frac{\partial\rho}{\partial x} u + \frac{\partial\rho}{\partial y} v + \frac{\partial\rho}{\partial z} w + \frac{\partial\rho}{\partial t}$$

Equation 1-31

By comparing Equation 1-26 and Equation 1-31, it is clear that the substantial derivative is the same as the total derivative with respect to time (Rieutord, 2015, p. 5).

1.3.1.2 Mass conservation

Conservation of mass is very intuitive and can be observed in the environment (Kleinstreuer, 2010, p. 51). The principle of conservation of mass dictates that the mass of a fixed volume of fluid particle is constant (Hauke, 2008, p. 75). In other words, in a fluid that contains the same number of fluid particles, “matter neither be created nor destroyed” (Tu & Yeoh, Guan Heng, 2007, p. 65). Following material derivative was used as provided in Rieutord (2015).

Mass of fixed volume particle of v is,

$$M = \int_{(v)} \rho dV$$

Equation 1-32

If, mass flux density (variation with time) = ρv

Overlapping Surface = (S)

Volume = (V)

dS be the surface element oriented by the external normal n so that $dS = ndS$

Hence,

$$\frac{dM}{dt} = - \int_{(s)} \rho v \cdot dS \leftrightarrow \int_{(v)} \frac{\partial \rho}{\partial t} dV = - \int_{(v)} \nabla \cdot \rho v dV$$

Equation 1-33

$$\leftrightarrow \int_{(v)} \left(\frac{\partial \rho}{\partial t} + \nabla \cdot \rho v \right) dV = 0$$

Equation 1-34

In Equation 1-33, orientation of the surface (S) is the reason for the minus sign.

Hence, when v is parallel to dS the mass M decreases.

Equation 1-34 is valid for any volume, thus,

$$\frac{\partial \rho}{\partial t} + \nabla \cdot \rho v = 0$$

Equation 1-35

Equation 1-35 is also known as the continuity equation.

When the fluid is incompressible, the continuity equation can also be expressed using the material derivative of ρ . Since the mass is constant, Equation 1-36 proves that the density of a fluid can be changed because the volume variation is expressed by $\nabla \cdot v$ (Rieutord, 2015, p. 12).

$$\frac{D\rho}{Dt} = -\rho \nabla \cdot v$$

Equation 1-36

Instead of the volume of the particle, the physical quantities of a fluid, such as energy and momentum are attached to the mass of the fluid particle. Hence, when evaluating the losses and gains of a fixed volume, as in Equation 1-33, it is crucial to understand the quantity of the mass flux carried over across (S). Flux is the amount of property carried across a surface per unit time (Hauke, 2008, p. 26). If μ is a physical quantity such as energy or momentum and S_μ is the volumetric sources,

Variations of μ in $V = \mu$ carried by v through S + Sources of μ

Or in mathematical terms,

$$\frac{d}{dt} \int_v \rho \mu \, dv = - \int_{(s)} \rho \mu \cdot dS + \int_{(v)} S_\mu \, dV$$

Equation 1-37

Hence,

$$\begin{aligned} \int_v \frac{\partial \rho \mu}{\partial t} \, dv &= - \int_{(s)} \nabla \cdot (\rho \mu v) \, dv + \int_{(v)} S_\mu \, dV \\ \Leftrightarrow \int_v \left(\mu \frac{\partial \rho}{\partial t} + \rho \frac{\partial \mu}{\partial t} \right) \, dV &= - \int_v (\mu \nabla \cdot \rho v + \rho \nabla \cdot \mu v) \, dv + \int_v S_\mu \, dv \end{aligned}$$

Using the continuity equation,

$$\int_v \rho \frac{\partial \mu}{\partial t} dv + \int_v dv \cdot \nabla \mu dV = \int_v S_\mu dv$$

Equation 1-38

Thus,

$$\int_v \rho \frac{D\mu}{Dt} dv = \int_v S_\mu dv$$

Equation 1-39

Since this equation is valid for any volume of fluid, hence it is valid locally as,

$$\rho \frac{D\mu}{Dt} = S_\mu$$

Equation 1-40

Equation 1-40 can be derived using volume change of rate $V(t)$ attach to the fluid. Since the volume contains the same number of fluid particles,

Variations of μ in $V(t)$ = Sources of μ

In mathematical terms,

$$\frac{d}{dt} \int_{v(t)} \rho \mu dv = \int_{v(t)} s_\mu dV$$

Thus,

$$\frac{d}{dt} \int_{v(t)} \rho \mu dv = \int_{v(t)} \left(\frac{D(\rho \mu)}{Dt} + \rho \mu \nabla \cdot v \right)$$

$$dv = \int_{v(t)} \left[\mu \left(\frac{D\rho}{Dt} + \rho \nabla \cdot v \right) + \rho \frac{D\mu}{Dt} \right] dV$$

Using the mass conservations Equation 1-36,

$$\rightarrow \frac{d}{dt} \int_{v(t)} \rho \mu dv = \int_{v(t)} \rho \frac{D\mu}{Dt} dV$$

Equation 1-41

Equation 1-41 is similar to Equation 1-40. This method of material derivation will be used for the next two conservations laws. This equation structure can be used for other fluid properties such as momentum, energy or entropy. Then μ will become velocity field, internal energy or entropy per mass unit, respectively (Rieutord, 2015, pp. 11-13).

To sum up, in a flow that consists of the same molecules and with density of (x, t) , velocity of $V(x, t)$ and fluid domain volume of δv ; its mass $\delta m = \rho \delta v$ must remain constant (Zikanov, 2010, p. 14).

1.3.1.3 Momentum Conservation

Newton's second law of motion describes the rate of change in the momentum of a body and defines this change as being equal to the net force acting on it. This law describes the conservation of momentum in fluids (Zikanov, 2010, p. 16). A fluid body would have momentum both due to its local acceleration, that is change of location in space and due to convective acceleration, and because a fluid particle may move to a location with different velocity (Pedley, 1997). The following momentum conservation equation is derived using the methods described in (Wendt, Anderson, & Von Karman Institute, 2008) and (Zikanov, 2010).

$$\frac{d}{dt}(mV) = F$$

Equation 1-42

Since Equation 1-42 is a vector function, it could be divided in to three scalar relations along the x , y , and z axes of the Cartesian coordinate system (see Figure 11).

Considering the left side of Equation 1-42, the mass of the fluid can be defined as,

$$m = \rho (dx dy dz)$$

Equation 1-43

Also, the time rate of change of velocity is defined as acceleration. Hence, the left hand side of Equation 1-42 can be replaced by the material derivative.

$$F = \rho \frac{D}{Dt} (V)$$

Where,

$$\rho \frac{D}{Dt} (V) = \rho \left[\frac{\partial}{\partial t} (V) + (V \cdot \nabla)V \right]$$

Equation 1-44

Equation 1-45 can be written in Cartesian notation,

$$\rho \frac{D\rho}{dt} = \rho \left[\frac{\partial u}{\partial x} u + \frac{\partial u}{\partial y} v + \frac{\partial u}{\partial z} w + \frac{\partial u}{\partial t} \right]$$

$$\rho \frac{D\rho}{dt} = \rho \left[\frac{\partial v}{\partial x} u + \frac{\partial v}{\partial y} v + \frac{\partial v}{\partial z} w + \frac{\partial v}{\partial t} \right]$$

$$\rho \frac{D\rho}{dt} = \rho \left[\frac{\partial w}{\partial x} u + \frac{\partial w}{\partial y} v + \frac{\partial w}{\partial z} w + \frac{\partial w}{\partial t} \right]$$

Equation 1-45

As discussed in section 1.2.4, there are two kinds of forces continually acting on a fluid element.

Hence, using Equation 1-19 and Equation 1-20,

$$\text{Where } \rho \frac{D\rho}{dt} = ma_x \text{ and } \frac{\partial \tau_{xx}}{\partial x} + \frac{\partial \tau_{yx}}{\partial y} + \frac{\partial \tau_{zx}}{\partial z} = F_x$$

$$\rho \frac{D\rho}{dt} = \rho f_x + \frac{\partial \tau_{xx}}{\partial x} + \frac{\partial \tau_{yx}}{\partial y} + \frac{\partial \tau_{zx}}{\partial z}$$

Equation 1-46

$$\rho \frac{D\rho}{dt} = \rho f_y + \frac{\partial \tau_{xy}}{\partial x} + \frac{\partial \tau_{yy}}{\partial y} + \frac{\partial \tau_{zy}}{\partial z}$$

Equation 1-47

$$\rho \frac{D\rho}{dt} = \rho f_z + \frac{\partial \tau_{xz}}{\partial x} + \frac{\partial \tau_{yz}}{\partial y} + \frac{\partial \tau_{zz}}{\partial z}$$

Equation 1-48

The surface forces applied on the x direction are illustrated in Figure 12. For illustrative purposes, τ_{ij} represent the stress applied towards the j -direction on the plane perpendicular to the i -axis. Also, on the $abcd$ face in Figure 12, it is assumed that the only force in the x direction is due to shear stress, $\tau_{yx} dx dz$. Moreover, the face $efgh$ is parallel to the $abcd$ face with a distance of d_y .

Hence, the shear force acting towards x direction from the face $efgh$ is,

$$\left[\tau_{yx} + \left(\frac{\partial \tau_{yx}}{\partial y} \right) dy \right] dx dz$$

Equation 1-49

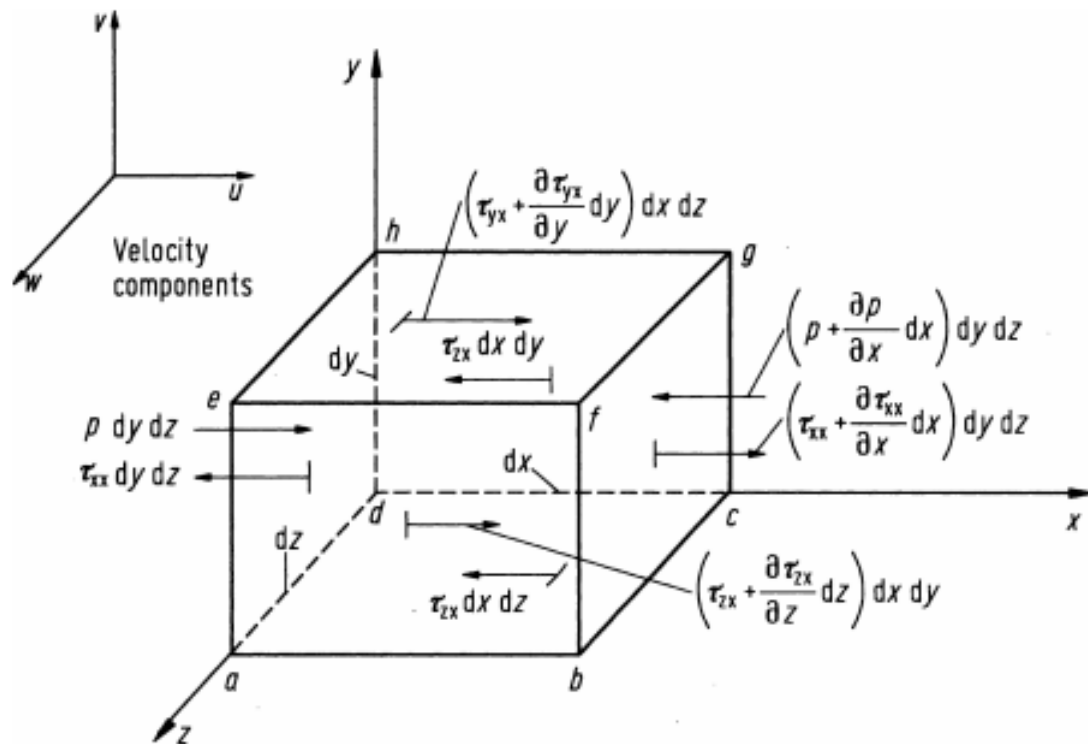


Figure 12 Surface forces acting on the x-direction of a fluid particle (Wendt, Anderson, & Von Karman Institute, 2008)

It is important to highlight that the shear forces acting on the bottom of faces $abcd$ and $efgh$ are towards the negative x -direction $[\tau_{zx} dx dy]$ and those acting on the top of the faces are towards the positive x direction $\left[\tau_{yx} + \left(\frac{\partial \tau_{yx}}{\partial y} \right) dy \right], \left[\tau_{zx} + \left(\frac{\partial \tau_{zx}}{\partial z} \right) dz \right]$.

The directions of these forces can be proven using the components of velocity. In Figure 12, It is acknowledged that the velocities u, v and w are in the positive direction of the axes. In other words, the value of u increases with positive y direction. Hence, velocity on top of the $efgh$ face is slightly higher than on the $efgh$ face. As a result, it creates a tugging motion that tries to move the fluid particle towards the positive x direction. Conversely, velocity is lower underneath the $abcd$ face than on the $abcd$ face. Hence, it creates a dragging motion on the fluid particle towards the negative x directions.

Similarly, other stress forces and directions are illustrated in Figure 12 can be justified in the same manner. However, the face $adhe$ is perpendicular to the x axis and the only force towards x direction is the pressure force ($p \, dx \, dy$) acting towards the fluid particle.

With reference to Figure 12,

$$\begin{aligned} & \left\{ \begin{array}{l} \text{Net forces acting} \\ \text{on X direction} \end{array} \right\} \\ &= \left[p - \left(p + \frac{\partial p}{\partial x} dx \right) dydz \right] + \left[\left(\tau_{xx} + \frac{\partial \tau_{xx}}{\partial x} dx \right) - \tau_{xx} \right] dydz \\ &+ \left[\left(\tau_{yx} + \frac{\partial \tau_{yx}}{\partial y} dy \right) - \tau_{yx} \right] dx dz + \left[\left(\tau_{zx} + \frac{\partial \tau_{zx}}{\partial z} dz \right) - \tau_{zx} \right] dx dy \end{aligned}$$

Equation 1-50

Referring to Equation 1-4 from section 1.2.4.1, body forces acting in x direction is,

$$F_x = \rho f_x (dx \, dy \, dz)$$

Hence, by combining Equation 1-4 and Equation 1-50; and using algebraic simplification,

$$F_x = \left(-\frac{\partial p}{\partial x} + \frac{\partial \tau_{xx}}{\partial x} + \frac{\partial \tau_{yx}}{\partial y} + \frac{\partial \tau_{zx}}{\partial z} \right) dx dy dz + \rho f_x dx dy dz$$

Equation 1-51

Recalling Newton's second law and Equation 1-43,

$$m = \rho (dx dy dz)$$

Also, acceleration in x direction is,

$$a_x = \frac{Du}{Dt}$$

Equation 1-52

Combining Equation 1-42, Equation 1-43, Equation 1-51 and Equation 1-52, the momentum equation of x direction is,

$$\rho \frac{Du}{Dt} = -\frac{\partial p}{\partial x} + \frac{\partial \tau_{xx}}{\partial x} + \frac{\partial \tau_{yx}}{\partial y} + \frac{\partial \tau_{zx}}{\partial z} + \rho f_x$$

Equation 1-53

Similarly, the momentum equation for the y and z directions are,

$$\rho \frac{Dv}{Dt} = -\frac{\partial p}{\partial y} + \frac{\partial \tau_{xy}}{\partial x} + \frac{\partial \tau_{yy}}{\partial y} + \frac{\partial \tau_{zy}}{\partial z} + \rho f_y$$

$$\rho \frac{Dw}{Dt} = -\frac{\partial p}{\partial z} + \frac{\partial \tau_{xz}}{\partial x} + \frac{\partial \tau_{yz}}{\partial y} + \frac{\partial \tau_{zz}}{\partial z} + \rho f_z$$

Equation 1-54

Comparing Equation 1-46 and Equation 1-53, the difference in Equation 1-53 is due to the added pressure force of viscous actions acting on the surface.

Since the fluid particle is moving with the flow, Equation 1-53 and Equation 1-54 are in non-conservation form. Instead, they are designated as scalar equations. These equations, called Navier-Stokes equations, can be transformed into conservation form using the following method.

The left hand side of the Equation 1-53 can be written in substantial derivative form,

$$\rho \frac{Du}{Dt} = \rho \frac{\partial u}{\partial t} + \rho \vec{V} \cdot \nabla u$$

Equation 1-55

By rearranging,

$$\frac{\partial(\rho u)}{\partial t} = \rho \frac{\partial u}{\partial t} + u \frac{\partial \rho}{\partial t}$$

Hence,

$$\rho \frac{\partial u}{\partial t} = \frac{\partial(\rho u)}{\partial t} - u \frac{\partial \rho}{\partial t}$$

Equation 1-56

Using the vector identity for the divergence,

$$\nabla \cdot (\rho u \vec{V}) = u \nabla \cdot (\rho \vec{V}) + (\rho \vec{V}) \cdot \nabla u$$

Rearranging,

$$\rho \vec{V} \cdot \nabla u = \nabla \cdot (\rho u \vec{V}) - u \nabla \cdot (\rho \vec{V})$$

Equation 1-57

Using Equation 1-56 and Equation 1-57 in Equation 1-55,

$$\rho \frac{Du}{Dt} = \frac{\partial(\rho u)}{\partial t} - u \frac{\partial \rho}{\partial t} - u \nabla \cdot (\rho \vec{V}) + \nabla \cdot (\rho u \vec{V})$$

$$\rho \frac{Du}{Dt} = \frac{\partial(\rho u)}{\partial t} - u \left[\frac{\partial \rho}{\partial t} + \nabla \cdot (\rho \vec{V}) \right] + \nabla \cdot (\rho u \vec{V})$$

Equation 1-58

Referring to Equation 1-35 it is shown that $\partial \rho / \partial t + \nabla \cdot \rho \mathbf{v} = 0$. Hence, Equation 1-58 can be written as,

$$\rho \frac{Du}{Dt} = \frac{\partial(\rho u)}{\partial t} + \nabla \cdot (\rho u \vec{V})$$

Equation 1-59

Using Equation 1-59 in Equation 1-53,

$$\frac{\partial(\rho u)}{\partial t} + \nabla \cdot (\rho u \vec{V}) = -\frac{\partial p}{\partial x} + \frac{\partial \tau_{xx}}{\partial x} + \frac{\partial \tau_{yx}}{\partial y} + \frac{\partial \tau_{zx}}{\partial z} + \rho f_x$$

Equation 1-60

Likewise, Equation 1-54 can be written as,

$$\frac{\partial(\rho u)}{\partial t} + \nabla \cdot (\rho u \vec{V}) = -\frac{\partial p}{\partial y} + \frac{\partial \tau_{xy}}{\partial x} + \frac{\partial \tau_{yy}}{\partial y} + \frac{\partial \tau_{zy}}{\partial z} + \rho f_y$$

$$\frac{\partial(\rho u)}{\partial t} + \nabla \cdot (\rho u \vec{V}) = -\frac{\partial p}{\partial z} + \frac{\partial \tau_{xz}}{\partial x} + \frac{\partial \tau_{yz}}{\partial y} + \frac{\partial \tau_{zz}}{\partial z} + \rho f_z$$

Equation 1-61

Equation 1-60 and Equation 1-61 are the conservation form of Navier-stokes equations.

Newton identified that shear stress in a fluid is proportional to the time rate-of-strain (velocity gradients), and he called them Newtonian fluids. Virtually all the engineering aerodynamics problems are considered to involve Newtonian fluids.

Hence,

$$\tau_{xx} = \lambda \nabla \cdot \vec{V} + 2\mu \frac{\partial u}{\partial x}$$

$$\tau_{yy} = \lambda \nabla \cdot \vec{V} + 2\mu \frac{\partial v}{\partial y}$$

$$\tau_{zz} = \lambda \nabla \cdot \vec{V} + 2\mu \frac{\partial w}{\partial z}$$

$$\tau_{xy} = \tau_{yx} = \mu \left(\frac{\partial v}{\partial x} + \frac{\partial u}{\partial y} \right)$$

$$\tau_{xz} = \tau_{zx} = \mu \left(\frac{\partial u}{\partial z} + \frac{\partial w}{\partial x} \right)$$

$$\tau_{yz} = \tau_{zy} = \mu \left(\frac{\partial w}{\partial y} + \frac{\partial v}{\partial z} \right)$$

Equation 1-62

Stokes made the assumption that,

$$\lambda = -\frac{2}{3}\mu$$

Where, λ is the molecular viscosity coefficient and μ is the bulk viscosity coefficient.

By combining Equation 1-60 and Equation 1-62, Navier-stokes equations in conservation form can be obtained.

$$\begin{aligned}
& \frac{\partial(\rho u)}{\partial t} + \frac{\partial(\rho u^2)}{\partial x} + \frac{\partial(\rho uv)}{\partial y} + \frac{\partial(\rho uw)}{\partial z} \\
&= -\frac{\partial p}{\partial x} + \frac{\partial}{\partial x} \left(\lambda \nabla \cdot \vec{v} + 2\mu \frac{\partial u}{\partial x} \right) + \frac{\partial}{\partial y} \left[\mu \left(\frac{\partial v}{\partial x} + \frac{\partial u}{\partial y} \right) \right] + \frac{\partial}{\partial z} \left[\mu \left(\frac{\partial u}{\partial z} + \frac{\partial w}{\partial x} \right) \right] \\
&+ \rho f_x
\end{aligned}$$

Equation 1-63

Similarly, Equation 1-61 can also be written in conservation form,

$$\begin{aligned}
& \frac{\partial(\rho v)}{\partial t} + \frac{\partial(\rho uv)}{\partial x} + \frac{\partial(\rho v^2)}{\partial y} + \frac{\partial(\rho vw)}{\partial z} \\
&= -\frac{\partial p}{\partial y} + \frac{\partial}{\partial x} \left[\mu \left(\frac{\partial v}{\partial x} + \frac{\partial u}{\partial y} \right) \right] + \frac{\partial}{\partial y} \left(\lambda \nabla \cdot \vec{v} + 2\mu \frac{\partial v}{\partial y} \right) + \frac{\partial}{\partial z} \left[\mu \left(\frac{\partial w}{\partial y} + \frac{\partial v}{\partial z} \right) \right] \\
&+ \rho f_y
\end{aligned}$$

$$\begin{aligned}
& \frac{\partial(\rho w)}{\partial t} + \frac{\partial(\rho uw)}{\partial x} + \frac{\partial(\rho vw)}{\partial y} + \frac{\partial(\rho w^2)}{\partial z} \\
&= -\frac{\partial p}{\partial z} + \frac{\partial}{\partial x} \left[\mu \left(\frac{\partial u}{\partial z} + \frac{\partial w}{\partial x} \right) \right] + \frac{\partial}{\partial y} \left[\mu \left(\frac{\partial w}{\partial y} + \frac{\partial v}{\partial z} \right) \right] + \frac{\partial}{\partial z} \left(\lambda \nabla \cdot \vec{v} + 2\mu \frac{\partial w}{\partial z} \right) \\
&+ \rho f_z
\end{aligned}$$

Equation 1-64

1.3.1.4 Energy conservation

Conservation of energy equations can be derived in the same way as mass conservation and momentum conservation. The basic theory behind conservation of energy is the first principle of thermodynamics in a fluid element.

$$\left\{ \begin{array}{l} \text{Ratio of change} \\ \text{of energy} \\ \text{inside the fluid particle} \end{array} \right\} = \left\{ \begin{array}{l} \text{Net flux of heat} \\ \text{going in to the} \\ \text{fluid particle} \end{array} \right\} + \left\{ \begin{array}{l} \text{rate of motion due to} \\ \text{body and surface} \\ \text{forces} \end{array} \right\}$$

$$\Delta E_{\text{system}} = Q_{\text{in}} + W_{\text{ext}}$$

Equation 1-65

W_{ext} is the rate of motion due to body and surface forces. Recalling section 1.2.4.1, body forces can be represented as,

$$\rho \vec{f} \cdot \vec{V}(dx dy dz)$$

Equation 1-66

As described in section 1.3.1.3, surface forces acting on a fluid particle are a combination of pressure forces plus shear and normal stresses. With reference to Figure 12, work done in the x direction is a function of the velocity and forces acting on the surfaces. In order to highlight the energy equations, forces acting in the x direction are redrawn in Figure 13.

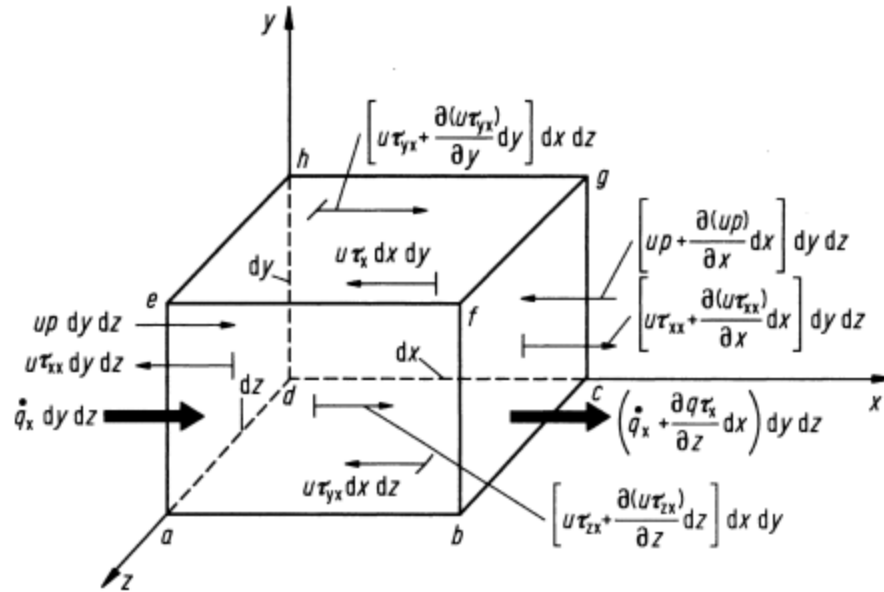


Figure 13 Energy acting on the x direction of a fluid particle (Wendt, Anderson, & Von Karman Institute, 2008)

Analyzing the forces acting on the face $adhe$ and $bcgf$ in Figure 13, the net rate of work applied by pressure in the x directions is,

$$\left[up - \left(up + \frac{\partial(up)}{\partial x} dx \right) \right] dy dz = - \frac{\partial(up)}{\partial x} dx dy dz$$

In the same manner, net rate of work applied by shear stresses on the x direction on the face $adhe$ and $bcgf$ is,

$$\left[\left(u\tau_{yx} + \frac{\partial(u\tau_{yx})}{\partial y} dy \right) - u\tau_{yx} \right] dx dy = \frac{\partial(u\tau_{yx})}{\partial y} dx dy dz$$

Bearing in mind that in Figure 13, the net rate of work implemented on the moving fluid particle is,

$$F_x = \left[- \frac{\partial(up)}{\partial x} + \frac{\partial(u\tau_{xx})}{\partial x} + \frac{\partial(u\tau_{yx})}{\partial y} + \frac{\partial(u\tau_{zx})}{\partial z} \right] dx dy dz$$

Similarly, the net forces acting in the y and z directions are, respectively,

$$F_y = \left[-\frac{\partial(vp)}{\partial y} + \frac{\partial(v\tau_{xy})}{\partial x} + \frac{\partial(v\tau_{yy})}{\partial y} + \frac{\partial(v\tau_{zy})}{\partial z} \right] dx dy dz$$

$$F_z = \left[-\frac{\partial(wp)}{\partial z} + \frac{\partial(w\tau_{xz})}{\partial x} + \frac{\partial(w\tau_{yz})}{\partial y} + \frac{\partial(w\tau_{zz})}{\partial z} \right] dx dy dz$$

Equation 1-68

Hence, the net rate of work acting on a moving fluid particle is equal to the total surface forces acting in x , y and z directions plus the body forces. Thus, Q_{in} can be represented by combining Equation 1-66, Equation 1-67 and Equation 1-68,

$$W_{ext} = \left[-\left(\frac{\partial(up)}{\partial x} + \frac{\partial(vp)}{\partial y} + \frac{\partial(wp)}{\partial z} \right) + \frac{\partial(u\tau_{xx})}{\partial x} + \frac{\partial(u\tau_{yx})}{\partial y} + \frac{\partial(u\tau_{zx})}{\partial z} + \frac{\partial(v\tau_{xy})}{\partial x} + \frac{\partial(v\tau_{yy})}{\partial y} + \frac{\partial(v\tau_{zy})}{\partial z} + \frac{\partial(w\tau_{xz})}{\partial x} + \frac{\partial(w\tau_{yz})}{\partial y} + \frac{\partial(w\tau_{zz})}{\partial z} \right] dx dy dz + \rho \vec{f} \cdot \vec{V}(dx dy dz)$$

Equation 1-69

The net flux of heat in the fluid particle is denoted by Q_{in} part of the Equation 1-65.

Volumetric heating related to absorption or emission of radiation and heat transfer due to temperature gradients are the two contributors to Q_{in} .

If the rate of volumetric heat addition per unit mass is defined as \dot{q} ,

$$\left\{ \begin{array}{l} \text{Volumetric heating} \\ \text{of the element} \end{array} \right\} = \rho \dot{q} dx dy dz$$

Equation 1-70

Referring back to Figure 13, the heat conveyed by thermal conduction across the face *adhe* in *x* direction is,

$$\dot{q}_x dy dz$$

Equation 1-71

Where, \dot{q}_x is per unit time, per unit area.

Also, the heat conveyed out of the face *bcfg* is

$$\left[\dot{q}_x + \left(\frac{\partial \dot{q}_x}{\partial x} \right) dx \right] dy dz$$

Equation 1-72

Hence, by combining Equation 1-71 and Equation 1-72, the net heat conveyed in the *x* direction is,

$$-\frac{\partial \dot{q}_x}{\partial x} dx dy dz$$

Similarly, heat conveyed in *y* and *z* direction is,

$$-\frac{\partial \dot{q}_y}{\partial y} dx dy dz$$

$$-\frac{\partial \dot{q}_z}{\partial z} dx dy dz$$

Thus,

$$\left\{ \begin{array}{l} \text{Heating due to} \\ \text{thermal conduction} \end{array} \right\} = - \left(\frac{\partial \dot{q}_x}{\partial x} + \frac{\partial \dot{q}_y}{\partial y} + \frac{\partial \dot{q}_z}{\partial z} \right) dx dy dz$$

Equation 1-73

Q_{in} is the summation of Equation 1-70 and Equation 1-73,

$$Q_{in} = \left[\rho \dot{q} - \left(\frac{\partial \dot{q}_x}{\partial x} + \frac{\partial \dot{q}_y}{\partial y} + \frac{\partial \dot{q}_z}{\partial z} \right) \right] dx dy dz$$

Equation 1-74

Heat conveyed is relative to the local temperature gradient,

$$\dot{q}_x = -k \frac{\partial T}{\partial x}, \quad \dot{q}_y = -k \frac{\partial T}{\partial y}, \quad \dot{q}_z = -k \frac{\partial T}{\partial z}$$

Where, k is the thermal conductivity of the fluid.

Equation 1-74 can be re-written as,

$$Q_{in} = \left[\rho \dot{q} + \frac{\partial}{\partial x} \left(k \frac{\partial T}{\partial x} \right) + \frac{\partial}{\partial y} \left(k \frac{\partial T}{\partial y} \right) + \frac{\partial}{\partial z} \left(k \frac{\partial T}{\partial z} \right) \right] dx dy dz$$

Equation 1-75

Referring back to Equation 1-65, ΔE_{system} is the time rate of change of energy of the fluid particle.

$$\Delta E_{system} = \left\{ \begin{array}{l} \text{sum of internal} \\ \text{energy per} \\ \text{unit mass} \end{array} (e) \right\} + \left\{ \begin{array}{l} \text{kinetic energy} \\ \text{per unit mass} \end{array} \left(\frac{V^2}{2} \right) \right\}$$

Since the particle is in motion, the time rate of change of energy per unit mass should be in substantial derivative form. Hence,

$$\Delta E_{system} = \rho \frac{D}{Dt} \left(e + \frac{V^2}{2} \right) dx dy dz$$

Equation 1-76

The energy equation, Equation 1-65, can be represented using Equation 1-69, Equation 1-75 and Equation 1-76,

$$\begin{aligned} \rho \frac{D}{Dt} \left(e + \frac{V^2}{2} \right) &= \rho \dot{q} + \frac{\partial}{\partial x} \left(k \frac{\partial T}{\partial x} \right) + \frac{\partial}{\partial y} \left(k \frac{\partial T}{\partial y} \right) + \frac{\partial}{\partial z} \left(k \frac{\partial T}{\partial z} \right) - \left(\frac{\partial(u\dot{p})}{\partial x} + \frac{\partial(v\dot{p})}{\partial y} + \frac{\partial(w\dot{p})}{\partial z} \right) \\ &+ \frac{\partial(u\tau_{xx})}{\partial x} + \frac{\partial(u\tau_{yx})}{\partial y} + \frac{\partial(u\tau_{zx})}{\partial z} + \frac{\partial(v\tau_{xy})}{\partial x} + \frac{\partial(v\tau_{yy})}{\partial y} + \frac{\partial(v\tau_{zy})}{\partial z} \\ &+ \frac{\partial(w\tau_{xz})}{\partial x} + \frac{\partial(w\tau_{yz})}{\partial y} + \frac{\partial(w\tau_{zz})}{\partial z} + \rho \vec{f} \cdot \vec{V} \end{aligned}$$

Equation 1-77

Equation 1-77 is the energy equation in non-conservation form. Therefore, the substantial derivative method used in section 35 should be used to transform it into conservation form.

Hence,

$$\begin{aligned} \frac{\partial}{\partial t} \left[\rho \left(e + \frac{V^2}{2} \right) \right] + \nabla \cdot \left[\rho \left(e + \frac{V^2}{2} \vec{V} \right) \right] \\ = \rho \dot{q} + \frac{\partial}{\partial x} \left(k \frac{\partial T}{\partial x} \right) + \frac{\partial}{\partial y} \left(k \frac{\partial T}{\partial y} \right) + \frac{\partial}{\partial z} \left(k \frac{\partial T}{\partial z} \right) \\ - \left(\frac{\partial(u\dot{p})}{\partial x} + \frac{\partial(v\dot{p})}{\partial y} + \frac{\partial(w\dot{p})}{\partial z} \right) \frac{\partial(u\tau_{xx})}{\partial x} + \frac{\partial(u\tau_{yx})}{\partial y} + \frac{\partial(u\tau_{zx})}{\partial z} + \frac{\partial(v\tau_{xy})}{\partial x} \\ + \frac{\partial(v\tau_{yy})}{\partial y} + \frac{\partial(v\tau_{zy})}{\partial z} + \frac{\partial(w\tau_{xz})}{\partial x} + \frac{\partial(w\tau_{yz})}{\partial y} + \frac{\partial(w\tau_{zz})}{\partial z} + \rho \vec{f} \cdot \vec{V} \end{aligned}$$

Equation 1-78

Equation 1-78 is the energy equation in conservation form.

1.4 Computational Fluid Dynamics (CFD)

Computational Fluid Dynamics (CFD) is the method of applying the governing equations of fluid dynamics and advancing these equations in space and/or time to obtain an approximate solution to a fluid dynamics and heat transfer practical application (Zikanov, 2010, p. 1). The governing equations and derivation of those equations are explained in section 1.3.

Initially, CFD was only reserved for high end applications like astronautics or aeronautics. But, with the advancement of technology, CFD has spread to other engineering fields as a replacement for wind tunnel or other experimental tests (Tu & Yeoh, Guan Heng, 2007, p. 1). Moreover, some of the CFD software tools are available on the web for free as open source systems. Commercial CFD tool, on the other hand, are relatively expensive, but normally produce results with greater accuracy. However, regardless of the CFD tool that used, it is important to use experimental analysis in order to verify theories and validate CFD results (Kleinstreuer, 2010, p. 523).

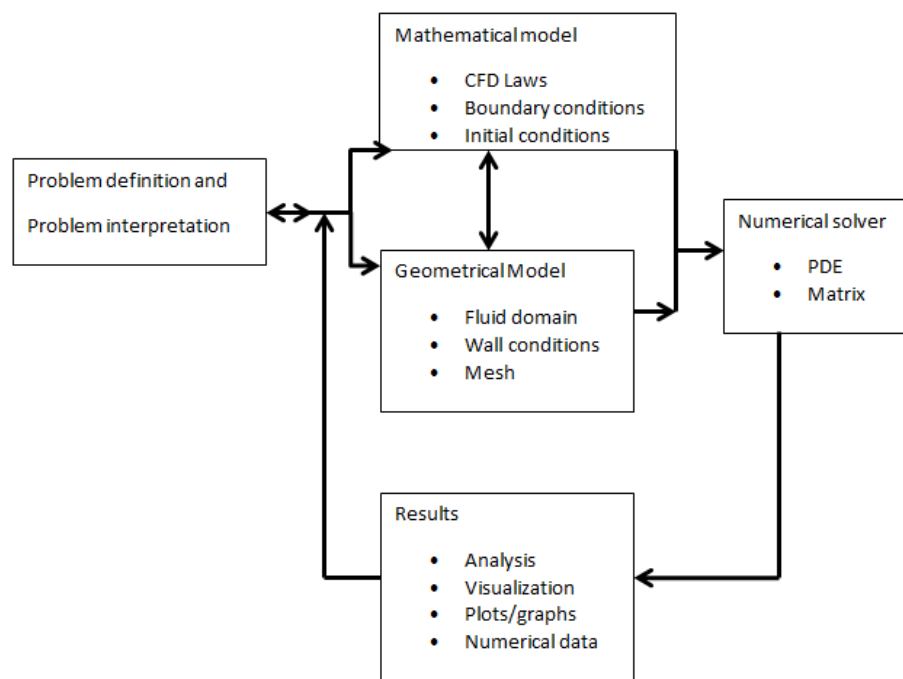


Figure 14 Flow process of a CFD modeling

As illustrated in Figure 14, a key aspect of CFD is to understand the CFD problem and have the ability to improve the model based on the results or analysis. By using CFD methods, one can help to better understand the key elements of fluid flow and heat transfer of modeled objects (Tu & Yeoh, Guan Heng, 2007, p. 6). CFD can be used to identify a variety of creative solutions to various problems. However, critical elements of any successful CFD simulation are to identify the nature of the problem correctly and apply the appropriate methods to solve a particular challenge (Kleinstreuer, 2010, p. 526).

In order to identify the problem and solutions of CFD simulations, CFD codes are broken down to three main elements; pre-processor, solver and post-processor (Tu & Yeoh, Guan Heng, 2007, p. 30). With that in mind, Figure 15 illustrates the relationship of individual elements of a CFD simulation.

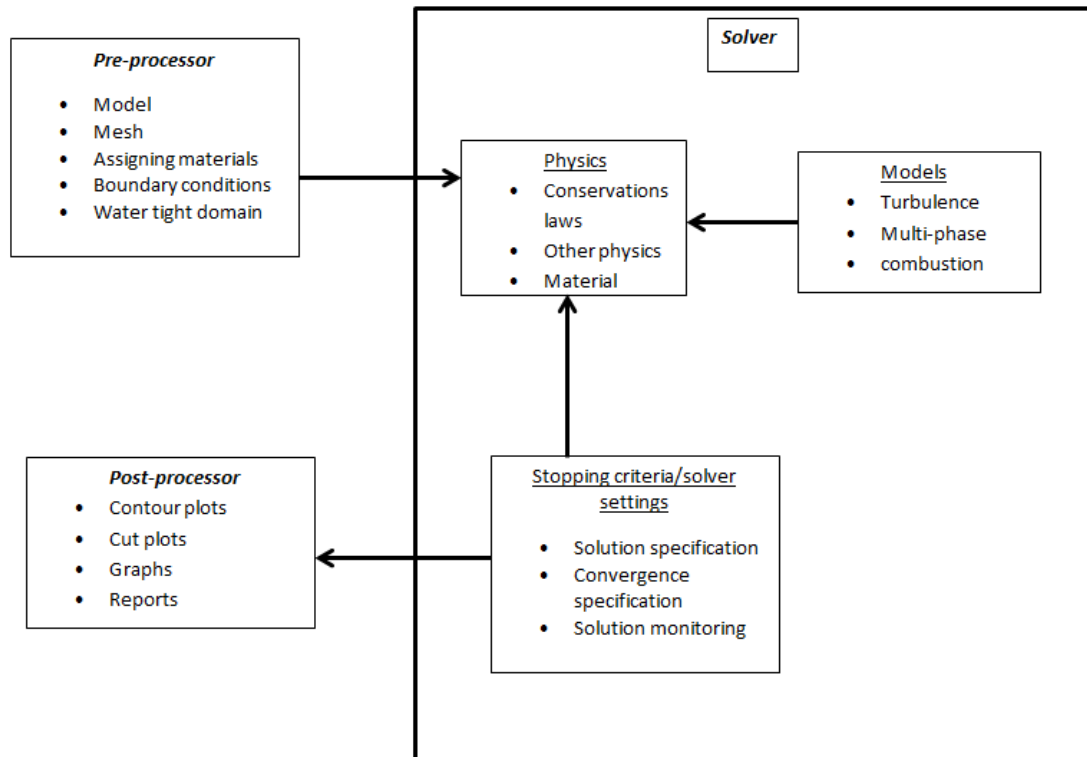


Figure 15 Relationship of the main elements

1.4.1 Problem Identification and Pre-Process

1.4.1.1 Creating the Model

The first and the most fundamental step in a CFD simulation is creating the model with the correct geometry and computational domain. Usually, models are created using CAD (Computer Aided Design) software that can handle advanced geometrical features. However, these complex geometrical models need to be simplified before they are imported into CFD tools (Wendt, Anderson, & Von Karman Institute, 2008, p. 305).

The computational domain consists of a grid or mesh, and defines cells or controls volume (Kleinstreuer, 2010, p. 526). It is important to understand the concept of a computational domain because the computational domain is not always the solid part of the

model. Most CFD tools require modeling the computational domain or empty spaces of a model, rather than modeling the solid parts. The computational domain is an important factor as it holds and computes all the dependent variables throughout the domain. To illustrate, Figure 16 (also referred to as model 1) shows the fluid flowing between two parallel plates and Figure 17, (also referred to as model 2) shows the fluid flowing around two cylinders (Tu & Yeoh, Guan Heng, 2007, p. 33). It is important to understand the limitations of the physical domain and the computational domain. For the purposes of demonstrating the CFD simulation of model 1 and 2, a two-dimensional computational domain is assumed.

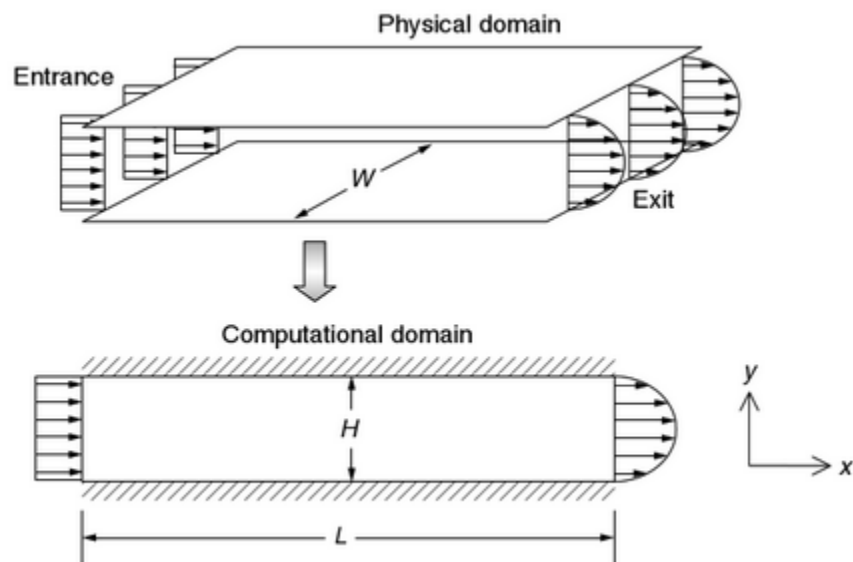


Figure 16 Model 1: flowing between two plates (Tu & Yeoh, Guan Heng, 2007, p. 34)

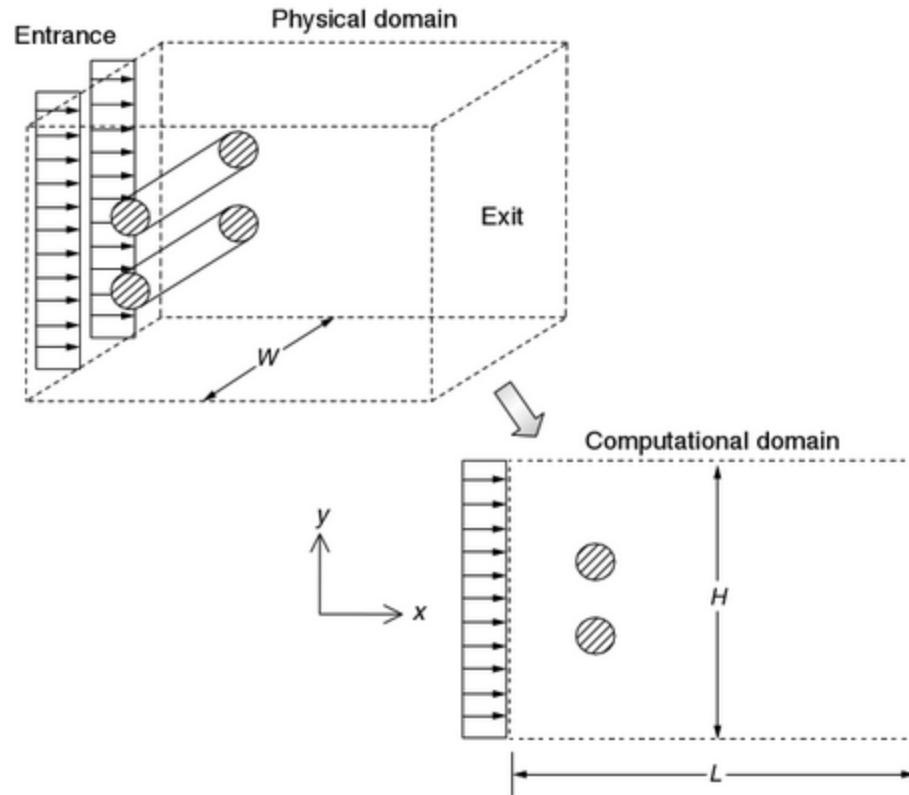


Figure 17 Model 2: Flowing around two cylinders (Tu & Yeoh, Guan Heng, 2007, p. 34)

Analyzing the two models, it is evident that model 1 is an internal flow simulation and model 2 is an external flow simulation. Also, in both models, flow is entering through the left side boundary and exiting through the right side boundary. However, the main difference is that the computational domain of model 1 is limited by the two horizontal plates. Meaning, the area of the computational domain is restricted by rigid physical external walls. On the other hand, in model 2, the computational domain is not restricted by physical walls (Tu & Yeoh, Guan Heng, 2007, p. 34). It is important to pay attention to the model geometry, as some CFD tools require modeling the empty space (or fluid domain) and some require modeling the physical space.

1.4.1.2 Computational Mesh Generation

The next step is to create a computational mesh; this step is crucial in a simulation, as the mesh resolution decides the resolution of the results. The mesh generation is the process of breaking down the fluid domain into a number of smaller, non-overlapping subdomains (Tu & Yeoh, Guan Heng, 2007, p. 35). Generally, mesh generation starts at the edges, and then moves to the faces, and finally to the volume of the domain (Wendt, Anderson, & Von Karman Institute, 2008, p. 310).

Improving the mesh geometry or increasing the mesh density will improve the accuracy of the results. However, it also increases the use of computer resources and calculation time as well. An important point to consider while creating a mesh design is to identify the appropriate balance between creating a satisfactory mesh and the use of reasonable amounts of computer resources. There are two main meshing categories and each category serves a different purpose (Tu & Yeoh, Guan Heng, 2007, p. 36).

When large blocks of a fluid domain are broken down to into discrete cells, it is called structured mesh generation. In the same manner, when variable cells are directly surrounded by complex geometric domains, it is called unstructured mesh generation (Kleinstreuer, 2010, p. 527). Generating a successful mesh takes the most time and resources in most CFD projects (Tu & Yeoh, Guan Heng, 2007, p. 36). It is up to the user to identify the best method of mesh generation to optimize any particular CFD simulation.

Referring back to model 1 in Figure 16, the structured method is used for mesh generation. It is a relatively straightforward method and it is constructed using simple rectangular cells that are stacked together. Figure 18 shows the mesh in model 1 with 20 (L) x 30 (H) cells resulting a total of 400 cells.

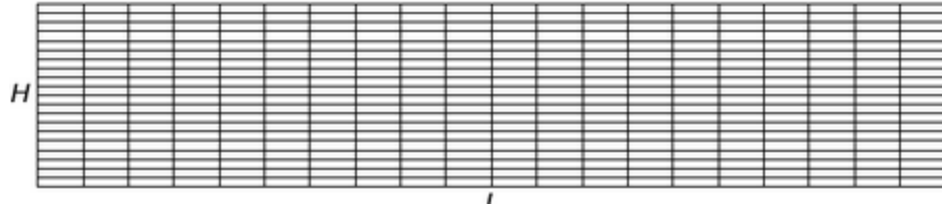


Figure 18 simple structured meshing for Model 1 (Tu & Yeoh, Guan Heng, 2007, p. 36)

In contrast, Figure 19 shows a more complex unstructured mesh generation with triangular shaped cells. Triangles (or other regular geometric shapes) can be used for more complex and tight geometrical areas. In model 2, there are 16,637 cells in the computational domain (Tu & Yeoh, Guan Heng, 2007, p. 36).

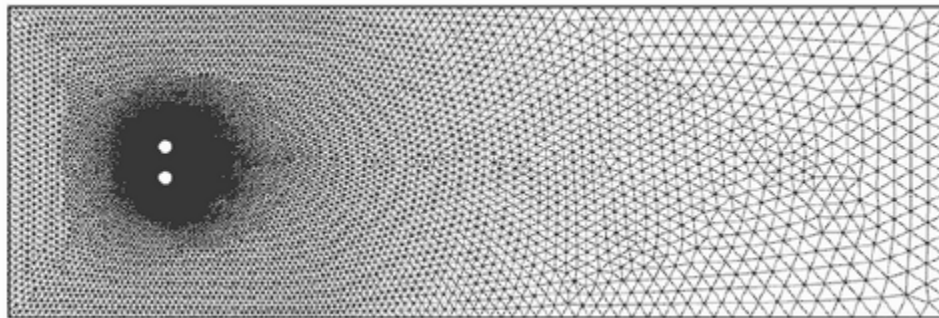


Figure 19 complex unstructured meshing for Model 2 (Tu & Yeoh, Guan Heng, 2007, p. 37)

As a final point, it is acceptable to interchange or combine structured and unstructured methods in creating mesh designs. Also, in some geometry, both the structured and unstructured method is used as a combination of two; it is called the hybrid method (see Figure 20 Hybrid mesh (Kleinstreuer, 2010, p. 528). Rectangular cells are mostly used near the boundary wall and prismatic or triangular cells are used in the volume of the domain (Wendt, Anderson, & Von Karman Institute, 2008, p. 314).

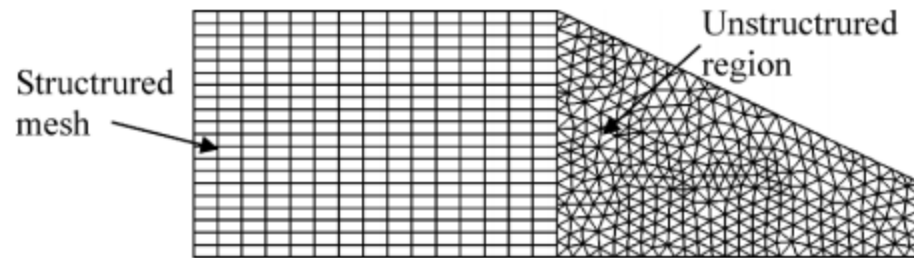


Figure 20 Hybrid mesh (Kleinstreuer, 2010, p. 528)

1.4.1.3 Physics and fluid characteristics

The perfection of the CFD solution depends on the accurate selection of the physics and fluid properties. Since, fluid flow involves many different forms of physical properties, it is up to the user to select and apply the best flow physics for the application. Therefore, in a complex CFD problem, the user is required to have extensive knowledge regarding the behavior and physics of the problem before applying it to a CFD tool.

In order to assist the selection of physics, the following flow chart (See Figure 21) can be used as a guideline. However, it is up to the user to apply correct physics and methods for a successful CFD simulation (Tu & Yeoh, Guan Heng, 2007, p. 38). Also, one must bear in mind that the physical properties change with different fluid applications. Therefore, it is important to apply the physics to the correct fluid domains.

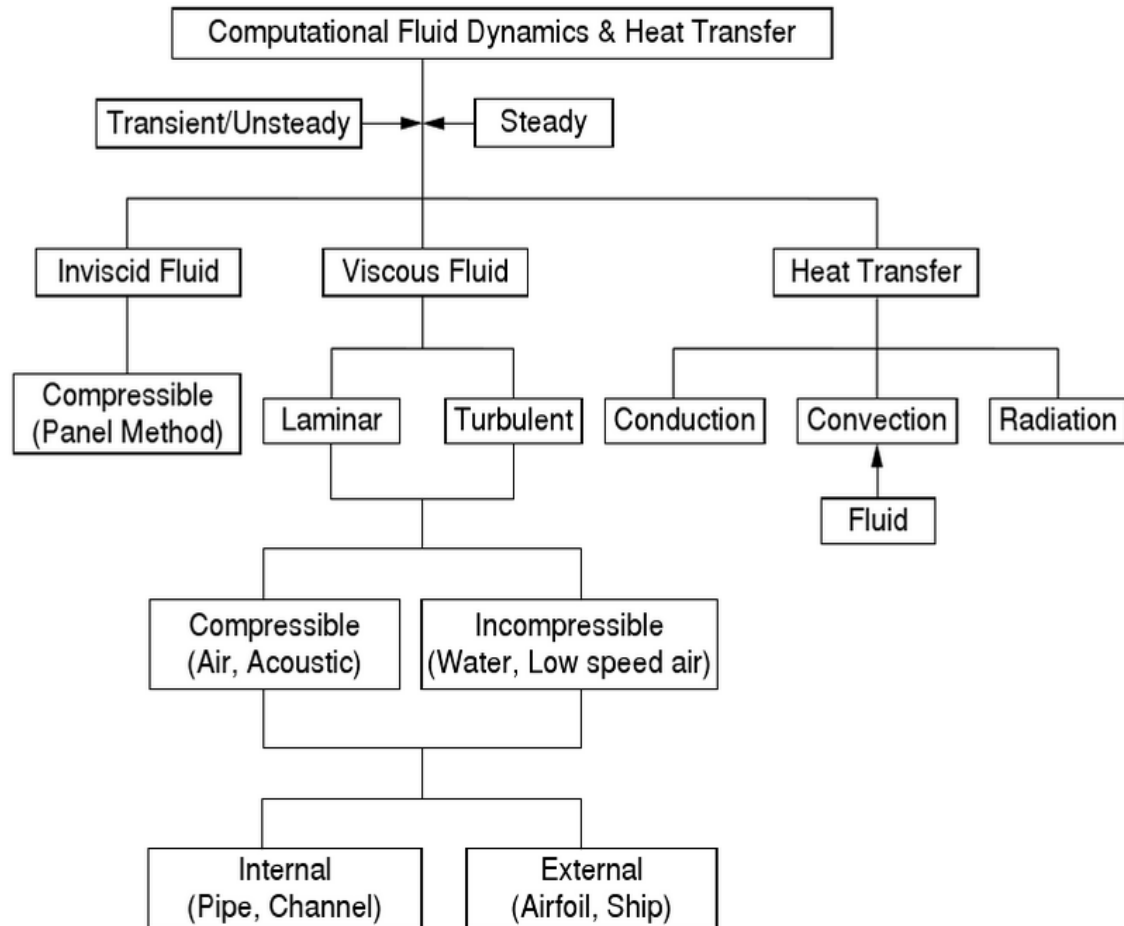


Figure 21 Flowchart for applying various physics for CFD tools (Tu & Yeoh, Guan Heng, 2007)

1.4.1.4 Boundary conditions

Boundary conditions are defined at each face of a three dimensional model and each edge of a two dimensional model (Kleinstreuer, 2010, p. 527). The purpose of the boundary conditions is to define the flow field within the boundaries of the flow region, and to mimic the actual physical representation of the application (Wendt, Anderson, & Von Karman Institute, 2008, p. 306).

Typical flow movements relevant to boundary conditions are inlets, outlets, walls or fan conditions. Other boundary conditions such as solid walls, heat sources or fluid subdomain walls

also need to be defined accordingly. Figure 22 and Figure 23 represents the boundary conditions of model 1 and 2 (see 1.4.1.1 for more details about the model).

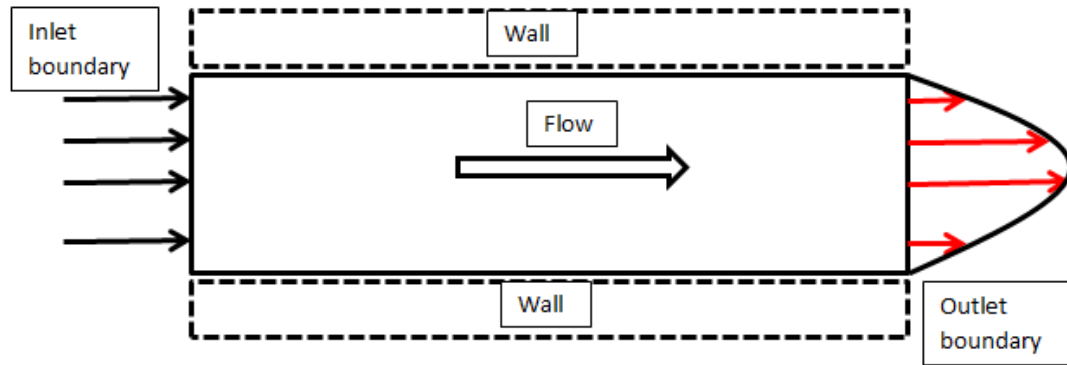


Figure 22 Basic boundary condition of a simple Model

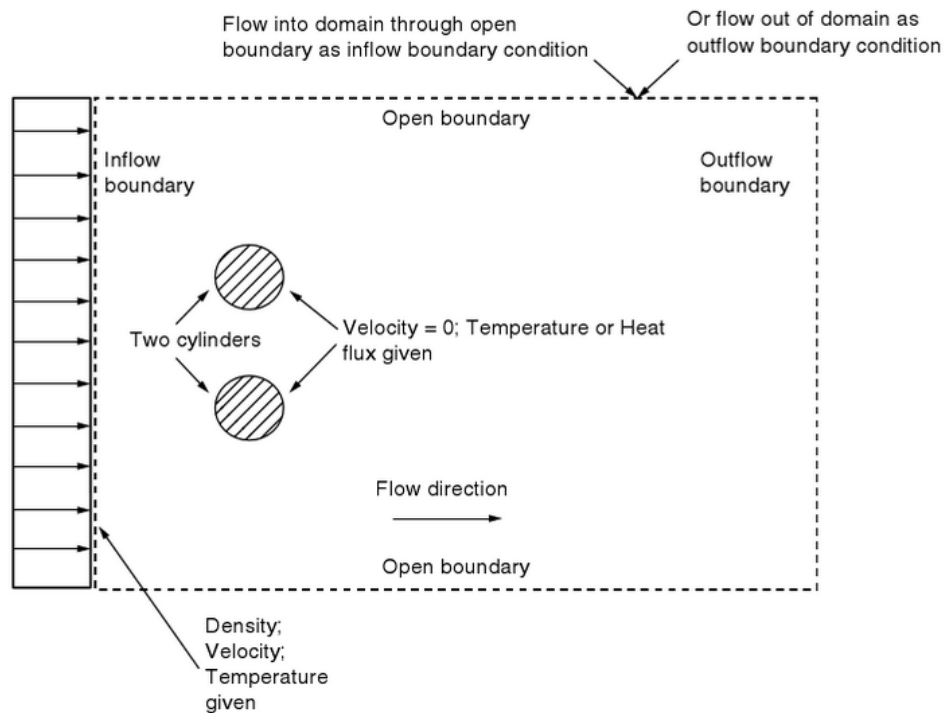


Figure 23 Boundary conditions of model 2 (Tu & Yeoh, Guan Heng, 2007, p. 42)

Each flow characteristic has a unique set of boundary conditions. The following are some of the boundary conditions that are used in simple flow simulations. For turbulent compressible flow; inlet or outlet velocity components, total or static pressure, flow direction, temperature and turbulence variables are assigned. For incompressible flow with heat transfer or laminar compressible flow; wall temperature or heat transfer rates should be defined (Wendt, Anderson, & Von Karman Institute, 2008, p. 325). For external or internal fans; pressure difference, rpm and blade diameter needs to be specified.

Referring back to Figure 22, the velocity at the external solid walls bounding the fluid domain is zero. Also, in Figure 23, velocity at the fixed cylinder walls is zero. The flow direction is obtained by the fluid entering through the inlet and the fluid exiting through the outlet; this is defined by the user as appropriate to the application. In general, if the inlet is defined as a volume or mass flow rate, then the outlet is typically defined as a pressure opening with relative pressure.

Nevertheless, the above mentioned boundary conditions and definitions are only valid if the fluid flow is below the speed of sound, sub-sonic flow. There is a distinct range of boundary conditions if the flow is above the speed of sound. But, supersonic flow is beyond the scope of this paper and will not be addressed. Interested readers are advised to refer to Wendt, Anderson, & Von Karman Institute, 2008 and Tu & Yeoh, Guan Heng, 2007 for more detailed information's about supersonic flow.

1.4.2 Numerical Analysis and CFD Solver

The next step in CFD simulation is to program the parameters of the solver. The solver contains two important parts; initialization and solution control.

Since fluid flow calculation is a complex process, results are determined using an iterative solution approach. Iterative process requires all the flow properties such as, velocity, pressure, temperature and other relevant characteristics to be initialized before the computational process. In other words, initial conditions are the starting point of the calculations, and theoretically, can be entirely arbitrary.

That being said, by using initial conditions appropriate to the application, users can achieve quick and accurate results. For example, by using initial conditions that are closer to the final results, the iteration process will be simplified; resulting in less computational time. Also, if improper initial conditions are used, the convergence process can be disorganized; resulting in higher computational times or incorrect results (Tu & Yeoh, Guan Heng, 2007, p. 47).

The next crucial step in the solver category is properly tracking the convergence process. Convergence is the process used to determine the point at which the solution to the algebraic equations is close to that of the partial differential equations. However, in order to a solution to properly converge, consistency and stability of the solution is essential and compulsory. (Tu & Yeoh, Guan Heng, 2007, p. 192).

Convergence is achieved by monitoring the imbalance or residuals brought forward by the numerical calculations of each iteration step. These imbalances reflect and report the global flow property conservation to the CFD tool. Modern CFD software provides a graphical user interface (GUI) tool that can be used to monitor the convergence sequence.

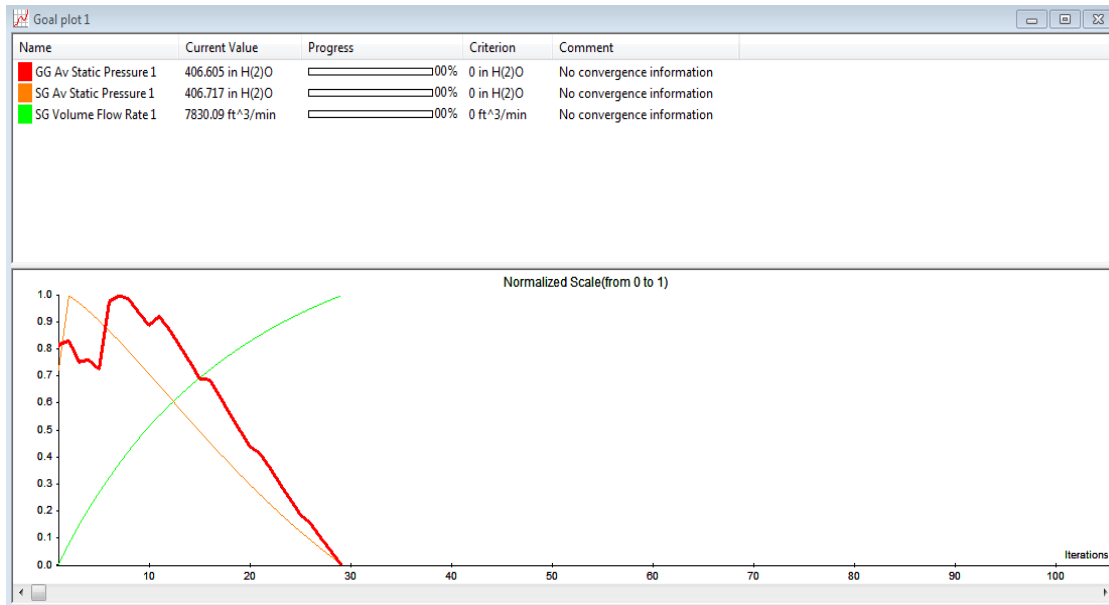


Figure 24 monitoring the iterations using a GUI in FloEFD software

The descending trend in Figure 24 shows the continual removal of surplus residuals leading to a convergent solution. When the trend is ascending, it means the residuals are possibly accumulating, resulting in divergent solution or no solution at all. The results are considered to be stable when the residuals fall below a pre-determined number that is embedded in the software.

1.4.3 Results, analysis and visualization

Once the results have converged and are stable, the next step is to perform an analysis and visualization of the data. Commercial CFD software can display the results in graphical images, and some programs can generate colorful animations. Consequently, these visualizations help to convert the numerical data into a more presentable graphical format.

It is important to understand the different graphical representations, as each helps one to understand and evaluate the results. For example, cut plots display the distribution of the selected parameter on a user-configured two-dimensional plane. Depending on the software

used, users can select vector functions designated with arrows. However, any cut plots have the ability to display the perspective view of the flow property in a two-dimensional plane with appropriate magnitude. On the other hand, X-Y plots can be used to compare and contrast the numerical data. These are traditionally used to directly compare numerical data with the experimental data.

Nevertheless, it is up to user to organize the data in a creative and presentable way. Not to mention, some software provides animations of the air flow particles and some provides complete analytical reports. To sum up, the post-processor step provides the simulation results as numerical data. However, different methods can be used to convert the numerical data into graphical visualizations that help to better understand the solutions.

1.4.4 Finite Volume Method (FVM)

The basic theory of computational involves fluid dynamic is applying the conservation laws on closed volume surfaces. In order to represent the laws in their integral form, the laws have to discretize the integral form of the equations instead of the differential form. This conversion technique is the basis of finite volume method (Wendt, Anderson, & Von Karman Institute, 2008, p. 134). Moreover, most modern general purpose CFD tools use the finite volume technique rather the conventional finite element method (Zikanov, 2010, p. 86).

The mathematics behind the FVM method involves subdividing the computational domain or the flow field into a finite number of non-over-lapping cells that cover the entire fluid region. This is so that exact conservation of properties occurs inside each individual piece of the control volume (Tu & Yeoh, Guan Heng, 2007, p. 134). These cells can be either structured or unstructured grid, hence, they can be of either a triangular or rectangular shape (Wendt,

Anderson, & Von Karman Institute, 2008, p. 278). Therefore, the FVM method has the ability to accommodate any type of grid, shape or location (Tu & Yeoh, Guan Heng, 2007, p. 134).

1.5 MTU Onsite Energy Generators

MTU Onsite Energy offers a cost-effective, reliable power system solution in the form of stationary generator sets. MTU offers a variety of energy solutions, from emergency power to continuous power, heating and cooling. They have customer databases around the world with a wide range of applications, such as healthcare, data centers, airports, farms and independent power stations. These generators range from diesel-powered generator sets up to 3,250 KW, gasoline-powered cogeneration systems up to 2,500 KW and natural gas-powered turbines up to 50, 00 KW. Whatever the applications or the fuel sources used, these generators have a common set-up, where the engine is mounted in the middle, with the generator mounted behind and the radiator and cooling package located in front of the engine (See Figure 25) (MTU Onsite Energy).



Figure 25 18V 2000 Generator Set (MTU Onsite Energy)

These generators operate under a wide range of conditions, on the tops of buildings, inside buildings or out in the open air. Also, MTU generators are located all the around the world; from densely populated areas to isolated farm lands.

Therefore, one of the main requirements for a stationary generator is to have an enclosure that protects all the electrical and non-electrical equipment from rain, snow or other debris (see Figure 26). Also, the enclosures are specially designed to restrict the sound emitted from the generators to the spaces around it (Blanks, 1997, p. 1). However, when designing an enclosure there are other consideration; such as, air flow requirements, bird protection screen and water proofing.



Figure 26 (MTU Onsite Energy)

An important aspect of engine performance is providing for an adequate amount of air flow that will efficiently transfer the heat from the radiator and other cooling assemblies to the environment. A fan at the end of the engine is used to force feed the air through the enclosure. In other words, air will enter the enclosure through the inlet and move through the enclosure and radiator, and then exits through the outlet. However, sometimes the absence of pressure created by these forced fed air movements will allow the rain water to move inside the

enclosure. There are numerous electrical components located inside the enclosure and rainwater penetration could lead to equipment failure or even possible encourage danger of electrocution. For these reasons, standards and regulations must be followed to avoid any rain water penetration.

Underwriter's Laboratories (UL) created a set of standards that has been unanimously adopted throughout the power generation community. UL is a global independent safety science company employing experts in safety standards and regulations (UL Standards).

The standards for stationary engine generator assemblies are listed under section UL2200. They cover stationary engine generator assemblies rated at 600 volts or less. These standards are in accordance with the National Fire Prevention Agency (NFPA) requirements and regulations (UL Standards).

1.6 Rain water testing

An outdoor-use generator should go through UL2200 rain testing before being introduced into the market. Depending on the classification of the enclosures, test results can vary. When the enclosure is rated as rainproof, there should be no wetting of live parts or entrance of water above the lowest live part, and when the enclosure is rated as rain tight, there should be no entrance of water into the enclosure at all. Also, after being subjected to a rain test, the generator should have an insulation resistance of not less than 50,000 ohms between live parts and interconnected dead metal, and, it should withstand a Dielectric voltage-withstand test as well (UL Standards).

The water spray equipment used in the testing has to have three consistent spray heads mounted on to a rack as illustrated in Appendix A-1. Each spray nozzle should be constructed as

shown in Appendix A-2 and mounted rigidly to the structure. The spray is directed at 45 degrees vertically towards the louvers or any other opening of the generator, and the structure should be placed so that the center nozzle is 1.5 meters away from the generator. The water pressure should be maintained at 5 psi during the 4 hours of testing (UL Standards).

1.7 Behavior of water droplets

Rain water droplets fall when their falling velocity exceeds the upward wind speed or lift velocity of the air (Mook, 2003) . When a water droplet falls on to a solid surface, it splashes, spreads or breaks into smaller particles. There are plenty of examples of water droplets hitting a solid surface; rainfall is a natural example that can be observed everywhere. Also, inkjet printing provides another example of a drop impact application (Lagubeau, et al., 2012, p. 50).

Depending on the properties of the impact surface solid, typically, when a water droplet hits on a solid it typically creates a splash, spreading or bouncing (Durickovic & Varland, 2005). One could summarize the behavior of a water droplet based on three primary factors, the nature and inclination of the surface, the properties of the liquid and the velocity and the size of the droplet (Villermaux & Bossa, 2011, p. 413). From the materials view, droplet behavior is determined by kinetic energy, the surface energy of the drop, and the energy created by the internal motion of the water droplet (Durickovic & Varland, 2005).

A droplet only holds kinetic energy before the impact. When the drop touches the surface, the surface area of the droplet will increase because the impact will deform the droplet and the shock wave will spread quickly away from the center of the droplet. Hence, the surface energy will be increased. Also, part of the kinetic energy will transform into internal energy such as heat (Durickovic & Varland, 2005).

Depending on the droplet's initial kinetic energy, sometimes, the surface tension will absorb the energy upon impact like a spring, and the forces of restitution will make the drop to recoil away from the surface. Hence, this recoil motion will make the droplet shrink, thereby increasing the kinetic energy. Thus, the deformation will create a jet shape in the center of the droplet which can cause the droplet to lift off and bounce back (Durickovic & Varland, 2005).

Conversely, when the initial kinetic energy is higher, the drop spreads upon impact because the surface tension is not adequate to stop the outward motion. Hence, the deformation will create a rim while the center part will flatten to the surface. Thus, the outward velocity of the particle will exceed the surface tension; as a result, the main droplet breaks away and creates smaller droplets. This is called splashing.

During this phenomenon, a droplet will exhibit different behaviors; as illustrated in Figure 27, a droplet can either attach to the surface, also known as deposition Figure 27(A), or it can partially rebound Figure 27(B) or it can completely rebound Figure 27(C). If it is a complete rebound, the entire droplet elevates away off the surface. If it partially rebounds, part of the droplet sticks to the surface while other part will elevate away from the surface. Also, Figure 27(D) shows the break-up behavior whereby the satellite drops are ejected and the main drop and satellite drops all have a tendency to bounce off of the solid. Finally, Figure 27(E) shows the splashing effect, whereby the small secondary droplets form up on impact. (Van der Wal, 2006, p. 69).

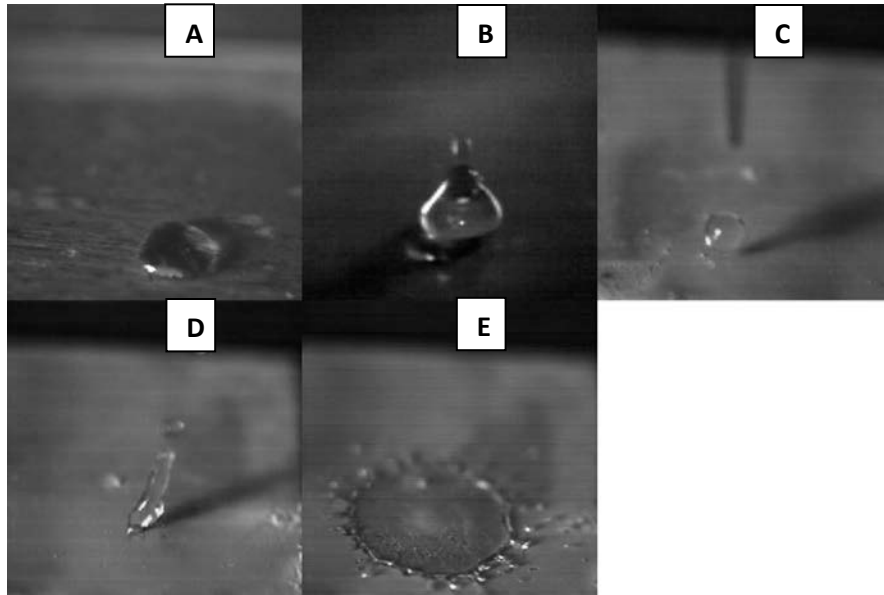


Figure 27 drop motion A) deposition, B) partial rebound, C) full rebound, D) break up, E) splashing (Van der Wal, 2006)

However, in actuality, the mechanics of fluid droplet velocity and deformation will depend on many other characteristics that are beyond the scope of this project (Oqielat , Turner, Belward, & McCue, 2011).

In short, when calculating the behavior of a fluid droplet on a flat solid surface, two dynamical dimensionless numbers, Weber's number (We) and Reynolds's number (Re) are the main determinants.

The inertia with capillary effects of the droplet is calculated by Weber number (We). To explain, the liquid inside the droplet is held together by the surface tension of the liquid (see Figure 28) and the droplet shape can be deformed if the surface tension changes. Also, the change of inertia created by the impact will affect the shape of the droplet. Hence, the ratio between the inertial force and the surface tension will govern the amount of the deformation.

If the drop diameter is $D = 2R_0$ and velocity at impact is V_0 ,

$$We = \frac{\rho D v_0^2}{\gamma}$$

Equation 1-79

Where ρ and γ are, respectively, the liquid density and the surface tension coefficient

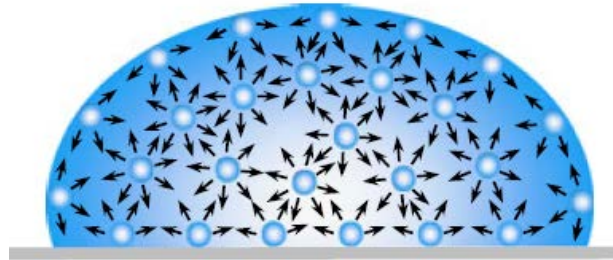


Figure 28 surface tension acting on a droplet (Yuan & Lee, 2013)

In analyzing Equation 1-79, if $We > 1$, inertial forces are higher and will likely cause the drop shape to change up on impact. If $We < 1$, the surface tension is higher and the drop will be stable upon impact (Van der Wal, 2006, p. 76).

Likewise, upon impact, the droplet deforms and encounters a shear force that is created by its shear viscosity. Hence, Inertia with viscous effects are calculated by the Reynolds's number (Re),

$$Re = \frac{\rho D V_0}{\nu}$$

Equation 1-80

Where, ρ is the density and ν is the kinematic viscosity of the fluid.

Apart from Weber's number and Reynolds's number, several other factors influence the energy dissipation of a droplet upon impact. Viscous dissipation, contact angle hysteresis, and after the lift-off, a droplet might rotate and/or oscillate thereby dissipating internal energy.

1.7.1 Droplet Diameter

Calculating the droplet diameter is virtually impossible because several factors influence the size of the droplet. For rainwater, it is theorized that the minimum droplet diameter is around 0.1 mm and the maximum will be around 7 mm. The upper limit of 7mm diameter is defined as droplets any larger will break apart during the fall. The lower limit of 0.1 mm is defined because a droplet has to overcome the updraft (or the lift) of the wind (Mook, 2003).

The shape of the droplet depends on the magnitude of its diameter as well. Perfect spherical shapes at terminal velocity are only observed in droplets that are less than 0.3mm (see Figure 29). Droplets that are larger than 1mm look alike spheroids with flat bases (Mook, 2003).

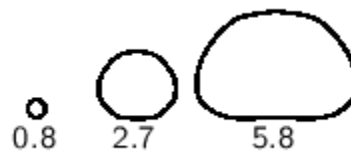


Figure 29 Rainwater droplet size vs. shape (Mook, 2003)

1.7.2 Droplet Terminal velocity

The terminal velocity of a droplet is very important for the rainwater penetration test, as the behavior of the droplet on impact is dependent upon the droplet's terminal velocity. The motion of the droplet is due to gravitational force and drag/lift forces of the air.

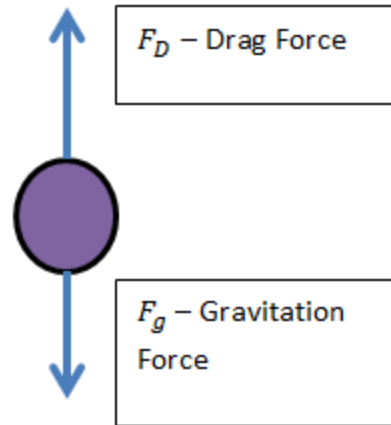


Figure 30 Free body diagram of a rain water droplet

Hence,

$$m_D \frac{du}{dt} = F_g - F_D$$

$$m_D \frac{du}{dt} = m_D g - \frac{1}{2} C_d \rho_a v^2 A$$

Equation 1-81

Where, m_D = mass of the droplet, u = droplet velocity, C_d = drag coefficient in air (function of Re), ρ_a = density of air, v = wind velocity, A droplet area.

However, the droplet shape is not going to be a perfect sphere every time; therefore, the area in Equation 1-81 cannot be calculated precisely. However, by combining Equation 1-80 and Equation 1-81, the area of the droplet can be estimated using the Reynolds's number.

$$m_D \frac{du}{dt} = m_D g - \frac{\pi}{8} v Re C_d D (u - v)$$

Equation 1-82

Where, ν is the kinematic viscosity, D droplet diameter.

The terminal velocity is the maximum vertical velocity a rain particle can obtain. However, this is assuming that there are no horizontal forces acting up on the droplet, as these would affect the shape of the droplet and create additional drag (Mook, 2003).

Since the terminal velocity of a droplet is hard to calculate, an approximation for the formula was obtained using the data collected by Gunn & Kinzer, 1949. Hence, the terminal velocity of a droplet can be approximated as a function of the droplet's diameter (Gunn & Kinzer, 1949 ; Mook, 2003).

$$V_t \approx 9.40 [1 - e^{x(-1.57 \times 10^3 D^{1.15})}]$$

Equation 1-83

Where, V_t is the terminal velocity and D is the droplet diameter in meters.

1.7.3 Coefficient of Restitution

For small diameter droplets, a measure of elasticity is introduced as they dissipate less energy through internal vibrations. This measure is called the coefficient of restitution and its denoted by c ,

$$c = \frac{V_f}{V_i} = \sqrt{\frac{h}{H}}$$

Equation 1-84

Where, V_f and V_i is the velocity before and after the impact. Also, h is the height the drop bounce after impact and H is the height from which the droplet was originally released. The coefficient of restitution is dimensional less number that rest between 0 and 1.

Calculating the maximum diameter of a droplet after an impact is a cumbersome process. Hence, several estimates have taken this into account, and the following formula gives the maximum diameter on a hydrophobic surface (Van der Wal, 2006, p. 9).

$$D_{max} \approx D_0 We^{\frac{1}{4}}$$

Equation 1-85

Where, D_0 is the initial diameter.

A hydrophobic material will repel water on the molecular level upon impact. These material repel water by making large contact angles on the droplet surface (Figure 31). The contact angle is the geometrical angle created by the interaction of the liquid-solid interface (Yuan & Lee, 2013). Some materials are super-hydrophobic and they can create contact angles up to 170° (Durickovic & Varland, 2005, p. 2).

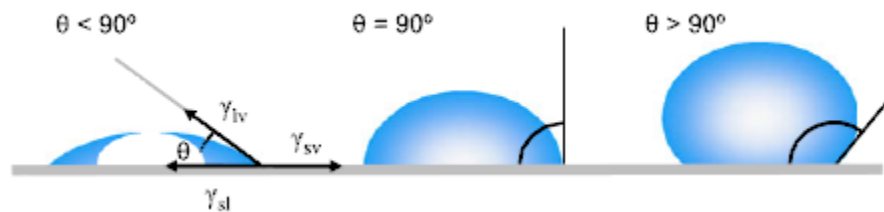


Figure 31 Contact angle on a smooth solid (Yuan & Lee, 2013, p. 4)

Therefore, in super-hydrophobic materials, there will be very little contact with surface of the droplet and solid. Hence, bouncing and splashing happens more frequently. As the surface interaction is low, it assists the droplet to leave the surface, creating a bouncing behavior; or, the droplet simply breaks apart, creating increased splashing behavior.

2 OM924 Generator CFD Model Design

The design of the CFD model is based on the OM924 50Hz generator supplied by MTU. The CFD tool used was FloEFD for Creo by Mentor Graphics. The PTC Creo Computer Aided Drawing (CAD) tool was used in MTU for design and drafting purposes of the CAD models (Figure 32).



Figure 32 OM924 Generator Enclosure Original CAD Model

The purpose of a CAD model is to convey details to other parties such as, customers and product engineers. The original CAD drawing of OM924 contained complex geometrical outlines and advanced design details, from the engine and generator down to small details such as, nuts, washers and tubing (Figure 33). Thus, it made the model very detailed and complex. However, for CFD simulations these advance details are not compulsory. Also, by including details which are insignificant to the CFD Model, the calculation time will increase and the simulation will use more computing power.

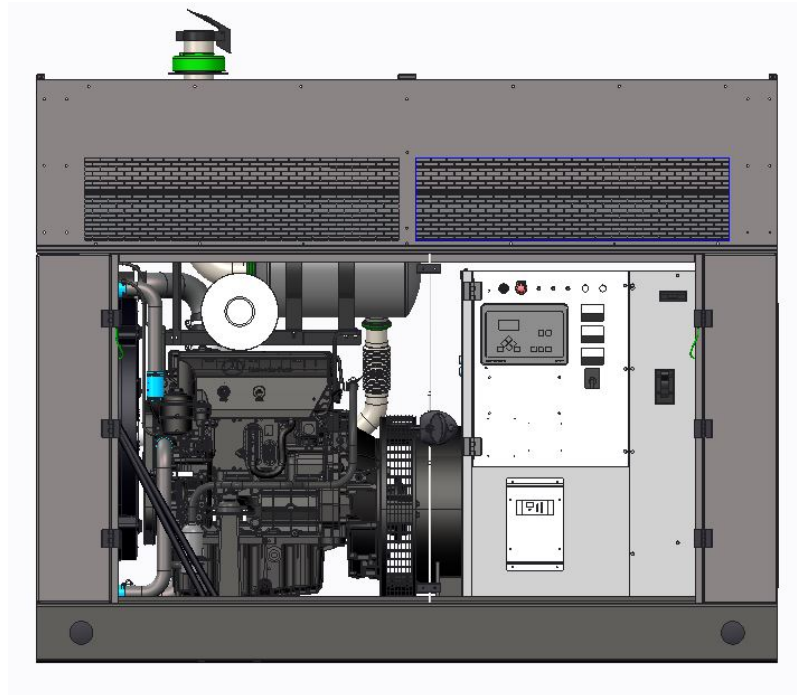


Figure 33 OM924 original model – Doors has been removed to illustrate the inside of the enclosure

The actual enclosure of the generator is made out of sheet metal parts combined together. Thus, the enclosure of the original CAD model was designed using sheet metal parts as well. Unlike solid metal parts, models made out of sheet metal parts are not completely sealed.

When the original CAD model was imported to FloEFD, it reported a water leak error. Meaning, that there are internal and external leaks in the original CAD model and it is not impervious. The simulation requires the fluid domain to be waterproof; any open areas should be designated as boundary conditions such as inlets, outlets or pressure openings. Also, the sheet metal parts were not mated using the coincided option in Cero CAD tool. Hence, improper mating of parts contributed to the water leak error as well.

2.1.1 OM924 CFD Model 1

OM924 CFD Model 1 was created as a replica of the original CAD model. Therefore, all the original dimensions were preserved in the CFD model. However, any parts that were not

relevant to the fluid domain behavior were removed; the engine, exhaust, generator, just to name a few. The CFD model is only considers in the fluid domain (or empty space). Therefore, all the physical boundaries were built as solids and extrusion tools were used to construct individual shapes. For the purpose of waterproofing the model, the CFD model 1 assembly only contained solid parts. Moreover, when parts were imported, they were mated as coincident style (Figure 34).

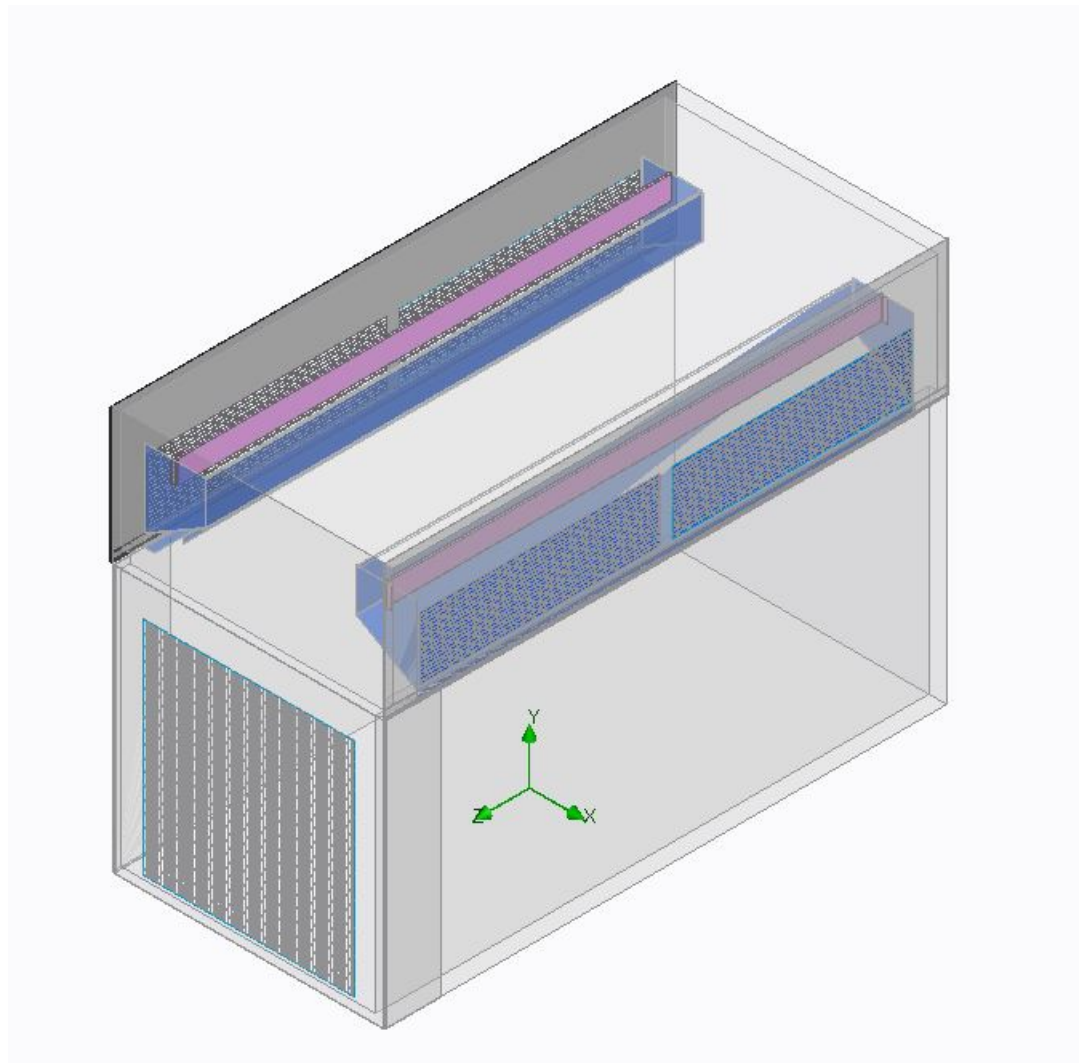


Figure 34 CFD Model 1 - crucial components for air flow were imported from the original model and mated as coincident style

Also, all crucial components that control air flow, such as the front grill, side air inlet grill, baffle plates and the middle blade were directly imported from the original CAD model as independent parts (Refer to Appendix E for more details). In addition, any individual part that was imported from the original model was assembled as a coincident mating structure to avoid any leakage of the CFD model. However, it should be pointed out that the CFD model is not a 100% match to the original CAD model.

Consequently, inlet and outlet grill areas were extended by creating covers, and lids were placed on top of the covers to seal the fluid domain. The covers serve as an extension for the inlet and outlet grills. Since the grill is made out of many small squares, it is difficult to create lids for each individual square. Instead, the simplest solution is to create a cover and put a lid on the cover. Also, the outlet cover helps to reduce the vortex effect. In a pressure opening, the flow will try to circulate back into the model and this is called the vortex effect.

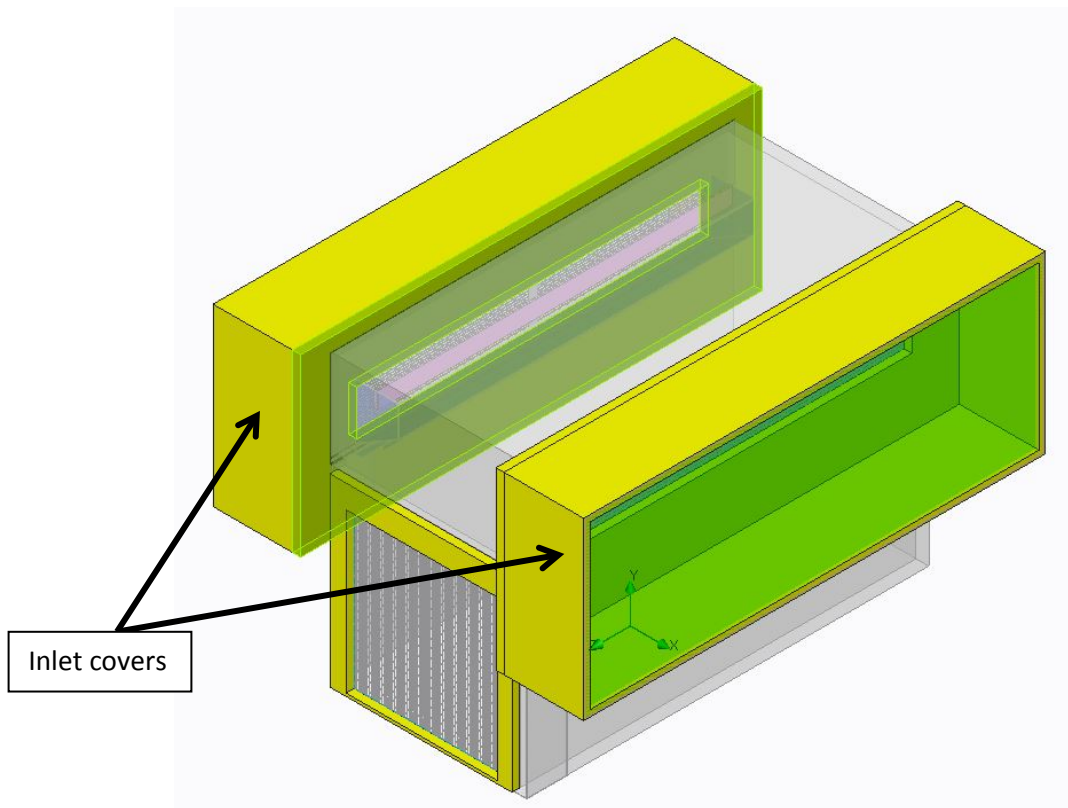


Figure 35 CFD Model 1 with inlet and outlet covers (in yellow). The fluid domain is sealed using lids (in green). Each lid will act as and boundary as well.

Finally, Model 1 was tested for any water leaks or boundary condition errors using FloEFD. After testing, the inlet boundary condition was defined as a volumetric flow opening with 8,386 CFM of volumetric flow (see section 3.2.1 for more details about the air flow data) and the outlet boundary condition was defined as a pressure opening. Finally, the simulation was solved and converged without any error reports.

2.1.2 OM924 CFD Model 2

In order to remove excess heat from the radiator and the charge air cooler, air is blown through the enclosure using a fan that is coupled to the engine. Then the engine power is used to flow or push the air across the enclosure. In the engine, chemical energy is converted into mechanical energy and it is used to drive the fan. The fan converts this energy into kinetic

energy in the moving air particles. However, in CFD model 1, the fan was not integrated, and it was assumed that the air was blown using an outside force. Thus, the inlet boundary condition was defined as a volumetric flow rate of 8,386 CFM.

After verifying that the CFD model 1 solved the simulation without any problems, for CFD model 2, a fan boundary condition was introduced. The fan used in OM924 generator is from Multi-Wing America Incorporation. For more details regarding the fan specification, refer to Appendix B.

In the OM924 generator, the fan was an internal fan and located between the radiator and engine. However, in the CFD model 2, the fan boundary condition was defined as an external outlet fan to simplify the model. Hence, the fan and the radiator shroud were located outside the enclosure (Figure 36). However, the radiator shroud and the fan dimensions are exactly the same as the original model. Also, since these simulations are not focused on thermal analysis, the radiator was not modeled in the CFD model 2.

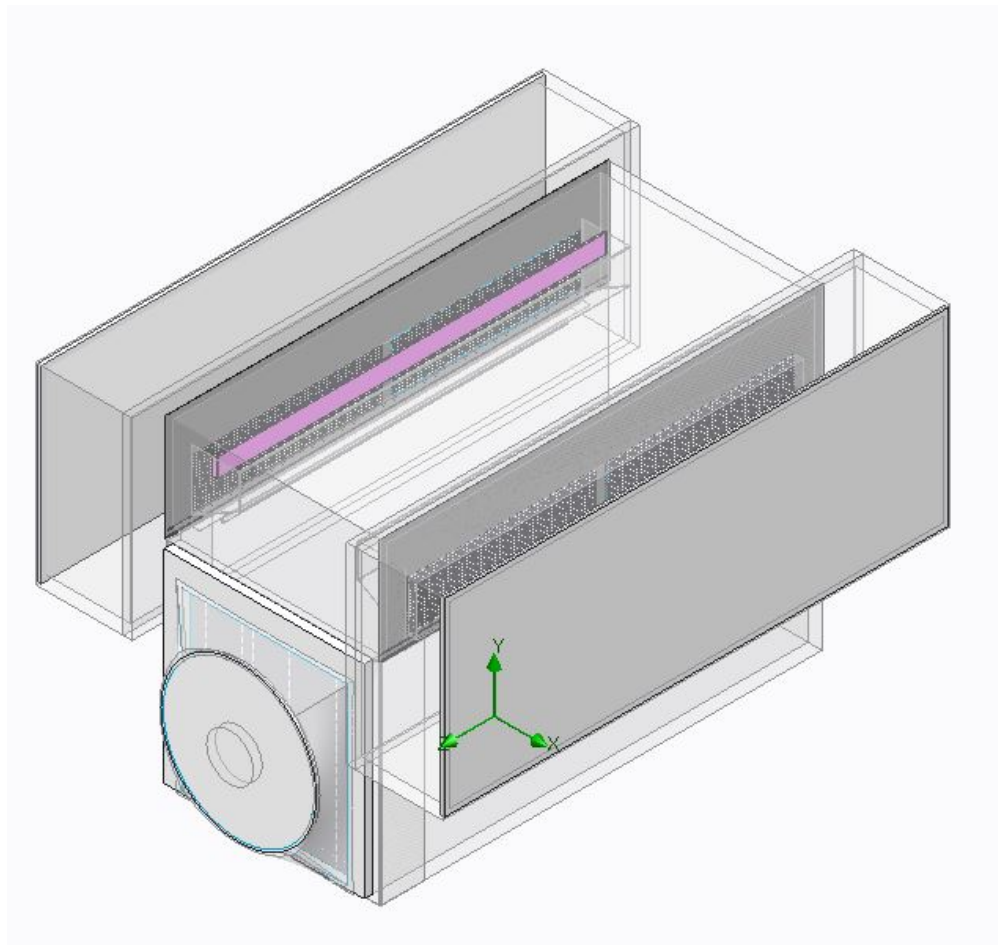


Figure 36 CFD model 2 - fan is located outside the enclosure as an external outlet fan

2.1.3 OM924 CFD Model 3

The final step is to add the internal components of the OM924 generator into the CFD model. The engine and generator assemblies, however, are comprised of extremely complex geometrical parts. Hence, re-drawing those parts will be a very difficult and time consuming task. The CFD model is only concerns the physical boundaries or the outer shell of the internal components.

Therefore, the engine, the generator and the master box assembly were imported as a “shrink wrap” volume feature in Creo. By doing so, the outer geometry of the parts were

preserved with the original shape and the internal components were removed (Figure 37).

However, an insignificant amount of surface deformation can be observed.

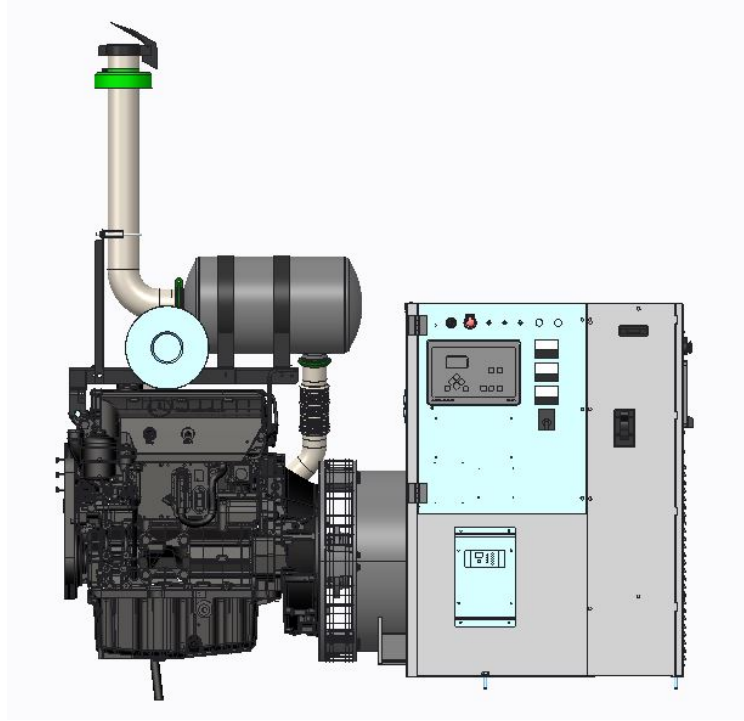


Figure 37 volume shrink-wrap of the engine, generator and the master box assembly. The part is hollow inside and only the outer shell is visible.

Finally, the engine, the generator and the master box were imported to CFD model 3 as a whole part. In actuality, the engine and generator are positioned on top of a solid base. However, the base part was omitted in the CFD model 3 design because it is not relevant to fluid flow behavior. Hence, in the CFD model 3, the engine and the generator combination looks as it is floating within the enclosure (Figure 38).

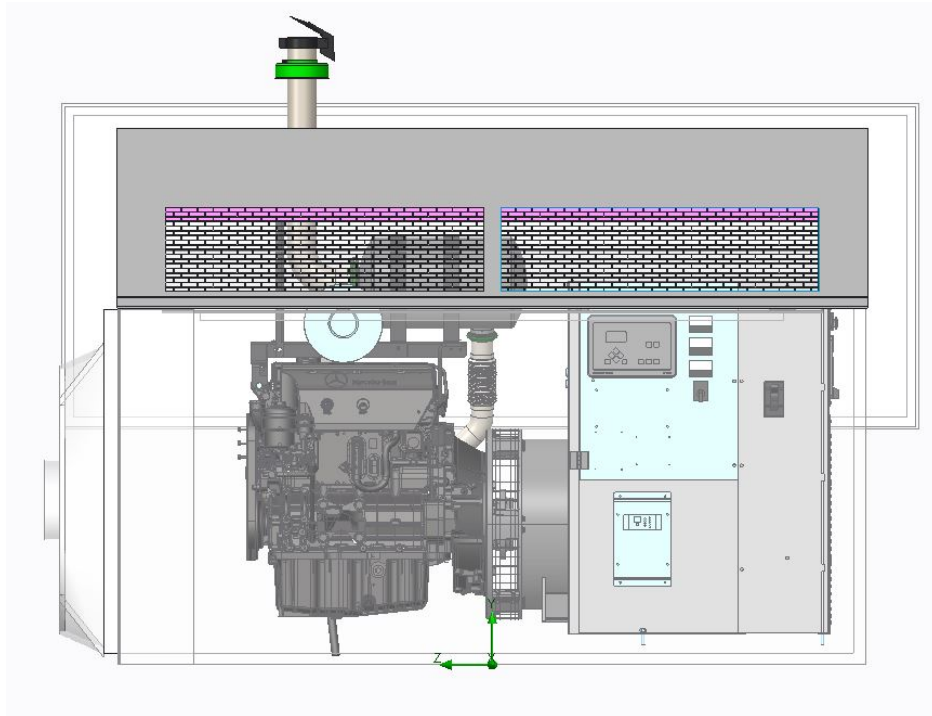


Figure 38 CFD model 3

3 Validation of the Model

Given that, modeling and simulation are an approximation of the real application, the model needs to be validated before evaluating the data. Therefore, three main validation areas were examined; velocity points, air flow rate and pressure difference.

Data taken from experiments was compared to the theoretical data obtained from the simulation. However, it should be expected that these two sets of data will not be an exact match; instead, the simulated data will be an approximation of the experimental data.

3.1 Velocity Data

The OM924 generator was brought up to full load and the air speed was measured near the two inlet grills and the outlet grill. Measurements were taken at each air inlet using an anemometer that was placed on the plane at which air enters the enclosure, in other words the anemometer blades were perpendicular to the air flow. Moreover, for accuracy, the anemometer was fixed to a flat plate and that plate was placed parallel to the inlet louvers (Figure 39 is just for illustration purpose only. Not the actual OM924 enclosure).



Figure 39 Anemometer is attached to a flat plate, so that the air flow is parallel to the anemometer.

3.1.1 Measured Air Velocity Values

Each inlet grill was separated by a solid wall in the middle. Therefore, for identification purposes, the inlet grills are referred as right side inlet 1, right side inlet 2, left side inlet 1 and left side inlet 2 (See Figure 40).

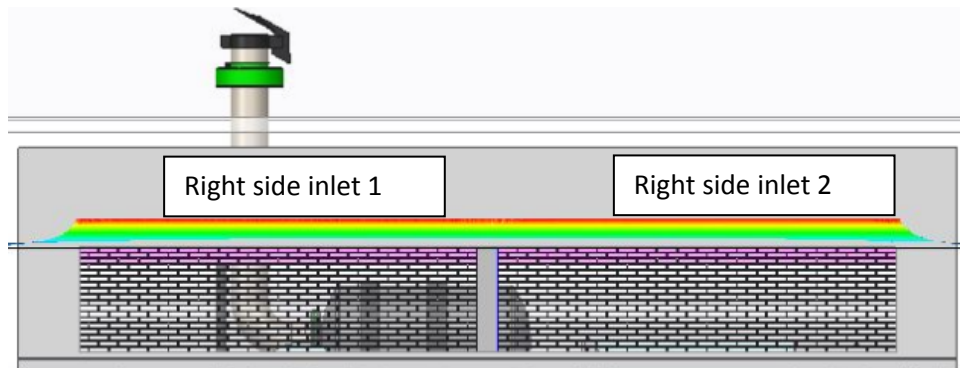


Figure 40 Anemometer was placed on each inlet 1 and 2 according to a grid pattern.

In order to collect uniform air speed data, the anemometer was placed in front of the inlet grill based on a grid pattern yielding nine equally spaced data points. The same process was repeated for the left side inlet 1 and 2.

Similarly, air speed was measure on the outlet grill as well. For data collection identification purpose, the outlet grill was divided in half and labeled as outlet 1 and outlet 2. Outlet 1 had 15 equally divided data collection points and outlet 2 had 20 equally divided points. The following table contains the average air flow velocity of the enclosure. Appendix F contains more details about the data point locations and air speeds measured at those locations.

Left Side		Right Side	
Inlet 1	Inlet 2	Inlet 1	Inlet 2
469.11	485.22	507.22	477.44
	Outlet 1	Outlet 2	
	822.06	638.6	

Table 1 Average measured air flow velocity of the enclosure

3.1.2 Simulated Air Velocity Values

Velocity at the left and right side inlet were visualized using a contour plot. Figure 41 illustrates the air speed at the inlet. Also, the flow path vs. velocity was visualized using a flow trajectory plot (Figure 42).

By observing the contour plot and the flow trajectory plot, it was concluded that further investigation is needed to accurately pin point the different air velocities. Also, the air speed measured using the anemometer only represents the air particles which are moving perpendicular to the inlet; in the simulation, it will be the velocity in x direction. Being that velocity is a vector, and the $x = 0$ point is at the center of the enclosure, the right side inlet velocity will be a negative value and left side inlet velocity will be a positive value.

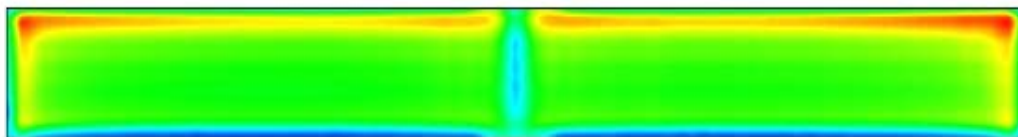


Figure 41 Air velocity at the right side inlet. High of 1471 ft/min [red] and low of 0 ft/min [Blue]

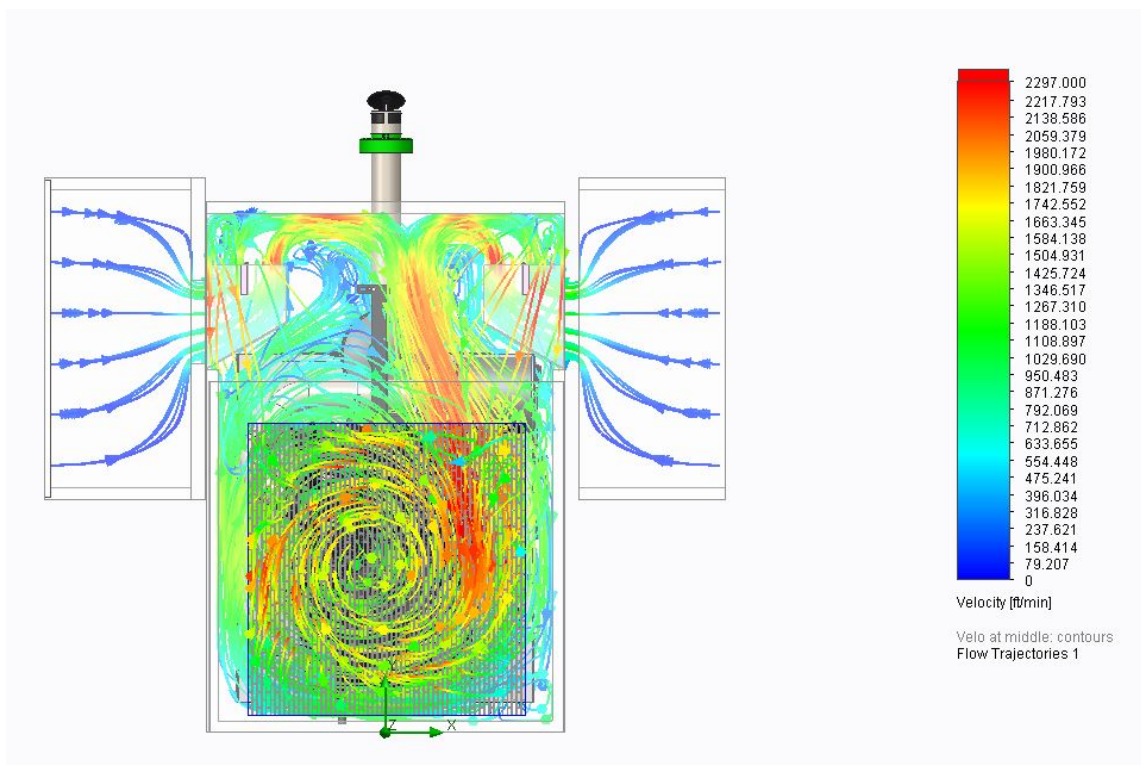


Figure 42 Flow trajectories of the air particles.

To investigate the air velocity further, a point study on the inlet surfaces was conducted.

Figure 43 shows the locations of the points at which that the air velocity in x direction was simulated.

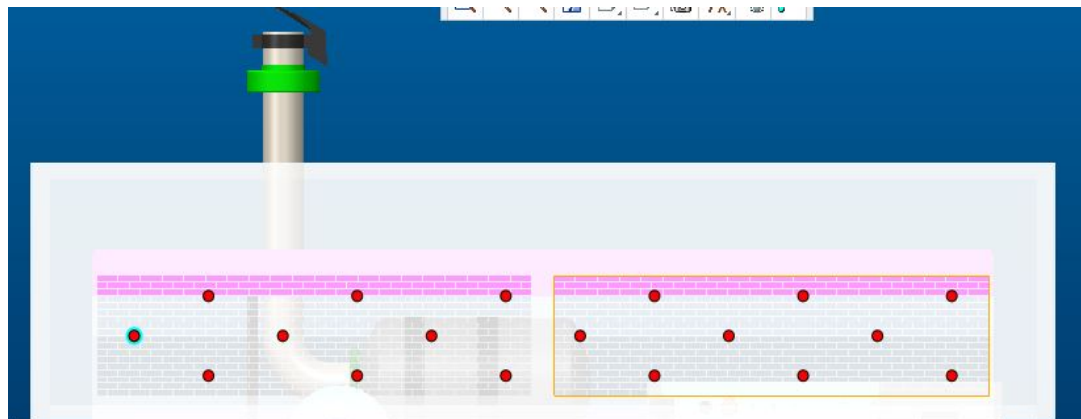


Figure 43 The red dots marks the locations at which the velocity was simulated

Table 2 illustrates the magnitude of the velocity simulated on the right side inlet. For identification purpose, the velocity values were color coded according to 100 *ft/min* increments.

Right side Inlet 1			Right side Inlet 2		
922	889	848	883	905	945
789	726	727	700	721	743
741	723	736	735	730	790

Table 2 Simulated velocity magnitude on the right side inlet grill. Yellow – 700 range, green – 800 range, red – 900 range.

Comparing the measured and the simulated average velocity data, the percent error between measured and simulated data for the right side inlet was,

$$\% \text{ error for air velocity in } x \text{ direction} = \left\{ \frac{|492 - 792|}{492} \right\} \times 100 = 60.00\%$$

Equation 3-1

Similarly, Table 3 illustrates the magnitude of the velocity simulated on the left side. The percent error between the measured and simulated for the left side inlet was 48.84%.

Left Side Inlet 1			Left Side Inlet 2		
839	809	770	802	801	823
711	662	660	632	643	651
675	658	663	658	644	685

Table 3 Simulated velocity magnitude on the left side inlet grill. Yellow – 600 range, green – 700 range, blue – 800 range, red – 900 range, purple – 1000 range.

Table 4 summarizes the air velocity values at the outlet. The percent error between the measured and simulated for the outlet was 30.41% .

Outlet Air Velocity

504	776	883	899	864	637	407
913	1096	1222	1199	1038	829	818
1058	1259	1413	1430	1307	995	936
895	1035	1137	1197	1131	967	810
770	841	899	933	884	768	571

Table 4 Summary of the outlet air velocity

For comprehensive details of the point vs. velocities tables, refer to Appendix H.

3.2 Volumetric Flow Rate data

Volumetric flow rate can be calculated using the air velocity and cross-sectional area.

According to the conservation laws, the volume flow rate values should be a constant throughout the enclosure. Hence, the inlet volume flow rate can be calculated using,

$$\text{Volume flow rate} = \text{Average air velocity} \times \text{Inlet area}$$

Equation 3-2

3.2.1 Measured Volumetric Flow Rate Values

Using the air flow velocity data collected in Section 3.1 and the inlet cross sectional area, an average inlet volume flow rate of 4755 CFM was calculated. Similarly, the average outlet air flow was calculated as 7711 CFM. However, according to the conservations laws, the inlet flow rate and the outlet flow rate should be the same. Hence, the data collected needed to be investigated for errors.

One explanation is, since the enclosure is made out of multiple sheet metal parts, there are leaks in the enclosure and outside air can be pulled into the enclosure through the leaks and forced out through the outlet. Hence, the outlet air flow values can be higher than those measured at the inlet. Another explanation is in regard those human and equipment errors that may be influencing the data. Especially since the volumetric flow rate was calculated using air speed, even a small error in measuring the air speed will impact the flow rate exponentially.

Therefore, as volumetric flow rate values, outlet flow rate values were used instead of the inlet flow rate values. Also, the air consumed by the engine in the combustion process is expelled through the exhaust manifold and the exhaust pipe. Therefore, the air consumption of the engine was added to the outlet air flow values as well. Hence, the final corrected air flow number is, 8,386 CFM, and this figure was used for all the analysis. Refer to Appendix F for more information about volumetric flow rate and engine air consumption calculations.

3.2.2 Simulated Volumetric Flow Rate Values

In CFD model 3, a goal area was created for maximum flow rate and it was assigned to the outside face of the outlet lid. That means that, in the simulation, the maximum flow rate was used as one of the stopping criteria for the solver. Table 5 illustrates the volume flow rate as reported by FloEFD.

Goal Name	Unit	Value	Averaged Value	Minimum Value	Maximum Value
SG Volume Flow Rate		10302.6949	10215.7821		10302.6949
1	[ft ³ /min]	2	2	10149.12215	2

Table 5 Volumetric flow rate at outlet

With reference to the practical volume flow rate measured in section 3.2.1 and using the average flow rate values obtained from the simulation, the percent error between the practical and simulated volumetric flow rate is,

$$\% \text{ error volumetri flow rate} = \left\{ \frac{|8386 - 10215|}{8386} \right\} \times 100 = 21.81\% \text{ CFM}$$

Equation 3-3

Similarly, by using the outside face of the inlet lids, the surface parameter study calculated a combined flow rate of 10,302 CFM. As mentioned earlier, the measured inlet flow rate was not considered for data analysis. Hence, inlet percent error was not calculated.

Also, by doing a surface parameter study on the outside faces of the outlet lid, a total volumetric flow rate of -10,322 CFM was calculated. The negative value signifies that the fluid is flowing away from the outlet lid. Refer to Appendix G for a detailed report of the surface parameter studies.

3.3 Pressure Lost Data

One of the purposes of an enclosure is to restrict the noise level generated by the engine and the generator. Therefore, the inlet should be large enough so that it will supply the required air flow needed. However, it should be small enough so that it will constrain the noise. Because of this size limitation, the inlet acts as an orifice plate or a restrictor of air flow. As a result, the pressure inside the enclosure will change when the generator is operating.

Regardless of whether the fluid particles are in motion or not, the pressure will apply to any part of the fluid domain. There are two kinds of pressure, static pressure and dynamic pressure. Static pressure is the pressure applied on a surface when the fluid is at rest relative to the flow, not the pressure created by the motion of fluid particles. Dynamic pressure is the

pressure applied as a result of moving particles, and is only exerted in the direction of the flow. Therefore, measuring only the dynamic pressure is difficult and always requires some degree of calculation.

Hence, every particle in the fluid domain has its own static pressure P_S , dynamic pressure P_D and total pressure P_T , regardless of the fluid speed. Thus, the total pressure along a streamline is,

$$P_S + P_D = P_T$$

Equation 3-4

By applying a simplified version of Bernoulli's equation, the Equation 3-4 can be written as,

$$P_S + \frac{1}{2}\rho v^2 = P_T$$

Equation 3-5

Where, ρ is the density of the fluid and v is the flow velocity.

Also, static and dynamic pressures can vary during the course of the fluid flow, but the total pressure will be constant along the streamline of air flow. Therefore, depending on the changes in dynamic pressure, static pressure will also change.

Moreover, because dynamic pressure cannot be easily measured, static pressure is measured instead. So the changes in the static pressure are to some extent a reflection of the changes in dynamic pressure. Therefore, the static pressure is measured relative to atmospheric pressure or relative to two points in the stream line.

Using the Equation 3-2, it can be concluded that the air velocity at the inlet will be higher than that outside of the enclosure. To explain this further, according to the conservation laws, the flow rate should be constant throughout the generator. However, the inlet acts as an orifice to the air flow; hence, air velocity is higher inside the enclosure than outside. Referring back to the Equation 3-5, this higher velocity will create a higher dynamic pressure. However, the total pressure should be constant along the streamline. Hence, static pressure will drop in order to accommodate the rise in dynamic pressure.

3.3.1 Measured Static Pressure Values

While the generator is in full load, static pressure drop across the enclosure was measured using a manometer. A measurement was taken inside the enclosure in-between the fan and the engine. An assumption was made that the static pressure values will be the same in other parts of the enclosure. Hence, differential pressure of $0.12'' H_2O$ was used throughout the analysis.

3.3.2 Simulated Pressure Values

A cut plot was used to visualize the dynamic pressure inside the enclosure (Figure 44 and Figure 45). However, since the simulation calculates and visualizes the pressure in each fluid particle, it was difficult to obtain an average value for the pressure lost. By analyzing the contour plot, it was theorized that the dynamic pressure inside the enclosure ranged from $0'' H_2O$ to $0.33'' H_2O$.

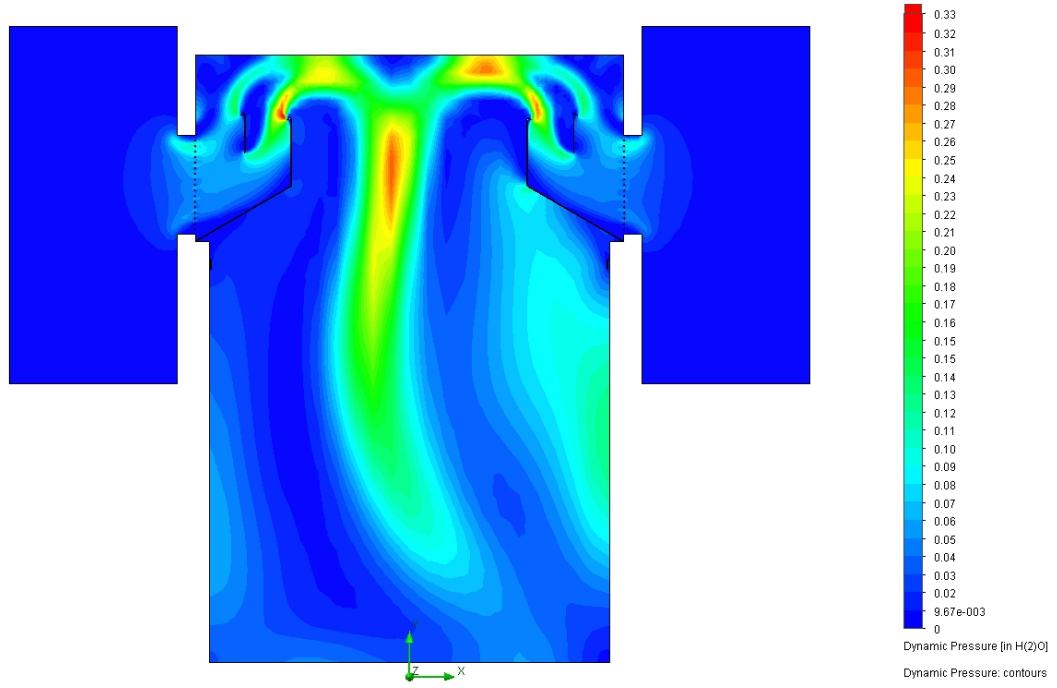


Figure 44 front view Cut plot of dynamic pressure inside the enclosure. The cut plot was placed in the middle of the enclosure ($y=0$)

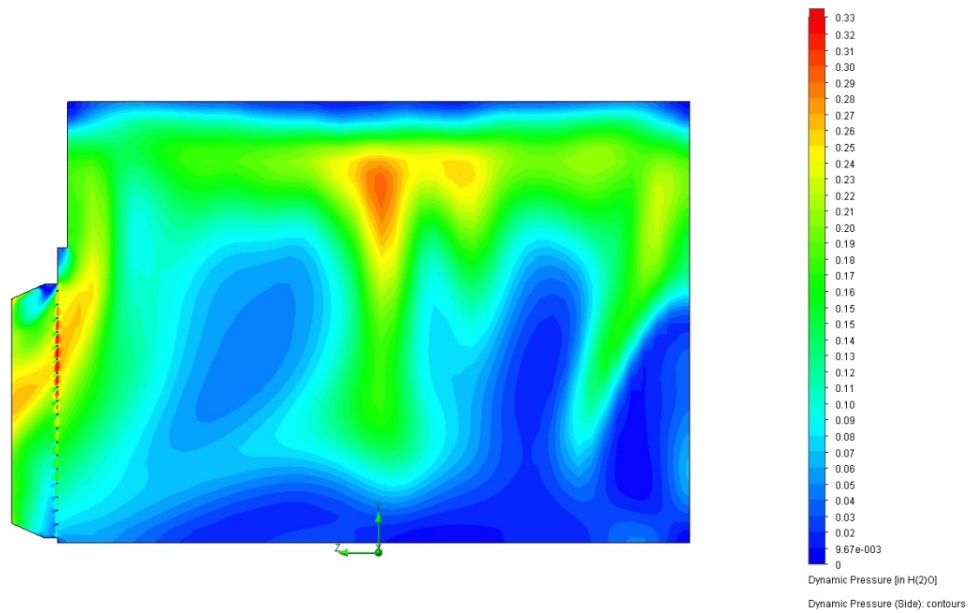


Figure 45 side view Cut plot of dynamic pressure inside the enclosure. Cut plot was placed in the middle of the enclosure ($x=0$)

The next step was to identify the static pressure throughout the system. For identification purposes, the range was narrowed down to 4 spans. Figure 46 illustrates a simplified contour plot of average static pressures in the system at the front of the enclosure. Likewise, Figure 47 illustrates the static pressure at the back of the enclosure. The higher pressure denoted in red should reflect the ambient environmental pressure (406.7823" H_2O). However, the simulated pressure calculated at the inlet cover was determined to be 406.7168" H_2O . The reason hypothesized for this difference is that the boundary of the fluid domain is at the end of the inlet covers and not at the entrance to the enclosure. Therefore, inside the inlet covers there is a significant amount of air movement, thus, there is a static pressure drop of 0.06586" H_2O . So, when calculating the simulated static pressure drop across the enclosure, the static pressure inside the inlet covers should be considered as well.

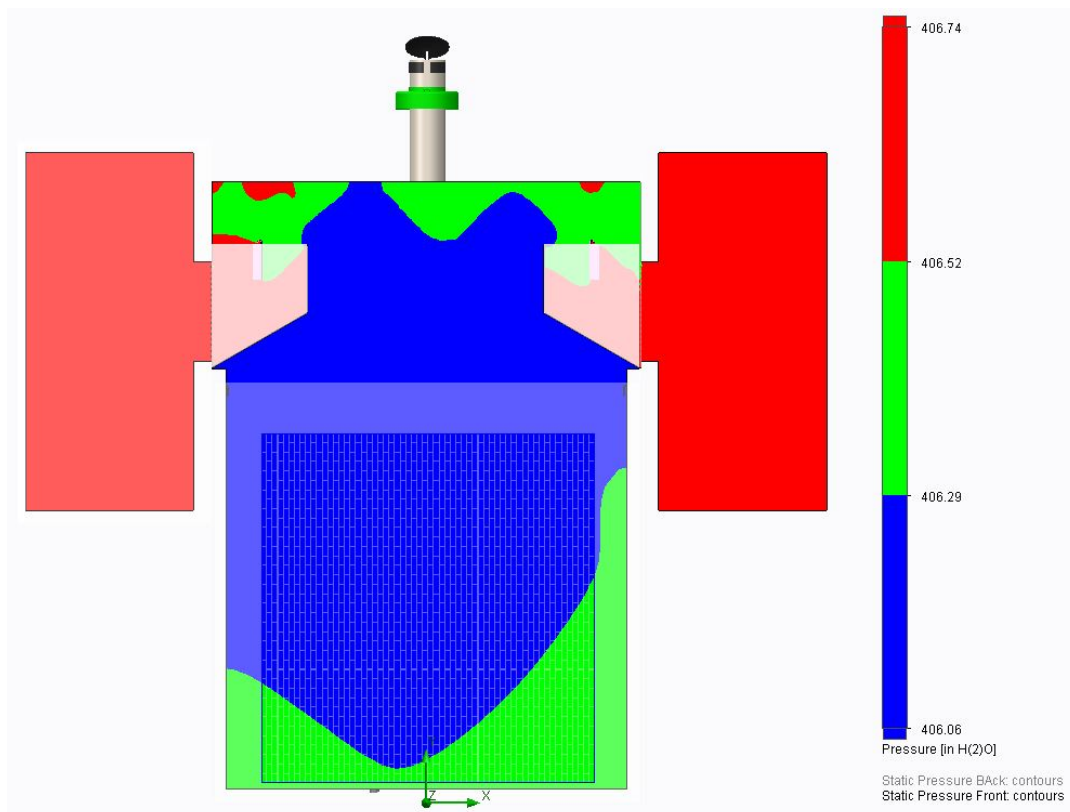


Figure 46 Static pressure at the front of the enclosure

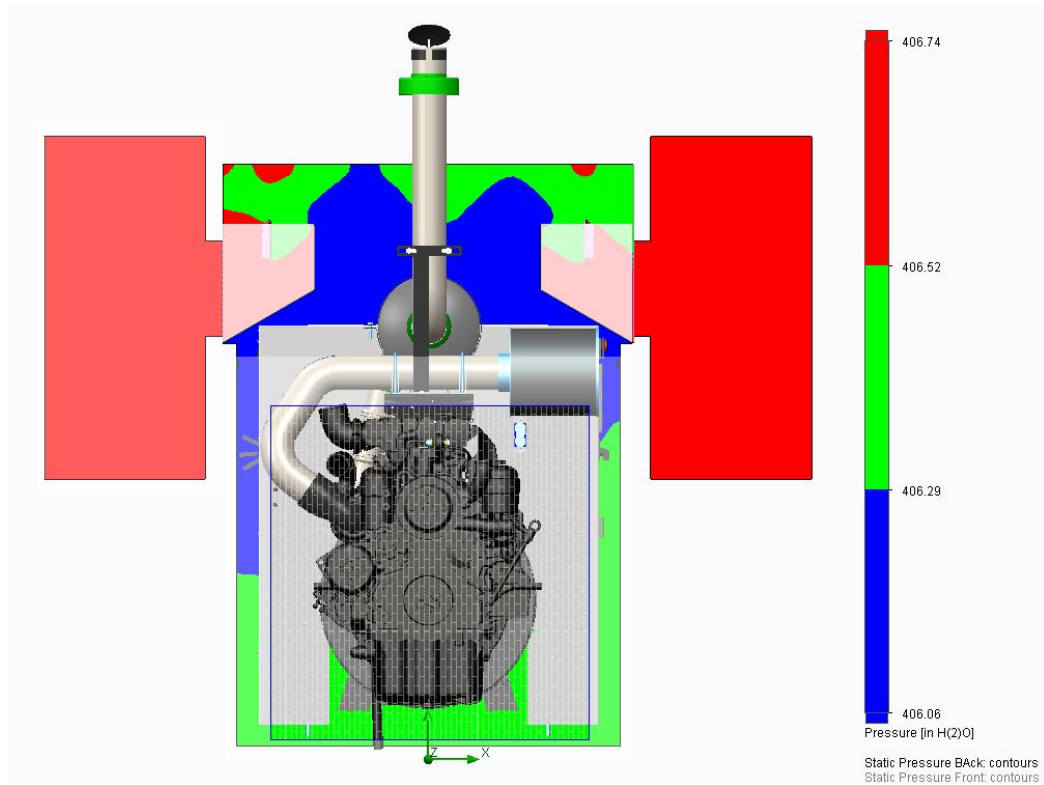


Figure 47 Static pressure at the back of the enclosure

Finally it was decided to conduct a point study at the two inlet covers and at the center of the enclosure. A plane parallel to the front of the enclosure was selected at the central point of the enclosure ($z = 0$). Also, another plane was positioned at the midpoint, parallel to the side of the enclosure. The Table 6 summarizes the data from the static pressure point study.

Static Pressure: <u>Left Inlet</u>	Static Pressure: <u>inside the enclosure</u>	Static Pressure: <u>Right Inlet</u>
406.7168365	Right Side 406.2755348 Front Side 406.2245889 Average 406.2500619	406.7160575

Table 6 Static pressure values inside and outside the enclosure

Thus, the simulated static pressure drop just inside the enclosure is,

$$\text{Static Pressure Drop} = \left(\frac{406.7168365 + 406.7160575}{2} \right) - 406.2500619$$

$$\text{Static Pressure Drop} = 0.466 \text{ "H}_2\text{O}$$

Compared to the measured static pressure drop, the percent error was 288%. However, it is important to point out that the measured pressure drop was taken only with two points while the simulated static pressure drop was calculated for more than 80 points. Also, as discussed earlier, the real enclosure is not completely water tight. Therefore, the measured pressure drop might predict to be lower than the actual pressure drop. Refer to Appendix I for a detailed list of static pressure data.

3.4 Discussion of the CFD model

As mentioned earlier, the CFD model is an approximation of the real application. Also, it is very difficult to apply all the real world conditions in a CFD model. For example, in an actual enclosure, the inside walls are covered with a sound absorbing material. This material acts as a restrictor to the air flow. However, in the CFD model, the wall conditions were defined as an adiabatic wall. Meaning, the simulation assumes that the wall surfaces have no effect on the air

flow conditions. Likewise, many other assumptions were made in the CFD model. Other examples of assumptions that were not considered in the CFD model, to name a few, were: heat conditions were not accounted for, vibrations were ignored and flow was considered to be in ideal conditions.

Analyzing the difference between the measured and simulated air velocities, error percentages were calculated at 60% for the right side inlet, 48.84% for the left side inlet and 30.41% for the outlet. Even though the inlet error percentages are high, the measured and simulated velocities exhibit similar behaviors.

Table 7 compares the raw measured and simulated velocity values for the inlets. In both data tables, the velocity values increase as it moved towards the right of the table (highlight in light green and dark green). Although the figures vary between the measured and simulated velocities (587, 589, 614 ft/min and 802, 801 and 823 ft/min) the pattern of variation is consistent in both of the tables. To illustrate, in the measured data set, the difference between the first two velocity values (587, 589 ft/min) was two. Likewise, in the simulated data, the difference between the first two velocity values (802, 801 ft/min) was one. Moreover, the third velocity value (614 ft/min) of the measured data set got increased by 25; the corresponding simulated value (823 ft/min) got increased by 22.

Measured - Left Side Inlet 2			Simulated - Left side Inlet 2		
587	589	614	802	801	823
486	445	506	632	643	651
370	366	404	658	644	685

Table 7 Measured Vs. Simulated velocity values - right side inlet 2

Also, analyzing the bottom row of Table 7, both data values demonstrated that the first and the second column (370, 366 ft/min and 658, 644 ft/min) had an almost identical data range, and the third column values (404 and 685 ft/min) were higher (highlighted in yellow and red).

Likewise, other measured and simulated inlet air velocity values demonstrated similar trends. Moreover, for the two inlet grills, the lowest measured air velocity was at the bottom row or the bottom data point locations. In a like manner, referring to all the simulated inlet velocity data values, the bottom row had the lowest air velocity values.

Moreover, in the simulation, the location at which velocity was calculated had an enormous effect on the velocity values. For example, when the plane was moved 10 mm away from its current location, the velocity values changed dramatically. The highest velocity values are simulated nearest to the inlet grill. However, it is impossible to use the same location to measure the velocity in the actual enclosure. Therefore, depending on the location, the measured and simulated velocities can vary considerably.

The measured volumetric flow rate is based on the measured air velocity values. Hence, any error applied to the velocity values will be reflected in the volume flow rate values. On the other hand, simulation considered smooth wall interactions. Thus, the simulation may be predicted to demonstrate higher flow values.

With reference to static pressure differences between the measured and simulated situations, the measured only used one data point; while the simulated used more than 80 data points. Also, the range of the pressure drop is from 0.0793 " H_2O to 0.5590 " H_2O . Thus, it may not contain an accurate pressure reading of the whole enclosure. However, the measured static pressure loss (0.12 " H_2O) is in the simulated static pressure range. Also, the actual enclosure is

not a 100% water tight enclosure. Therefore, the static pressure drop between the measured and simulated situation differed significantly.

To conclude, it is very difficult to rate the level of validation. A model can fail in one validation point by 200% while, the same model can pass by 20% for a different validation point. However, there is not a conventional ratio that differentiates between a good model and bad model. Also, the mesh setting plays an important role in the model calculations. For an example, CFD model 3 can solve the simulation within 5 hours or it can solve it within 48 or more hours. However, between the 5 hour solver and 48 hour solver, the flow rate was 400 CFM lower in the 48 hour solver. In other words, a finer mesh will calculate results more accurately, but will involve greater expense in terms of time and computing power.

4 Rain water penetration Analysis

As discussed in section 1.6, generators should undergo rainwater penetration testing before releasing it to the market. Even a single water droplet moving past the baffle plates is considered water penetration. When the generator is in full load, there are three main explanations for rain water penetration.

1. Free flowing
2. Dripping
3. Splashing

In order to observe the rain water behavior in the computational environment, a particle study was conducted in the simulation to replicate the water droplet motion. For the particle study, properties such as, velocity, diameter, particle material and wall conditions needed to be

defined. Water was selected as the default particle and the maximum number of droplets selected was 200.

The rainwater test apparatus mentioned in Appendix A is used to mimic the natural rain fall phenomenon. However, as discussed in section 1.7, droplet velocity and diameter changes throughout the droplets fall. Hence, to mimic the natural rain fall phenomena in a computational environment, the diameter and the terminal velocity needs to be defined. Therefore, velocity and the diameter values were assumed in individual analyses. Also, the wall conditions were selected based on the analysis type.

The next step was to define the wall conditions. The user has to configure the wall conditions according to the analysis type. There are three differing types of wall conditions; absorption, ideal reflection and reflection. If the wall condition is defined as absorption, the particles will be absorbed by the wall. If it is ideal reflection, the particle will reflect in the opposite direction at the same magnitude of the impact velocity. Finally, in reflection condition, the user can assign the coefficient of restitution.

The coefficient of restitution will depend on many variables, such as, paint, rust resistant coatings, material type, among others. Also, measuring the coefficient of restitution is a cumbersome process which requires specialized testing equipment. Hence, it was decided to calculate the reflection rate using observational methods.

The rain test apparatus was set-up next to a baffle plate so that the rain water would collide with the sheet metal surface of the baffle plate. Using a slow motion camera that was placed parallel to the surface of the impact area, pictures and videos were taken of the water droplet behavior. The vertical distance between the test apparatus and the baffle plate was 5 m. Also, the pressure in the system was maintained at 5 psi. After analyzing the data, it was

observed that the water droplets did not bounce back more than 5 cm. Hence, the assumption was made that the coefficient of restitution is very low and was assigned a value of 0.1.



Figure 48 The camera was placed parallel to the impact surface.

4.1 Free flowing

Because of the high air velocity and the static pressure drop created near the inlet, rain water droplets can get carried through the air stream into the enclosure. In order to stop the free flowing penetration, baffle plates are placed at the back of the inlet grill (Figure 49). The purpose of the baffle plate is to act as a barrier, directing the air flow towards the ceiling of the enclosure.

The purpose of the baffle plate is to separate the water droplets from the air particles. Because of the change in momentum permitted by altering the direction, the relatively heavier water droplets will bump into the inner face of the baffle while the lighter air particles will flow in their natural path. Also, there is a blade in the middle of the baffle to stop any water droplets flowing perpendicular to the inner face.

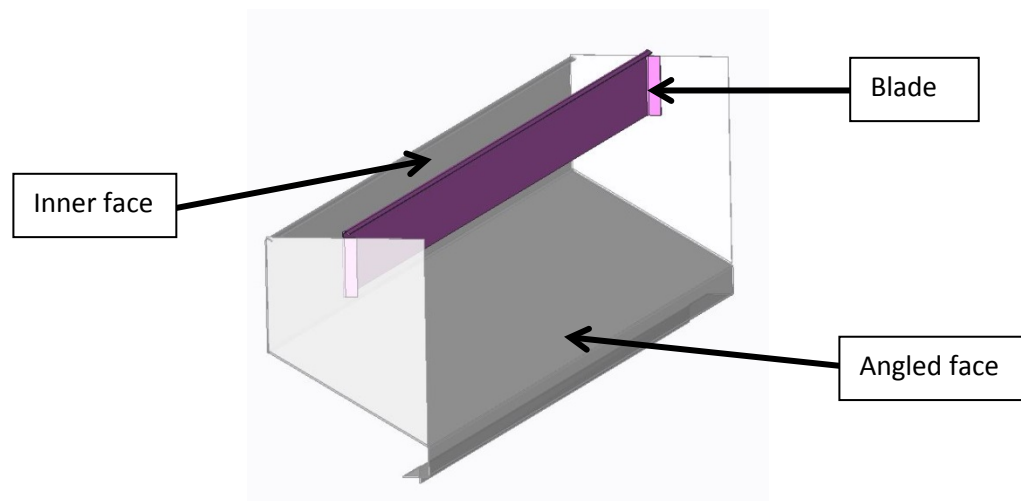


Figure 49 Baffle plate and the blade.

When the direction of the air flow is suddenly changed, it creates high and low velocity areas (Figure 50). The loss of velocity creates static pressure drops and influences the volumetric flow rate. Hence, an angled face is used to ease the directional change of the air flow, making the transition smoother.

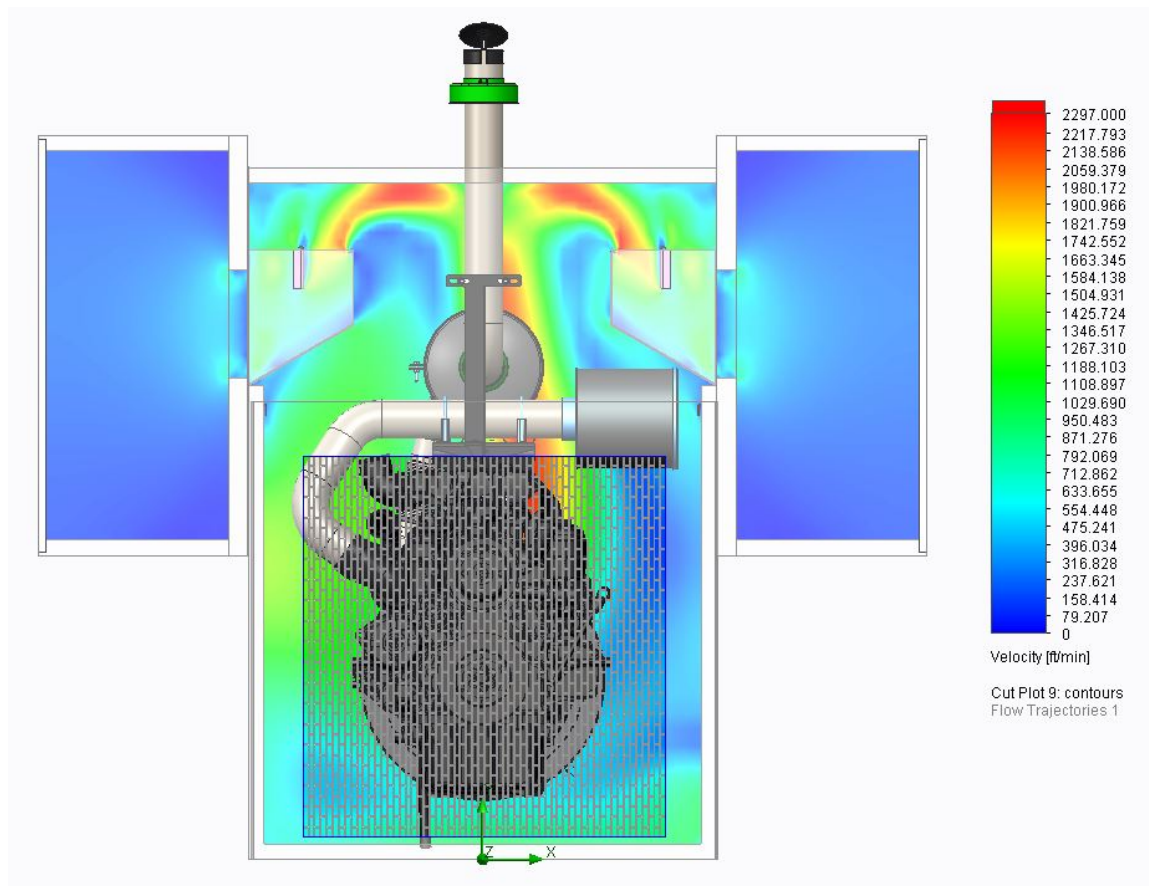


Figure 50 Contour plot in velocity at middle of the enclosure.

In order to simulate the free flowing water droplets, the terminal velocity and the diameter of the droplets need to be calculated. Initially, terminal velocity was to be calculated using the rain test apparatus. However, the complex geometry of the nozzle and lack of information about the apparatus made the calculation extremely difficult. Hence, using Equation 1-83, the droplet velocity was estimated as a function of the droplet diameter (Table 8). A lower limit of 0.1 mm and an upper limit of 2.0 mm diameter were selected. Depending on the simulation results, the upper limit could have been increased.

$$V_t = 9.4 (1 - \exp(-1.57 \cdot 10^3 D^{1.15}))$$

D (mm)	Vt [m/s]	Vt [ft/min]	Relative Velocity [ft/min]
0.1	0.36349	71.55295	228.4470547
0.2	0.787675	155.0538	144.9462439
0.3	1.223985	240.9414	59.05861552
0.5	2.086765	410.7797	-110.7796615
1	4.01481	790.3153	-490.315269
2	6.669396	1312.871	-1012.87064

Table 8 Terminal Velocity as a function of diameter

The next step was to define the wall conditions. Since this analysis was focused on water droplets that are free flowing, the behavior of the droplets after impact was not considered. Hence, all the wall conditions are selected as absorptions. In other words, if a water droplet hits the wall, the simulations assume the droplet is absorbed by the wall. As a result, the simulation only displayed the droplets that will flow without any obstructions.

The droplets were injected at a 45 degree plane with respect to the enclosure (Figure 51). By doing so, droplets experienced the maximum horizontal and vertical terminal velocities. At this location, the droplets encountered the air flow. As a result, the flow velocity influenced the droplet velocity. Hence, the droplet velocity was assigned as being relative to the flow velocity. The flow velocity at the injection point was calculated as 300 ft/min. Therefore, in Table 8, the absolute value of the relative velocity was used as the droplet injection velocity.

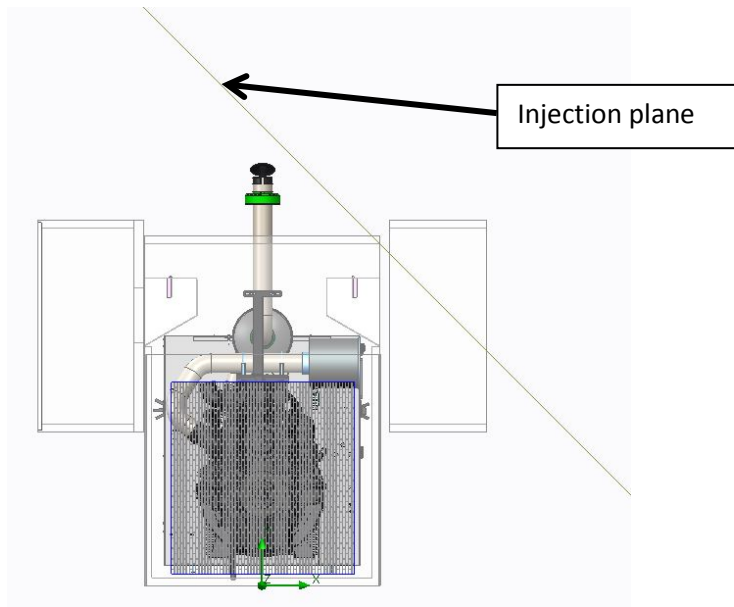


Figure 51 water droplet injection plane.

At the end of the particle study, it was concluded that only 0.1 mm water droplets will penetrate the enclosure in free flow situations (Figure 52). The air flow will carry these droplets and collide on the enclosure ceiling. All the other droplets will collide with the baffle plate surfaces and will not penetrate.

Therefore, it can be concluded that the baffle plates act as an effective barrier for water droplets that are larger than 0.1 mm. Droplets with diameter sizes larger than 2 mm were not analyzed because initial results concluded that only the smaller droplets (0.1 mm or below) penetrated, while droplets larger than 0.1mm collided with the baffle plate and did not penetrate into the enclosure. Moreover, referring to Figure 50, it can be concluded that the water penetration path is consistent with the high velocity areas. Refer to Appendix J for more information about the free flow study.

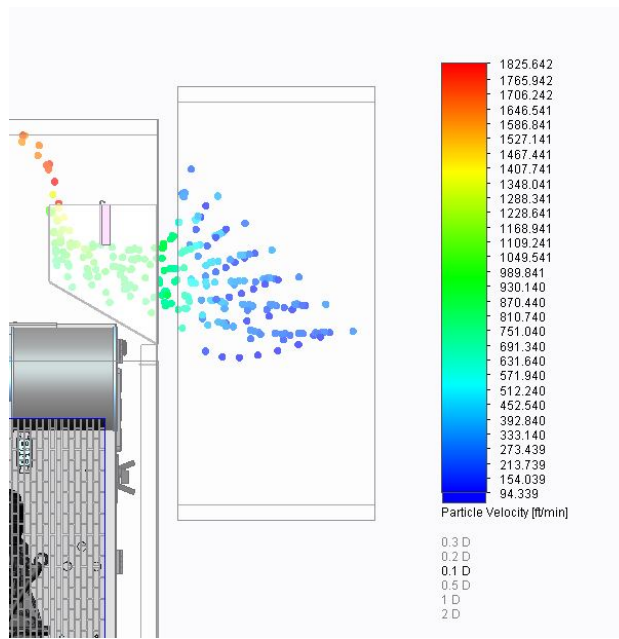


Figure 52 Water droplet size 0.1 mm. Some of the droplets get carried by the air flow

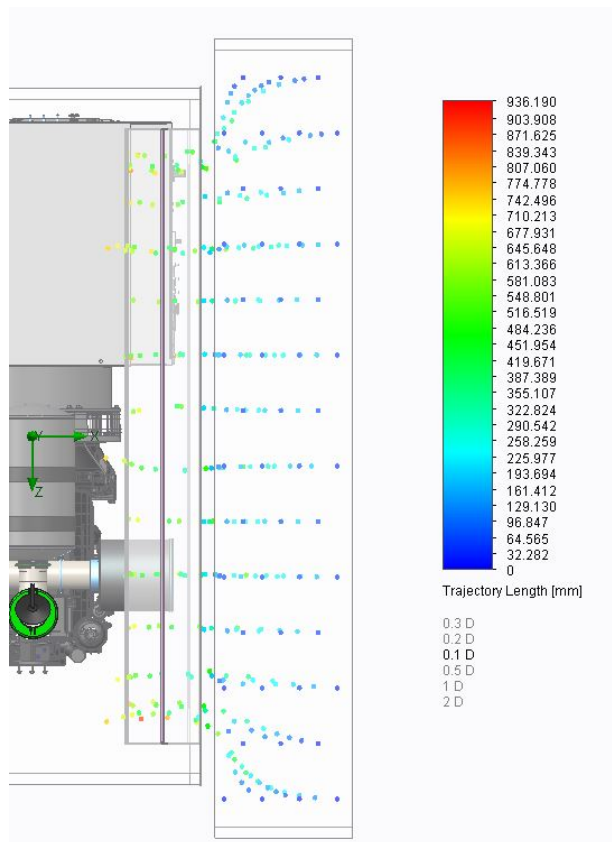


Figure 53 Top view of the 0.1 mm diameter droplets

4.2 Dripping

The main purpose of the angled face of the baffle plate and the blade is to stop water droplets from entering the enclosure. However, because of surface tension, the water droplets that collide with the inner face and the blade will attach themselves to their surfaces. Droplets can climb up through the surfaces due to forces created by the air flow, and can get swept up into the flowing air. To avoid that, a lip is placed on top of the inner face and the blade (Figure 54). As a result of this lip, droplet diameters will increase as the smaller droplets coalesce until the point that the gravitational force acting on them is higher than the surface tension, causing them to drop down the angled face.

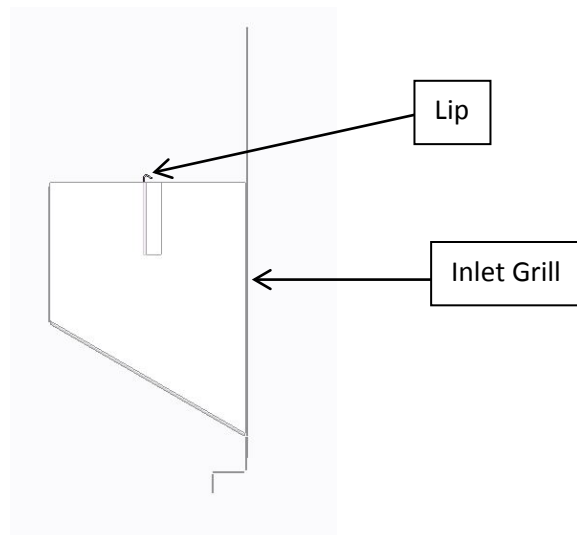


Figure 54 Baffle plate, blade and the inlet grill. Front view

However, some of these falling droplets can still get carried through the air stream into the enclosure. This occurrence is called penetration by dripping. It is important to highlight that the diameter of the falling droplets cannot be calculated. Because the enclosure suffers heavy vibrations and this vibration energy will affect the downward force of the droplets. In other words, the combination of vibration energy and the gravitational forces are both acting on

surface tension. Also, it is important to mention that heat transfer was not accounted for in the simulations, and that heat energy will affect the water's properties. Therefore the droplet diameter is not a constant and it was assumed to range of 0.1mm to 2.5 mm. Also, depending on the results, the diameter could have been increased if needed. Dripping will occurred in two locations, at the inlet grill and at the middle blade.

4.2.1 Dripping at the inlet grill

Since this particle study is focused on the water droplet formation on top of the inlet grill surface, the injection point was defined as the entire surface of the inlet grill. Also, the wall condition of the inlet grill was defined as ideal reflection. As the study concerns a variety of droplet formation locations, including the droplet formation at the top part of the grill surface, this definition was required. In this condition the droplets that form on top of the grill slide down until get caught up in the air stream in the simulation.

Moreover, wall conditions for the blade, inner face and the lips were defined as absorption. Meaning, the water droplets which collided with those surfaces were assumed to be retained by the lips and prevented from penetrating into the enclosure (see section 4.1 for more details about absorption).

As the velocity of dripping droplets is near zero and the simulation applies the gravitational forces to the droplets. The relative velocity type was selected and the velocity was defined as zero in all three planes ($V = [0]_{xyz}$) and the simulation automatically calculated the applicable velocity to be in a downward direction. Based on observational data, the coefficient of restitution in the angled face was selected as 0.1. Finally, the diameters of the water droplets were selected as 0.1, 0.25, 0.5, 0.75, 1.0, 1.5, 2.0, 2.5 mm and the number of each sized particles was selected as 50.

It was concluded that, when the droplet diameter is 0.1 mm, droplets will get carried through the air stream (Figure 55). When the droplet diameter size is 0.25mm to 2.5 mm, the baffle plates and the blade will retain the droplets from penetrating the enclosure.

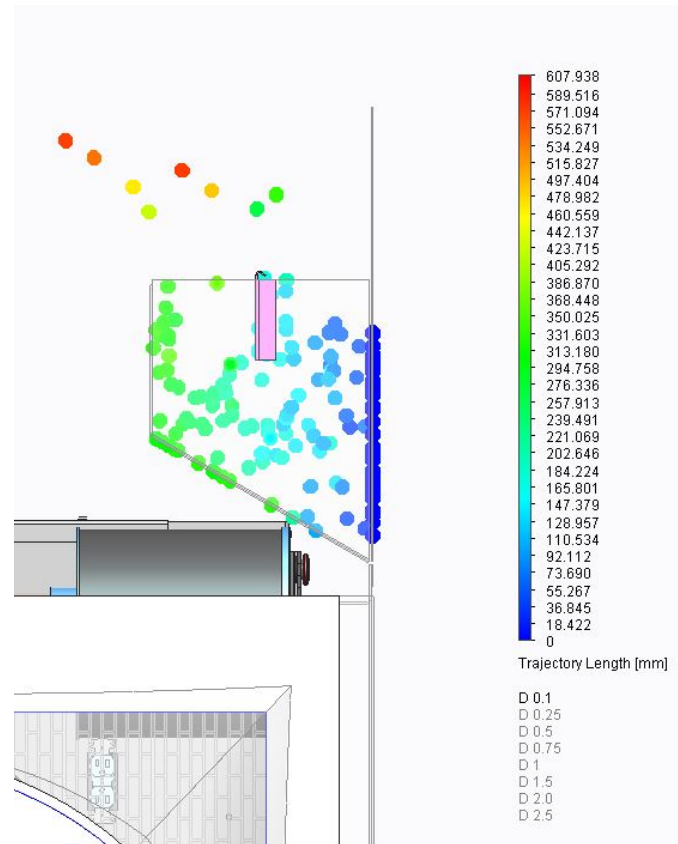


Figure 55 0.1 mm diameter droplets will penetrate the enclosure

However, after further investigation the 0.1 mm study, it was determined that the penetration will only occur only in few locations (Figure 56). Upon investigating the top view of the study, water penetration was detected near the middle and the two sides.

In Figure 56, locations marked “1” are the two sides of the baffle plate. These surfaces do not have lips on their top edges. Hence, the droplets can be impelled up these surfaces by the combination of wind forces and surface tension and get caught up with the flow stream.

Moreover, at location “3” there is a solid wall dividing and supporting the grill. The air particles go around this solid wall.

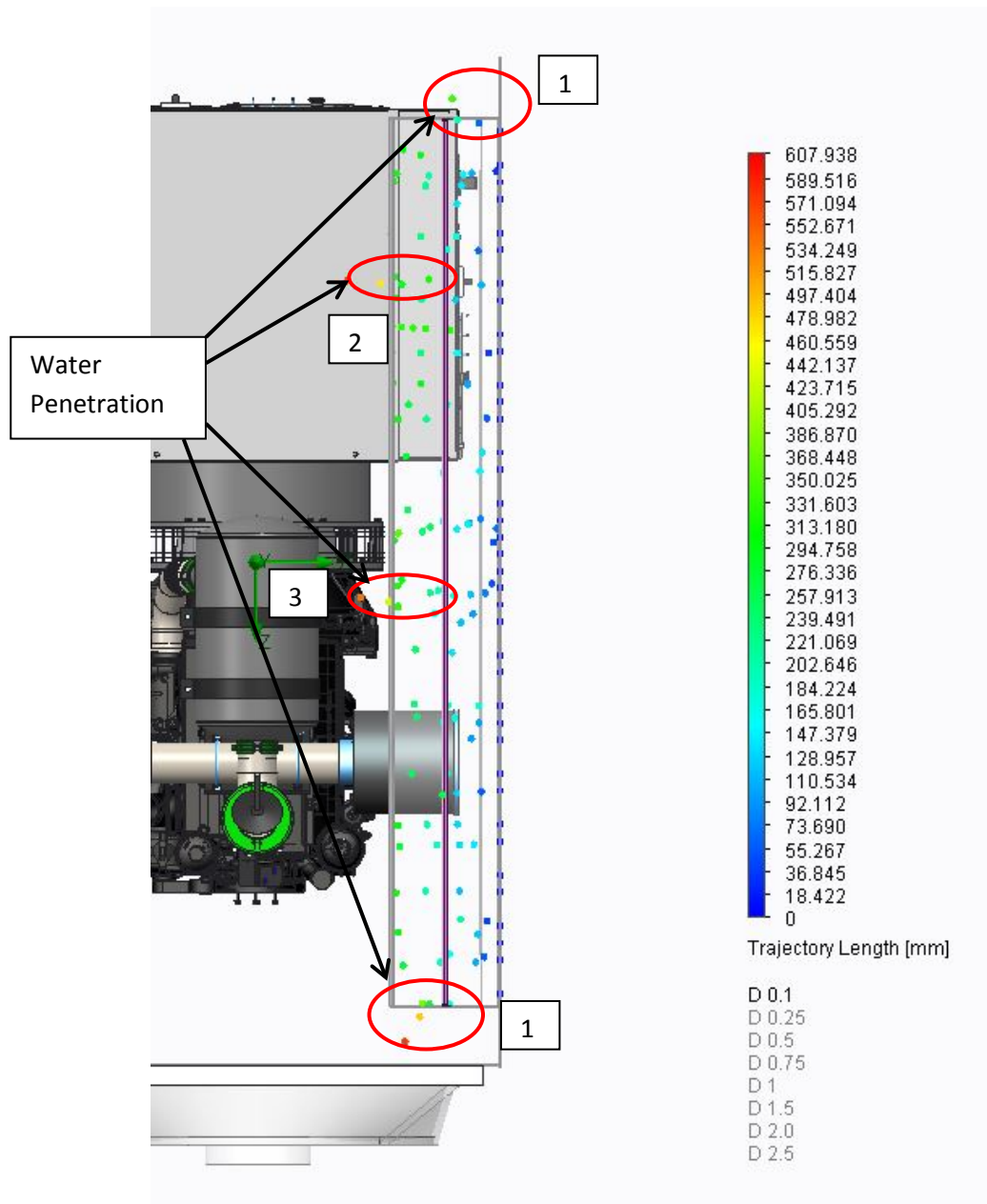


Figure 56 0.1 mm droplet size penetration location. Top view

Also, the air velocities are higher at the two sides of the baffle plate and near the solid dividing wall of the grill (Figure 57).

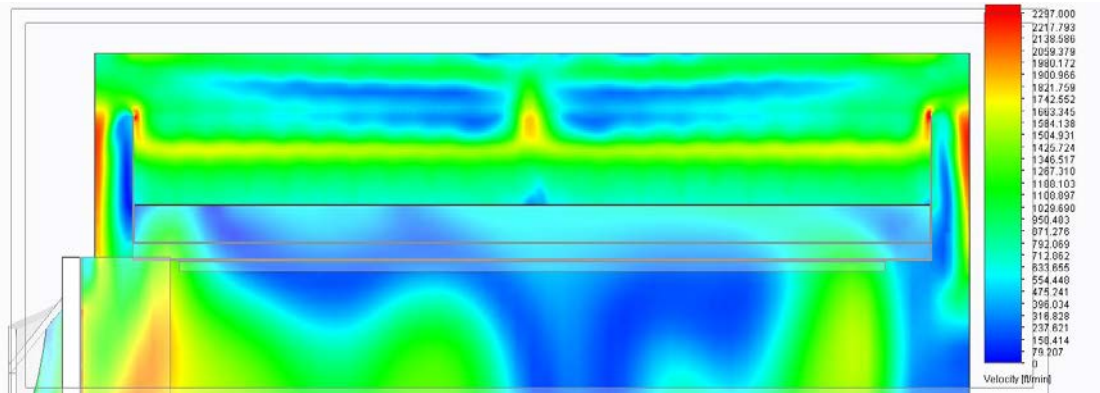


Figure 57 Contour plot across the baffle plate illustrate high velocity near the solid wall and the two sides of the baffle plate

Therefore, it can be concluded that when dripping occurs at the inlet grill, the water droplets will not penetrate if the droplet diameter is higher than 0.1 mm. However, as mentioned previously, the droplet diameter cannot be computed as well as there are no upper or lower limits. Also, for future recommendations, using lips at the two sides of the baffle will stop the penetrations from the sides. This study was not able to address the problem of water penetration posed by the middle solid wall, nor does it suggest any solution. Refer to Appendix J, for more information about the dripping at the inlet grill study.

4.2.2 Dripping at the blade

Similar to dripping from the inlet grill, water droplets can accumulate at the bottom edge of the blade as well. Therefore, the injection point was defined as the bottom face of the blade (Figure 58). Since this study concentrated only on the droplet behavior inside the enclosure from the blade and beyond, wall conditions for inlet grill itself were not defined.

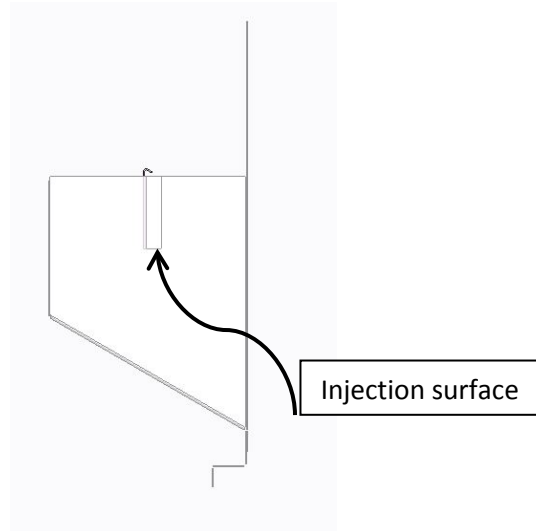


Figure 58 Injection point was defined as the bottom surface

However, the wall conditions for the inner face were defined as absorption and the coefficient of restitution for the angled face was kept at 0.1. The droplet velocity was defined as $V = [0]_{xyz}$ and the number of droplets chosen was, once again, 50. As mentioned in section 4.2.1, the droplet diameter cannot be accurately calculated due to vibrations and other forces. Therefore, the diameter of the droplets was assumed to be in the range of 0.1 mm to 2.5 mm.

After conducting the study, it was concluded that water penetration occurs when the droplet diameter is in the range of 0.1 mm to 1.0 mm. However, each of these diameter sizes exhibit a unique set of behaviors and the droplet behavior can best be generally explained using the air flow velocity at the baffle plate.

Figure 59 illustrates the higher air flow velocity near the lip areas, specifically at the top of the inner face lip. On the other hand, right behind or right underneath the blade plate, velocity is virtually zero. This velocity difference is important for understanding the dripping phenomena. To explain, water droplets that build up at the bottom of the blade are more likely to be swept up into the air flow if the velocity is higher in that area. This process continues until the droplet

mass is higher than the lift forces created by the air stream. Hence, when the droplet diameter is increases, the droplets collide with the inner face and drops down to the angled face.

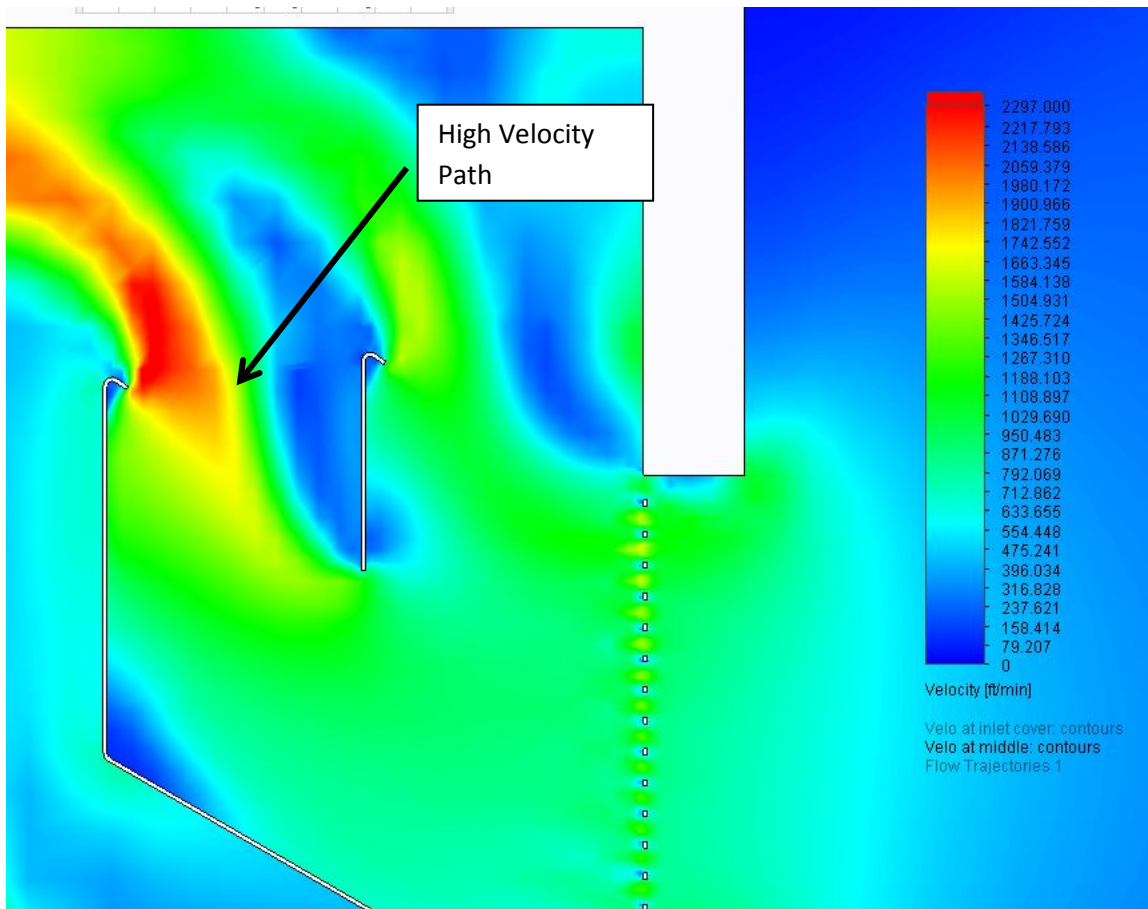


Figure 59 Air flow velocity at the baffle plate. Zoomed into highlight the blade and the lips

Analyzing Figure 60, it is clear that the water penetration path is consistent with the high velocity path illustrated in Figure 59. It is also apparent that none of the droplets collide with the inner face; therefore, the lips will not prevent water penetration. This behavior continues until the droplet diameter is equal to 0.75 mm.

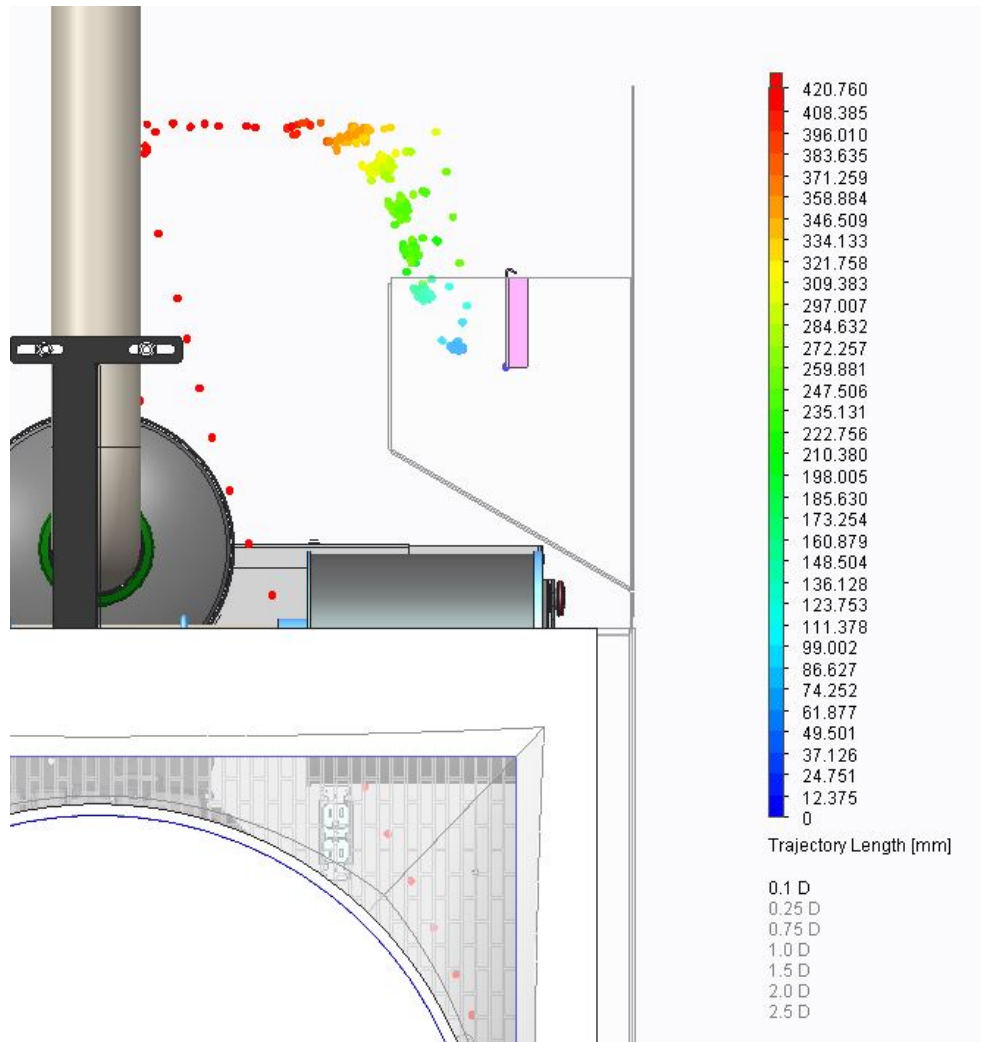


Figure 60 0.1mm diameter size. Penetration occurs severely

When droplet diameter falls between 0.75 mm and 1.0 mm, the penetration occurs in a slightly different way. Figure 61 demonstrates the behavior of water droplets when the diameter is 0.75 mm. However, the penetration only happens at the two sides and the middle part of the baffle. In order to examine this behavior further, a contour velocity plot was combined with the particle study.

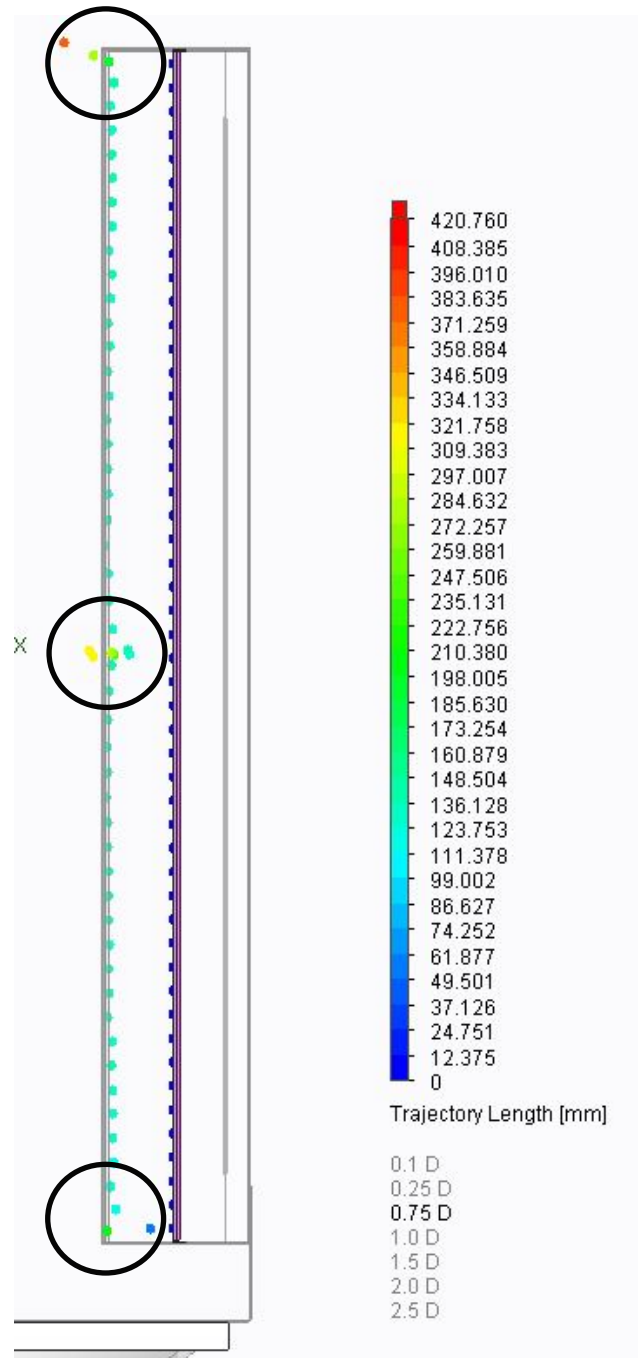


Figure 61 0.75 mm diameter size. Penetration occurs at the middle and two sides (black circle)

Then, the contour plot with velocity as a parameter was placed in between the blade and the inner face. After that, water droplet appearance was changed into lines instead of spheres. Figure 62 visualize the combination of contour plot and particle study in one picture.

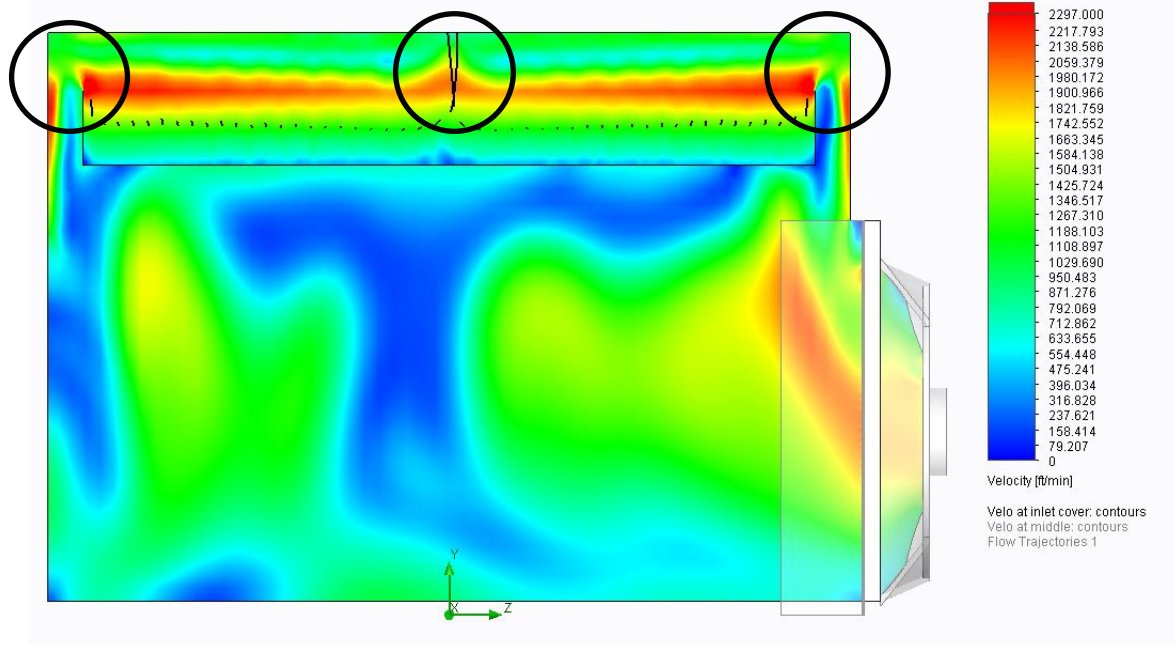


Figure 62 Combination of contour plot of velocity and particle study data. This view is presented from the left side in order to bring the particles in front of the plot. The higher simulated velocities near the midpoint and at the two sides are highlighted in the black circles.

In the analysis of Figure 62, it is notable that the velocities at the two sides and near the middle part of the baffle plate are higher than the in other areas. Therefore, in those areas, greater upward forces will exist; thus, these greater velocities will carry droplets that are heavier than in other areas.

However, these higher velocities have their limits as well. When the diameter size is 1.0 mm, penetration only occurs near the middle (Figure 63). When the diameter is 1.5 mm or larger, however, no penetration will occur (Figure 64). Instead, all the droplets will collide with the inner face.

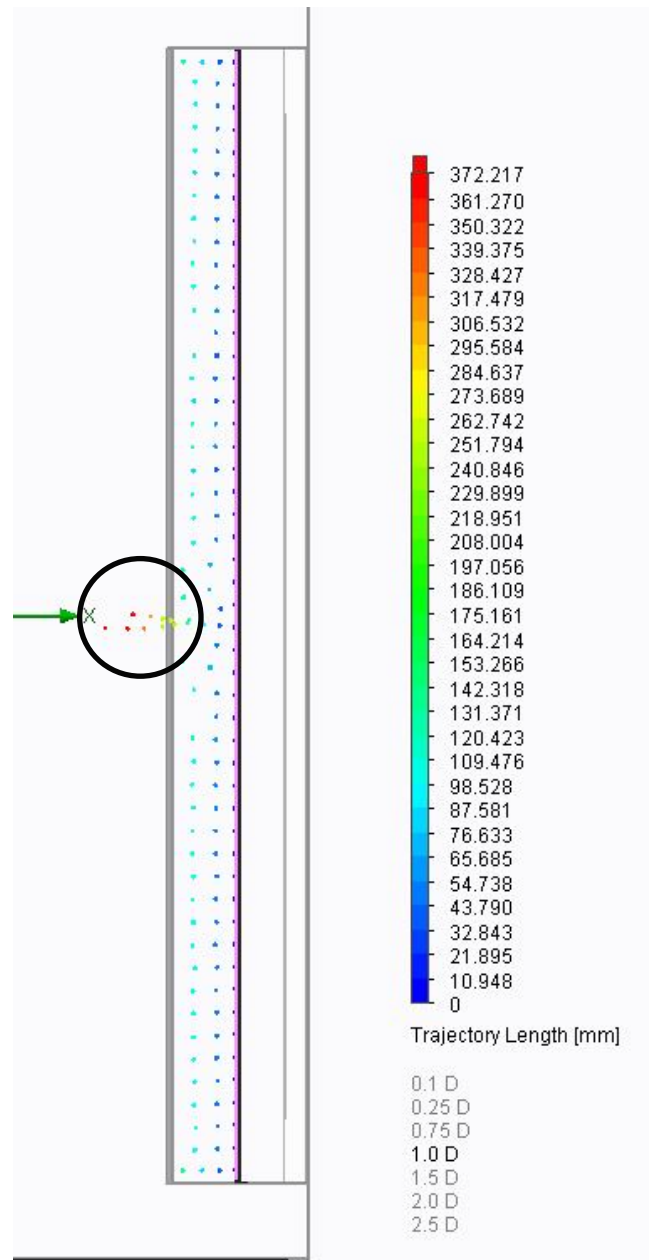


Figure 63 Droplet size 1.0 mm. Penetration only happens near the middle

To conclude, water penetration due to dripping at the blade will only happen when the droplet diameter is in the range of 0.1 mm to 1.00 mm. Also, in between the inner face and the blade, the droplet penetration path is consistent with the high velocity path. Overall, however, the baffle plate design is a fairly successful one because it generates low velocity areas right

behind and right underneath the blade. Therefore, it does not create high velocity paths that can carry larger droplets ($D \leq 1.5$ mm).

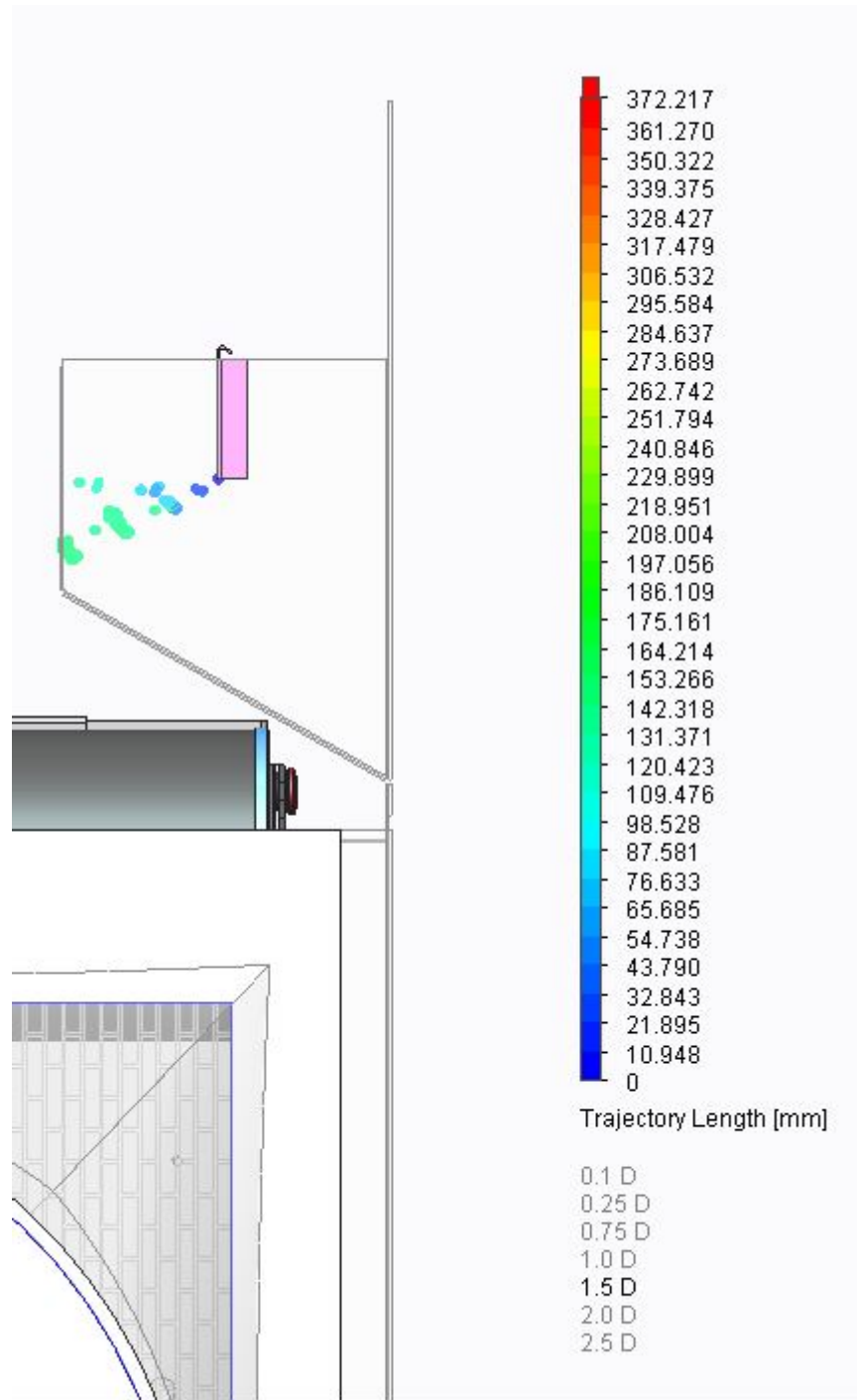


Figure 64 1.5 mm diameter. No penetration

4.3 Splashing

Splashing occurs when water droplets collide with any solid surface, breaking them into smaller droplets with different velocity profiles. In applying this principle to the generator enclosure, splashing can occur at the inlet grill and at the angled face. However, due to lack of information about surface tension of water with sheet metal, coefficient of restitution and an lacking an exact method to determine the water droplet break up, many assumptions had to be made regarding these phenomena. Also, splashing at the angled face was not considered as the co-efficient of restitution is low, and even if droplets were to bounce back, they would exhibit similar behavior to the free flowing droplets.

The first step in the splashing particle study was to define the velocity of the droplets after impact. As mentioned earlier, the co-efficient of restitution was assumed to be 0.1. However, co-efficient of restitution only applies to those droplets that bounce back without breaking apart. The droplets created as a result of splashing will exhibit a variety of diameter size and velocity. Due to limits of testing equipment and thus, lack of data, the velocity of these smaller droplets created by impact had to be assumed as well.

Again an observational method was used to investigate the velocity of the splashing droplets (refer to Section 4 for more details about the observational method chosen). After analyzing slow motion videos, it was observed that the splashing droplets do not bounce far away from the grill. Hence, it was assumed that the velocity of splashing droplets is nearly zero. In other words, the behavior of splashing droplets can be simulated the same way as the behavior of those dripping at the inlet grill (section 4.2.1).

5 Discussion and Recommendations

In the current model, the difference between the measured and simulated static pressure should have been examined further. In particular, the measured static pressure should have been taken in multiple locations and examined for errors. Also, the techniques for measuring air velocity should be re-examined in an attempt to improve the precision of the measurements.

One great improvement for potential future models would be to factor in the heat generation of the engine and the generator. The heat energy that is produced by the engine could be calculated using brake specific fuel consumption of the engine and by measuring the exhaust gas flow. Also, the charge air radiator heat dissipation rate would need to be calculated as well.

Next, the coolant and charge air radiator should be modeled as a heat exchanger. Instead of modeling the complete design, the radiator could be modeled as a porous media. By this method, a porous media could account for the heat exchange rate or the porosity of the radiator, as opposed to only considering the air flowing through the radiator. Also, the air pressure lost due to the restriction of flow created by the radiator would need to be accounted for.

Finally, more realistic wall conditions should be incorporated into the model. The current model's wall conditions are defined as adiabatic conditions. This means, walls have no effect on air flow or heat transfer. However, in an actual enclosure, the inside walls are covered with a sound absorbing material which does restrict the flow and affects heat transfer.

6 Bibliography

- (n.d.). Retrieved from MTU Onsite Energy: <http://www.mtuonsiteenergy.com/about-us/>
- Sokolowski, J. A., & Banks, C. M. (2010). *Modeling and Simulation Fundamentals: Theoretical Underpinnings and Practical Domains*. John Wiley & Sons.
- Basniev, K., Dmitriev, N. M., & Chilingar, G. V. (2012). *Mechanics of Fluid Flow*. Somerset, NJ, USA: John Wiley & Sons. Retrieved from <http://www.ebrary.com>
- Blanks, J. E. (1997). Optimal Design of an Enclosure for a Portable Generator. Retrieved from <http://scholar.lib.vt.edu/theses/available/etd-145110201974500/unrestricted/etd.pdf>
- Bungartz, H.-J., Zimmer, S., Buchholz, M., & Pfluger, D. (2014). *Modeling and Simulation - An application oriented introduction*. Springer.
- Deshmukh, A. (2009). International Assessment of Research and Development in Simulation-Based Engineering and Science - Engineering Simulations. *World Technology Evaluation Center, Inc* (pp. 79-88). Baltimore, Maryland: World Technology Evaluation Center, Inc. Retrieved from http://www.wtec.org/sbes/SBES-GlobalFinalReport_BW.pdf
- Donea, J., Huerta, A., Ponthot, J., & Rodriguez-Ferran, A. (2004). Arbitrary Lagrangian–Eulerian Methods. In S. ERWIN, T. HUGHES, & R. BORST (Eds.), *Encyclopedia of Computational Mechanics* (Vol. 1). John Wiley & Sons. Retrieved from http://eu.wiley.com/legacy/wileychi/ecm/pdfs/Volume_1_Chapter_14.pdf
- Durickovic, B., & Varland, K. (2005). *Between bouncing and splashing: Water drops on a solid surface*. Arizona: Applied Mathematics thesis University of Arizona.
- Durst, F. (2008). *Fluid Mechanics - An Introduction to the Theory of Fluid Flows*. Springer.
- Fayek, A.-M. M. (2002). *Introduction to Combined Discrete-Continuous Simulations Using SIMSCRIPT 11.5*. CACI.
- Fortmann-Roe, S. (2014). Insight Maker: A general-purpose tool for web-based modeling & simulation. *Simulation Modelling Practice and Theory*, 47, 28-45. Retrieved from <http://www.sciencedirect.com/science/article/pii/S1569190X14000513>
- Glotzer, S. C. (2009). International Assessment of Research and Development in Simulation-Based Engineering and Science - Introduction. *World Technology Evaluation Center, Inc* (pp. 1-12). Baltimore, Maryland: World Technology Evaluation Center, Inc. Retrieved from http://www.wtec.org/sbes/SBES-GlobalFinalReport_BW.pdf
- Goldsman, D., Nance, R. E., & Wilson, J. R. (2010). *A Brief History of Simulation Revisited*. Baltimore, Maryland: Winter Simulation Conference. Retrieved from <http://www.informs-sim.org/wsc10papers/051.pdf>

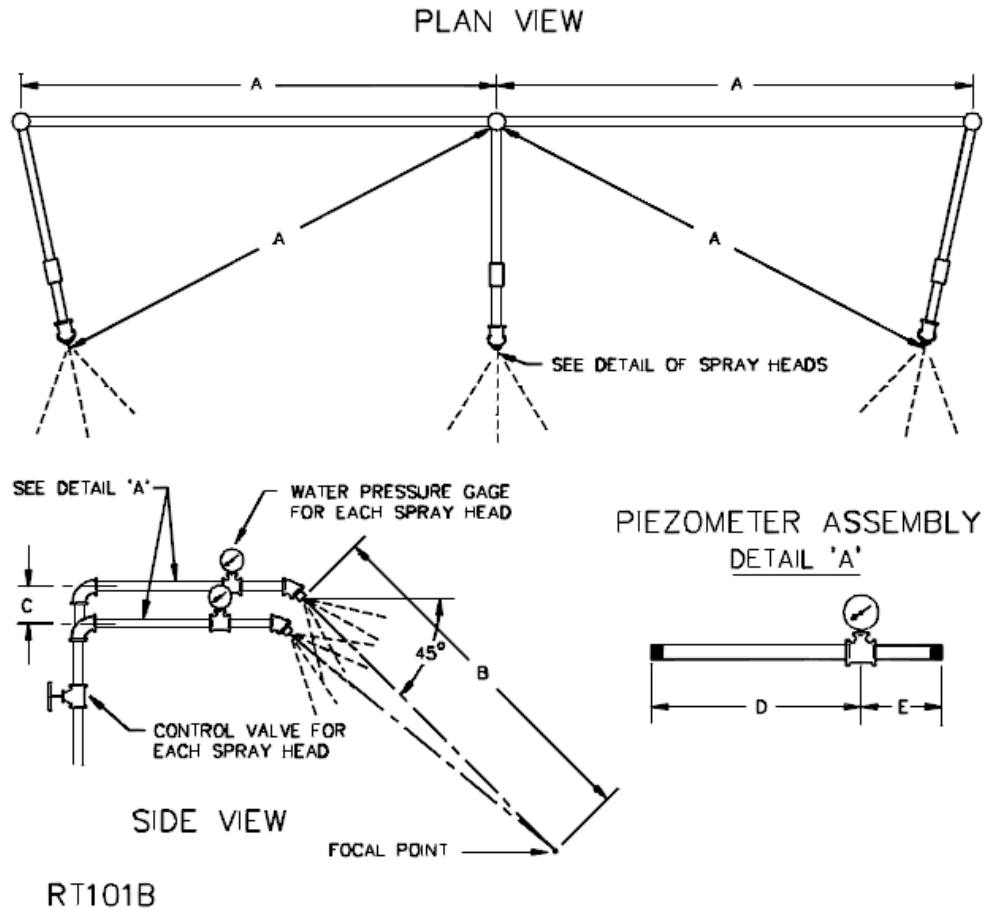
- Grier, D. A. (2004 Jul-Sep). Annals of the History of Computing. *IEEE*, P2. Retrieved from <http://www.columbia.edu/cu/computinghistory/eniac.html>
- Gunn, R., & Kinzer, G. (1949). The terminal velocity of fall for water droplets in stagnant air. *Journal of Meteorology* 6, 243-248.
- Habil, I., & Kolev, N. I. (2005). *Multiphase Flow Dynamics 1*. Berlin Heidelberg: Springer Berlin Heidelberg.
- Hauke, G. (2008). *An Introduction to Fluid Mechanics and Transport Phenomena*. Springer.
- Issa, R. (2003). *Numerical Modeling of the Dynamics and Heat Transfer of Impacting Sprays for a Wide Range of Pressures*. Pittsburgh: University of Pittsburgh.
- Kelton, D. W., Sadowski, R. P., & Sadowski, D. A. (1997). *Simulation with Arena*. McGraw-Hill College. Retrieved from <http://web.iitd.ac.in/~nomesh/MEL770/kelton.pdf>
- Kleinstreuer, C. (2010). *Modern Fluid Dynamics - Basic Theory and Selected Applications in Macro- and Micro-Fluidics*. Springer Netherlands.
- Lagubeau, G., Fontelos, M., Josserand, C., Maurel, A., Pagneux, V., & Petitjeans, P. (2012). Spreading dynamics of drop impacts. *Journal of Fluid Mechanics*, 713, 50-60.
- Maria, A. (1997). *INTRODUCTION TO MODELING AND SIMULATION*. Binghamton, NY USA: State University of New York at Binghamton, Department of Systems Science and Industrial Engineering. Retrieved from <http://imap.acqnotes.com/Attachments/White%20Paper%20Introduction%20to%20Modeling%20and%20Simulation%20by%20Anu%20Maria.pdf>
- Mook, F. (2003). *Driving rain on building envelopes*. ProQuest Dissertations & Theses Global.
- National Training and Simulation Association. (2011). *National Training and Simulation Association*. Retrieved from Trainingsystems: <http://www.corporatepress.com/clientfiles/ntsa/>
- Oqielat, M., Turner, I., Belward, J., & McCue, S. (2011). Mathematics and Computers in Simulation. *Modelling water droplet movement on a leaf surface*, 81, 1553-1571.
- Pedley, T. J. (1997). *Introduction to Fluid Dynamics* (Vols. 61 (Supl. 1): 7-24). London, UK: SCIENTIA MARINA.
- Pegden, D. C., Sadowski, R. P., & Shannon, R. E. (1991). *Introduction to Simulation Using SIMAN*. McGraw-Hill Companies.
- Pozrikidis, C. (2009). *Fluid Dynamics - Theory, Computation, and Numerical Simulation*. Springer US.

- Reikher, A., & Barkhudarov, M. R. (2007). *Introduction to fluid dynamics*. London: Springer London.
- Richard, D., & Quéré, D. (2000). Bouncing water drops. *Europhys. Lett.*, 50(6), 769-775.
- Rieutord, M. (2015). *Fluid Dynamics - An Introduction*. Springer International Publishing.
- Shrader, C. R. (2006). *History of Operations Research in the United States Army* (Vol. 1). Department of Army. Retrieved from http://www.history.army.mil/html/books/hist_op_research/CMH_70-102-1.pdf
- Tocher, K. D., & Owen, D. G. (2008). The automatic programming of simulations. *Journal of Simulation*.
- Tom, B. (2015). *Grc.nasa.gov*. Retrieved from Dynamic Pressure: <http://www.grc.nasa.gov/WWW/k-12/airplane/dynpress.html>
- Tu, J., & Yeoh, Guan Heng. (2007). *Computational Fluid Dynamics : A Practical Approach*. Burlington, MA: Butterworth-Heinemann.
- UL Standards* . (n.d.). Retrieved from UL: <http://ul.com/aboutul/>
- Van der Wal, B. (2006). *Static and Dynamic Wetting of Porous Teflon Surfaces*. Netherlands: University of Groningen.
- Villermaux, E., & Bossa, B. (2011). Drop fragmentation on impact. *Journal of Fluid Mechanics*, 668, 412-435.
- Wendt, J. F., Anderson, J. D., & Von Karman Institute. (2008). *Computational fluid dynamics: An introduction*. Berlin; London: Springer. Berlin, London: Springer.
- Yuan, Y., & Lee, T. (2013). Contact Angle and Wetting Properties. In *Surface Science Techniques* (pp. 3-34). Houston: Springer Berlin Heidelberg.
- Zeigler, B. P., Praehofer, H., & Kim, T. G. (2000). *Theory of Modeling and Simulation: Integrating Discrete Event and Continuous Complex Dynamic Systems*. Academic Press.
- Zhao, F., Liu, D., & Tanh, G. (2008). Multiple steady fluid flows in a slot-ventilated enclosure. *International Journal of Heat and Fluid Flow*, 29(5), 1295-1308.
- Zikanov, O. (2010). *Essential computational fluid dynamics*. Hoboken, N.J: Wiley.

Appendix A

Appendix A-1

Test Structure

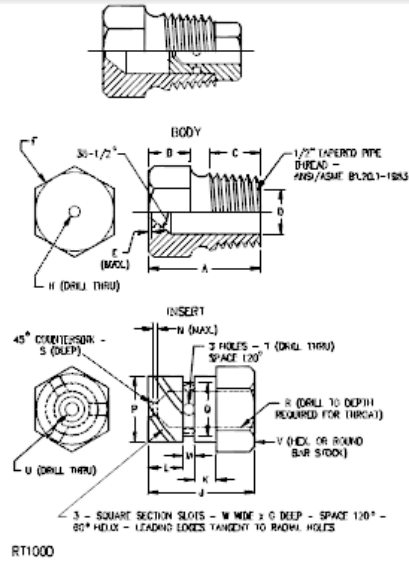


Item	inch	mm
A	28	710
B	55	1400
C	2-1/4	55
D	9	230
E	3	75

Figure 65 Rain water test structure

Appendix A-2

Nozzle Design of the rain test structure



Item	inch	mm	Item	inch	mm
A	1-7/32	31.0	N	1/32	0.80
B	7/16	11.0	P	.575	14.61
C	9/16	14.0		.576	14.53
D	.578	14.68	Q	.453	11.51
	.580	14.73		.454	11.53
E	1/64	0.40	R	1/4	6.35
F	c	c	S	1/32	0.80
G	.06	1.52	T	(No. 35) ^b	2.80
H	(No. 9) ^b	5.0	U	(No. 40) ^b	2.50
J	23/32	18.3	V	5/8	16.0
K	5/32	3.97	W	0.06	1.52
L	1/4	6.35			
M	3/32	2.38			

^a Nylon Rain – Test spray Heads are available from Underwriters Laboratories

^b ANSI B94.11M Drill Size

^c Optional – To serve as a wrench grip.


Figure 66 Rain water test structure nozzle design



Figure 67 Water droplet formation at the nozzle

Appendix B


Fan Curve Data and Specifications

	
33.98/4-8/16.5°/PAG/4ZL/Tp 1 %/Orifice Plate	
DATE: 3/18/2015	
COMPANY: -MTU Onsite Energy ATTN: -S. Andawatta	FROM: Multi-Wing America, Inc. Amanda Pilarczyk
Current Working Point	
Airflow 3.09 m3/s Static Pres 258 Pa Dynamic Pressure 14.1 Pa	Total Pres Power Efficiency 273 Pa 1.74 kW 48 %
	Propagation 1/8 Spherical Sound Power N.A
OPERATIONAL DATA:	
Tip Speed: 82 m/s Temperature: 64 °C Air Velocity: 5.28 m/s Torque: 9.16 Nm Axial Force: 159 N	
OPERATIONAL IMPELLER LIMITS:	
Tip Speed: 121 m/s (2678 RPM) Temperature: -40°C - 120 °C Diameter range: 17.5 - 35.04 in Blade, load factor: 46.3 % Hub, load factor: 24.8 % Power, load factor: N.A. %	
Static impeller data:	
Moment of Inertia: 0.0686 kgm2 Blade Centrifugal force: 1940 N Solidity factor: 0.13 Mass with std. boss: 2.96 kg	
IMPELLER INFORMATION:	
Impeller Diameter: 33.98 in No of blades: 4 Pitch: 16.5 ° Blade Material: PAG Blade Type: 4Z Impeller Rotation: L	
Tests are carried out according to methods described in ANSI / AMCA 210-99 (ISO 5801, DIN 24163) Sound data is calculated and should be used as guideline only	
APPLICATION:	
Speed: 1815 RPM Tip Clearance: 1 % Temperature 64 °C Altitude: 304 m Density: 1.011 kg/m3	
Disclaimer Load factors in Optimiser are based on static operation.	
REMARKS: - - - -	
Multi-Wing America, Inc. USA	P.O. Box 425 15030 Berkshire Industrial Park Burton Ohio, 44021
440-287-5461 Telephone 440-8340449 Fax Optimiser Version: 9.0.1.13	athomas@multi-wing.net http://www.multi-wing.net 3/11/2015 8:11:39 AM

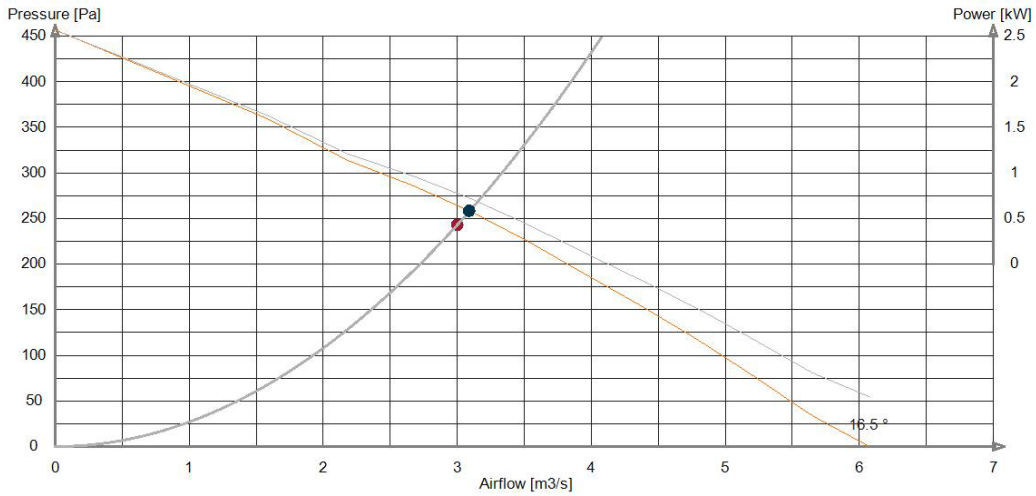
All Optimiser selections require validation and approval in writing by Multi-Wing Sales to qualify for a warranty investigation and to be usable in real world installations. This software, its use and subsequent orders to Multi-Wing has been designed to be used by professionals and is NOT suitable and cannot be used by consumers. Multi-Wing or its group companies, associates and subsidiary companies are not responsible for and shall have no liability for any loss or damage (direct or indirect) for issues or faults arising out of selections, which have not been validated and approved by Multi-Wing Sales. Multi-Wing's acceptance of a purchase order or contract does not constitute validation and approval of product application. The warranty liability of Multi-Wing is limited to the product application information provided by the Buyer in the Optimiser selections and further validated and approved by Multi-Wing in writing. Multi-Wing reserves the rights to update the software without any prior notice.



Figure 68 Fan data - 1



33.98/4-8/16.5°/PAG/4ZL/Tp 1 %/Orifice Plate		DATE: 3/18/2015
COMPANY: -MTU Onsite Energy		
ATTN: -S. Andawatta	FROM: Multi-Wing America, Inc. Amanda Pilarczyk	



<p>IMPELLER INFORMATION:</p> <p>Impeller Diameter: 33.98 in No of blades: 4 Pitch: 16.5 ° Blade Material: PAG Blade Type: 4Z Impeller Rotation: L</p> <p>Tests are carried out according to methods described in ANSI / AMCA 210-99 (ISO 5801, DIN 24163) Sound data is calculated and should be used as guideline only</p>	<p>APPLICATION:</p> <p>Speed: 1815 RPM Tip Clearance: 1 % Temperature: 64 °C Altitude: 304 m Density: 1.011 kg/m³</p> <p>Disclaimer Load factors in Optimiser are based on static operation.</p>
--	---

REMARKS:

-

-

-

-

Multi-Wing America, Inc. USA	P.O. Box 425 16030 Berkshire Industrial Park Burton Ohio, 44021	440-287-5451 Telephone 440-8340449 Fax Optimiser Version: 9.0.1.13	athomas@multi-wing.net http://www.multi-wing.net 3/11/2015 8:11:39 AM
---------------------------------	---	--	---



All Optimiser selections require validation and approval in writing by Multi-Wing Sales to qualify for a warranty investigation and to be usable in real world installations. This software, its use and subsequent orders to Multi-Wing has been designed to be used by professionals and is NOT suitable and cannot be used by consumers. Multi-Wing or its group companies, associates and subsidiary companies are not responsible for and shall have no liability for any loss or damage (direct or indirect) for issues or faults arising out of selections, which have not been validated and approved by Multi-Wing Sales. Multi-Wing's acceptance of a purchase order or contract does not constitute validation and approval of product application. The warranty liability of Multi-Wing is limited to the product application information provided by the Buyer in the Optimiser selections and further validated and approved by Multi-Wing in writing. Multi-Wing reserves the rights to update the software without any prior notice.

Figure 69 Fan data - 02



33.98/4-8/16.5°/PAG/4ZL/Tp 1 %/Orifice Plate		DATE: 3/18/2015
COMPANY: -MTU Onsite Energy ATTN: -S. Andawatta	FROM: Multi-Wing America, Inc. Amanda Pilarczyk	

Point #	Airflow m3/s	Static Pres Pa	Dynamic Pressure Pa	Total Pres Pa	Power kW	Efficiency % (T-S-D)	Speed RPM
0	6.08	0	54.5	54.5	1.372	24-0-24	1815
1	5.65	33.9	47.1	81	1.403	33-14-19	1815
2	5.22	76.3	40.3	117	1.525	40-26-14	1815
3	4.8	117	34	151	1.614	45-35-10	1815
4	4.37	154	28.2	183	1.669	48-40-7.4	1815
5	3.95	190	23	213	1.703	49-44-5.3	1815
6	3.52	225	18.3	244	1.737	49-46-3.7	1815
7	3.1	258	14.2	272	1.741	48-46-2.5	1815
8	2.67	286	10.5	297	1.729	46-44-1.6	1815
9	2.19	313	7.06	321	1.678	42-41-0.92	1815
10	1.58	360	3.68	363	1.586	36-36-0.37	1815
11	0.0607	453	0.00544	453	1.268	2.2-2.2-0	1815

IMPELLER INFORMATION:

Impeller Diameter: 33.98 in
 No of blades: 4
 Pitch: 16.5 °
 Blade Material: PAG
 Blade Type: 4Z
 Impeller Rotation: L

Tests are carried out according to methods described in ANSI / AMCA 210-99 (ISO 5801, DIN 24163)
 Sound data is calculated and should be used as guideline only

APPLICATION:

Speed: 1815 RPM
 Tip Clearance: 1 %
 Temperature: 64 °C
 Altitude: 304 m
 Density: 1.011 kg/m3

Disclaimer
 Load factors in Optimiser are based on static operation.

REMARKS:

-
-
-
-
-

Multi-Wing America, Inc.
USA

P.O. Box 425
15030 Berkshire Industrial Park
Burton Ohio, 44021

440-287-5451 Telephone
440-8340449 Fax
Optimiser Version: 9.0.1.13

athomas@multi-wing.net
http://www.multi-wing.net
3/11/2015 8:11:39 AM



All Optimiser selections require validation and approval in writing by Multi-Wing Sales to qualify for a warranty investigation and to be usable in real world installations. This software, its use and subsequent orders to Multi-Wing has been designed to be used by professionals and is NOT suitable and cannot be used by consumers. Multi-Wing or its group companies, associates and subsidiary companies are not responsible for and shall have no liability for any loss or damage (direct or indirect) for issues or faults arising out of selections, which have not been validated and approved by Multi-Wing Sales. Multi-Wing's acceptance of a purchase order or contract does not constitute validation and approval of product application. The warranty liability of Multi-Wing is limited to the product application information provided by the Buyer in the Optimiser selections and further validated and approved by Multi-Wing in writing. Multi-Wing reserves the rights to update the software without any prior notice.

Figure 70 Fan data - 03

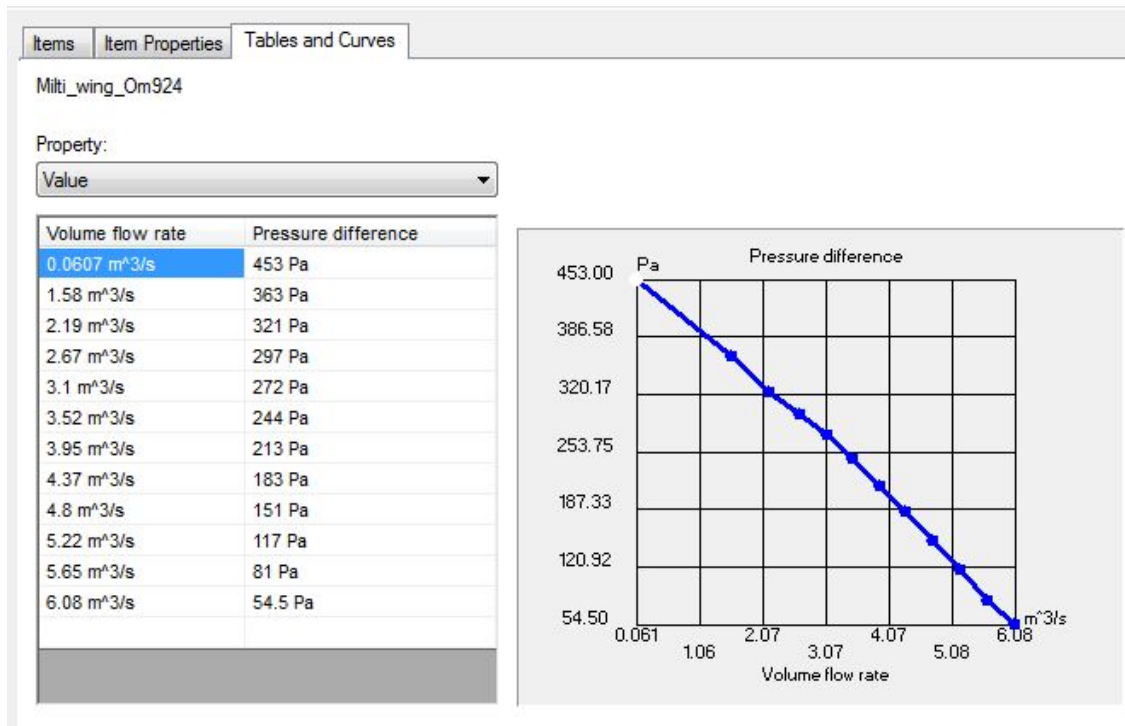


Figure 71 Fan data was entered to the engineering data base in FloEFD. The curve is developed using the data supplied by multi-wing

Appendix C

FloEFD simulation reports for CFD model 3

FULL REPORT

System Info

Product	FloEFD FEP14.0.0. Build: 2960
Computer name	USMKTDT0557
User name	andawattak
Processors	Intel(R) Xeon(R) CPU W3565 @ 3.20GHz
Memory	24573 MB / 8388607 MB
Operating system	Windows 7 Service Pack 1 (Build 7601)
CAD version	Pro/Engineer Creo 2.0 M150
CPU speed	3200 MHz

General Info

Model	OM924_RAIN_DESIGN_4.ASM
Project name	Rain Test_D4
Project path	G:\Engineering\01 Application Engineering\13

	CFD\SAK\OM924_designs\OM924_Design_4\2
Units system	MTU Flow
Analysis type	Internal
Exclude cavities without flow conditions	On
Coordinate system	Global coordinate system
Reference axis	X

INPUT DATA

Initial Mesh Settings

Automatic initial mesh: On

Result resolution level: 8

Advanced narrow channel refinement: Off

Refinement in solid region: Off

Geometry Resolution

Evaluation of minimum gap size: Manual

Minimum gap size: 15.000 mm

Evaluation of minimum wall thickness: Manual

Minimum wall thickness: 15.000 mm

Local Mesh Settings

Local Initial Mesh 1

Components	SUA106857--0001-GEHAEUSETAIL___-135 SUA106857--0001-GEHAEUSETAIL___-130 XG2106100023--0001-TABLEAU____-67 XG2106100023--0001-TABLEAU____-72
Solid/fluid interface	Small solid features refinement level: 3 Curvature refinement level: 0 Curvature refinement criterion: 0.451 rad Tolerance refinement level: 3 Tolerance refinement criterion: 5.217 mm
Refining cells	Refine fluid cells: Off Refine solid cells: Off Refine partial cells: Off
Narrow channels	Advanced narrow channel refinement: On Characteristic number of cells across a narrow channel: 14 Narrow channels refinement level: 4

	The minimum height of narrow channels: Off
	The maximum height of narrow channels: Off

Computational Domain

Size

X min	-1145.016 mm
X max	1145.016 mm
Y min	38.184 mm
Y max	1857.361 mm
Z min	-1405.612 mm
Z max	1486.974 mm

Boundary Conditions

2D plane flow	None
At X min	Default
At X max	Default
At Y min	Default

At Y max	Default
At Z min	Default
At Z max	Default

Physical Features

Heat conduction in solids: Off

Time dependent: Off

Gravitational effects: On

Rotation: Off

Flow type: Laminar and turbulent

High Mach number flow: Off

Humidity: Off

Default roughness: 0 micrometer

Gravitational Settings

X component	0 m/s ²
Y component	-9.81 m/s ²
Z component	0 m/s ²

Default wall conditions: Adiabatic wall

Initial Conditions

Thermodynamic parameters	Static Pressure: 406.78 in H(2)O Temperature: 20.05 °C
Velocity parameters	Velocity vector Velocity in X direction: 0 ft/min Velocity in Y direction: 0 ft/min Velocity in Z direction: 0 ft/min
Turbulence parameters	

Material Settings

Fluids

Air

Boundary Conditions

Environment Pressure 1

Type	Environment Pressure
Faces	

Coordinate system	Global coordinate system
Reference axis	X
Thermodynamic parameters	Environment pressure: 406.78 in H(2)O Temperature: 20.05 °C
Turbulence parameters	Boundary layer parameters
Boundary layer type: Turbulent	

Fans

External Outlet Fan 1

Type	External Outlet Fan
Fan curve	Milti_wing_Om924
Outlet faces	Face<17>@LID559_-253
Outlet coordinate system	Face Coordinate System
Outlet reference axis	X
Outlet flow parameters	Outlet flow vector direction: Normal to face
Thermodynamic parameters	Environment pressure: 406.78 in H(2)O
Toggle	On

Goals

Surface Goals

SG Av Static Pressure 1

Type	Surface Goal
Goal type	Static Pressure
Calculate	Average value
Faces	LID558-252 LID557-251
Coordinate system	Global coordinate system
Use in convergence	On

SG Volume Flow Rate 1

Type	Surface Goal
Goal type	Volume Flow Rate
Faces	LID558-252 LID557-251
Coordinate system	Global coordinate system
Use in convergence	On

Calculation Control Options

Finish Conditions

Finish Conditions	If one is satisfied
Maximum travels	4
Goals convergence	Analysis interval: 5.000000e-001

Solver Refinement

Refinement: Disabled

Results Saving

Save before refinement	On
------------------------	----

Advanced Control Options

Flow Freezing

Flow freezing strategy	Disabled
------------------------	----------

RESULTS

General Info

Iterations: 359

CPU time: 99134 s

Calculation Mesh

Basic Mesh Dimensions

Number of cells in X	54
Number of cells in Y	42
Number of cells in Z	68

Number Of Cells

Total cells	3197005
Fluid cells	2164468
Solid cells	273690
Partial cells	758847
Irregular cells	0
Trimmed cells	0

Maximum refinement level: 5

Goals

Name	Unit	Value	Progress	Use in convergence	Delta	Criteria
SG Av Static Pressure 1	in H(2)O	406.72	100	5.2200296e-005	5.20760275e-005	On
SG Volume Flow Rate 1	ft ³ /min	10302.6949	100	249.252823	153.572776	On

Min/Max Table

Name	Minimum	Maximum
Pressure [in H(2)O]	402.16	408.40
Temperature [°C]	19.92	20.06
Density (Fluid) [kg/m ³]	1.19	1.21
Velocity [ft/min]	0	3241.820
Velocity (X) [ft/min]	-2876.195	3010.013
Velocity (Y) [ft/min]	-2407.387	2788.213

Velocity (Z) [ft/min]	-2399.155	2426.605
Temperature (Fluid) [°C]	19.92	20.06
X (cartesian) [mm]	-1142.731	1142.731
Y (cartesian) [mm]	40.000	1855.545
Z (cartesian) [mm]	-1402.725	1458.274
Phi (cylindrical) [rad]	0.070	3.072
Radius r (cylindrical) [mm]	40.087	2179.097
Z-axis (cylindrical) [mm]	-1402.725	1458.274
Phi (spherical) [rad]	0.070	3.072
Theta (spherical) [rad]	-1.538	1.539
Position Vector R (spherical) [mm]	49.257	2599.131
Mach Number []	0	0.05
Axial Velocity [ft/min]	-2399.155	2426.605
Radial Velocity [ft/min]	-2446.063	2872.025
Circumferential Velocity [ft/min]	-3140.469	3009.666

Normal Velocity [ft/min]	-3241.820	3241.820
Tangential Velocity [ft/min]	0	3241.820
Velocity RRF (X) [ft/min]	-2876.195	3010.013
Velocity RRF (Y) [ft/min]	-2407.387	2788.213
Velocity RRF (Z) [ft/min]	-2399.155	2426.605
Total Pressure [in H(2)O]	402.16	408.55
Dynamic Pressure [in H(2)O]	0	0.66
Friction Coefficient []	0	148.4053
Shear Stress [in H(2)O]	0	6.44
Reference Pressure [in H(2)O]	406.78	406.78
Relative Pressure [in H(2)O]	-4.62	1.62
Specific Heat (Cp) [J/(kg*K)]	1006.6	1006.6
Dynamic Viscosity [Pa*s]	1.8140e-005	1.8147e-005
Prandtl Number []	0.7073881	0.7073900
Fluid Thermal Conductivity [W/(m*K)]	0.0258	0.0258
Stanton Number []	0	0

Heat Transfer Coefficient [W/m ² /K]	0	0
Surface Heat Flux [W/m ²]	0	0
Wall Temperature [°C]	19.95	20.06
Turbulent Viscosity [Pa*s]	8.0460e-014	0.1103
Turbulent Time [s]	3.407e-005	110.806
Turbulence Length [m]	1.242e-006	0.076
Turbulence Intensity [%]	0.03	1000.00
Turbulent Energy [J/kg]	3.476e-009	48.898
Turbulent Dissipation [W/kg]	3.14e-011	398912.33

Engineering Database

Gases

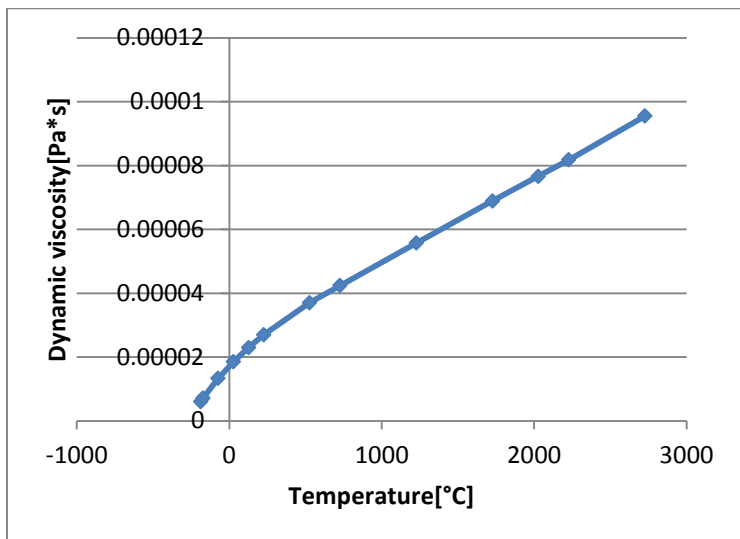
Air

Path: Gases Pre-Defined

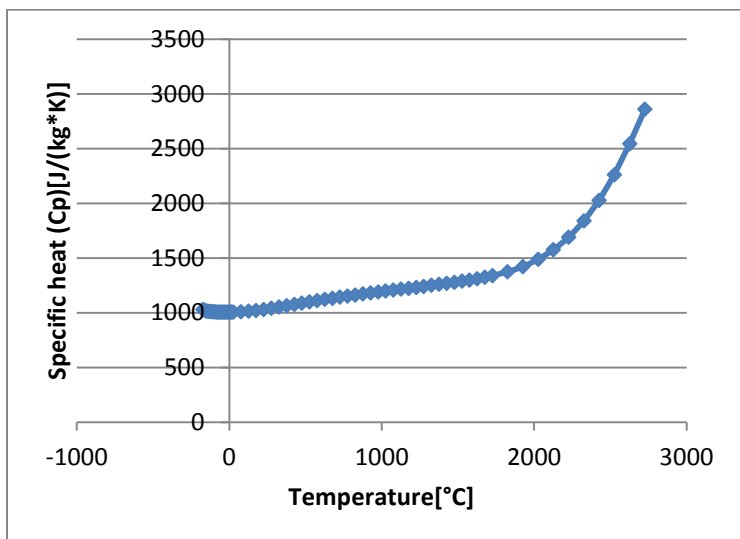
Specific heat ratio (Cp/Cv): 1.399

Molecular mass: 0.0290 kg/mol

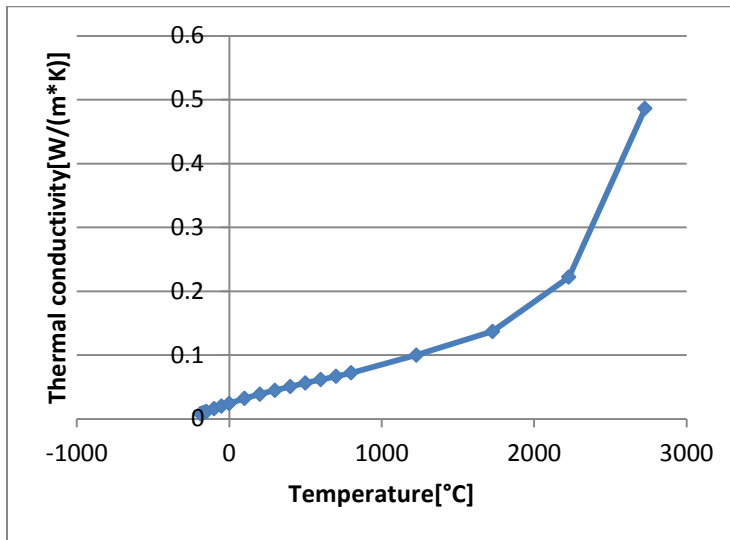
Dynamic viscosity



Specific heat (Cp)



Thermal conductivity



Fan Curves

Milti_wing_Om924

Path: Fans User Defined

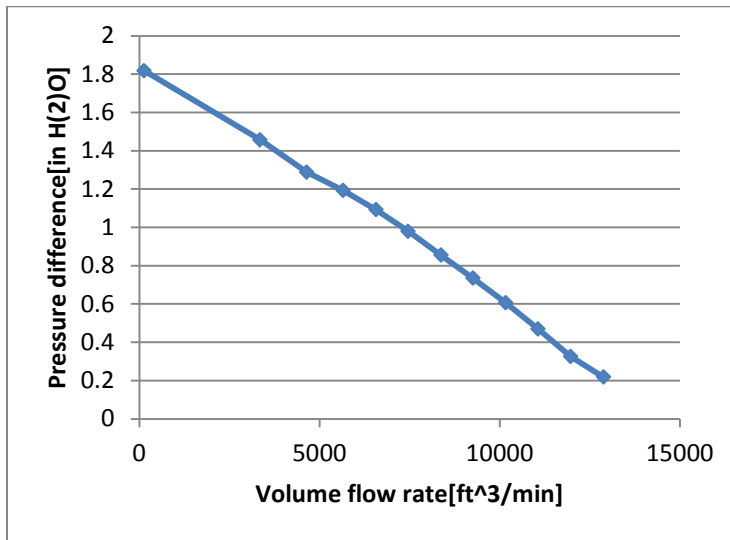
Fan Type: Axial

Set up reference density: Yes

Reference density: 1.01 kg/m³

Mass/Volume flow rate: Volume flow rate

Value



Rotor speed: 190.066 rad/s

Outer diameter: 863.092 mm

Hub diameter: 265.938 mm

Direction of rotation: Clockwise

Appendix D

OM924 Engine and Generator Assembly

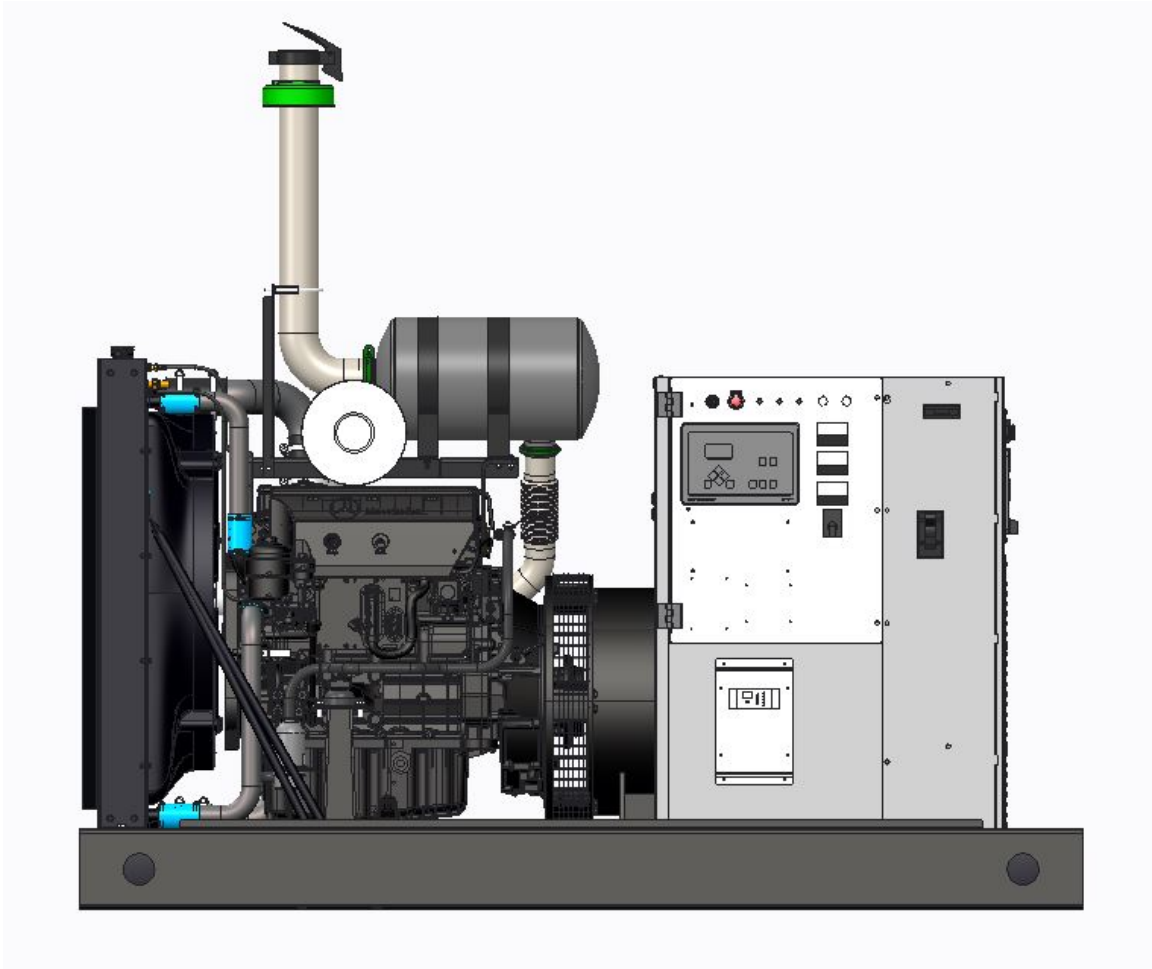


Figure 72 OM924 Engine and Generator, without the enclosure

Appendix E

Appendix E.1

CFD Model 1

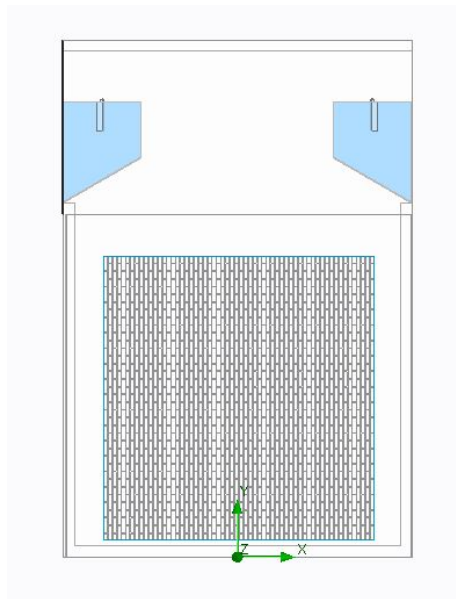


Figure 73 CFD Model 1 front view

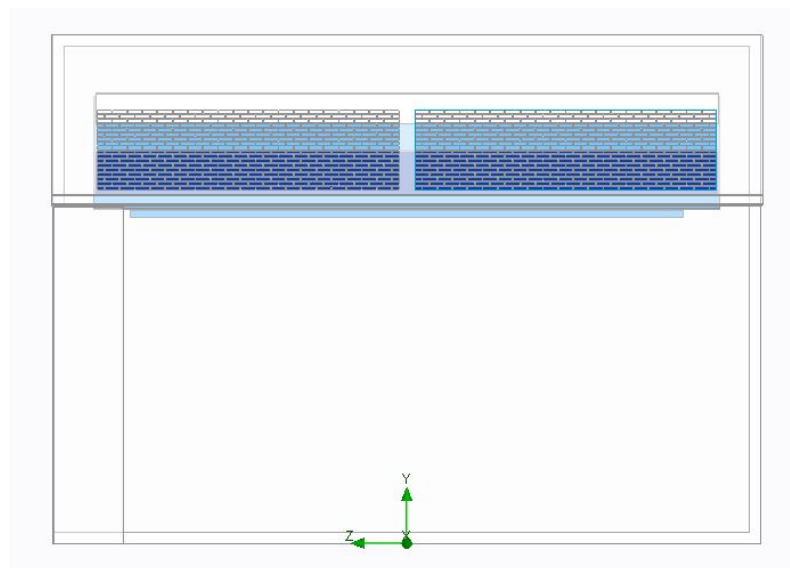


Figure 74 CFD Model 1 Side View

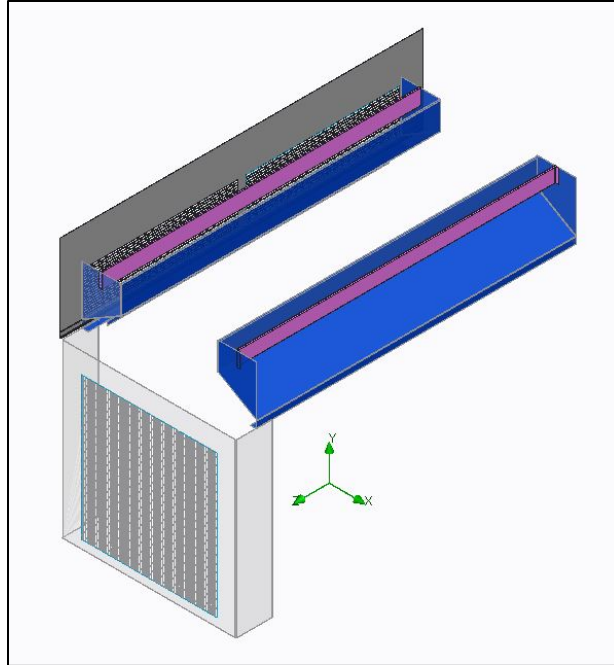


Figure 75 Baffle plates and blades helps to stop water penetration

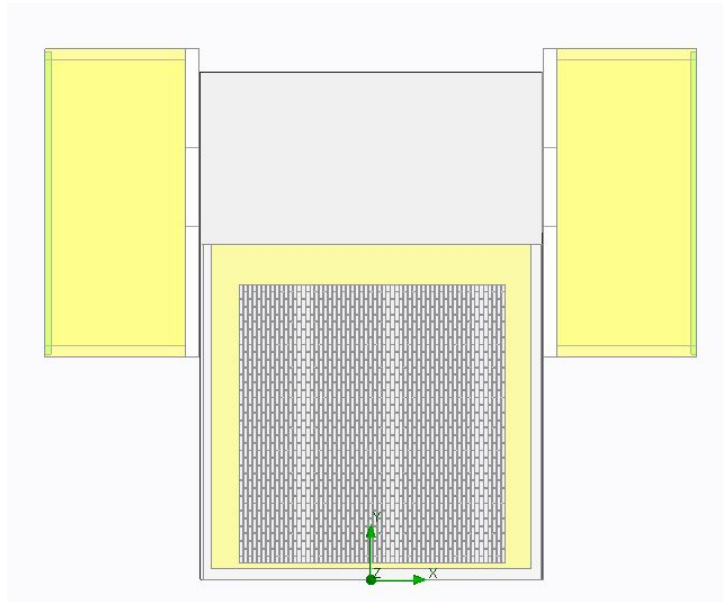


Figure 76 CFD model 1 front view

Appendix E.2

CFD Model 2

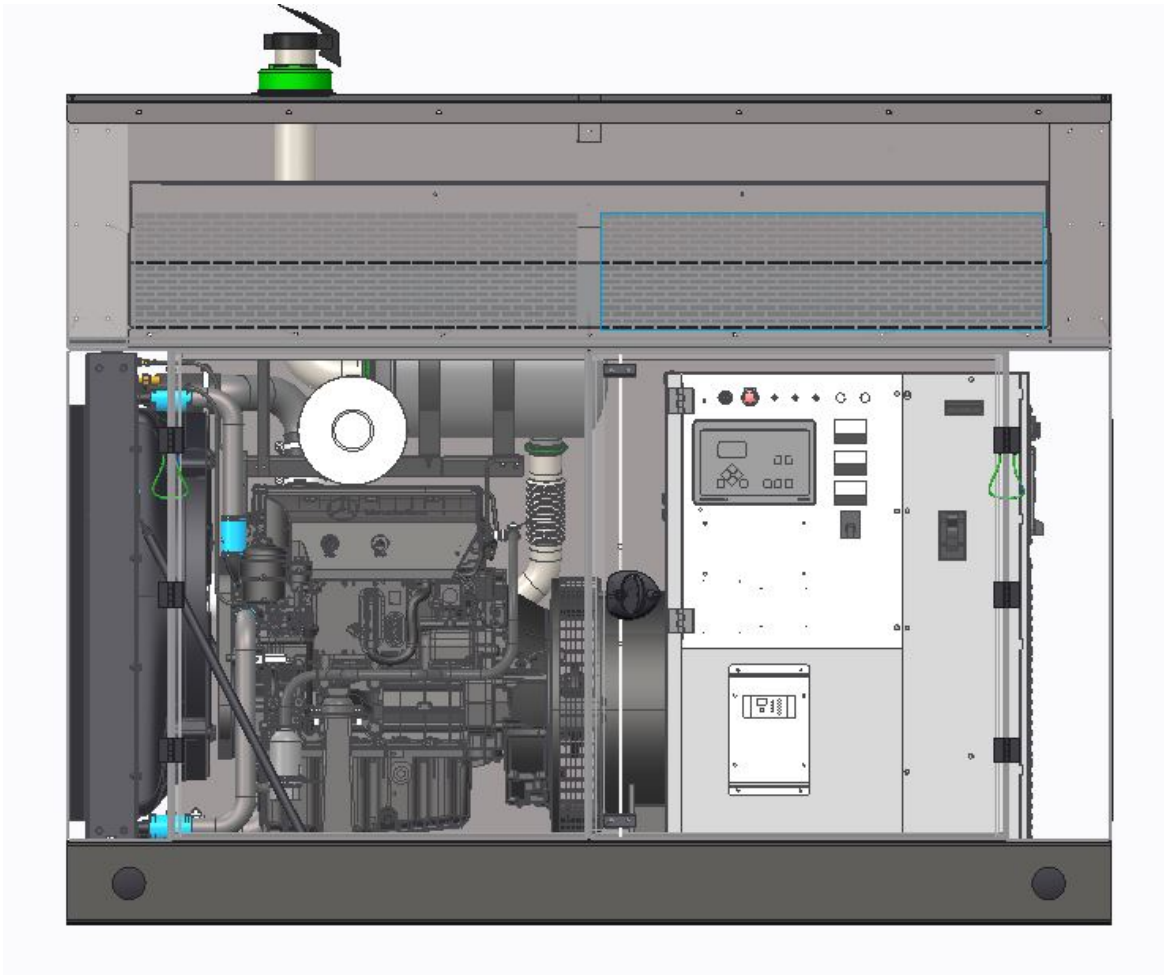


Figure 77 in the original CAD model, the fan is located inside the enclosure next to the engine

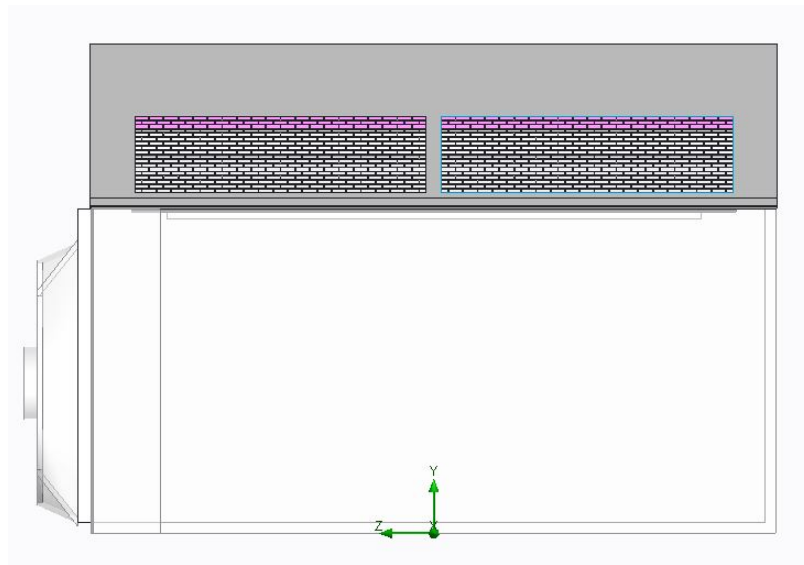


Figure 78 CFD model 2 – the fan is located outside the enclosure

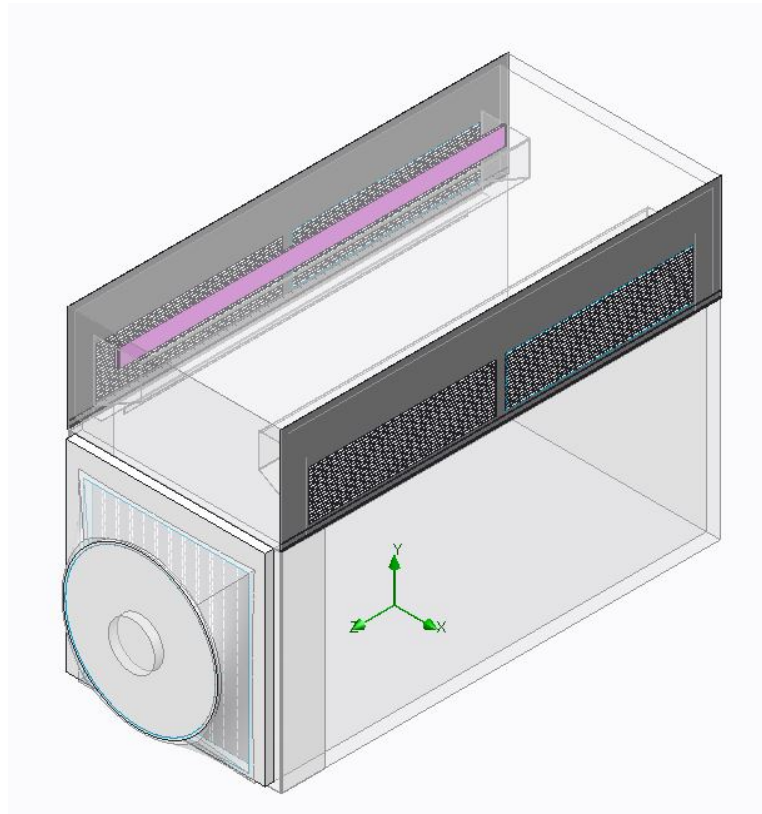


Figure 79 CFD model 2, isometric view without side air inlet covers

Appendix E.3

CFD model 3

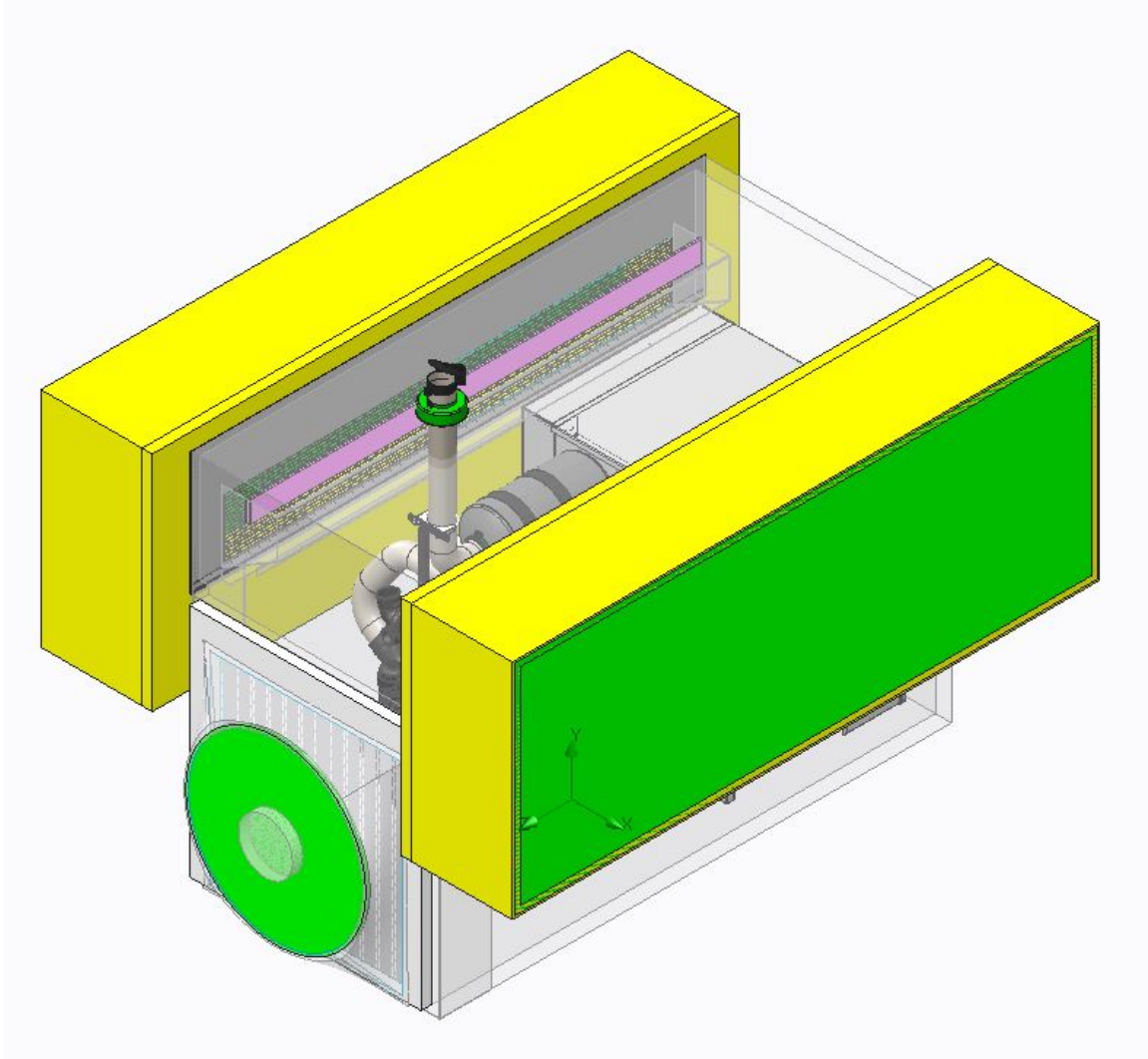


Figure 80 Complete CFD model 3 in isometric view

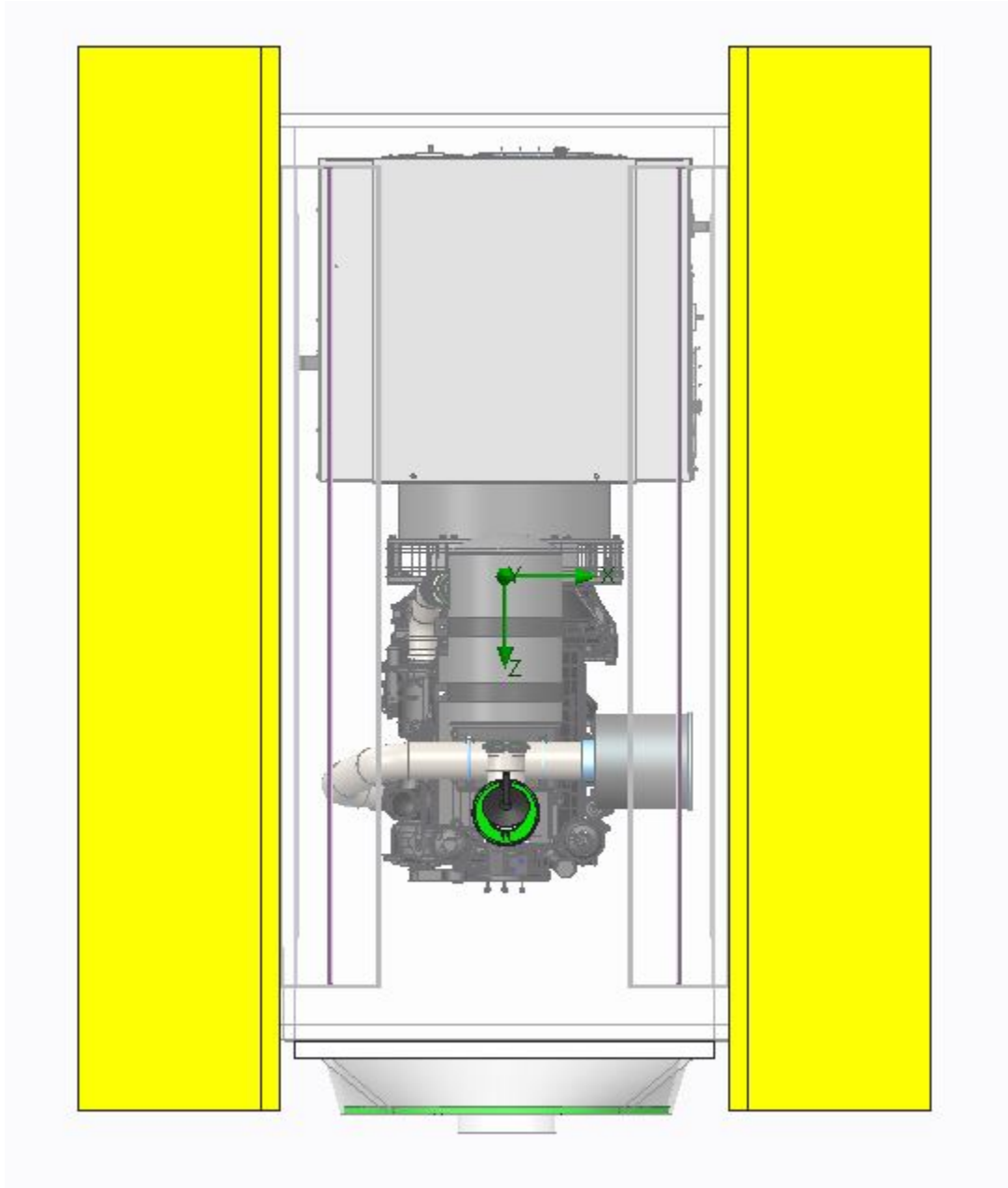


Figure 81 CFD model 3. Top view

Appendix F

OM924 Inlet Air flow data

Unit Specifications		Test Conditions	
Genset Model	OM924	Intake Temp	68.7 °F
Engine Model		Altitude	794 Feet
Cooling Package Model	50C	Wind Speed	0 MPH
Fan Model	33.98/4-8/16.5/PAG/42	Humidity	0 %
Housing Level	L2	Air Density	1.169092555 kg / m ³
Job / Prototype Number	P2135	Date	2/9/2015

Notes
50Hz Lv2 housing without scoop
-.12 inches water restriction

Intake Dimensions

Intake 1		
Width	42.25	Inches
Height	11	Inches
Rows	3	Number
Columns	3	Number

Left

Intake 2		
Width	42.25	Inches
Height	11	Inches
Rows	3	Number
Columns	3	Number

Left

Intake 3		
Width	42.24	Inches
Height	11	Inches
Rows	3	Number
Columns	3	Number

Right

Intake 4		
Width	42.25	Inches
Height	11	Inches
Rows	3	Number
Columns	3	Number

Right

Width		Inches
Height		Inches
Rows		Number
Columns		Number

Width		Inches
Height		Inches
Rows		Number
Columns		Number

Intake Diagrams

Intake 1 Left		
577	559	581
465	451	461
382	352	394

Intake 2 Left		
587	589	614
486	445	506
370	366	404

630	583	644
522	502	504
404	378	398

565	602	595
476	461	482
384	368	364

Intake Results

Intake 1		
Velocity	469.1111	Feet / Min.
Area	2.452847	Feet ²
Airflow	1150.658	CFM

Intake 2		
Velocity	485.2222	Feet / Min.
Area	2.452847	Feet ²
Airflow	1190.176	CFM

Intake 3		
Velocity	507.2222	Feet / Min.
Area	2.452267	Feet ²
Airflow	1243.844	CFM

Intake 4		
Velocity	477.4444	Feet / Min.
Area	2.452847	Feet ²
Airflow	1171.098	CFM

Intake 5		
Velocity	0	Feet / Min.
Area	0	Feet ²
Airflow	0	CFM

Intake 6		
Velocity	0	Feet / Min.
Area	0	Feet ²
Airflow	0	CFM

Intake 7		
Velocity	0	Feet / Min.
Area	0	Feet ²
Airflow	0	CFM

Intake 8		
Velocity	0	Feet / Min.
Area	0	Feet ²
Airflow	0	CFM

Intake 9		
Velocity	0	Feet / Min.
Area	0	Feet ²
Airflow	0	CFM

Intake Summary		
Total Airflow	4755.776	CFM
Corrected Airflow	4698	SCFM
Average Velocity	484.75	Feet / Min.

Exhaust Dimensions

Exhaust 1		
Width	17.4	Inches
Height	39.2	Inches
Rows	5	Number
Columns	3	Number

Exhaust 2		
Width	35.9	Inches
Height	39.2	Inches
Rows	5	Number
Columns	4	Number

Figure 82 OM924 inlet air flow data and points

OM924 Outlet Air Flow data

Exhaust Dimensions

Exhaust 1		
Width	17.4	Inches
Height	39.2	Inches
Rows	5	Number
Columns	3	Number
Description: Charge Air		

Exhaust 2		
Width	35.9	Inches
Height	39.2	Inches
Rows	5	Number
Columns	4	Number
Description: Radiator		

Exhaust Diagrams

Exhaust 1		
703	693	758
654	923	1022
860	1110	766
742	943	980
850	667	660

Exhaust 2			
721	687	646	715
612	780	845	728
0	541	827	789
528	671	679	600
545	541	624	693

Exhaust Results

Exhaust 1		
Velocity	822.0667	Feet / Min.
Area	3.606475	Feet ²
Airflow	2964.763	CFM

Exhaust 2		
Velocity	638.6	Feet / Min.
Area	7.432699	Feet ²
Airflow	4746.521	CFM

Exhaust Summary		
Total Airflow	7711	CFM
Corrected Airflow	7621	SCFM
Average Velocity	730.3333	Feet / Min.

Figure 83 OM924 outlet air flow data and points

Appendix G

Goal plot 1- Maximum Volumetric Flow Rate

OM924_RAIN_DESIGN_4.ASM [Rain Test_D4 [OM924_RAIN_DESIGN_4]]

Goal Name	Unit	Value	Averag ed Value	Minimu m Value	Maxim um Value	Progr ess [%]	Use In Converge nce	Delta	Criteri a
SG Volume	[ft^3	10302						153.5	249.2
Flow Rate	/min	.6949	10215.	10149.	10302.			72775	52823
1]	2	78212	12215	69492	100	Yes	5	1

Table 9 Goal plot 1 with stopping criteria. The average floe rate value should be used for calculations

Surface Parameter Study – at the outlet lid

Integral Parameters

Integral Parameter	Value	X- componen t	Y- componen t	Z- componen t	Surface Area [ft^2]
Volume Flow Rate [ft^3/min]	10322.011 33				6.61725558

Table 10 Surface parameter for volumetric flow rate. Outside face of the outlet lid was selected. The value is a negative number indicating the air is flowing outside that face.

Surface Parameter Study – at the right side inlet lid

Integral Parameters

Integral Parameter	Value	X- componen t	Y- componen t	Z- componen t	Surface Area [ft ²]
Volume Flow Rate [ft ³ /min]	5430.6680 83				30.96131192

Table 11 Surface parameter for volumetric flow rate. Outside face of the right-side inlet lid was selected.

Surface Parameter Study – at the left side inlet lid

Integral Parameters

Integral Parameter	Value	X- componen t	Y- componen t	Z- componen t	Surface Area [ft ²]
Volume Flow Rate [ft ³ /min]	4872.026 84				30.96131192

Table 12 Surface parameter for volumetric flow rate. Outside face of the left-side inlet lif was selected.

Appendix H

Appendix H.1

Right Velocity [Rain Test_D4 [OM924_RAIN_DESIGN_4]]

Global Coordinate System

Medium - Fluid; Iteration = 359

X [mm]	Y [mm]	Z [mm]	Velocity [ft/min]	Velocity (X) [ft/min]
663.4365916	1402.257442	1012.664557	814.6681403	-789.6958697
663.4365916	1308.065772	828.5437226	823.3021335	-741.3895617
663.4365916	1496.449113	828.5437226	945.8893045	-922.2349918
663.4365916	1402.257442	644.4228888	734.0815828	-726.7302784
663.4365916	1308.065772	460.3020549	805.2881864	-723.7518128
663.4365916	1496.449113	460.3020549	913.0444929	-889.1807792
663.4365916	1402.257442	276.181221	733.3307214	-727.0398905
663.4365916	1308.065772	92.06038713	803.139274	-736.1987725
663.4365916	1496.449113	92.06038713	875.1648786	-848.0166541
663.4365916	1402.257442	-92.06044674	711.5208446	-700.9988203
663.4365916	1308.065772	-276.1812806	815.6712724	-735.5705089
663.4365916	1496.449113	-276.1812806	909.3102136	-883.8634054
663.4365916	1402.257442	-460.3021145	728.8086873	-721.9527993
663.4365916	1308.065772	-644.4229484	816.1131987	-730.9300719
663.4365916	1496.449113	-644.4229484	929.2133561	-905.4539812

663.4365916	1402.257442	-828.5437822	752.4932633	-743.6408106
663.4365916	1308.065772	-1012.664557	869.4656082	-790.4822778
663.4365916	1496.449113	-1012.664557	983.239338	-945.343959
Average			831.3191387	-792.3597358

Table 13 Right Side Air Velocity Point Study

Appendix H.2

Left Velocity [Rain Test_D4 [OM924_RAIN_DESIGN_4]]

Global Coordinate System

Medium - Fluid; Iteration = 359

X [mm]	Y [mm]	Z [mm]	Velocity [ft/min]	Velocity (X) [ft/min]
-663.4365916	1402.257442	-1012.664557	735.7287507	711.0431381
-663.4365916	1496.449113	-828.5437226	860.9595584	839.9335628
-663.4365916	1308.065772	-828.5437226	748.9800089	675.6840873
-663.4365916	1402.257442	-644.4228888	669.7614557	662.8999986
-663.4365916	1496.449113	-460.3020549	830.8724349	809.411011
-663.4365916	1308.065772	-460.3020549	733.8700617	658.0287298
-663.4365916	1402.257442	-276.181221	666.7964975	660.8424942
-663.4365916	1496.449113	-92.06038713	794.7657022	770.3224563
-663.4365916	1308.065772	-92.06038713	725.2263354	663.7584951
-663.4365916	1402.257442	92.06044674	642.3015697	632.9199977
-663.4365916	1496.449113	276.1812806	823.1524815	802.0320399
-663.4365916	1308.065772	276.1812806	731.846524	658.1001855
-663.4365916	1402.257442	460.3021145	650.5097821	643.9876369
-663.4365916	1496.449113	644.4229484	822.53209	801.8837723
-663.4365916	1308.065772	644.4229484	719.715739	644.8851887
-663.4365916	1402.257442	828.5437822	660.1426399	651.6384322

-663.4365916	1496.449113	1012.664557	857.5886895	823.7520894
-663.4365916	1308.065772	1012.664557	756.1232893	685.5523707
Average			746.159645	710.926427

Table 14 Left Side Air Velocity Point Study

Appendix H.3

Outlet Velocity [Rain Test_D4 [OM924_RAIN_DESIGN_4]]

Global Coordinate System

Medium - Fluid; Iteration = 359

X [mm]	Y [mm]	Z [mm]	Velocity [ft/min]	Velocity (Z) [ft/min]
-337.685402	904.9871748	1197.789906	1500.945226	504.7379237
-340.0293562	218.2085064	1197.789906	1184.748006	770.242354
-330.6535393	579.1774993	1197.789906	1652.235771	1058.703625
-337.685402	750.2861778	1197.789906	1649.118587	913.1466718
-337.685402	365.8776399	1197.789906	1469.484725	895.1807713
381.9085453	900.2992658	1197.789906	1440.79313	407.5065883
-227.5195534	904.9871748	1197.789906	1650.301925	776.2589549
-126.7295217	907.3311293	1197.789906	1659.928823	883.4318776
-9.531810369	902.6432203	1197.789906	1693.805753	899.608707
112.3538094	904.9871748	1197.789906	1839.312873	864.6365745
245.9592002	902.6432203	1197.789906	2227.94188	637.3763675
-232.2074618	759.6619958	1197.789906	1662.28326	1096.096756
-239.2393245	583.8654083	1197.789906	1567.729924	1259.539731
-239.2393245	372.9095034	1197.789906	1503.738192	1035.495524
-239.2393245	222.8964154	1197.789906	1393.346112	841.0268141
-126.7295217	757.3180413	1197.789906	1585.212011	1222.349903
-124.3855674	588.5533173	1197.789906	1450.651023	1413.635286
-133.7613843	370.5655489	1197.789906	1514.559111	1137.994406

-133.7613843	225.2403699	1197.789906	1549.095588	899.1747994
-7.187856143	766.6938593	1197.789906	1598.618374	1199.445443
-7.187856143	586.2093628	1197.789906	1491.616034	1430.376636
-21.2515815	382.2853214	1197.789906	1545.0103	1197.750836
-28.28344417	232.2722334	1197.789906	1627.97802	933.7844084
110.0098551	766.6938593	1197.789906	1763.209692	1038.53903
93.60217556	588.5533173	1197.789906	1623.531607	1307.603573
100.6340382	386.9732304	1197.789906	1574.865934	1131.37205
105.3219467	229.9282789	1197.789906	1591.27887	884.6250112
248.3031545	769.0378138	1197.789906	2261.534408	829.5010121
250.6471087	583.8654083	1197.789906	1906.043886	995.320515
238.9273376	384.6292759	1197.789906	1584.582004	967.5559686
231.8954749	227.5843244	1197.789906	1436.011239	768.3915877
386.5964538	766.6938593	1197.789906	1850.906342	818.8527029
388.940408	583.8654083	1197.789906	1959.77233	936.0962805
384.2524996	384.6292759	1197.789906	1585.938029	810.3451547
388.940408	227.5843244	1197.789906	1049.696939	571.835048
Average			1618.452169	952.5011113

Outlet Data Points

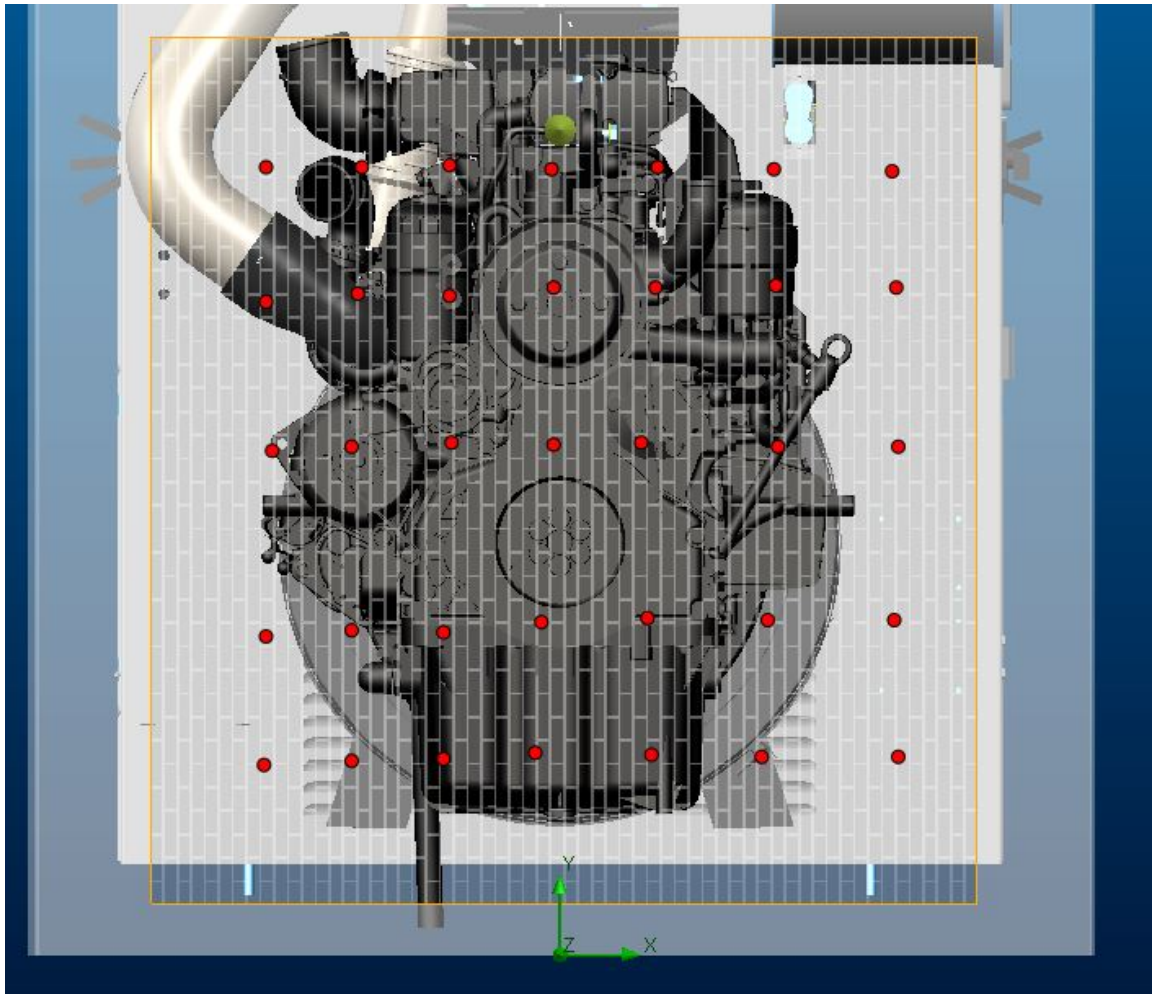


Figure 85 Outlet air velocity point study locations

Flow trajectory vs. velocity

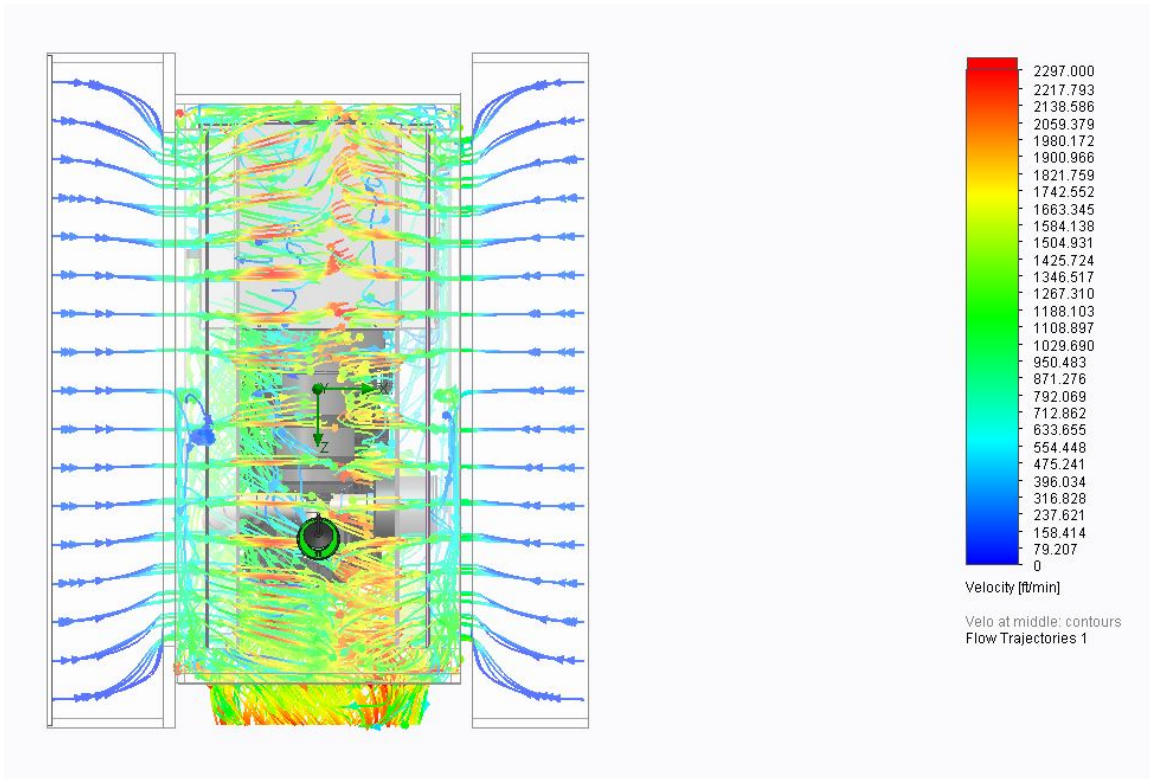


Figure 86 Flow trajectory

Appendix I

Left inlet pressure data

Pressure Left side -Outside [Rain Test_D4

[OM924_RAIN_DESIGN_4]]

Global
Coordinate
System

Medium - Fluid;
Iteration = 359

X [mm]	Y [mm]	Z [m m]	Pressure [in H(2)O]	Total Pressure [in H(2)O]	Dynamic Pressure [in H(2)O]	Reference Pressure [in H(2)O]	Relative Pressure [in H(2)O]
- 760. 081	1718. 73148 5	0	406.6990 776	406.700366 9	0.001289521	406.7823147	- 0.083237145
- 893. 556	1721. 98697 7	0	406.6985 877	406.700676 8	0.002089576	406.7823147	- 0.083727074
- 1049 .82	1725. 24247	0	406.6982 589	406.700525 5	0.0022671	406.7823147	- 0.084055891
- 747. 059	1497. 35800 2	0	406.6997 285	406.711009 9	0.01128332	406.7823147	- 0.082586286

-	1503.	0	406.7064	406.710950	0.004497288	406.7823147	-
900.	86898		544	9			0.075860379
067	7						
-	1510.	0	406.7074	406.710696	0.003280398	406.7823147	-
1049	37997		163	1			0.074898492
.82	2						
-	1373.	0	406.7060	406.717283	0.011277992	406.7823147	-0.07630719
750.	64929		076	9			
315	1						
-	1376.	0	406.7121	406.716968	0.004834257	406.7823147	-0.07017942
900.	90478		353	8			
067	4						
-	1380.	0	406.7135	406.716871	0.003276265	406.7823147	-
1066	16027		959	6			0.068718847
.097	6						
-	1207.	0	406.7194	406.725177	0.005738456	406.7823147	-
750.	61918		395	2			0.062875239
315							
-	1210.	0	406.7218	406.724884	0.00305765	406.7823147	-
906.	87467		275	8			0.060487219
578	2						
-	1217.	0	406.7221	406.724592	0.002475995	406.7823147	-
1056	38565		166	2			0.060198166

.331	7						
-	1080.	0	406.7295	406.730979	0.001441559	406.7823147	-
753.	65497		383	7			0.052776442
57	6						
-	1083.	0	406.7292	406.730925	0.001640225	406.7823147	-
909.	91046		852	3			0.053029502
834	9						
-	1087.	0	406.7291	406.730770	0.001656399	406.7823147	-
1056	16596		141	3			0.053200613
.331	1						
-	943.9	0	406.7370	406.737224	0.000190286	406.7823147	-
747.	24295		339	2			0.045280845
059	8						
-	943.9	0	406.7367	406.737560	0.000785313	406.7823147	-
913.	24295		753	5			0.045539488
089	8						
-	940.6	0	406.7366	406.73772	0.00105539	406.7823147	-0.04565006
1053	68803		647				
.075	4						
			406.7168	406.720288	0.003452055	406.7823147	-
			365				0.065478239

Table 15 Left Inlet static pressure data

Right inlet pressure data

Pressure Right side -Outside [Rain

Test_D4 [OM924_RAIN_DESIGN_4]]

Global
Coordinate
System

Medium - Fluid;
Iteration = 359

X [mm]	Y [mm]	Z [m]	Pressure [in H(2)O]	Total Pressure [in H(2)O]	Dynamic Pressure [in H(2)O]	Reference Pressure [in H(2)O]	Relative Pressure [in H(2)O]
760.081 1335	1718.73 1485	0	406.698739 2	406.7003285	0.001589628	406.7823147	-0.083575539
893.556 3083	1721.98 6977	0	406.698133 1	406.7006759	0.002543349	406.7823147	-0.084181643
1049.81 9928	1725.24 247	0	406.697735 9	406.7005289	0.002793528	406.7823147	-0.084578841
747.059 1652	1497.35 8002	0	406.697206 3	406.7110163	0.013812277	406.7823147	-0.085108485
900.067 2925	1503.86 8987	0	406.705448 2	406.7109652	0.005517976	406.7823147	-0.07686659

1049.81	1510.37		406.706672				
9928	9972	0	3	406.7107115	0.004039856	406.7823147	-0.075642453
750.314	1373.64		406.703524				
6573	9291	0	2	406.7173585	0.013836339	406.7823147	-0.078790519
900.067	1376.90		406.711049				
2925	4784	0	5	406.7169869	0.005938303	406.7823147	-0.07126527
1066.09	1380.16						
7388	0276	0	406.712854	406.7168897	0.004036311	406.7823147	-0.069460766
750.314	1207.61		406.718198				
6573	918	0	3	406.7252307	0.007033385	406.7823147	-0.06411649
906.578	1210.87		406.721144				
2766	4672	0	7	406.7248926	0.003748461	406.7823147	-0.06117009
1056.33	1217.38		406.721553				
0912	5657	0	9	406.7246005	0.003047021	406.7823147	-0.060760869
753.570	1080.65		406.729189				
1494	4976	0	7	406.7309728	0.001783241	406.7823147	-0.053125009
909.833	1083.91		406.728917				
7687	0469	0	2	406.7309302	0.002013186	406.7823147	-0.053397504
1056.33	1087.16		406.728739				
0912	5961	0	9	406.7307756	0.002035956	406.7823147	-0.053574839

747.059	943.924		406.736899				
1652	2958	0	7	406.7371294	0.000229815	406.7823147	-0.045415092
913.089	943.924		406.736595				
2607	2958	0	5	406.7375652	0.000969806	406.7823147	-0.045719209
1053.07	940.668		406.736433				
542	8034	0	8	406.7377228	0.001289071	406.7823147	-0.04588092
406.716057							
5 406.7202934 0.004236528 406.7823147 -0.066257229							

Table 16 Right Inlet static pressure data

Middle front, pressure data (Z=0)

Pressure Middle -Inside [Rain

Test_D4 [OM924_RAIN_DESIGN_4]]

Global
Coordinate
System

Medium - Fluid;
Iteration = 359

X [mm]	Y [mm]	Z [m]	Pressure [in H(2)O]	Total Pressure [in H(2)O]	Dynamic Pressure [in H(2)O]	Reference Pressure [in H(2)O]	Relative Pressure [in H(2)O]
485.589	1673.7	0	406.53928	406.610134	0.070858628	406.7823147	-0.243030299
7175	65154	0	44	406.610134	0.070858628	406.7823147	-0.243030299
298.398	1673.7	0	406.27061	406.3764632	0.105854426	406.7823147	-0.511702134
9204	65154	0	26	406.3764632	0.105854426	406.7823147	-0.511702134
131.554	1673.7	0	406.28145	406.3710115	0.089567297	406.7823147	-0.50086397
949	65154	0	08	406.3710115	0.089567297	406.7823147	-0.50086397

116.676	1669.6		406.33263				
3254	95789	0	32	406.4777567	0.145131535	406.7823147	-0.449681512
283.520	1673.7		406.18950				
2968	65154	0	82	406.3168479	0.127343376	406.7823147	-0.592806534
470.711	1673.7		406.50817				
0939	65154	0	71	406.56781	0.059640754	406.7823147	-0.27413767
-							
481.520	1490.6		406.61479				
3524	437	0	22	406.6343778	0.019588542	406.7823147	-0.167522495
-							
294.329	1494.7		406.23419				
5552	13066	0	63	406.2371892	0.002993392	406.7823147	-0.548118458
-							
123.416	1494.7		406.26913				
2187	13066	0	81	406.2773552	0.008218099	406.7823147	-0.513176633
116.676	1490.6		406.19394				
3254	437	0	35	406.3786154	0.184668459	406.7823147	-0.588371246
295.728	1494.7		406.15159				
3923	13066	0	6	406.1776191	0.026026427	406.7823147	-0.630718739
478.849	1486.5	0	406.58581	406.6177146	0.031908719	406.7823147	-0.196504393

8243	74334		04				
-							
485.589	1307.5		406.26438				
7175	22246	0	4	406.2795068	0.015124674	406.7823147	-0.517930713
-							
298.398	1323.7		406.23666				
9204	99709	0	08	406.305238	0.068582461	406.7823147	-0.545653913
-							
119.346	1323.7		406.25537				
8536	99709	0	38	406.2819161	0.026544707	406.7823147	-0.526940976
124.815	1323.7		406.20934				
0558	99709	0	24	406.4434617	0.234102666	406.7823147	-0.572972384
295.728	1331.9		406.20659				
3923	3844	0	39	406.2133951	0.006802061	406.7823147	-0.575720867
478.849	1336.0		406.62020				
8243	07806	0	01	406.6374125	0.017214812	406.7823147	-0.16211467
-							
481.520	1104.0		406.23484				
3524	53964	0	42	406.3108344	0.075993526	406.7823147	-0.547470562
-	1108.1	0	406.19439	406.283813	0.089421485	406.7823147	-0.587921388

294.329	23329		34				
5552							
-							
115.277	1116.2		406.17405				
4884	62061	0	7	406.2177359	0.043680825	406.7823147	-0.608257721
116.676	1120.3		406.19552				
3254	31426	0	49	406.4970915	0.301520625	406.7823147	-0.586789874
295.728	1128.4		406.22339				
3923	70158	0	58	406.2576587	0.034263991	406.7823147	-0.558918968
486.988	1132.5		406.22509				
5546	39523	0	72	406.243071	0.017975659	406.7823147	-0.557217587
-							
481.520	916.86		406.20132				
3524	31439	0	3	406.3113595	0.110034977	406.7823147	-0.58099178
-							
302.468	925.00		406.15860				
2855	18752	0	37	406.2694179	0.110811428	406.7823147	-0.623711023
-							
115.277	925.00		406.11338				
4884	18752	0	84	406.1577683	0.04438065	406.7823147	-0.66892638

116.676	937.20		406.17456				
3254	99721	0	64	406.4669595	0.292341598	406.7823147	-0.607748317
291.659	929.07		406.23909				
0271	12408	0	56	406.3121993	0.073101403	406.7823147	-0.543219119
491.057	937.20		406.24329				
9197	99721	0	44	406.2487155	0.00542159	406.7823147	-0.539020393
-							
477.450	717.46		406.19548				
9872	42272	0	7	406.3139362	0.11844284	406.7823147	-0.586827789
-							
302.468	729.67		406.14650				
2855	23241	0	12	406.2417087	0.095203877	406.7823147	-0.635813524
-							
99.0000	733.74		406.10934				
2778	16898	0	15	406.166728	0.05738567	406.7823147	-0.672973249
120.745	745.94		406.19871				
6906	97867	0	04	406.4420015	0.243251872	406.7823147	-0.58360434
291.659	741.88		406.26556				
0271	04211	0	54	406.3121951	0.046628279	406.7823147	-0.516749391
470.711	750.01	0	406.27235	406.2746859	0.00233414	406.7823147	-0.509962916

0939	91524		18				
-							
481.520	554.68		406.24595				
3524	96013	0	52	406.3330014	0.087041657	406.7823147	-0.536359514
-							
314.676	570.96		406.18963				
381	70639	0	28	406.267377	0.077740576	406.7823147	-0.592681911
-							
94.9306	570.96						
6262	70639	0	406.16649	406.2618044	0.095308351	406.7823147	-0.615824762
132.953	570.96		406.26763				
7861	70639	0	32	406.3778518	0.110207701	406.7823147	-0.514681551
303.867	591.31		406.28727				
1226	38921	0	25	406.3034377	0.016165148	406.7823147	-0.495042216
474.780	579.10		406.29943				
4591	57952	0	09	406.3071438	0.007713209	406.7823147	-0.48288388
-							
485.589	371.56		406.31416				
7175	81472	0	36	406.3469416	0.032777369	406.7823147	-0.468151164
-	371.56	0	406.29477	406.3450219	0.05024182	406.7823147	-0.487537318

318.745	81472		74				
7462							
-							
111.208	383.77		406.28449				
1232	62441	0	3	406.3565859	0.07208721	406.7823147	-0.497821759
116.676	371.56		406.30973				
3254	81472	0	72	406.3317664	0.02202872	406.7823147	-0.472577538
316.075	371.56		406.32379				
218	81472	0	87	406.3377371	0.013938364	406.7823147	-0.458516028
486.988	371.56		406.33725				
5546	81472	0	37	406.345339	0.0080854	406.7823147	-0.445061026
-							
477.450	176.23		406.34591				
9872	85961	0	68	406.3624766	0.016559601	406.7823147	-0.436397938
-							
330.953	184.37		406.33370				
8416	73274	0	08	406.3486541	0.014953142	406.7823147	-0.448613991
-							
131.554	188.44		406.32278				
949	6693	0	05	406.3473859	0.024604692	406.7823147	-0.459534199

116.676	196.58		406.33108				
3254	54243	0	7	406.3520513	0.020963747	406.7823147	-0.451227738
312.005	196.58		406.34489				
8529	54243	0	22	406.3597247	0.014832298	406.7823147	-0.437422573
491.057	192.51		406.35062				
9197	60587	0	3	406.385658	0.035034264	406.7823147	-0.431691791
			406.27553				
			48	406.3444752	0.06893794	406.7823147	-0.506779978

Table 17 Middle front, static pressure data

Middle – Side, pressure data (x = 0)

prESSURE IN MIDDLE [Rain Test_D4
[OM924_RAIN_DESIGN_4]]

Global
Coordinate
System

Medium - Fluid;
Iteration = 359

X [mm]	Y [mm]	Z [mm]	Pressure [in H(2)O]	Total Pressure [in H(2)O]	Dynamic Pressure [in H(2)O]	Reference Pressure [in H(2)O]	Relative Pressure [in H(2)O]
-		-					
0.063	1054.5	1074.5	406.15452				
4362	20011	59569	48	406.2274113	0.072888136	406.7823147	-0.627789971
-		-					
0.063	757.48	1074.5	406.22055				
4362	00253	59569	88	406.3222664	0.101704521	406.7823147	-0.561755952
-		-					
0.063	460.44	1074.5	406.33861				
4362	00098	59569	91	406.402876	0.064254094	406.7823147	-0.443695662
-		-					
0.063	163.39	1074.5	406.34506				
4362	99944	59569	24	406.3979754	0.052910585	406.7823147	-0.437252333

-	-	-	-	-	-	-	-
0.063	1351.5	1074.5	406.20184				
4362	59997	59569	2	406.2843598	0.082520727	406.7823147	-0.580472697
-	-	-	-	-	-	-	-
0.063	1648.5	1074.5	406.30452				
4362	99982	59569	9	406.3942704	0.089748676	406.7823147	-0.477785717
-	-	-	-	-	-	-	-
0.063	1054.5	778.17	406.16746				
4362	20011	88111	4	406.1898697	0.022407439	406.7823147	-0.614850763
-	-	-	-	-	-	-	-
0.063	757.48	778.17	406.20104				
4362	00253	88111	11	406.2153346	0.014294239	406.7823147	-0.581273667
-	-	-	-	-	-	-	-
0.063	460.44	778.17	406.28948				
4362	00098	88111	01	406.3514183	0.061936257	406.7823147	-0.492834644
-	-	-	-	-	-	-	-
0.063	163.39	778.17	406.33623				
4362	99944	88111	66	406.3884675	0.052227989	406.7823147	-0.446078095
-	-	-	-	-	-	-	-
0.063	1351.5	778.17	406.25381				
4362	59997	88111	88	406.2935973	0.039781474	406.7823147	-0.528495951

-	-	-	-	-	-	-	-	-
0.063	1648.5	778.17	406.33597					
4362	99982	88111		03	406.4755203	0.139555761	406.7823147	-0.44634443
-	-	-	-	-	-	-	-	-
0.063	1054.5	481.79	406.16167					
4362	20011	80826		34	406.2387417	0.077070846	406.7823147	-0.620641296
-	-	-	-	-	-	-	-	-
0.063	757.48	481.79	406.19519					
4362	00253	80826		37	406.2210634	0.025870637	406.7823147	-0.587121065
-	-	-	-	-	-	-	-	-
0.063	460.44	481.79						
4362	00098	80826	406.27525		406.2930727	0.017822739	406.7823147	-0.507064747
-	-	-	-	-	-	-	-	-
0.063	163.39	481.79	406.34919					
4362	99944	80826		07	406.3884469	0.039254449	406.7823147	-0.433124014
-	-	-	-	-	-	-	-	-
0.063	1351.5	481.79	406.23679					
4362	59997	80826		82	406.3133264	0.076531923	406.7823147	-0.545516567
-	-	-	-	-	-	-	-	-
0.063	1648.5	481.79	406.36387					
4362	99982	80826		29	406.5245167	0.160649599	406.7823147	-0.418441807

-	0.063	1054.5	185.41	406.15975				
4362	20011	73541		24	406.2379612	0.078210238	406.7823147	-0.622562337
-	0.063	757.48	185.41	406.16008				
4362	00253	73541		69	406.2329704	0.072882531	406.7823147	-0.622227831
-	0.063	460.44	185.41	406.27478				
4362	00098	73541		39	406.3535861	0.078797028	406.7823147	-0.507530838
-	0.063	163.39	185.41	406.31869				
4362	99944	73541		98	406.3377316	0.019031255	406.7823147	-0.463614959
-	0.063	1351.5	185.41	406.24574				
4362	59997	73541		74	406.3497773	0.104030042	406.7823147	-0.536567325
-	0.063	1648.5	185.41	406.39847				
4362	99982	73541		07	406.5446203	0.14615541	406.7823147	-0.383844006
-	0.063	1054.5	110.96	406.15599				
4362	20011	33744		58	406.2413621	0.08536587	406.7823147	-0.626318955

-								
0.063	757.48	110.96	406.11595					
4362	00253	33744	95	406.1881682	0.072206754	406.7823147	-0.666355287	
-								
0.063	460.44	110.96	406.24931					
4362	00098	33744	12	406.3792763	0.129950731	406.7823147	-0.533003594	
-								
0.063	163.39	110.96	406.33332					
4362	99944	33744	31	406.3645493	0.031225023	406.7823147	-0.448991642	
-								
0.063	1351.5	110.96	406.24162					
4362	59997	33744	12	406.3348096	0.09318873	406.7823147	-0.540693562	
-								
0.063	1648.5	110.96	406.38560					
4362	99982	33744	45	406.557039	0.171439182	406.7823147	-0.39671027	
-								
0.063	1054.5	407.34	406.19287					
4362	20011	41029	55	406.2637306	0.070857196	406.7823147	-0.589439226	
-								
0.063	757.48	407.34	406.13239					
4362	00253	41029	4	406.171181	0.038787824	406.7823147	-0.649920723	

-								
0.063	460.44	407.34	406.20470					
4362	00098	41029	55	406.2804903	0.075781754	406.7823147	-0.577609289	
-								
0.063	163.39	407.34	406.32130					
4362	99944	41029	79	406.3821197	0.060807785	406.7823147	-0.461006816	
-								
0.063	1351.5	407.34	406.27903					
4362	59997	41029	45	406.3220128	0.042981292	406.7823147	-0.50328026	
-								
0.063	1648.5	407.34	406.37915					
4362	99982	41029	63	406.5272596	0.148110315	406.7823147	-0.403158437	
-								
0.063	1054.5	703.72	406.20341					
4362	20011	48611	14	406.2857104	0.082301216	406.7823147	-0.578903355	
-								
0.063	757.48	703.72	406.12219					
4362	00253	48611	1	406.199539	0.077347424	406.7823147	-0.660123705	
-								
0.063	460.44	703.72	406.15778					
4362	00098	48611	18	406.2267746	0.068990787	406.7823147	-0.624532992	

-								
0.063	163.39	703.72	406.29509					
4362	99944	48611	74	406.387736	0.092629581	406.7823147	-0.487217318	
-								
0.063	1351.5	703.72	406.26603					
4362	59997	48611	19	406.295916	0.029887026	406.7823147	-0.516282825	
-								
0.063	1648.5	703.72	406.34038					
4362	99982	48611	1	406.4872789	0.146904685	406.7823147	-0.441933711	
-								
0.063	1054.5	1000.1	406.21002					
4362	20011	05619	52	406.3003044	0.090279713	406.7823147	-0.572289518	
-								
0.063	757.48	1000.1	406.06899					
4362	00253	05619	15	406.1927742	0.123776521	406.7823147	-0.713323218	
-								
0.063	460.44	1000.1	406.11162					
4362	00098	05619	94	406.2207549	0.109118111	406.7823147	-0.670685298	
-								
0.063	163.39	1000.1	406.26901					
4362	99944	05619	02	406.3869753	0.117951625	406.7823147	-0.513304591	

-	0.063	1351.5	1000.1	406.26945				
	4362	59997	05619	01	406.3075341	0.03808719	406.7823147	-0.512864627
-	0.063	1648.5	1000.1	406.30618				
	4362	99982	05619	14	406.4108327	0.104658918	406.7823147	-0.476133313
-	0.063	1054.5	1296.4	405.88500				
	4362	20011	86378	89	405.8874503	0.002441304	406.7823147	-0.897305841
-	0.063	757.48	1296.4	405.85353				
	4362	00849	86378	64	406.0010917	0.147546984	406.7823147	-0.928778343
-	0.063	460.44	1296.4	405.90454				
	4362	00098	86378	81	406.0414402	0.136880334	406.7823147	-0.877766689
-	0.063	163.39	1296.4	406.13539				
	4362	99944	86378	29	406.2400209	0.104619132	406.7823147	-0.646921798

406.22458

89 406.3050637 0.080474223 406.7823147 -0.557725805

Table 18 Middle side, static pressure data

Appendix J

Particle study for the free flowing water droplets

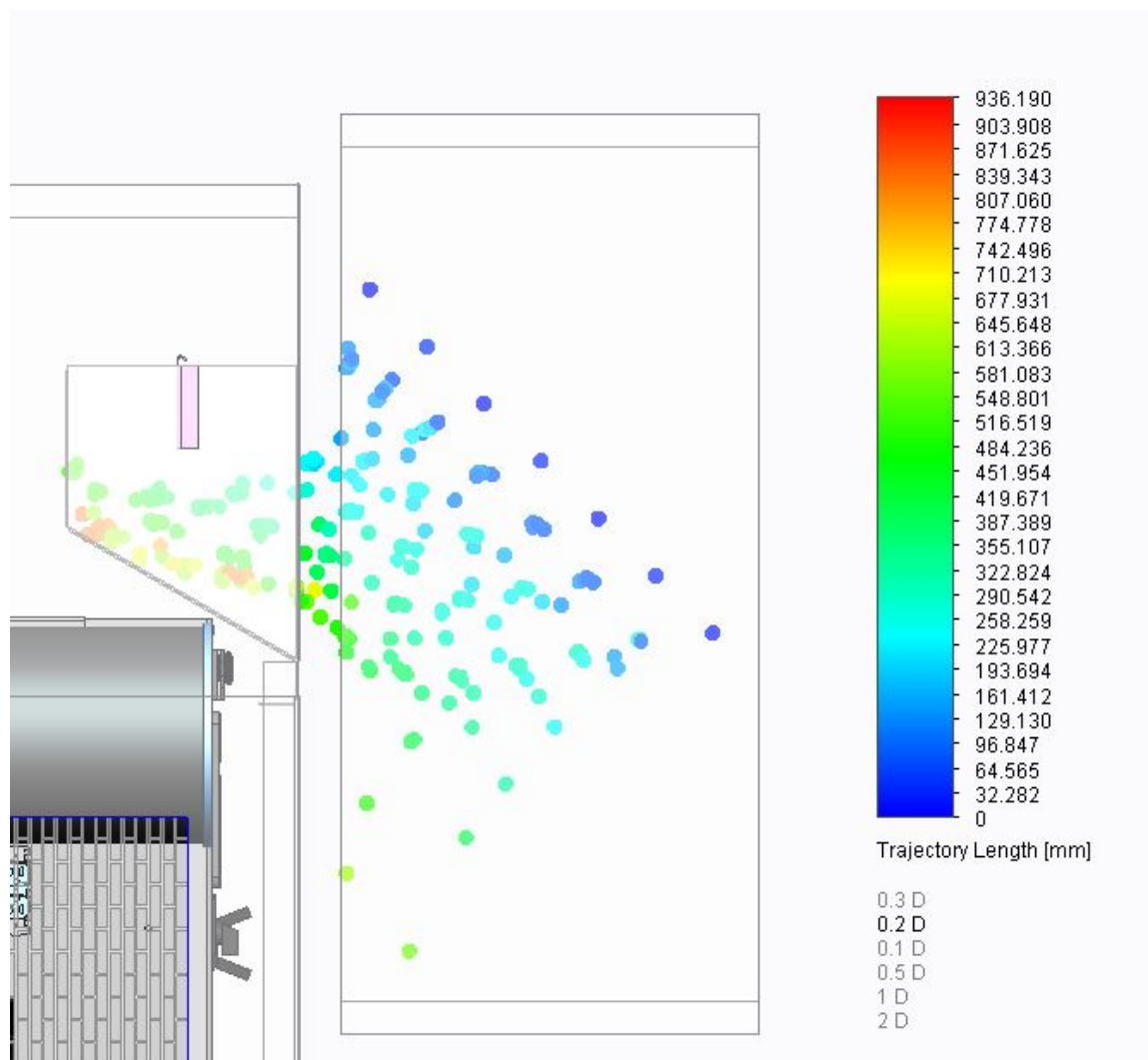


Figure 87 Droplet size 0.2 mm. No penetration

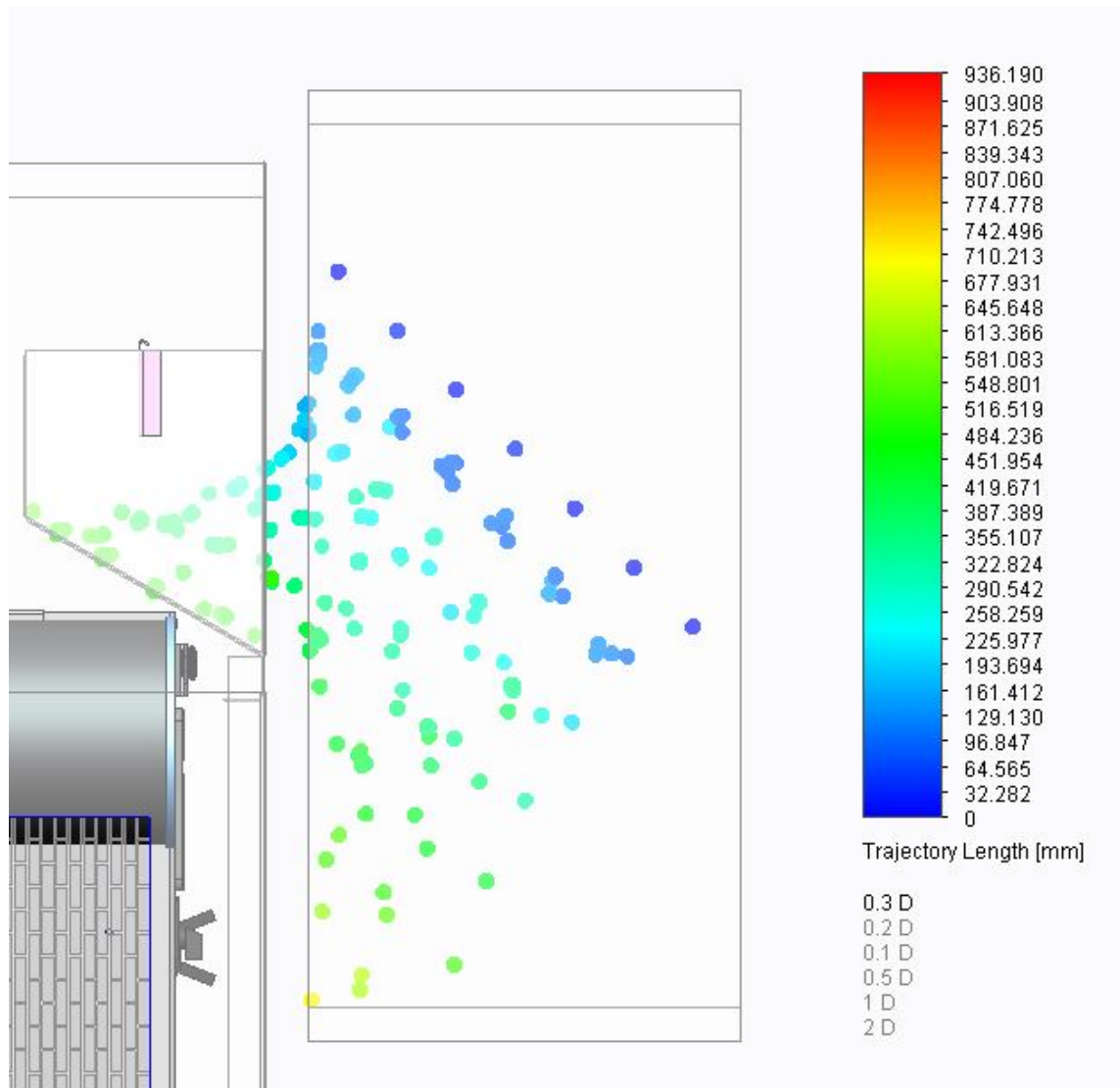


Figure 88 Droplet size 0.3 mm. No penetration

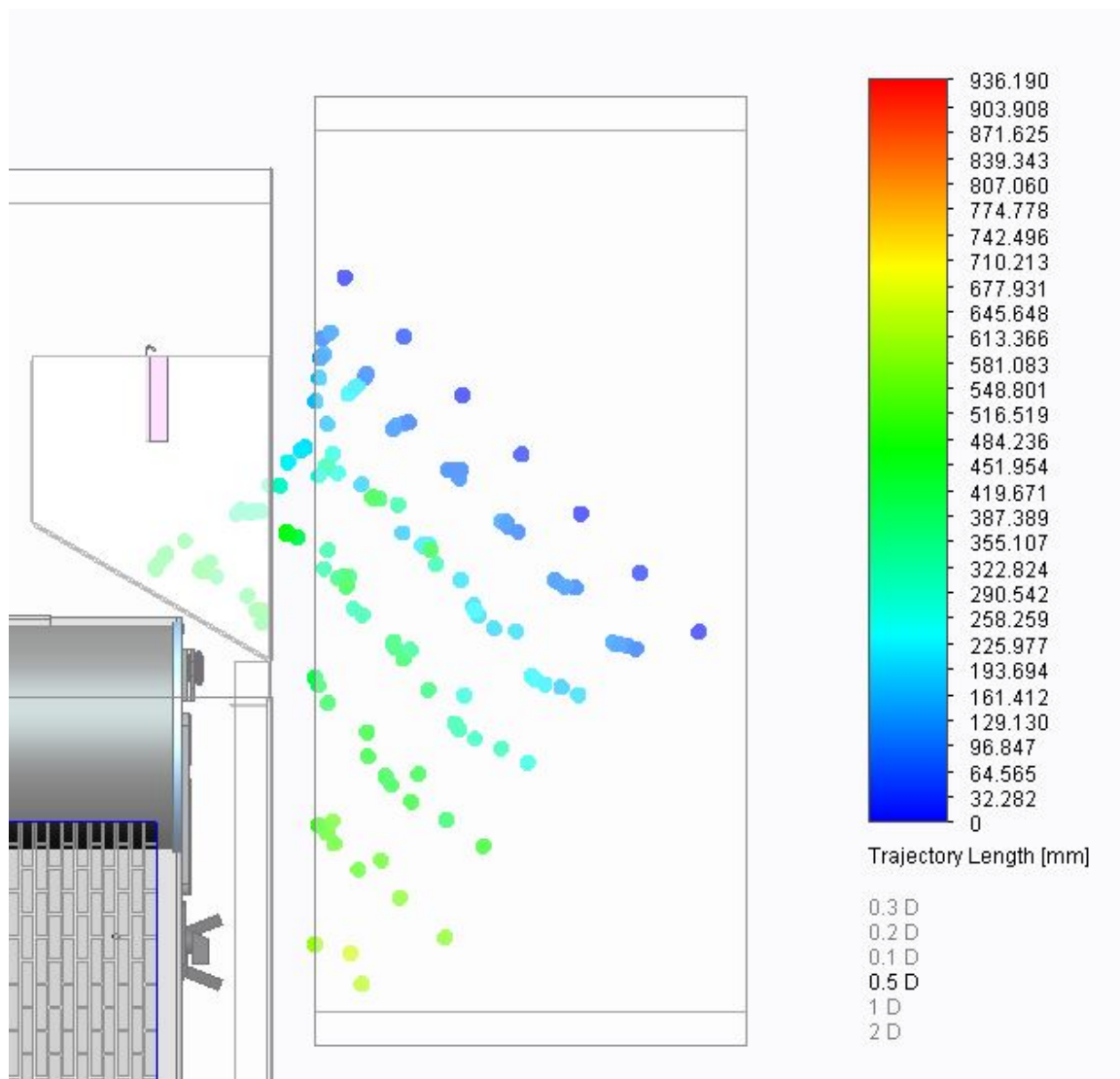


Figure 89 Droplet size 0.5 mm. No penetration

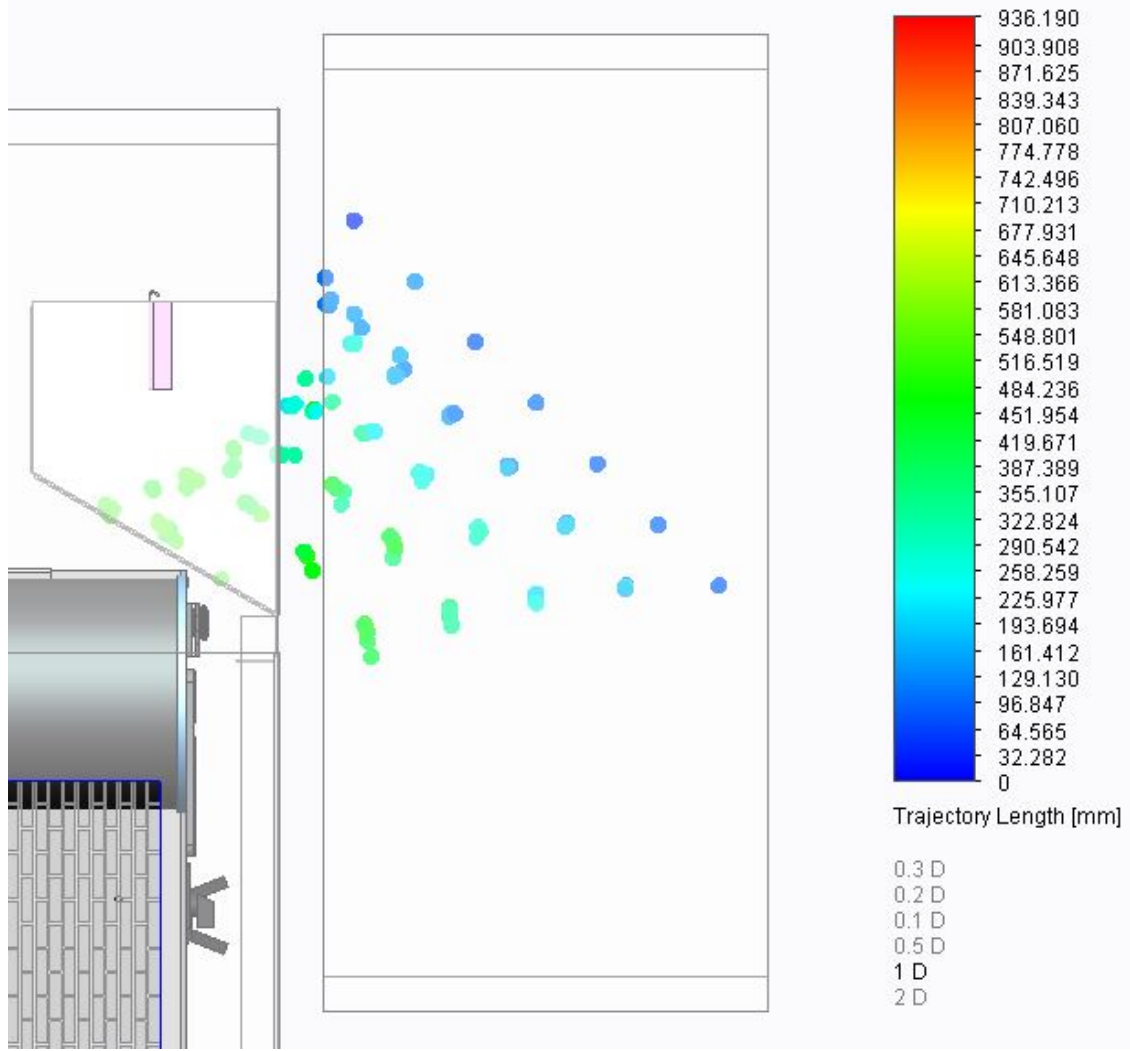


Figure 90 Droplet size 1 mm. No penetration

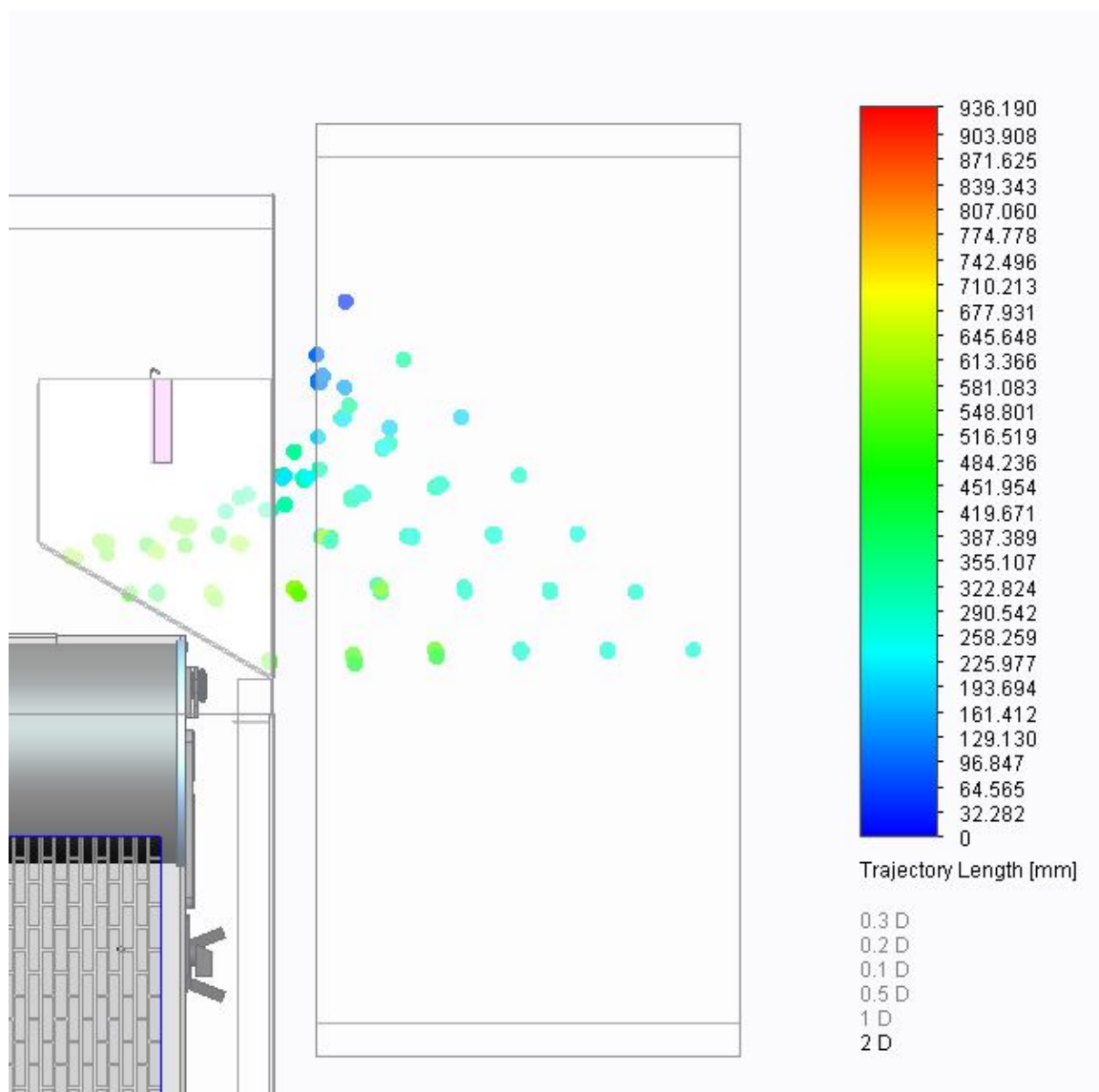


Figure 91 Droplet size 2mm. No penetration

Appendix K

Particle study of water droplets dripping at the inlet grill

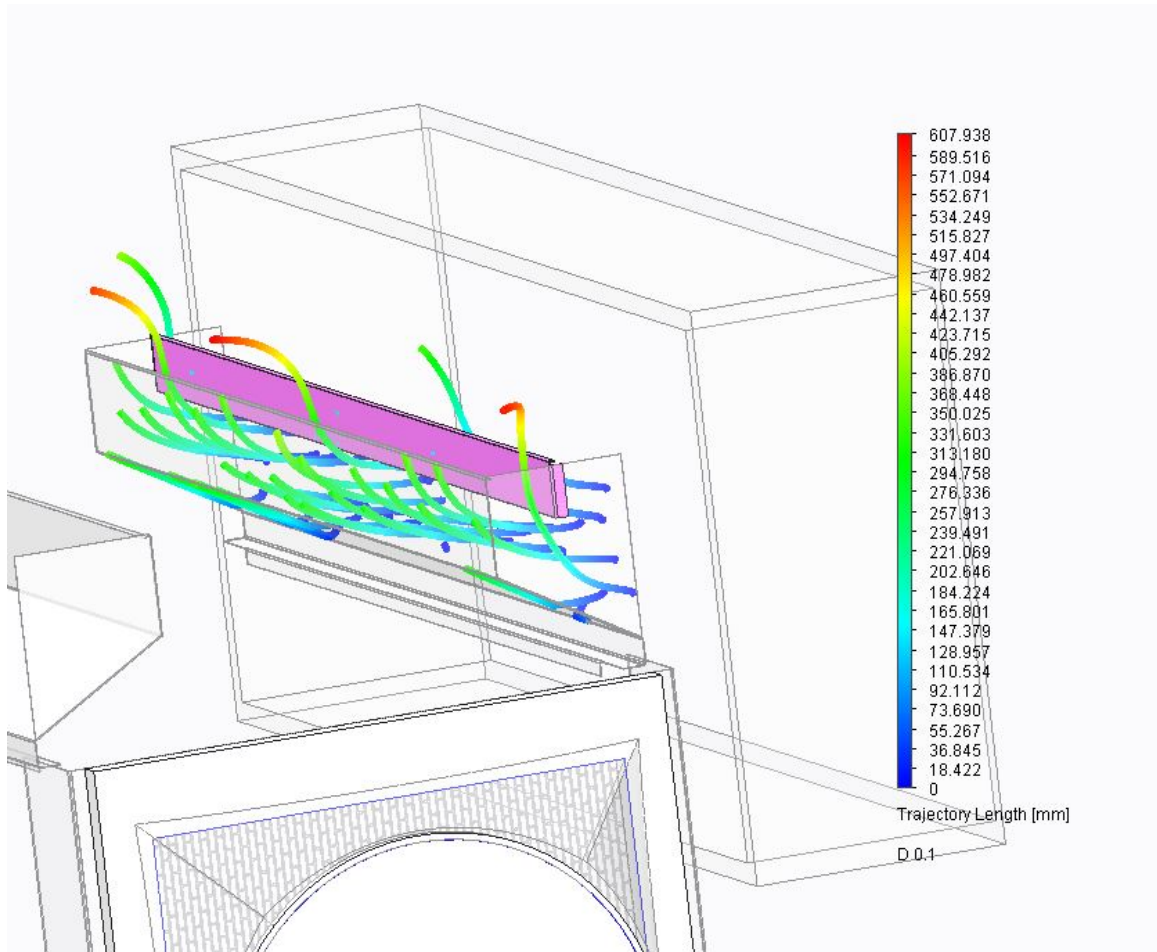


Figure 92 Droplet size 0.1 mm. The penetrating trajectory can be tracked using lines

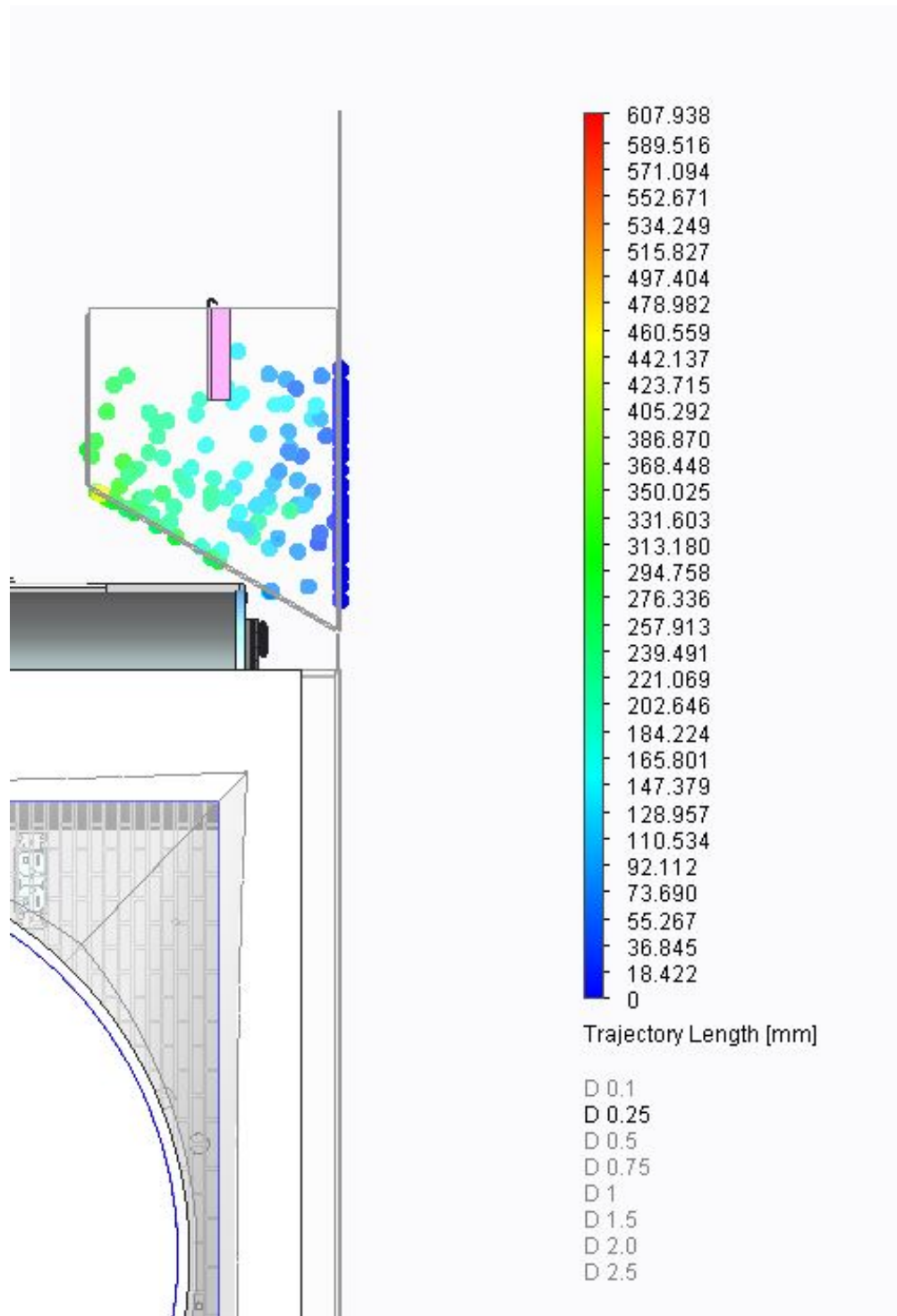


Figure 93 Droplet size 0.25 mm. No penetration

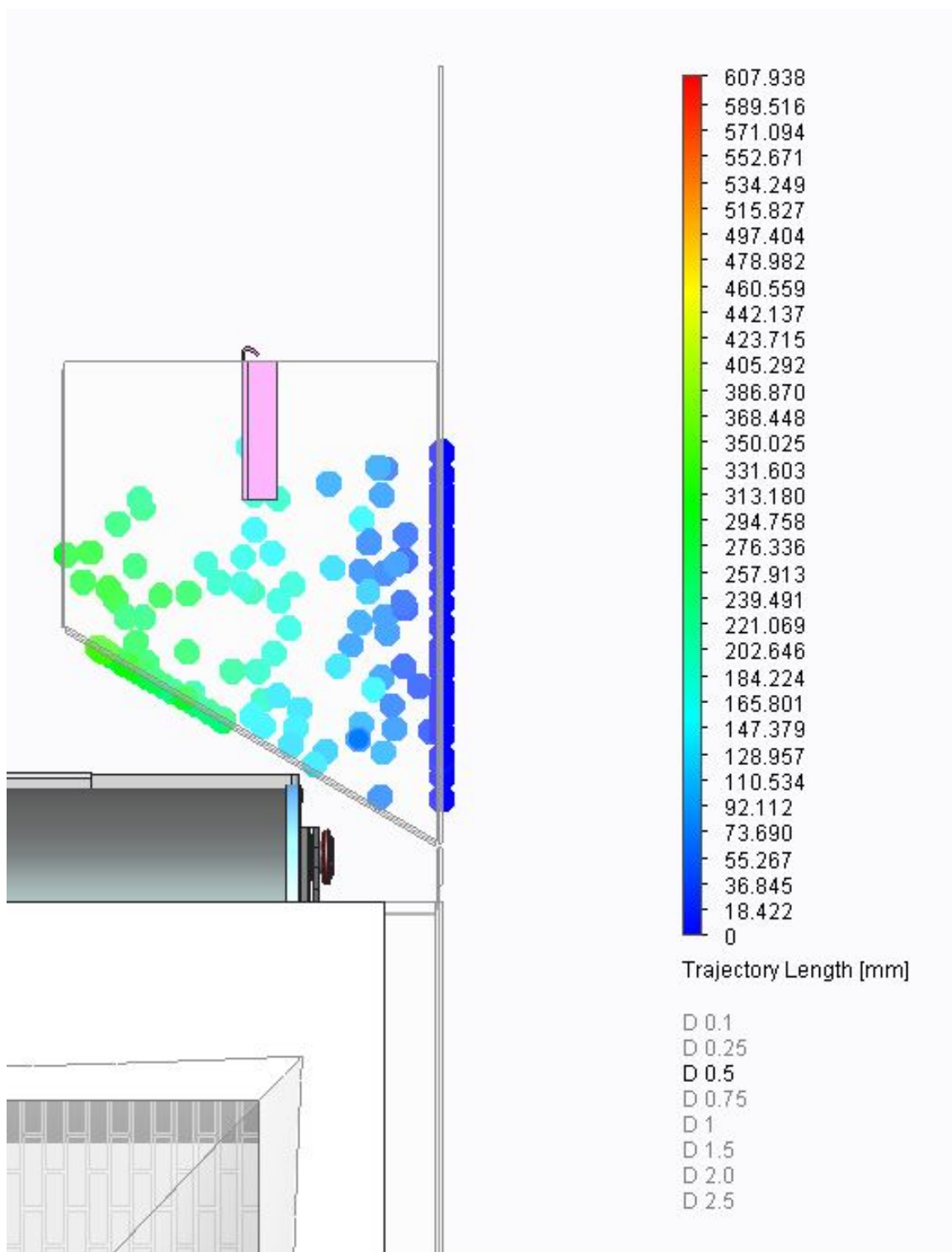


Figure 94 Droplet size 0.5 mm. No penetration

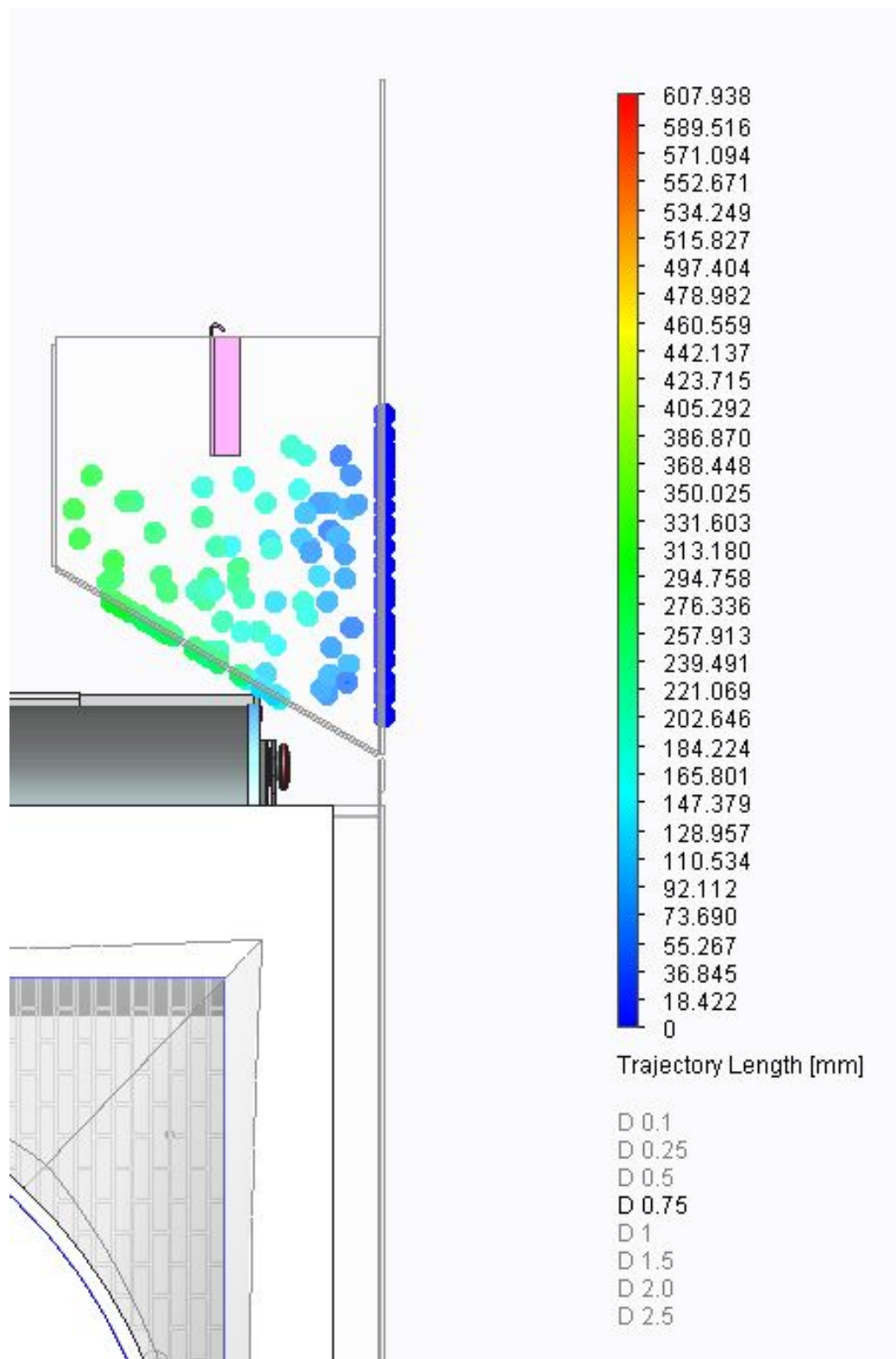


Figure 95 Droplet size 0.75 mm. No penetration

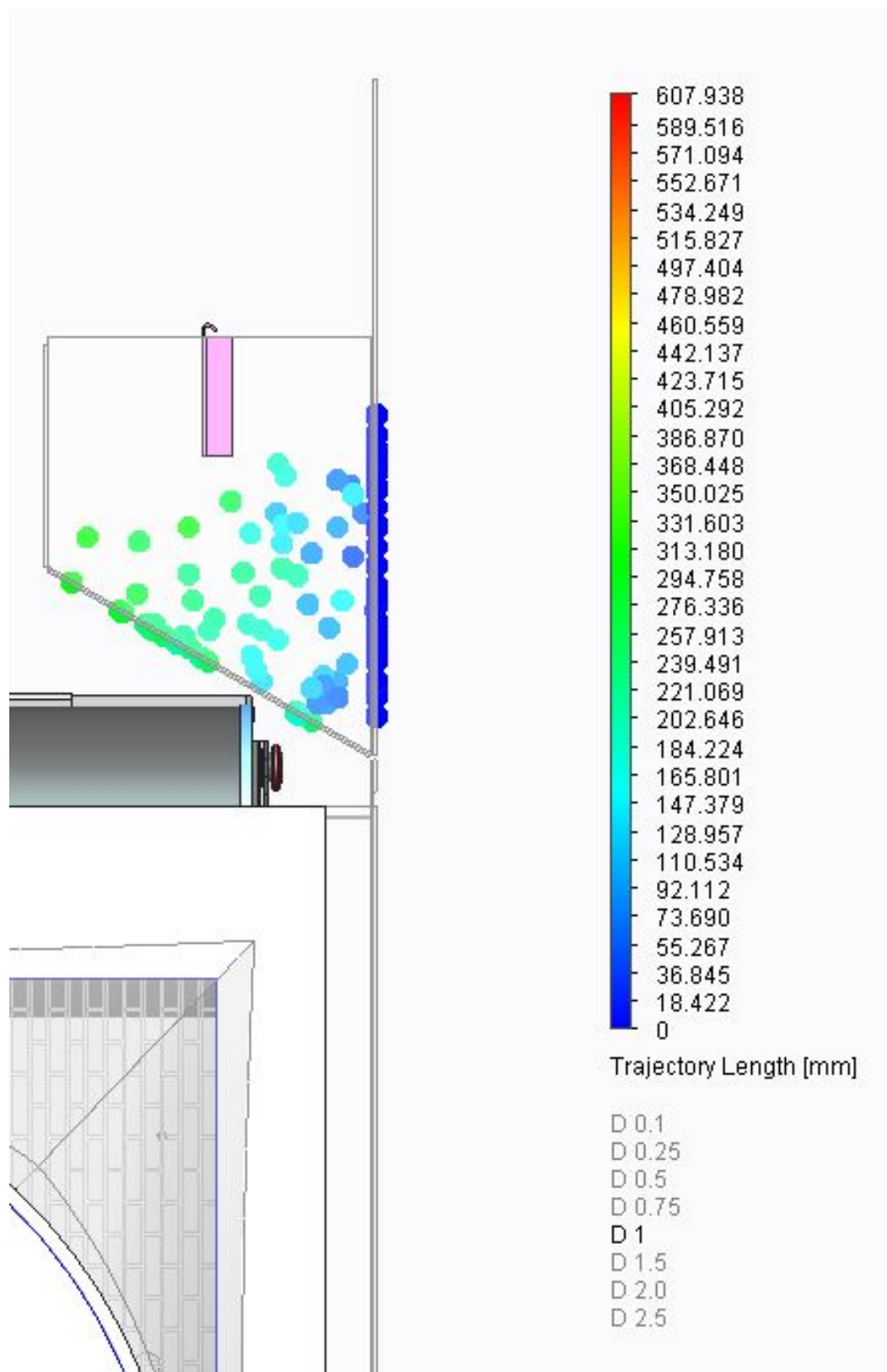


Figure 96 Droplet size 1.0 mm. No penetration

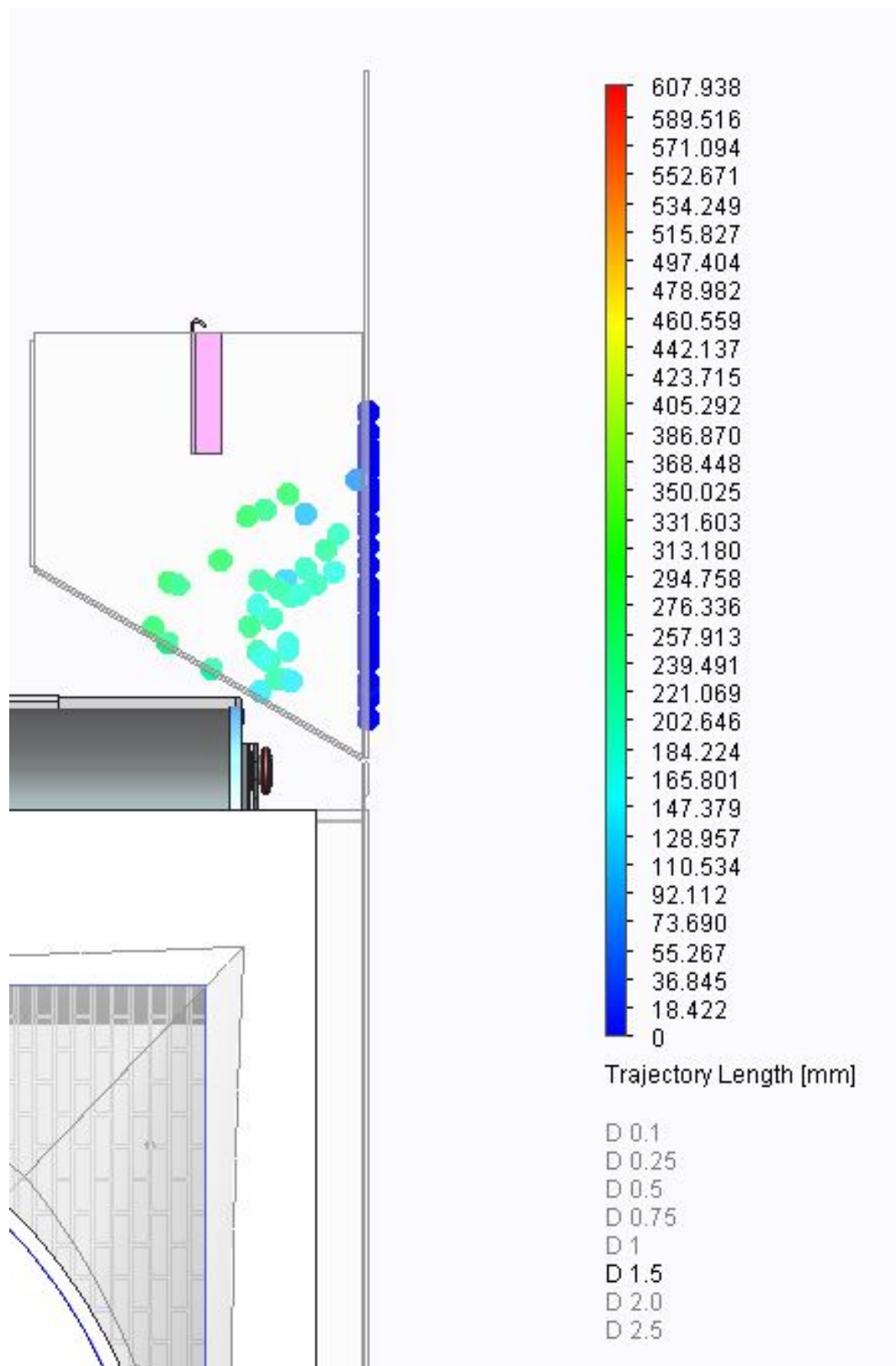


Figure 97 Droplet size 1.5 mm. No penetration

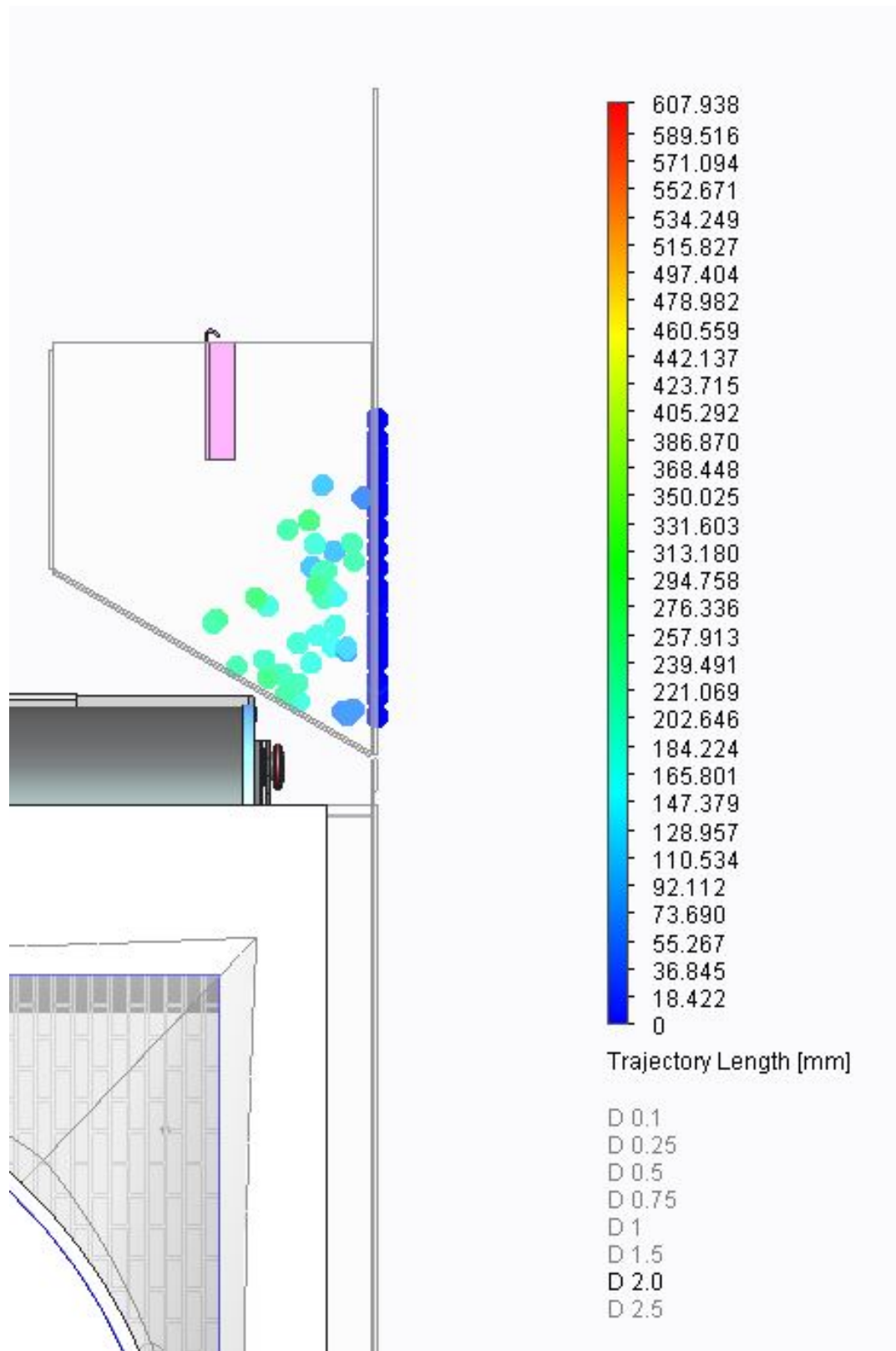


Figure 98 Droplet size 2.0 mm. No penetration

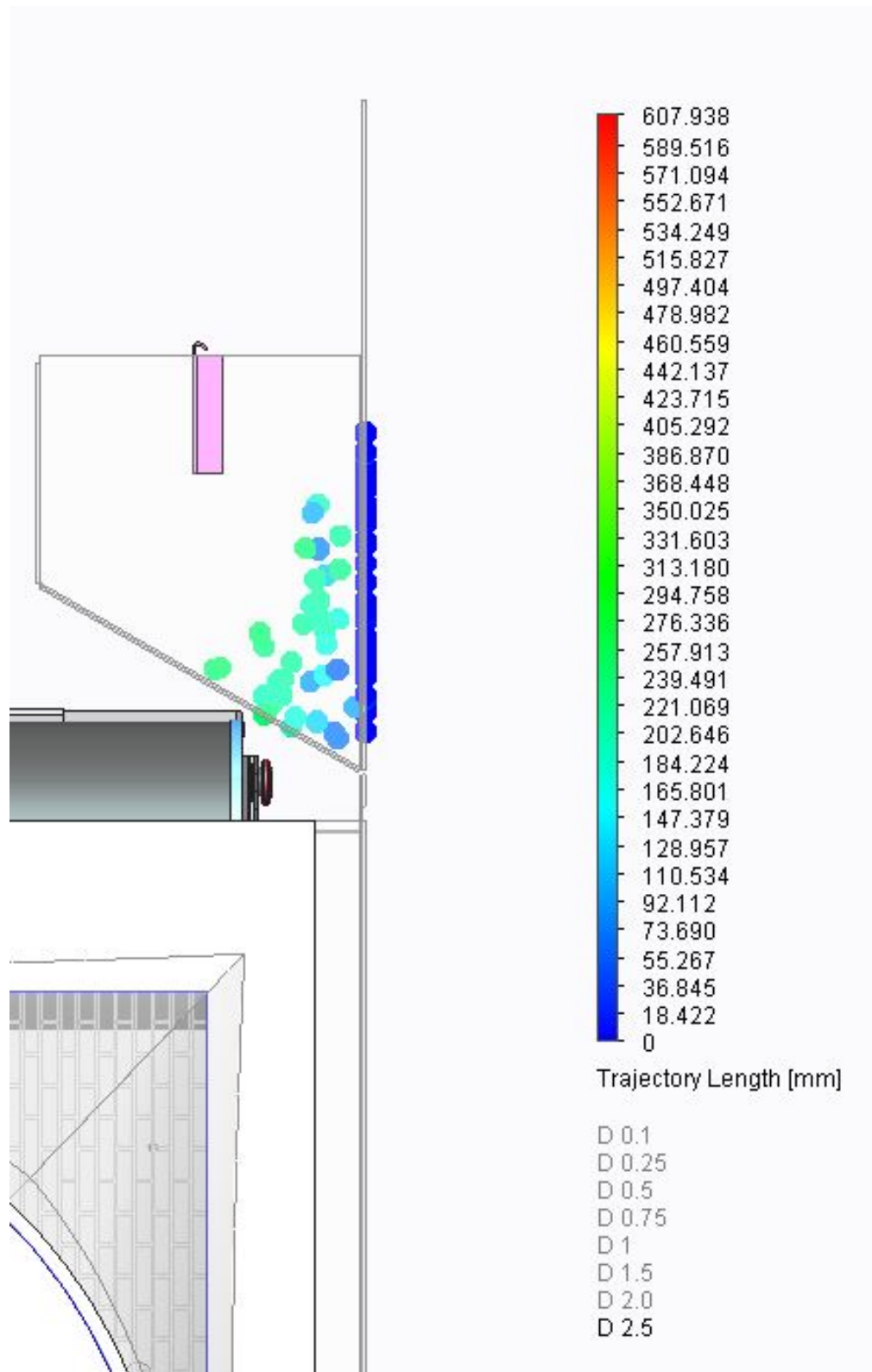


Figure 99 Droplet size 2.5 mm. No penetration

Appendix L

Particle study of water droplets dripping at the blade

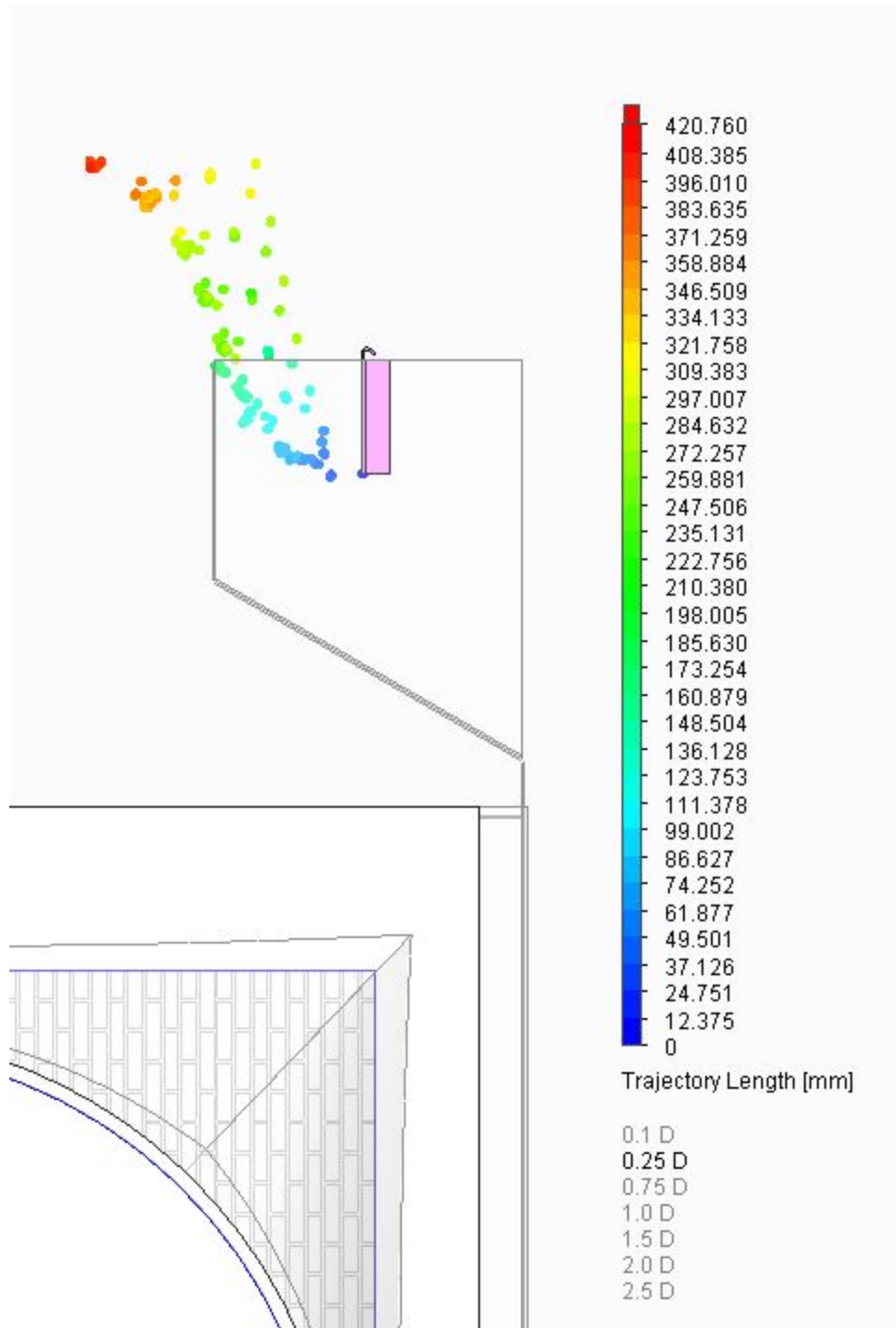


Figure 100 Droplet size 0.25 mm. Water penetration occurs

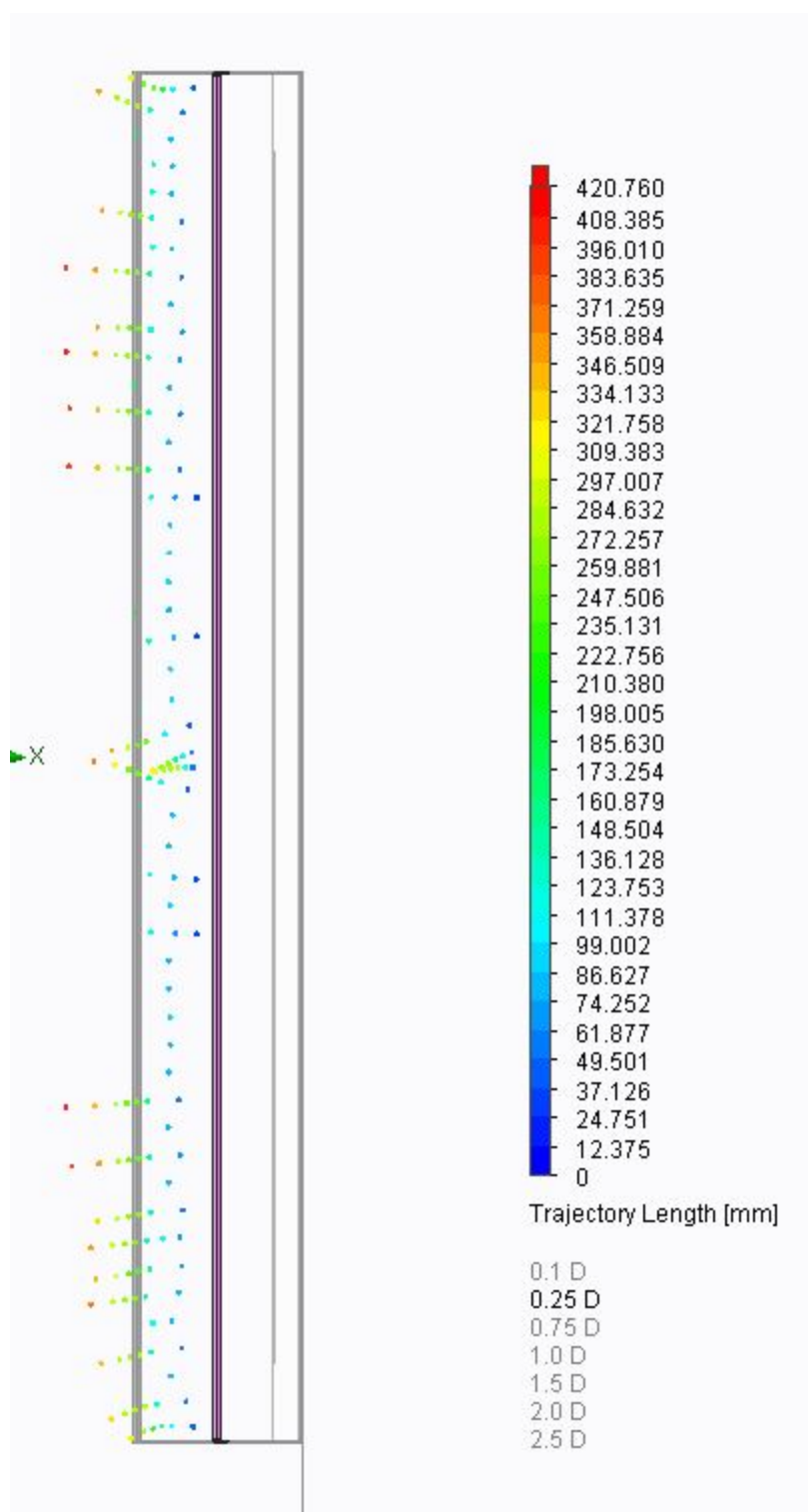


Figure 101 Droplet size 0.25 mm, top view. Water penetration occurs.

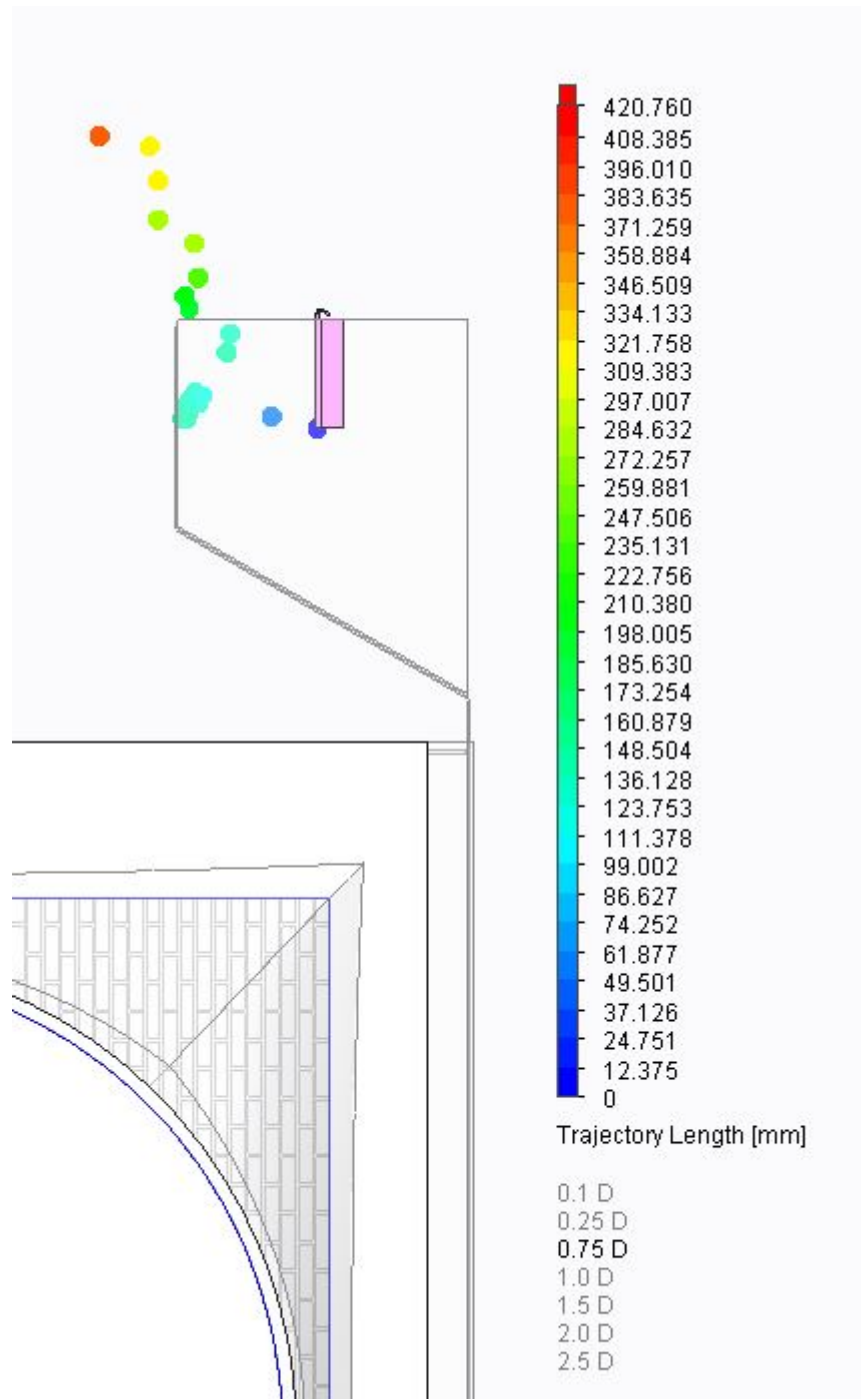


Figure 102 Droplet size 0.75 mm. Water penetration occurs

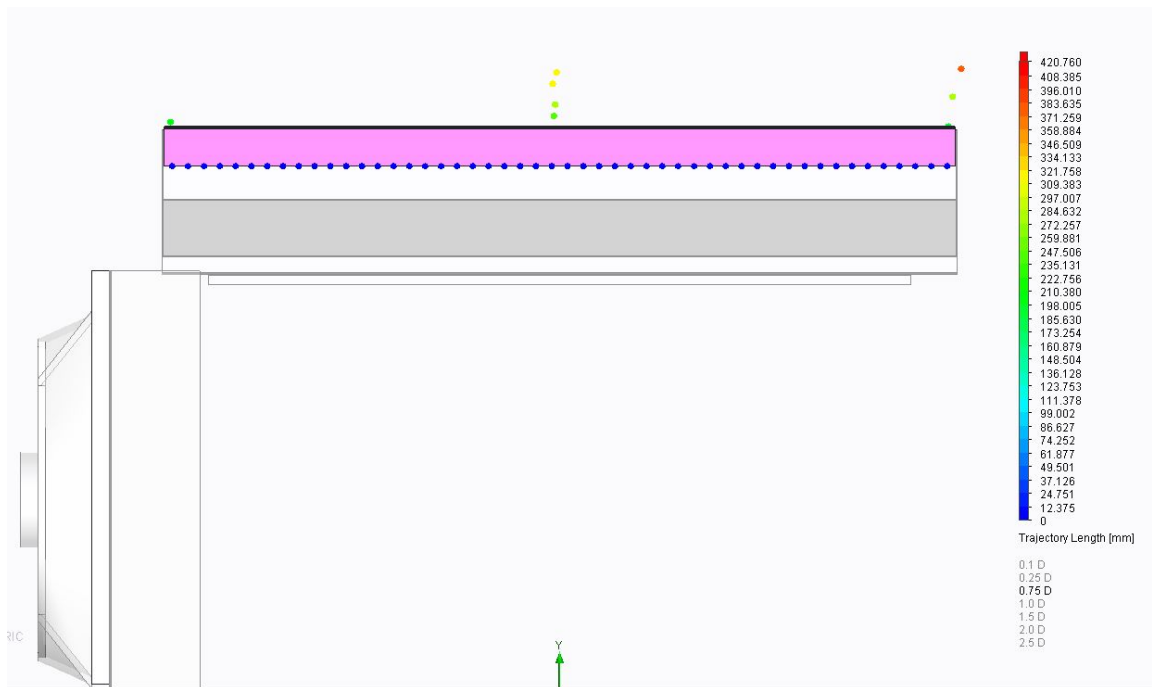


Figure 103 Droplet size 0.75 mm. Water penetration occurs at the middle and two sides

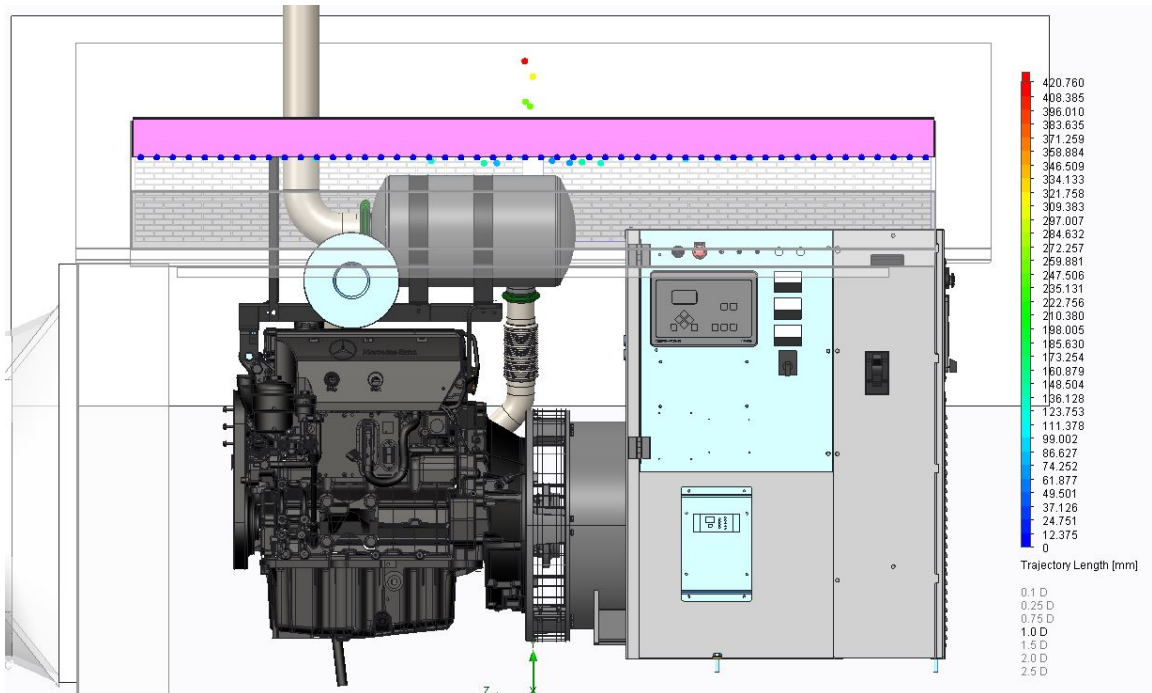


Figure 104 Droplet size 1.0 mm. Penetration only visible in the middle

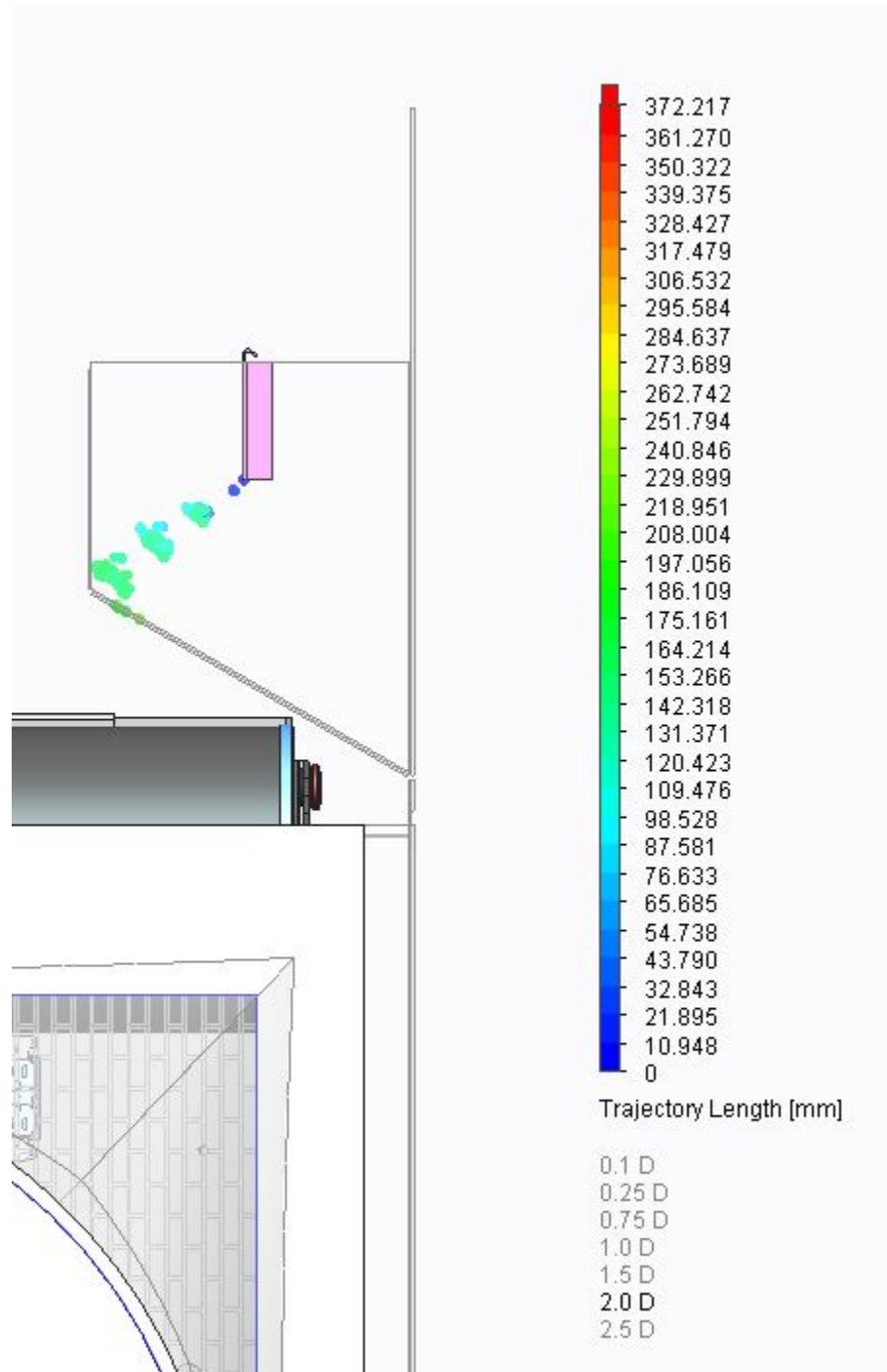


Figure 105 Droplet size 2.0 mm. No penetration

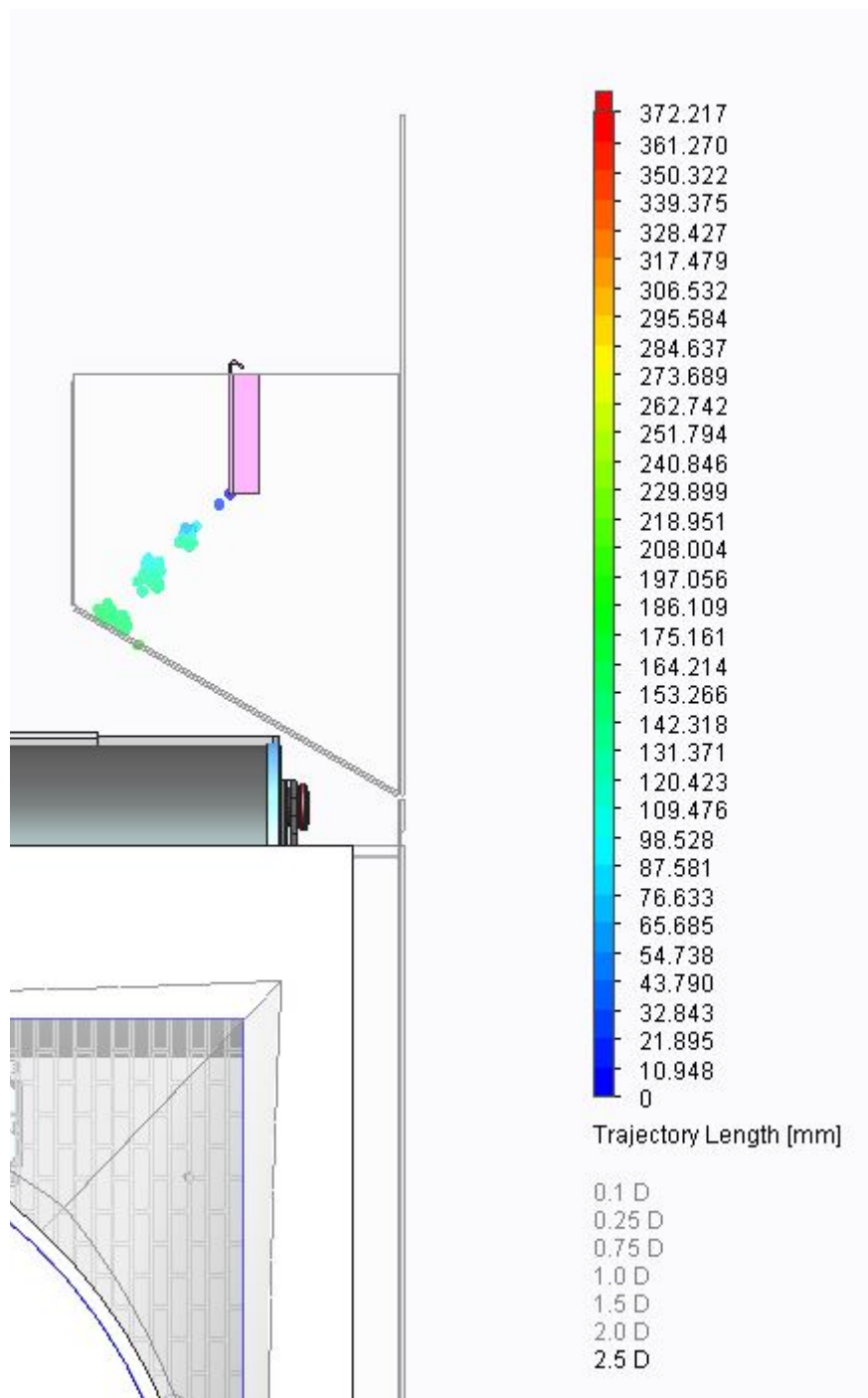


Figure 106 Droplet size 2.5 mm. No penetration

Appendix M

CFD Model Mesh

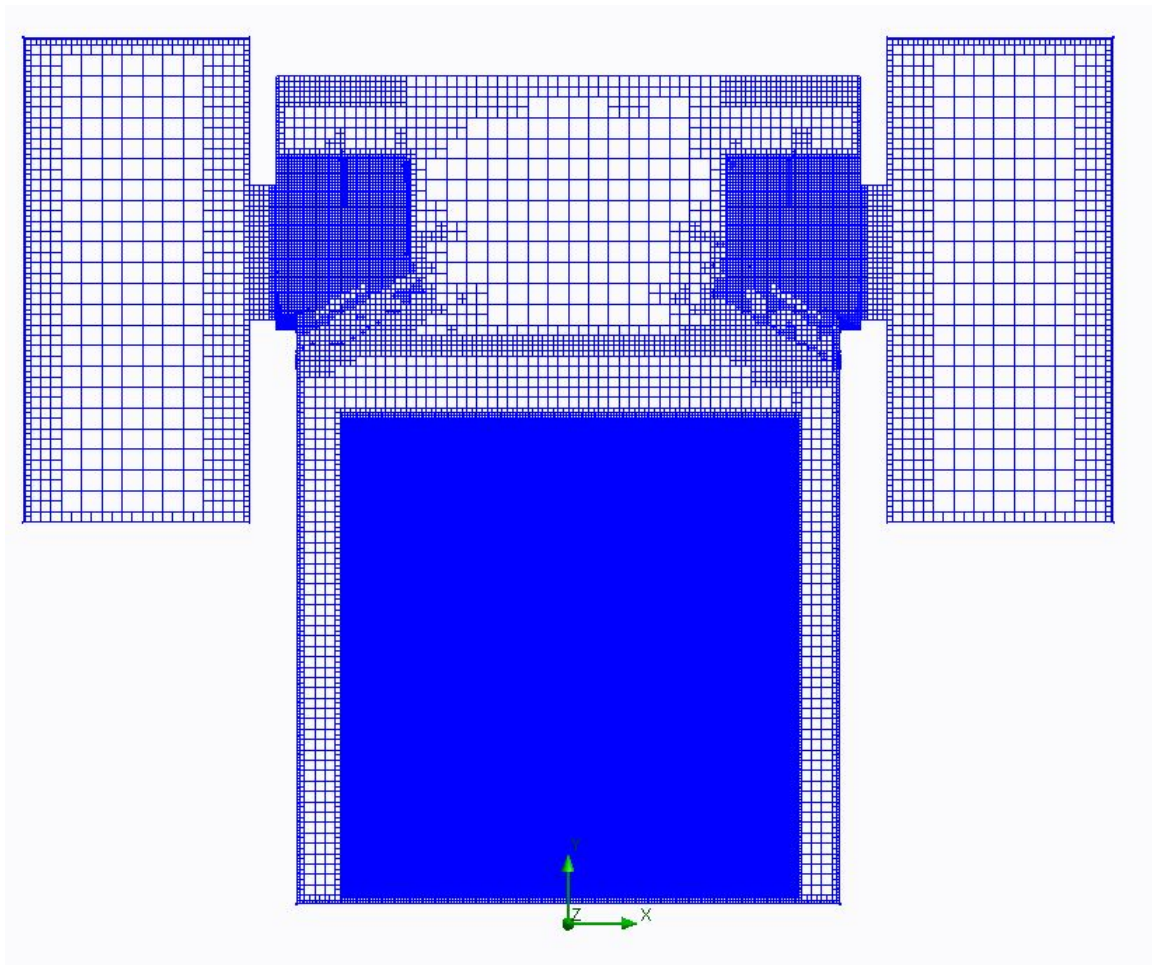


Figure 107 Mesh - Front view

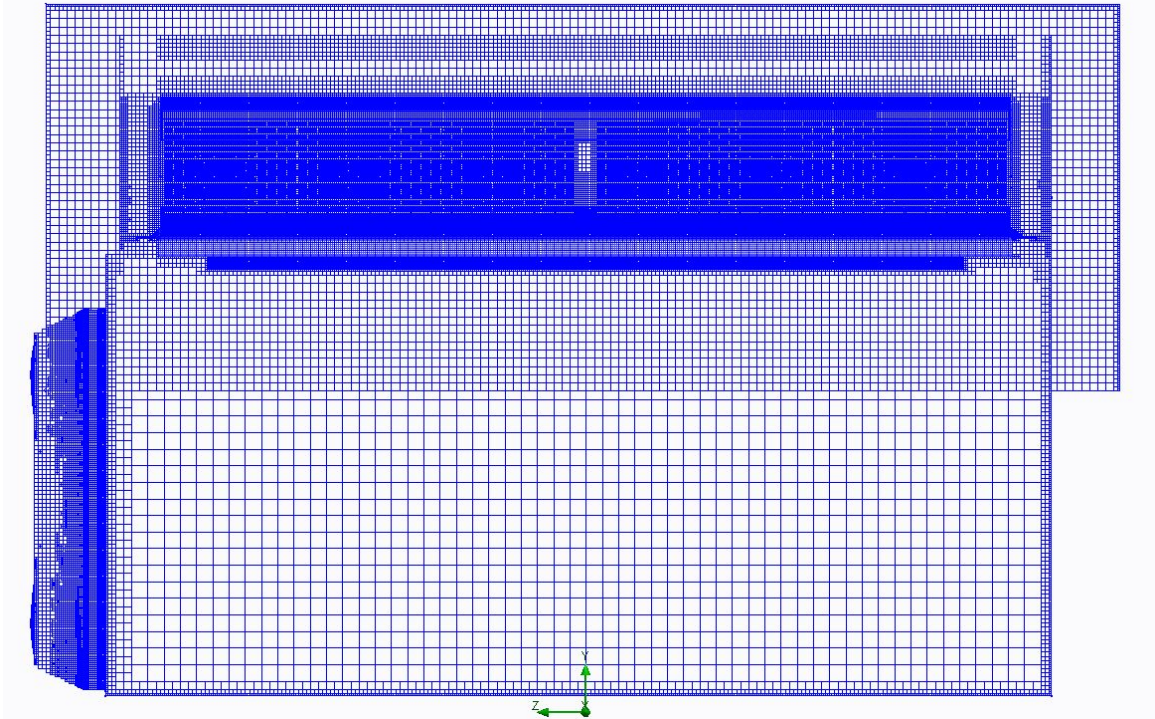


Figure 108 Mesh - Side view

Local finite mesh was assigned to the baffle plate and blade.

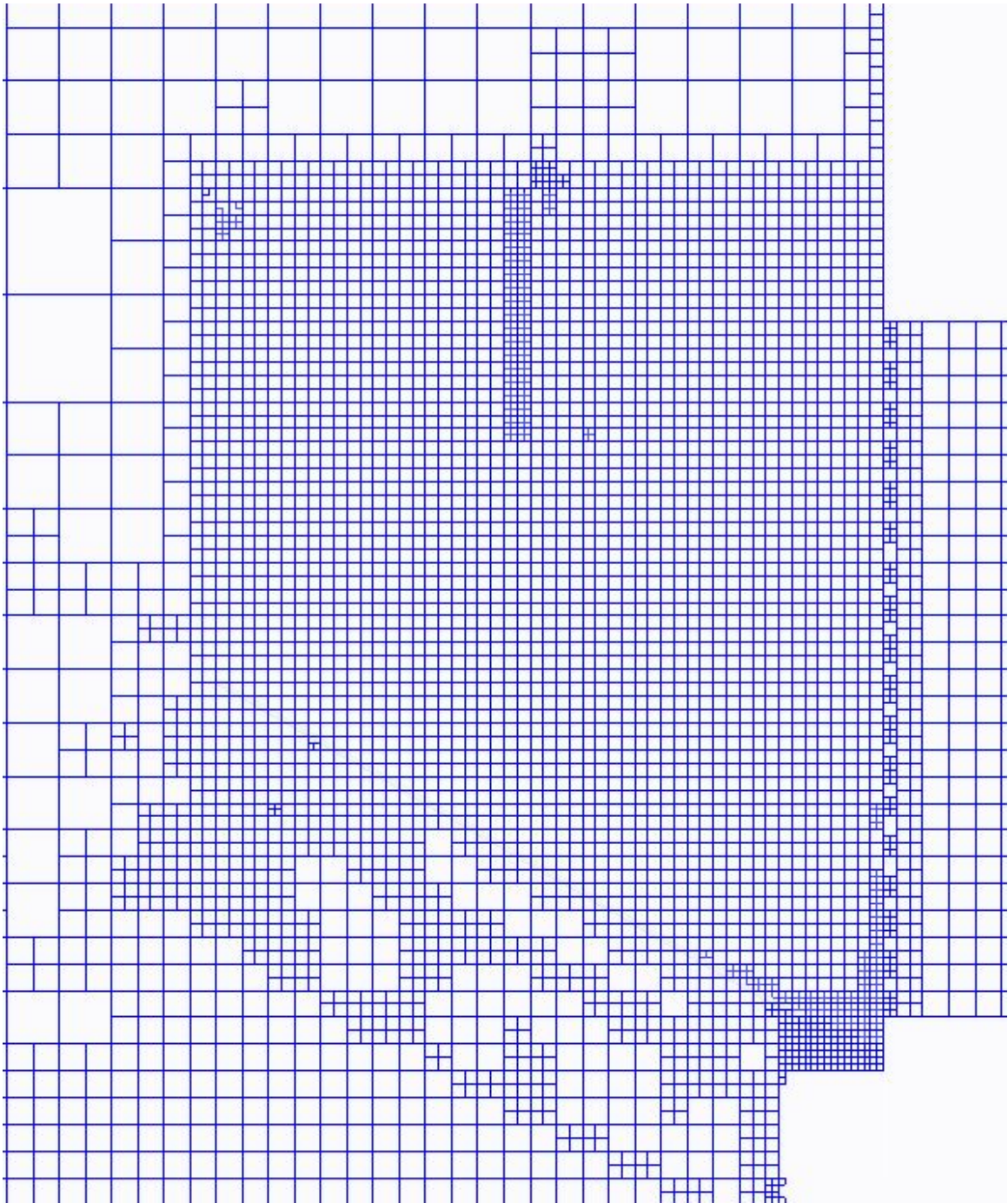


Figure 109 A local initial mesh was assign to baffle plates. Baffle lips are 10mm wide, hence this area needed to be precisely calculated.